Aus dem Bereich Biophysik

Theoretische Medizin und Biowissenschaften

der Medizinischen Fakultät

der Universität des Saarlandes, Homburg/Saar

Synthesis of coenzyme Q_{10} derivatives, their structural and electrochemical characterization, and functional studies on cellular metabolism

Dissertation zur Erlangung des Grades eines Doktors der Naturwissenschaften

der Medizinischen Fakultät

der UNIVERSITÄT DES SAARLANDES

2023

vorgelegt von: Nikolina Mitreska

geb. am: 10.03.1988 in Ohrid, Nordmazedonien

Tag der Promotion: 10.04.2024

Dekan: Univ.-Prof. Dr. med. Michael D. Menger

Berichterstatter: Prof. Dr. Markus Hoth

                       Prof. Dr. Peter Lipp

                       Prof. Dr. Martin Oberringer

Table of Contents

Summary

Quinones and their reduced forms, the hydroquinones, represent a large and vital class of redox-active biomolecules. Among these substances *p*-benzoquinones (*p*-BQ) are one of the most attention-grabbing group of molecules playing pivotal roles in numerous cellular processes. Coenzymes Q (Qs) are derivatives of *p*-BQs containing two neighbouring methoxy groups, a methyl group, and a sidechain whose length is species-dependent. Qs are present in the majority of aerobic organisms with coenzyme Q_{10} (Q_{10}) being the predominant variant in humans. A plethora of physiological roles have been ascribed to Q_{10} starting from its primary and widely recognized function as an electron and proton carrier within the mitochondrial respiratory chain up to its role as an antioxidant and regulator of the cellular redox homeostasis. However, the considerable amounts of Q_{10} found in non-mitochondrial membranes suggest additional cellular functions. Our group has identified a new class of Qs which are specifically modified at position 2- or 3- of the *p*-BQ ring by replacement of the corresponding methoxy group with a hydroxyl group to give mono-hydroxylated forms of Qs (HO-Qs). It has been suggested that HO-Qs have stronger antioxidant activity and improved abilities to transport Ca^{2+} across artificial bio-membranes than their corresponding Qs.

The high hydrophobicity of Q_{10} and its low solubility in numerous solvents impose a major limitation in studying Q_{10}. Therefore, less hydrophobic but still active derivatives of Q_{10}, coenzyme Q_1 (Q_1) and decylubiquinone (dUQ), were utilised here to explore the physico-chemical as well as biological properties of Qs with a particular focus on the HO-Qs.

The main goal of this study was to investigate the interactions between HO-Qs and Qs with Ca^{2+}, and to analyse their (patho-)physiological relevance in terms of a potential impact on cellular and mitochondrial functions.

Since HO-Q_1 and HO-dUQ are commercially not available methods for their synthesis were developed. Structural characterization of the newly synthesized products by mass spectrometry and nuclear magnetic resonance spectroscopy was performed. It was observed that the synthesis consistently yielded a mixture of two constitutional isomers, modified either at position 2- or 3- of the quinone ring, i.e., 2-HO-Q and/or 3-HO-Q.

The physico-chemical and redox properties of the newly produced HO-Q_1 and HO-dUQ as well as of Q_1 and dUQ were investigated by voltammetric techniques. Various conditions including aqueous (buffered and unbuffered) media, organic protic and aprotic solvents were applied to obtain insights into the redox behaviour of HO-Qs and Qs within biological membranes. For instance, in the inner mitochondrial membrane Q_{10} encounters a strong gradient transitioning from a non-aqueous (aprotic) environment within the membrane to increasingly protic conditions toward the membrane surface and ultimately to the fully aqueous environment in the mitochondrial matrix or intermembrane space. The redox processes of Qs and HO-Qs could proceed either as a simultaneous transfer of $2e^-$ in a single step or as a sequential transfer of $1e^-$ at a time, in two separate steps. The outcome depended on factors like solvent type, the presence or absence of protons, the availability of hydrogen bond donors or the presence of metal ions. In

addition, voltammetric studies were conducted to unravel the interactions between Ca^{2+} and Qs or HO-Qs. The data revealed the formation of ion pairs with several stoichiometries, not only between HO-Qs and Ca^{2+} but also between the Qs and Ca^{2+}. Moreover, HO-Qs showed enhanced antioxidant properties and higher affinity for interaction with Ca^{2+} when compared to the corresponding Qs. Biologically important was the finding that HO-Qs are present as monoanions at neutral pH, i.e., the −OH group at ring position 2 or 3 tends to deprotonate.

Finally, the potential physiological relevance of HO-Q_1 and HO-dUQ was assessed. At this point, additional related compounds such as mitoquinone (mQ), its hydroxylated form (HO-mQ), Q_{10} and HO-Q_{10} were included in the comparative studies. As the efficiency of cell treatment with Q_{10} and HO-Q_{10} is greatly hampered by their insolubility in aqueous media, water-soluble formulations of Q_{10} and HO-Q_{10} were prepared and used for applications to biological samples. Prior to the functional studies, the intracellular concentrations of Q_{10} and HO-Q_{10} in HEK-293 cells were determined before and after supplementation of the cells with water-soluble formulations of Q_{10} and HO-Q_{10}. Since Q_{10} is the predominant form of Qs in human cells, a certain amount of Q_{10} was detected in the untreated HEK-293 cells. In contrast, HO-Q_{10} was not detected in the untreated controls. HPLC data conducted 30 minutes after supplementation of the cells with the corresponding compounds showed significantly elevated contents of Q_{10} and HO-Q_{10} indicating that the compounds efficiently passed through the plasma membrane and were accumulated in the cells.

Assessing the toxicity of exogenously applied Qs and HO-Qs significant alterations in cell viability after treatment with mQ and to a lesser extent with HO-mQ were revealed. Additionally, mQ and HO-mQ substantially affected mitochondrial membrane potential, mitochondrial bioenergetics, and cellular Ca^{2+} homeostasis, strongly indicating cytotoxic effects.

Mitochondrial respiration was evaluated measuring O_2 consumption of isolated murine heart mitochondria using a *Clark*-type electrode. Notably, all HO-Qs hindered mitochondrial respiration. On the contrary, Qs showed diverse impacts, either by stimulating (Q_1 and dUQ) or inhibiting (Q_{10}, only in the presence of Ca^{2+}) the respiration. The most striking result was that only HO-Q_{10} and Q_{10} showed Ca^{2+}-dependent inhibitions of the respiration, whereas the other HO-Qs inhibited respiration independently of the presence of Ca^{2+}. However, no alterations in cytosolic Ca^{2+} levels following treatment of HEK-293 cells with Q_{10} and HO-Q_{10} were observed. Immediately after application of HO-dUQ, a gradual increase in the cytosolic Ca^{2+} levels of HEK-293 cells was observed which was caused by Ca^{2+} release from the intracellular Ca^{2+} stores, presumably from mitochondria.

In conclusion, Q_{10}-like compounds such as Q_1, dUQ, mQ and their hydroxylated derivatives albeit having similar redox properties showed different biological activities compared to Q_{10}. Their variable functions in living cells and isolated mitochondria clearly indicated that they cannot substitute for each other probably due to different interactions to relevant membrane and protein components, hence caution should be taken when designating them as analogues of Q_{10}.

Zusammenfassung

Chinone und ihre reduzierten Formen, die Hydrochinone, stellen eine große und wichtige Klasse von redoxaktiven Biomolekülen dar. Unter diesen Substanzen sind die *p*-Benzochinone (*p*-BQ) eine der interessantesten Molekülgruppen, die bei zahlreichen zellulären Prozessen eine wichtige Rolle spielen. Die Coenzyme Q (Qs) sind Derivate von *p*-BQs, die zwei benachbarte Methoxygruppen, eine Methylgruppe und eine Seitenkette enthalten, deren Länge von der Spezies abhängt. Die Qs sind in den meisten aeroben Organismen vorhanden, wobei Coenzym Q_{10} (Q_{10}) beim Menschen die Hauptvariante ist. Dem Q_{10} wird eine Vielzahl physiologischer Funktionen zugeschrieben, von seiner primären und weithin anerkannten Funktion als Elektronen- und Protonenüberträger innerhalb der mitochondrialen Atmungskette bis zu seiner Rolle als Antioxidans und Regulator der zellulären Redox-Homöostase. Die beträchtlichen Mengen an Q_{10}, die in nicht-mitochondrialen Membranen gefunden wurden, suggerieren allerdings zusätzliche zelluläre Funktionen. Unsere Gruppe hat eine neue Klasse von Qs identifiziert, die spezifisch an Position 2 oder 3 des *p*-BQ-Rings modifiziert sind, indem die entsprechende Methoxygruppe durch eine Hydroxylgruppe substituiert wird, um monohydroxylierte Formen von Qs (HO-Qs) zu erhalten. Den HO-Qs werden verbesserte Eigenschaften zugeschrieben als den entsprechenden Qs, z. B. eine stärkere antioxidative Aktivität und die Fähigkeit, um Ca^{2+} durch artifizielle Biomembranen zu transportieren.

Die ausgeprägte Hydrophobizität von Q_{10} und seine geringe Löslichkeit in zahlreichen Lösungsmitteln stellen eine große Einschränkung bei der Untersuchung von Q_{10} dar. Daher wurden hier Coenzym Q_1 (Q_1) und Decylubiquinon (dUQ) als weniger hydrophobe aber immer noch aktive Q_{10}-Derivate verwendet, um die physikalisch-chemischen und biologischen Eigenschaften von Qs mit besonderem Fokus auf den HO-Qs zu untersuchen.

Das Hauptziel dieser Studie bestand darin, die Interaktionen zwischen HO-Qs und Qs mit Ca^{2+} zu untersuchen und folglich ihre (patho-)physiologische Relevanz im Hinblick auf mögliche Auswirkungen auf zelluläre und mitochondriale Funktionen aufzuklären.

Da HO-Q_1 und HO-dUQ kommerziell nicht erhältlich sind, wurden Methoden für ihre Synthese entwickelt. Die neu synthetisierten Produkte wurden mittels Massenspektrometrie und Kernspinresonanzspektroskopie strukturell charakterisiert. Es wurde festgestellt, dass die Synthese konsistent ein Gemisch aus zwei konstitutionellen Isomeren ergeben hat, die entweder an der Position 2 oder 3 des Chinonrings modifiziert waren, d.h. 2-HO-Q und/oder 3-HO-Q.

Die physikalisch-chemischen und redoxspezifischen Eigenschaften der neu hergestellten HO-Q_1 und HO-dUQ sowie von Q_1 und dUQ wurden mit voltammetrischen Techniken untersucht. Verschiedene Bedingungen, darunter wässrige (gepufferte und ungepufferte) Lösungen, organische protische und aprotische Lösungsmittel wurden angewandt, um Einblicke in das Redoxverhalten von HO-Qs und Qs in biologischen Membranen zu erhalten. Beispielsweise trifft Q_{10} in der inneren Mitochondrienmembran auf einen Gradienten von Bedingungen, der von einem nichtwässrigen (aprotischen) Umfeld innerhalb der Membran zu mehr protischen Bedingungen an der Membranoberfläche und schließlich zu einer vollständig wässrigen

Umgebung in der Mitochondrienmatrix oder im Intermembranraum wechselt. Die Redoxprozesse von Qs und HO-Qs können entweder als gleichzeitiger Transfer von $2e^-$ in einem einzigen Schritt oder als sequentieller Transfer von jeweils $1e^-$ in zwei getrennten Schritten ablaufen. Der Verlauf war abhängig von Faktoren wie der Art des Lösungsmittels, der An- oder Abwesenheit von Protonen, der Verfügbarkeit von Wasserstoffbrückendonoren oder der Anwesenheit von metallischen Ionen. Voltammetrische Untersuchungen haben dazu beigetragen, die Interaktionen zwischen Ca^{2+} und Qs oder HO-Qs zu entschlüsseln. Die Daten zeigten die Bildung von Ionenpaaren mit verschiedenen Stöchiometrien, nicht nur zwischen HO-Qs und Ca^{2+}, sondern auch zwischen den Qs und Ca^{2+}. Außerdem zeigten die HO-Qs im Vergleich zu den entsprechenden Qs verbesserte antioxidative Eigenschaften und eine höhere Affinität zur Interaktion mit Ca^{2+}. Biologisch wichtig war die Feststellung, dass HO-Qs bei neutralem pH-Wert als Monoanionen existieren, d. h. die -OH-Gruppe an Ringposition 2 oder 3 tendiert zur Deprotonierung.

Schließlich wurde die potenzielle physiologische Bedeutung von $HO-Q_1$ und HO-dUQ bewertet. An diesem Punkt wurden weitere verwandte Substanzen wie Mitochinon (mQ), seine hydroxylierte Form (HO-mQ), Q_{10} und $HO-Q_{10}$ in vergleichende Studien einbezogen. Da die Effizienz der Zellbehandlung mit Q_{10} und $HO-Q_{10}$ durch ihre Unlöslichkeit in wässrigen Lösungen stark eingeschränkt ist, wurden wasserlösliche Formulierungen von Q_{10} und $HO-Q_{10}$ hergestellt und auf biologische Proben angewendet. Im Vorfeld zu den Funktionsstudien wurden die intrazellulären Konzentrationen von Q_{10} und $HO-Q_{10}$ in HEK-293-Zelllysaten unter physiologischen Bedingungen und nach Behandlung der Zellen mit Q_{10} und $HO-Q_{10}$ gemessen. Nachdem die Zellen für 30 Minuten den Substanzen exponiert waren, zeigten die HPLC-Daten einen dreifachen Anstieg der Q_{10}-Menge im Vergleich zu den unbehandelten Kontrollen. Obwohl $HO-Q_{10}$ unter physiologischen Bedingungen nicht gefunden werden konnte, war es nach seiner Anwendung deutlich im Zellhomogenat vorhanden.

Bei der Evaluierung der Toxizität von exogen applizierten Qs und HO-Qs wurden signifikante Veränderungen der Zellproliferation nur nach der Behandlung mit mQ und in geringerem Ausmaß mit HO-mQ gefunden. Weiterhin zeigten die Daten, dass mQ und HO-mQ das mitochondriale Membranpotenzial, die mitochondriale Bioenergetik und die zelluläre Ca^{2+}-Homöostase erheblich beeinflussten, was stark auf zytotoxische Wirkungen hinweist.

Die mitochondriale Respiration wurde durch Messung des O_2-Verbrauchs isolierter Mitochondrien des Mäuseherzens mit Hilfe einer *Clark*-Elektrode evaluiert. Bemerkenswert ist, dass alle HO-Qs die mitochondriale Respiration inhibierten. Im Gegensatz dazu zeigten die Qs unterschiedliche Effekte, indem sie die Respiration entweder stimulierten (Q_1 und dUQ) oder inhibierten (Q_{10}, nur in Anwesenheit von Ca^{2+}). Das auffälligste Ergebnis war, dass nur $HO-Q_{10}$ und Q_{10} eine Ca^{2+}-abhängige Inhibierung der Respiration zeigten, während die anderen HO-Qs die Respiration unabhängig von der Anwesenheit von Ca^{2+} inhibierten. Es wurden jedoch keine Veränderungen des zytosolischen Ca^{2+}-Niveaus nach der Behandlung von HEK-293-Zellen mit Q_{10} und $HO-Q_{10}$ beobachtet. Gleich nach der Applikation von HO-dUQ wurde ein gradueller

Anstieg des zytosolischen Ca^{2+}-Niveaus in HEK-293-Zellen beobachtet, der nachweislich auf die Freisetzung von Ca^{2+} aus den intrazellulären Ca^{2+}-Speichern, vermutlich aus den Mitochondrien, zurückzuführen ist.

Zusammenfassend kann festgestellt werden, dass Q_{10}-ähnliche Substanzen, obwohl sie ähnliche Redox-Eigenschaften haben, unterschiedliche biologische Aktivitäten im Vergleich zu Q_{10} zeigen. Die elektrochemischen Eigenschaften von Qs und HO-Qs sowie ihre unterschiedlichen Funktionen in lebenden Zellen und isolierten Mitochondrien wiesen eindeutig darauf hin, dass sie einander nicht ersetzen können und dass bei ihrer Benennung als Analoga von Q_{10} Vorsicht geboten ist.

Glossary

List of Abbreviations

Acronym	Definition
$[Ca^{2+}]$	concentration of calcium ions
$[Ca^{2+}]_c$	cytosolic concentration of calcium ions
$[Ca^{2+}]_i$	intracellular concentration of calcium ions
^1H NMR	proton nuclear magnetic resonance spectroscopy
2PHQ	2-palmitoylhydroquinone
ACN	acetonitrile
ADP	adenosine diphosphate
ANOVA	analysis of variance
ATP	adenosine triphosphate
AU	absorbance units
BN-PAGE	blue native polyacrylamide gel electrophoresis
BQ	benzoquinone
CE	counter electrode
CHDH	choline dehydrogenase
CI	complex I; NADH:ubiquinone oxidoreductase
CII	complex II; succinate dehydrogenase
CIII	complex III; ubiquinol-cytochrome *c* oxidoreductase
CIV	complex IV; cytochrome *c* oxidase
CV	complex V; ATP synthase
CYP450	cytochrome P450 enzyme
cyt *c*	cytochrome *c*
$CytB_5R_3$	cytochrome b_5 reductase 3
DHODH	dihydroorotate dehydrogenase
DPBS	*Dulbecco*'s phosphate-buffered saline, [-] $CaCl_2$, [-] $MgCl_2$
DPBS^{++}	*Dulbecco*'s phosphate-buffered saline, [+] $CaCl_2$, [+] $MgCl_2$
dUQ	decylubiquinone
EPR	electron paramagnetic resonance spectroscopy
ER	endoplasmic reticulum
ETC	electron transport chain
ETF-Q_0	electron transfer flavoprotein oxidoreductase
$FADH_2$	flavin adenine dinucleotide
FCS	fetal calf serum
Fe-S	iron-sulphur cluster
FMN	flavin mononucleotide
FSP1	CoQ oxidoreductase ferroptosis suppressor protein 1
G3PDH	glycerol-3-phosphate dehydrogenase
GCE	glassy carbon electrode
GPDH	FAD-glycerol-3-phosphate dehydrogenase
GPX4	glutathione peroxidase 4

Acronym	Definition
HEK-293 cells	human embryonic kidney 293 cell line
HO-dUQ	mono-hydroxylated decylubiquinone
HO-mQ	mono-hydroxylated mitoquinone
HO-Q	mono-hydroxylated quinone
HO-Q_1	mono-hydroxylated coenzyme Q_1
HO-Q_{10}	mono-hydroxylated coenzyme Q_{10}
IDH	NAD^+-isocitrate dehydrogenase
Im	ionomycin
IMM	inner mitochondrial membrane
IMS	intermembrane space
IP_3R	inositol-1,4,5-trisphosphate receptor
LC-MS	liquid chromatography - mass spectrometry
LDL	low density lipoprotein
LETM1	leucine zipper EF-hand-containing transmembrane protein 1
MCU	mitochondrial calcium uniporter
MEM	minimum essential medium
MM	mitochondrial matrix
mPTP	mitochondrial permeability transition pore
mQ	mitoquinone
MS	mass spectrometry
MS/MS	tandem mass spectrometry
NADH	nicotinamide adenine dinucleotide
NCLX	$Na^+/Ca^{2+}/Li^+$ exchanger
NCX	Na^+/Ca^{2+} exchanger
NMR	nuclear magnetic resonance spectroscopy
NQO1	NAD(P)H:quinone acceptor oxidoreductase 1
o-BQ	1,2-benzoquinone
OCR	oxygen consumption rate
ODH	oxoglutarate dehydrogenase
OMM	outer mitochondrial membrane
ORAI	calcium release-activated calcium modulator protein
OXPHOS	oxidative phosphorylation
p-BQ	1,4-benzoquinone
PCS	polyoxyethanyl-cholesteryl sebacate
PDH	pyruvate dehydrogenase
PMCA	plasma membrane calcium ATPase
PMRS	plasma membrane redox system
PRODH	proline dehydrogenase
Q	quinone
Q_1	coenzyme Q_1
Q_{10}	coenzyme Q_{10}

Acronym	Definition
qNMR	quantitative nuclear magnetic resonance
RB	respiration buffer
RE	reference electrode
RET	reverse electron transport
RFU	relative fluorescence unit
ROS	reactive oxygen species
RP-HPLC	reversed-phase high-performance liquid chromatography
RyR	ryanodine receptor
SC	supercomplex
SERCA	sarcoplasmic/endoplasmic reticulum calcium ATPase
SOCE	store-operated calcium entry
SQOR	sulfide:quinone oxidoreductase
STIM	stromal interaction molecule
TCA cycle	tricarboxylic acid cycle
Tg	thapsigargin
TMRM	tetramethylrhodamine methyl ester
TRPC	transient receptor potential channel
$TRPC_3$	canonical short transient receptor potential channel 3
UCP	uncoupling protein
UV-Vis	ultraviolet-visible spectroscopy
VDAC	voltage-dependent anion-selective channel
WE	working electrode

List of Symbols

Symbol (Unit)	Definition
A	absorbance
A (m^2)	area of the electrode
c (m/s)	velocity of light
c (mol/dm^3)	molar concentration
d (m)	path length
D (m^2/s)	diffusion coefficient
E	energy
e^-	electron
E (V)	equilibrium potential of the electrode/applied electrode potential
$E_{p,a}$ (V)	anodic peak potential
$E_{p,c}$ (V)	cathodic peak potential
$E_{p,mid}$ (V)	midpoint peak potential
$E_{p,net}$ (V)	net peak potential
E_{sw} (V)	square-wave amplitude
$E^{\theta\prime}$ (V)	formal potential of a redox couple Ox/Red
F	*Faraday*'s constant (96484.6 C/mol)

Symbol (Unit)	Definition
f (Hz)	square-wave frequency
h	*Planck*'s constant
I (A)	current
$I_{p,a}$ (A)	anodic peak current
$I_{p,c}$ (A)	cathodic peak current
$I_{p,net}$ (A)	net peak current
K_a	acid dissociation constant
K_d	dissociation constant
K_M	*Michaelis* constant
M (g/mol)	molar mass
m/z	mass-to-charge ratio
R	universal gas constant (8.314 J/K·mol)
T (K)	absolute temperature
δ (m)	thickness of diffusion layer
δ (ppm)	chemical shift
Δp	electrochemical proton gradient
$\Delta\Psi_m$	mitochondrial membrane potential
$\Delta\Psi_p$	plasma membrane potential
ε (dm^3/mol·cm)	molar absorption coefficient
λ (m)	wavelength
v (Hz)	frequency
v (V/s)	scan rate

List of Figures

List of Tables

1. Introduction

Quinones and their reduced forms, the hydroquinones, comprise a large and important class of redox active organic compounds. Their wide-spread distribution in nature, intriguing chemical properties, biological activity, and physiological relevance have prompted extensive studies of these systems across several disciplines from applied chemistry to life sciences. For instance, their well-known proficiency in biology for energy conservation/transduction has stimulated interest for application of quinones in Li/Na batteries[1]. On the other hand, biological activity and significance of quinones have been investigated and reported for decades. Therefore, some of them are already in use and presented among the essential medicines by the World Health Organization (WHO). Others are under clinical evaluation toward various diseases in phase II to phase IV clinical trials[1].

Benzoquinones (BQs), molecules with quinoid structure are one of the most attention-grabbing substances, playing an essential role in both, chemistry and biology. As shown in Figure 1-1, BQs are characterized by an ortho (*o*-; 1,2-) or para (*p*-; 1,4-) substituted dione which is conjugated either to an aromatic ring (a, b) or to a condensed polycyclic aromatic system as naphthoquinones (c, d), anthraquinones (e) as well as more complex polyquinones[2].
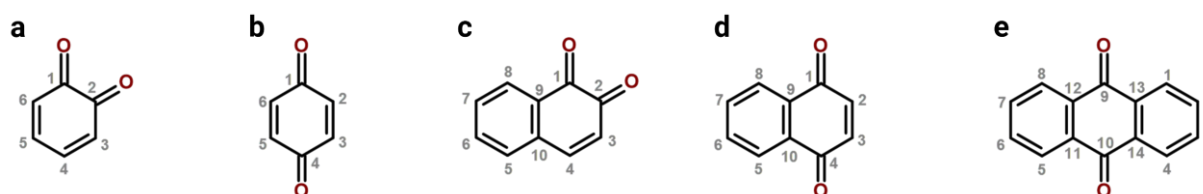
Figure 1-1 Chemical structures of quinones. a) 1,2-benzoquinone, *o*-benzoquinone; b) 1,4-benzoquinone, *p*-benzoquinone; c) *o*-naphthoquinone; d) *p*-naphthoquinone and e) anthraquinone. Numbers show the position of the substituent on the benzoquinone ring.

BQs are common constituents of biologically relevant molecules such as coenzyme Q_{10} (oxidative phosphorylation), plastoquinone (photosynthesis), dopamine (neurotransmission), vitamin K_1 (blood coagulation), catecholamine (cell signalling) and many other cellular processes[3,4].

Coenzymes Q (Qs), also known as ubiquinones, are derivatives of *p*-benzoquinones found in most aerobic organisms from bacteria to mammals, with coenzymes Q_{10} (Q_{10}) being the main species found in humans. Q_{10} was isolated from beef heart mitochondria for the first time by F. Crane in 1957[5]. In the same year, Morton[6] defined a compound obtained from vitamin A-deficient rat liver to be the same as Q_{10} introducing the name ubiquinone (ubiquitous, found everywhere). In 1958, Folkers *et al.*[7] at *Merck Inc.* determined the precise chemical structure of Q_{10}, synthesized it, and were the first to produce it by the process of fermentation. In 1978, Peter Mitchell[8] received the Nobel Prize in Chemistry for the formulation of chemiosmotic theory and his contribution to the understanding of biological energy transfer in cells which included the vital role of Q_{10} in such systems.

1.1 State of the art

Coenzymes Q (Qs) are a group of lipid-soluble quinones, based on the 1,4-benzoquinone (*p*-BQ) structure, where the ring is fully substituted with two adjacent methoxy groups at position 2- and

3-, a methyl group at 5-, and an isoprene sidechain at position 6- of the ring with a species-dependent length (Figure 1-2 a). In humans, coenzyme Q_{10} (Q_{10}) is the main species (Figure 1-2 b), rodents contain coenzyme Q_9 (Q_9) as the main Q analogue together with a small amount of Q_{10}, aerobic bacteria such as *Escherichia coli* (*E. coli*) and yeast like *Saccharomyces cerevisiae* (*S. cerevisiae*) have Q_8 and Q_6 as their main analogues, respectively. On the other hand, Qs with shorter isoprene sidechains than Q_6 are not observed in living organisms[9].
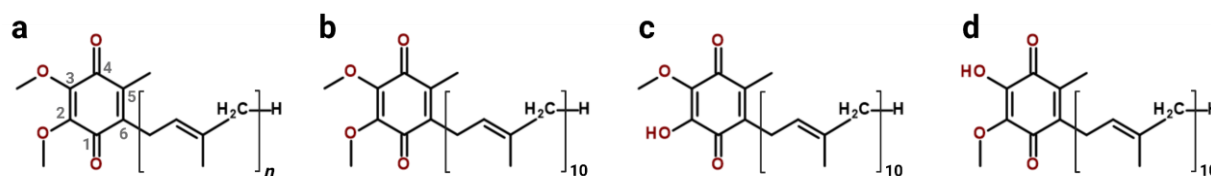
Figure 1-2 Chemical structures of coenzymes Q, coenzyme Q_{10} and its hydroxylated analogues. a) Coenzyme Q, numbers show the position of the substituent on the benzoquinone ring, *n* gives the number of isoprene units which is species-dependent, e.g., 10, 9, 8 and 6 in humans, rodents, *E. coli* and *S. cerevisiae*, respectively. b) Coenzyme Q_{10} (Q_{10}); c) 2-hydroxy coenzyme Q_{10} (2-HO-Q_{10}) and d) 3-hydroxy coenzyme Q_{10} (3-HO-Q_{10}).

In 2011, Bogeski *et al*.[10] synthesized demethylated Q derivatives of Q_{10} and coenzyme Q_1 (Q_1), in which either one or both methoxy groups were replaced with a hydroxyl group (Figure 1-2 c and d). To emphasize the introduction of the hydroxyl groups, the authors named these products as hydroxy coenzymes Q (HO-Q). Substitution of the methoxy group can be performed chemically by exposure of Qs to strong alkaline aqueous solutions[10–14] or upon action of cytochrome P450 enzyme (CYP450)[10]. Biologically relevant was the finding that Q_{10} could be biosynthetically transformed to the hydroxylated species by cytochrome P450 enzyme CYP1B1[10]. CYP1B1 is located in the membrane of the endoplasmic reticulum and probably like most of the CYP450 enzymes, is substrate unspecific. Bearing in mind that CYP450 enzymes catalyse *O*-dealkylation and hydroxylation of aromatic rings as well as their localization in the endoplasmic reticulum and mitochondria, the *in vivo* transformation of Q_{10} to its hydroxylated form is very likely. Furthermore, mono-hydroxylated Q is suggested to appear as an intermediate in the terminal stage of the biosynthesis of Q_{10}[15]. Recently in our group it was found that hydroxylated Q_{10} is detectable in extracts of bovine heart mitochondria corresponding to about 0.3% of total Q_{10} content[16].

As discussed in the voltammetric work of Brunmark and Cadenas[17] and Bailey and Ritchie[18] on various non-substituted quinones, hydroxylation reaction is occurring at high pH (≥12.5). Later on, Gordillo and Schiffrin[19] analysed the pH-dependence of Q_{10} adsorbed on a mercury electrode but did not observe or follow up decomposition reactions at high pH. In several papers[10–14] of our group clear evidence for a chemical transformation of *p*-BQs in alkaline media (pH ≥ 12) was found, revealing that substituted dimethoxy *p*-BQs and coenzyme Q-like compounds react with hydroxide (HO⁻) anions giving new hydroxylated *p*-BQs derivatives as products. By applying a wide range of techniques like voltammetry, ultraviolet-visible spectroscopy (UV-Vis), electron paramagnetic resonance spectroscopy (EPR), nuclear magnetic resonance spectroscopy (NMR) and mass spectrometry (MS), our group confirmed that *p*-BQs undergo significant structural changes and suggested that the reaction comply with S_N2 mechanism, i.e., a nucleophilic substitution reaction of the methoxy group with the HO⁻ anion as shown in Figure 1-3[10,14]. This

reaction known as alkaline hydrolysis was first described in 1964 by Pettersson[20] for 2,3-dimethoxy-5,6-dimethyl-1,4-benzoquinone. It involves HO⁻ anions (nucleophiles) attacking the electrophilic C-atom at the methoxy (leaving) group of the quinone ring including formation of an intermediate (transition state). The transition state contains both, the HO⁻ anion and the methoxy group, partially bonded to the C-atom. With the reaction proceeding a bond between HO⁻ and C-atom is formed, while the bond between the methoxy group and the C-atom is broken, forming the hydroxylated derivative of the Q-like *p*-benzoquinone (Figure 1-3).
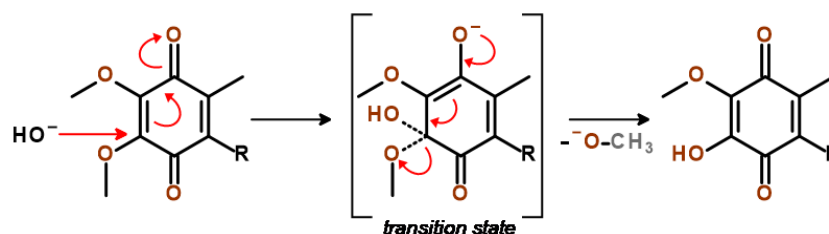
Figure 1-3 S$_N$2 mechanism of the chemical transformation of fully substituted *p*-benzoquinone in aqueous alkaline media (pH≥12)[10,14]. The S$_N$2 mechanism involves a nucleophile (HO⁻) attacking the electrophilic C-atom at the leaving (methoxy) group of the quinone ring, forming an intermediate (transition state). The transition state contains both, HO⁻ anion and methoxy group, partially bonded to the C-atom (denoted by dashed lines). As the reaction proceeds, a bond between HO⁻ and C-atom is formed and the bond between -OCH$_3$ and C-atom is broken, resulting in a hydroxylated derivative of the *p*-benzoquinone.

It was found that HO-Q$_1$ and HO-Q$_{10}$ exhibit a more negative redox potential than their respective native forms[10–13]. Due to the higher reducing potentials of the HO-Qs their antioxidant efficiency should be better than the corresponding native forms, Q$_1$ and Q$_{10}$. Indeed, Gulaboski *et al.*[11] demonstrated that the hydroxylated derivatives of 2,6-dimethoxy-1,4-benzoquinones are much better in scavenging superoxide anion radicals (O$_2$$^{\bullet-}$) than their native forms. Moreover, they showed that the reaction of the HO-Qs was slightly faster than the reaction of ascorbic acid and considerably faster than the reduction of O$_2$$^{\bullet-}$ by the spin probe CMH*. Similar antioxidant behaviour was observed for the hydroxylated form of Q$_0$ which showed a slightly higher antioxidant proficiency than vitamin E, based on the reduction of electrochemically oxidized ABTS†[12]. The introduction of a hydroxyl group at the quinone ring empowered BQ, Q$_0$, Q$_1$ and Q$_{10}$ to bind and transport calcium ions (Ca^{2+}) across biomimetic membranes. Bennett *et al.*[21] observed that 2-palmitoylhydroquinone (2PHQ), whose redox chemistry is based on the quinone/hydroquinone redox couple, is capable of binding and transferring Ca^{2+} across a liposome bilayer in a redox dependent manner. They proposed a redox-loop mechanism where reduced quinone binds Ca^{2+} and releases it upon oxidation[21]. In addition to this study Mirčeski *et al.*[22], employing mainly voltammetric methods, demonstrated the ability of reduced 2PHQ to not only interact with and transport Ca^{2+} but also other divalent metal ions such as Ba^{2+}, Sr^{2+} or Mg^{2+}. Both studies emphasised the key role of two adjacent oxygen atoms in the structure of 2PHQ which provide a binding site for cations. Such an arrangement of neighbouring oxygens is not found in any naturally occurring coenzyme Q compound, but it is a feature present in hydroxylated derivatives of Q$_0$, Q$_1$ and Q$_{10}$. Indeed, HO-Q but not the native Qs were able to bind Ca^{2+} and to a lower extent Mg^{2+} [10–13]. Furthermore, transport of Ca^{2+} across biomimetic membranes in a

---

* 1-hydroxy-3-methoxycarbonyl-2,2,5,5-tetramethylpyrrolidine hydrochloride.
† 2,2'-azino-bis(3-ethylbenzothiazoline-6-sulfonic acid).

redox-dependent manner was shown for HO-Q_1 and HO-Q_{10}[10]. It should be noted that all mentioned experiments with HO-Qs have been performed with reaction mixtures only and not with the purified substances[10–12]. Consequently, additional effects of possible side products of the reaction could not be excluded at this stage.

1.2 Redox chemistry of coenzyme Q_{10}

The benzoquinone head group in Q_{10} reflects its redox activity allowing Q_{10} to function as a donor or an acceptor of electrons as well as an antioxidant and under some conditions as a prooxidant. As shown in Figure 1-4, Q_{10} accepts one electron and one proton to form a semiubiquinone radical ($Q_{10}H^{\bullet}$). A second addition of an electron and a proton generates a fully reduced form of Q_{10}, ubiquinol ($Q_{10}H_2$). The redox reaction is reversible allowing Q_{10} to sweep between different protein complexes and to fulfil its function as an electron carrier.
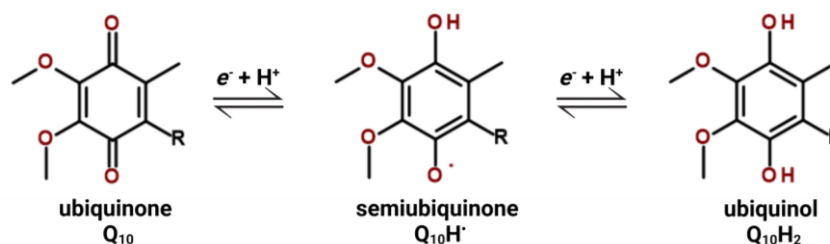
Figure 1-4 Redox reaction of Coenzyme Q_{10}. The stepwise reduction of Q_{10} by two electrons and two protons generating semiubiquinone ($Q_{10}H^{\bullet}$) and the fully reduced form, ubiquinol ($Q_{10}H_2$). R indicates the isoprenoid chain.

1.3 Distribution of coenzyme Q_{10} in biological tissues

Q_{10} is present in all animal tissues, although its level is variable. The highest concentration of Q_{10} is measured in organs with high rates of metabolic activity or high energy requirements such as the heart, kidney, liver, muscles, and pancreas. Additionally, due to its lipophilic nature Q_{10} distribution is highly dependent on the lipid content in the tissues. The highest subcellular distribution of Q_{10} has been shown for the mitochondrial inner membrane (50-60%), followed by about 12% for lysosomes, 10% for Golgi vesicles, 4% for plasma membranes and around 1% for cytosol[23].

1.3.1 Q_{10} in biological membranes

Although location and orientation of Q_{10} in biological membranes along with its effect on membrane physico-chemical properties have been of interest to researchers for many years, there is no unanimity regarding exact location. The location of coenzymes Q have been investigated with different liposome compositions in bio-membrane models and with various analytical methods making a direct comparison quite difficult. Although numerous experimental and computational studies have been performed with Q_{10} itself, many studies used its analogues such as Qs with shorter sidechains or derivatives with fluorescent tags on the sidechain. All these have different physico-chemical properties (hydrophobicity, solubility, conformation, etc.), thus making the comparison even harder. Unfortunately, studies although using similar methods have reported conflicting results. The benzoquinone group has been found in all three sections of the lipid bilayer: near lipid headgroups, within acyl chains and/or within the midplane of the two membrane leaflets[24,25].

Early investigations concerning Q_{10} location have considered its size compared to the size of the membrane[26]. The length of Q_{10} is approximately 56 Å, consequently Q_{10} could penetrate and span both leaflets of the bilayer including both hydrophilic and hydrophobic parts of the membrane. Q_{10} in its stretched form is too long to fit into the membrane. Nevertheless, when the sidechain is either folded and banded or oriented parallel to the membrane surface, it is located in the midplane of the leaflets. Two possible models for Q_{10} location are considered (Figure 1-5); in one model, part of Q_{10} molecule, i.e., the benzoquinone group resides closer to the polar headgroups of the lipid layer (Figure 1-5 a)[27] and in the other model, Q_{10} is totally embedded in the midplane of the membrane, i.e., sandwiched between the layers of the phospholipid bilayer at the end of fatty acid chains (Figure 1-5 b)[28]. It is also possible that Q_{10} molecules move between these two locations due to membrane fluidity.
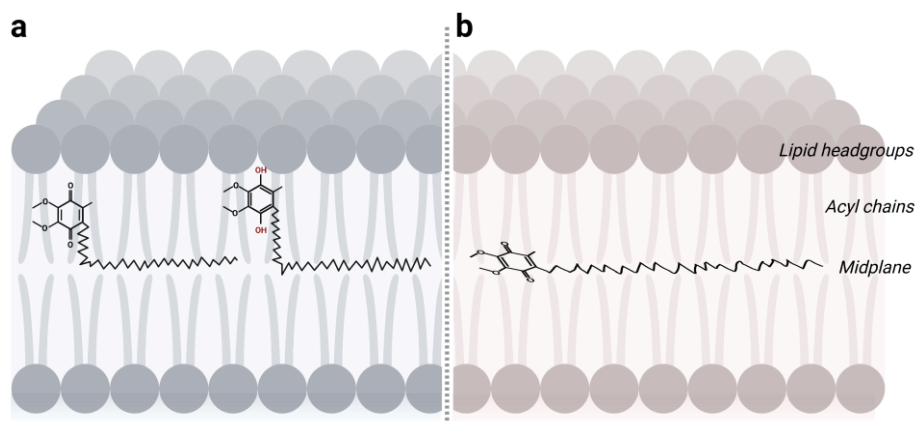
Figure 1-5 Proposed models of the location of Q_{10} within the lipid bilayer. a) Schematic model of the location of Q_{10} proposed by Afri *et al*.[27] where the benzoquinone headgroup of Q_{10} (left structure) is placed between acyl chains of phospholipids while the isoprene sidechain is located partly between acyl chains and partly in the midplane of the two leaflets. The reduced form of Q_{10}, $Q_{10}H_2$ (right structure) due to higher polarity of the headgroup is expected to be found closer to the lipid-water interface[25]. b) Proposed model for the location of Q_{10} according to Hauß *et al*.[28] where Q_{10} completely resides within the midplane of the two membrane leaflets.

Afri *et al*.[27] measuring NMR spectra of Q_{10} in different solvents and incorporated into liposomes, have estimated its surrounding in lipid membranes and have suggested Q_{10} to be embedded within phospholipids. According to their model (Figure 1-5 a) the benzoquinone headgroup is located near the polar region of the lipid bilayer but still distant from the lipid-water interface. The isoprene sidechain is mainly located in the midplane of the two leaflets with a considerable part found between acyl chains. This location empowers Q_{10} to increase the acyl chain ordering in the same way as cholesterol[29,30], consequently, changing the membrane properties. The more polar ubiquinol ($Q_{10}H_2$) is assumed to diffuse deeper into the polar phase of the membrane, closer to the water-lipid interface (Figure 1-5 a, right structure)[24,25,31]. Several studies[24,25,31–34] have revealed that the length of the sidechain determines the location of the headgroup, i.e., more polar derivatives of Q_{10} (Qs with shorter sidechains) are found closer to lipid-water interface than Qs with longer sidechains. For instance, Q_2 is found to be closer to the lipid-water interface than Q_4. Most likely the longer sidechain of Q_4 is embedding deeper into the midplane of the two leaflets due to the hydrophobic effect. In contrast, other studies[24,25] have shown that the type of the headgroup has the key influence on the location of Qs in the membrane. For instance, the Q_{10} headgroup is more polar than the headgroup of menaquinone (*p*-naphthoquinone with long isoprene sidechain), thus Q_{10} is found closer to the lipid-water interface than menaquinone.

On the other hand, in a model proposed by Hauß *et al.*[28] (Figure 1-5 b) the complete isoprene sidechain is integrated in the midplane between the two leaflets. Moreover, this model suggested that the benzoquinone headgroup is sandwiched between the layers of the membrane and the headgroup oscillates between the two leaflets, thus remaining at all times within a hydrophobic environment and enabling Q_{10} to move freely (Figure 1-5 b). An overall central location of Q_{10} has been suggested to have a destabilizing effect on the membrane by increasing its fluidity and permeability[35]. In contrast to this, other studies showed stabilization of the membranes, e.g., prevention of the lysis of red blood cells by inclusion of coenzyme Q_6 in the membrane[36]. In this line, inclusion of structurally similar molecules to Q_{10}, like vitamin E[37] and cardanol[38] in lipid membranes have been reported to stabilize the membranes and prevent leakage. Haines *et al.*[39] have suggested that Q_{10} could serve as a physical barrier to prevent proton leak in mitochondria. Indeed, Q_{10} enriched IMMs-mimicking membranes have shown a decreased leakage of small, hydrophilic molecules[30]. In a recent study[40] it has been reported that *E. coli* increased production of endogenous coenzyme Q_8 as a response to hyperosmotic salt media, providing stabilization of the membrane. These effects have been associated to Qs residing in the midplane between the two leaflets because molecules like solenasol[30,40] and hexadecane[30] mimicked the effect of Q_{10}[30] and Q_8[40], respectively. Oppositely, these effects were absent when short-chain Qs with 0 to 4 isoprene units were used, most probably due to their tendency to reside closer to lipid-water interface [40,41].

1.4 Physiological functions of Q_{10}

Since its discovery, a plethora of physiological functions have been attributed to Q_{10}[35,42]; from its main and well-recognized function as an electron carrier in mitochondrial electron transport chain, to acting as an antioxidant and controlling cellular redox state. Q_{10} is an essential cofactor of the mitochondrial uncoupling proteins (UCP)[43,44] and regulator of the mitochondrial permeability transition pore (mPTP)[45,46]. The significant quantities of Q_{10} found in both plasma membranes and non-mitochondrial internal membranes indicates potentially more functions of Q_{10} such as its involvement in lysosomal and plasma membrane electron and proton transport and protective effects on circulating lipoproteins[47,48]. These key biological functions of Q_{10} are linked to its structure (Figure 1-2 b) involving a *p*-benzoquinone headgroup, which confers the redox properties of the molecule and an isoprenoid tail, which is responsible for its lipophilicity and its location within biological membranes.

1.4.1 Q_{10} in oxidative phosphorylation

Q_{10} has been recognized as an essential component of the mitochondrial electron transport chain (ETC), which provides most of the energy utilized by cells. ETC is the fundamental connection between cellular metabolism and ATP production and Q_{10} has a unique function to mediate the electron transfer from complex I and II to complex III of the ETC.

Cellular metabolism comprehends the consumption of carbohydrates, fats, and proteins to synthesize energy. The resulting molecules from these metabolic pathways are processed in the tricarboxylic acid (TCA) cycle yielding substrates that enter the mitochondrial ETC to produce

adenosine triphosphate (ATP) through the process of oxidative phosphorylation (OXPHOS). During OXPHOS, electrons are passed along a series of protein complexes, known as ETC or OXPHOS molecular system. ETC is embedded in the inner mitochondrial membrane (IMM) and consists of five multisubunit protein complexes (CI, CII, CIII, CIV and CV) and two mobile electron carriers, Q_{10} and cytochrome c (cyt c)[49]. Figure 1-6 provides an overview of the mitochondrial ETC.
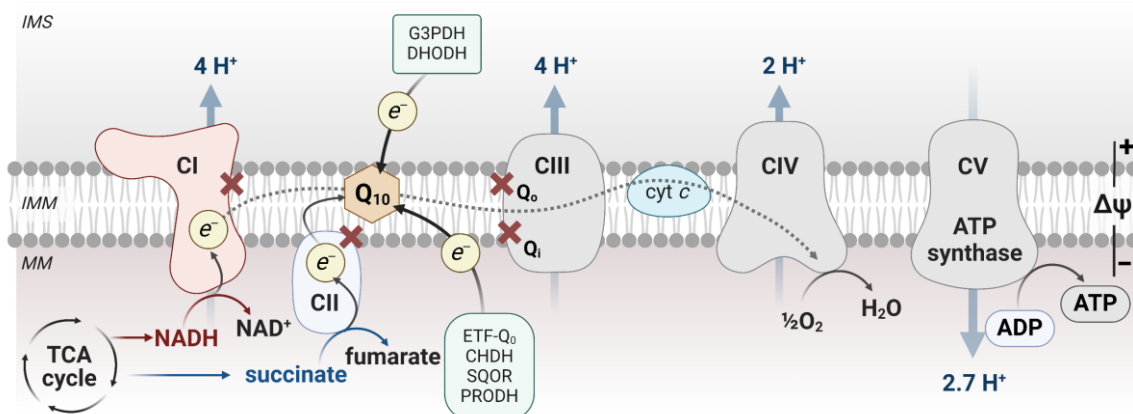
Figure 1-6 Scheme of the mitochondrial electron transport chain. The mitochondrial electron transport chain (ETC) contains five protein complexes CI-CV embedded in the inner mitochondrial membrane (IMM). The TCA cycle supplies NADH and succinate which are donating electrons to CI and CII, respectively, thus reducing Q_{10} to $Q_{10}H_2$. Two molecules of $Q_{10}H_2$ are oxidized at CIII, followed by reduction of two molecules of cyt c and one molecule Q_{10}. Electrons are further transferred from cyt c to CIV, where molecular oxygen O_2 is the final acceptor. A proton gradient, built up by translocation of protons from mitochondrial matrix (MM) to intermembrane space (IMS) at CI, CIII and CIV, is consumed by ATP synthase (CV) to produce ATP. The dashed grey arrow indicates the electron pathway in ETC. Red X marks indicate Q-binding sites of Q_{10} at CI, CII and CIII; CI–CV, complexes I–V; Q_{10}, coenzyme Q_{10}; cyt c, cytochrome c; H^+, protons; e^-, electrons; $\Delta\Psi$, mitochondrial membrane potential; TCA cycle, tricarboxylic acid cycle; G3PDH, glycerol-3-phosphate dehydrogenase; DHODH, the dihydroorotate dehydrogenase; ETF-Q_0, the electron transfer flavoprotein oxidoreductase; CHDH, the choline dehydrogenase; SQOR, the sulfide:quinone oxidoreductase; PRODH, the proline dehydrogenase. Figure contains information from [49–51].

NADH and succinate generated during TCA cycle supply electrons to ETC at different entry points. NADH donates electrons at CI, whereas succinate at CII (Figure 1-6). In Complex I, electrons derived from NADH traverse a series of cofactors including a flavin mononucleotide (FMN) and seven iron-sulphur (Fe-S) clusters with varying redox potentials. These electrons are subsequently accepted by Q_{10} reducing it to ubiquinol $Q_{10}H_2$. This electron transfer process results in translocation of H^+ by CI from the mitochondrial matrix (MM) into the intermembrane space (IMS). In addition to the electrons entering through CI, electrons can also be supplied to the ETC by complex II which is part of both, the TCA cycle and the ETC[49,50]. In a similar manner as at CI, electrons donated from succinate are sequentially transferred to Q_{10} via the three Fe-S clusters of CII. The electron transfer through CII does not include H^+ translocation from MM to the IMS. In addition to CI and CII, electrons could enter mitochondrial ETC via Q_{10} by other enzymes such as mitochondrial glycerol-3-phosphate dehydrogenase (G3PDH), the electron transfer flavoprotein oxidoreductase (ETF-Q_0), the dihydroorotate dehydrogenase (DHODH), the choline dehydrogenase (CHDH), the sulfide:quinone oxidoreductase (SQOR), and the proline dehydrogenase (PRODH)[51]. All these enzymes are proficient in feeding electrons to Q_{10} reducing it to $Q_{10}H_2$.

The electron transport from $Q_{10}H_2$ to CIII can be described by the Q-cycle concept, initially proposed by Mitchell[52] in 1975. CIII encompasses 11 subunits including three crucial respiratory

subunit proteins: the *Rieske* (2Fe-S) centre, cytochrome *c1* (cyt *c1*) and cytochrome *b* (cyt *b*). Furthermore, CIII provides two distinct binding sites, Q_o and Q_i, to which Q_{10} molecules are bound depending on their redox state (red X marks, Figure 1-6). Reduced Q_{10}, $Q_{10}H_2$, binds to the "outer" Q_o binding site of CIII (Q-binding site of CIII at the outer surface of IMM; IMM-IMS side, Figure 1-6), while the oxidized Q_{10} binds at the "inner" Q_i binding site of CIII (Q-binding site at the inner surface of the IMM; IMM-matrix side, Figure 1-6). One electron from $Q_{10}H_2$, which is bound at Q_o binding site, is transferred through the *Rieske* centre to cyt *c1* within CIII, and subsequently is reducing the mobile carrier cyt *c*. The second electron from $Q_{10}H_2$ is conveyed to cyt *b* within CIII, from where it is further transferred to Q_{10} that is bound at the Q_i binding site of CIII, generating ubisemiquinone ($Q_{10}H^{\bullet}$). At this point, a second $Q_{10}H_2$ molecule is attached at Q_o binding site which further delivers electrons in the same oxidation process. One electron that is branching through the *Rieske* centre and cyt *c1* reduces a second molecule of cyt *c*, whereas the other electron is passing through cyt *b* and finally reduces the $Q_{10}H^{\bullet}$ back to $Q_{10}H_2$. During this process at CIII four additional H^+ are pumped into the IMS[49,50].

The reduced cyt *c* transfers the electrons to CIV, where molecular oxygen is final acceptor of the electrons and is reduced to water (Figure 1-6). The transfer of electrons through CIV results in a translocation of four H^+. Two of these protons are used in the reduction of oxygen to water and the other two are translocated into the IMS. In a response to the electron transfer along the ETC a total of ten H^+ (4 H^+ at CI, 4 H^+ at CIII and 2 H^+ at CIV) are pumped out from the MM into the IMS, where they accumulate and build up the electrochemical proton gradient or protonmotive force (pmf) across IMM. The pmf consist of two components: a chemical part related to the difference in the proton concentration (ΔpH) across the membrane and an electric component associated to the mitochondrial membrane potential ($\Delta\Psi_m$). ATP synthase (Complex V, CV) utilizes the pmf established during electron transfer from CI to CIV to produce ATP. The movement of protons which flow through ATP synthase and re-enter the MM is thus providing energy for addition of P_i to ADP to produce ATP (Figure 1-6)[49,50].

1.4.1.1 Organization of ETC complexes in supercomplexes

Besides the well-known functional relevance of ETC, paramount efforts have been made to clarify and understand the nature of its physical organization in the IMM. Commonly, the organization of the ETC complexes is discussed in terms of two extreme models, "solid-state" and "fluid" model[53–55].

Chance and Williams[56] proposed the "rigid" or "solid-state" model based on the isolation of active units consisting of two or more complexes in defined stoichiometric ratios. According to this model (Figure 1-7 a), the complexes of ETC are anchored within a framework to ensure close contact between each other with higher catalytic activity, capable of catalysing a whole reaction pathway. This model indicated permanently bound Q and cyt *c* at the ETC complexes which transfer electrons along pre-defined, enclosed pathways between the corresponding complexes and thus have high efficiency in electron transfer.

Three decades later, based on the increased knowledge of the properties of IMM, Hackenbrock *et al.*[57] proposed the "fluid" model, where ETC complexes are independent entities embedded in the lipid bilayer of IMM and electron transfer depends on random encounters between the complexes and the mobile electron carriers, Q and cyt *c* (Figure 1-7 b). In contrast to the solid model, the fluid model implied that individual complexes of ETC diffuse freely in the membrane and the mobile electron carriers, Q and cyt *c*, move between them in an unrestricted and random manner. Studies by Hochman *et al.*[58] arose the so-called "dynamic aggregate" model which postulated existence of dynamic equilibrium between freely diffusing and associated forms (aggregates) of the ETC components. This model addressed the mechanism of proton flow in specific regions and the potential for controlling the direction and effectiveness of electron transfer[54]. It eventually received strong support by Schägger *et al.*[59] presenting new evidence for the simultaneous presence of individual ETC complexes and their supramolecular assemblies (called supercomplexes, SCs), mainly by using a quantitative approach in blue native polyacrylamide gel electrophoresis (BN-PAGE). A few years later, respirasomes, SCs including ETC complexes $CICIIICIII_2CIV$ or $CICIICIII_2CIV$ as well as Q and cyt *c* were found to respire on NADH and/or succinate[60]. This finding prompted the introduction of the so-called "plasticity" model by Acín-Pérez *et al.*[60,61], which integrated the experimental evidence in support of both, the "solid" and the "fluid" model (Figure 1-7 c), yet with fundamental corrections. As proposed with the "fluid" model, Acín-Pérez *et al.*[60,61] found that CIV, CII and relevant portion of CIII stand alone and most probably move freely in the IMM, whereas in contradiction to the "fluid" model, but similarly to the "solid" model the largest part of CI appeared to form associations with CIII, with CIII and CV, with CII, CIII and CIV or with CIII and CIV (Figure 1-7 c).
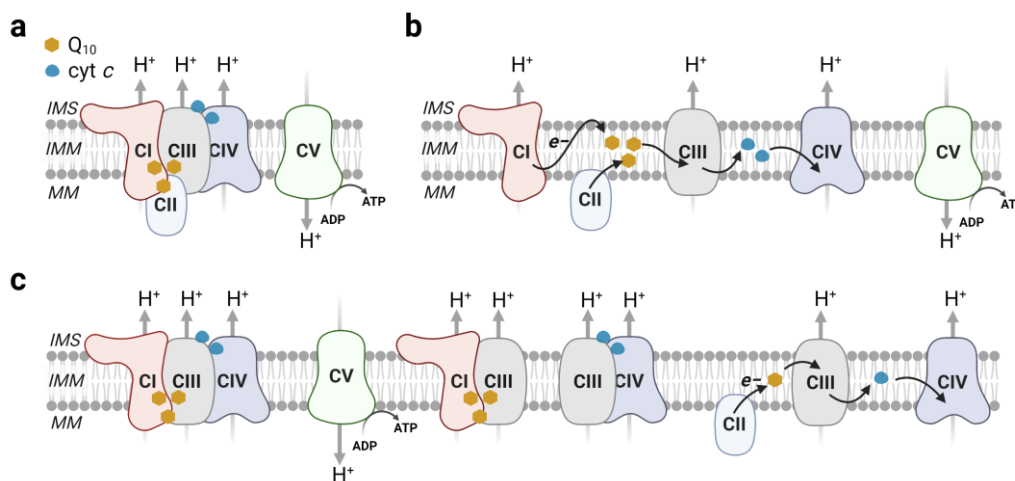
Figure 1-7 Schematic representation of the assembly models of the ETC complexes. a) The "rigid" or "solid-state" model proposed by Chance and Williams[56] where the ETC complexes are anchored within a framework to ensure close contact between each other and high catalytic activity. b) The "fluid" model proposed by Hackenbrock *et al.*[57] according to which ETC complexes are independent units embedded in the IMM and electron transfer depends on random collisions between the complexes and the mobile electron carriers, Q_{10} and cyt *c*. c) The "plasticity" model for the organization of ETC complexes introduced by Acín-Pérez *et al.*[60] which integrated both, the "solid" and the "fluid" model, for the organization of ETC. Only one complex unit of each type is represented in the different supercomplex (SC) assemblies although the definite stoichiometry varies. SC $CICIII_2CIV$ is also known as respirasome as it contains all components necessary for electron transfer from NADH to O_2. Q_{10} is represented as yellow hexagons; cyt *c* as blue circles. Black arrows indicate electron transfer direction. Grey arrows indicate proton translocation across IMM. IMS, intermembrane space; IMM, inner mitochondrial membrane; MM, mitochondrial matrix. Scheme encompasses information from [61–63].

Nowadays, structures of the SC $CICIII_2CIV_{1-4}$ (also known as the respirasome since it contains all the components required to transfer electrons from NADH to O_2)[64–68] as well as those of SC $CICIII_2$[68,69] and the most recently reported SC $CIII_2CIV$[70] from different mammalian species are available and resolved by cryogenic electron microscopy (cryo-EM) and X-ray diffraction studies. The structure and abundance of the SCs differ across organisms and tissues depending on the physiological conditions and on the lipid content of the IMM. In mammals the respirasome comprises most of CI (>90%), about 40-50% of CIII and 20-30% of CIV. In contrast to CI, significant amounts of CIII (50-60%) and CIV (70-80%) can be found as individual complexes within the IMM[51]. CIII always forms dimers and besides previously mentioned SCs is also present in SCs together with CIV ($CIII_2CIV$) which represents about 5% of the total amount of ETC structures[54]. CIV predominantly exists as a monomer, although it can assemble with CI, form dimers or heavier structures[71], whereas CV is generally sole, could form dimers and multimers[54]. Differently from CI, CIII and CIV, which can be assembled in non-covalent SCs, CII is always found as an individual complex. Participation of CII in the SCs have not been identified in most of the studies and their existence and importance for SCs is disputed[72]. However, monomeric to trimeric forms of CII[73] and potential incorporation in SCs[60,74] have been reported, representing a minor proportion of the overall amount of mitochondrial CII. Guo *et al.*[75,76] proposed CII to be part of megacomplexes such as oligomers of SCs.

Although the assembly of individual complexes of ETC into distinct SCs have been established, their function is still under intense debate. Major advantages attributed to the SCs formation are maintaining the integrity of the individual complexes, especially that of CI, reduced ROS production as well as increased efficiency of electron flux through substrate channelling or enhanced catalysis. Different studies have shown that association of CIII[77] and CIV[78] is crucial for the stabilization and activity of CI. Indeed, when either CIII or CIV fail to get assembled, consequently causing impairment in SCs formation, mitochondria display CI deficiency. On the contrary, absence of CI influences the SCs formation but does not impair the activity of the other complexes[77]. Furthermore, given that mitochondria-derived ROS are mainly produced by CI and CIII, SCs formation have been proposed to reduce ROS production by increasing electron efficiency and decreasing electron leakage between CI and CIII[79–81]. Lopez-Fabuel *et al.*[81] have shown that ROS production in astrocytes, where CI was abundantly detected as a single unit, was higher than that in neurons, where CI was predominantly assembled into SCs. Later on, more studies[54,63,71,81,82] have noticed the connection between decreased SCs formation and increased ROS levels in cells and tissues. All these studies were designed to alter the interaction between CI and CIII. Thus, most likely Q_{10} is important in ROS production by SCs which potentially is linked to the proximity of CI and CIII or IMM fluidity[71]. Moreover, in a recent study[82] it was reported that Na^+ modulates the production of ROS during acute hypoxia by regulating the IMM fluidity. It was observed that Na^+ influenced SCs CIICIII and G3PDH-CIII activities, but not SC CICIII activity. It was postulated that Na^+ interacts with phospholipids reducing IMM fluidity, thus hindering the mobility of free Q_{10} between CII and CIII, but not inside SCs CICIII. In other

words, the activity of CICIII does not depend completely on membrane fluidity since it could use Q_{10} (Q_{NADH})* that are trapped in the SC, while the transfer of Q_{10} (Q_{FAD}) from either CII or G3PDH to CIII is strongly dependent on membrane fluidity. In another study[83] it has been shown that the absence of mitochondrial Na^+/Ca^{2+} exchanger (animal models with knocked out gene that encodes NCLX) promotes greater ROS production during reperfusion. Since the main source of ROS during reperfusion is mitochondrial CI through reverse electron transport (RET), most probably Na^+ (by interaction with phospholipids thus modulating IMM fluidity) decreases ROS production by hindering the mobility of Q_{10}[83,84].

ROS production could be reduced through a highly controlled electron transfer in ETC and by segregation of two distinct Q pools*. Soon after the discovery of SCs, investigations on metabolic flux control performed on submitochondrial particles showed that CI and CIII were equally controlling the electron flux during respiration. These observations prompted the hypothesis that the Q_{10} pool sequestered within SCs CICIII$_2$ and it is responsible for directly transferring electrons between CI and CIII without intermingling with the remaining Q_{10} embedded in the membrane, i.e., Q_{10} (the substrate) would be channelled between the complexes and recycled in a closed system[78,79,85]. Moreover, the assembling of CIII$_2$ with CIV in SCs has been shown to enhance the electron transfer via cyt *c*[70,86,87]. However, the substrate channelling function of SCs as well as partitioning of Q_{10} and cyt *c* pools has recently been challenged by biochemical and structural data leaving this function controversial[53,71,88–90]. Fedor *et al.*[90] demonstrated that externally added oxidase could oxidize the Q_{10} reduced by CI, thus concluding that Q_{10} is not trapped within SCs but diffuses freely and it is exchanged between CI and its pool in IMM. Additionally, the long distance (~10 nm) between Q_{10}-binding sites at CIII and CI[67,76] and for cyt *c*-binding sites at CIII and CIV[67] speaks against Q_{10} or cyt *c* channeling[53].

1.4.2 Q_{10} as an antioxidant

In addition to its bioenergetic and modulating role of biophysical properties of membranes, Q_{10} is the only known lipid-soluble antioxidant that could be *de-novo* synthesized by organisms. Adopting three redox states including the semiubiquinone radical (Figure 1-4), Q_{10} expresses antioxidant and prooxidant properties. Its exceptional high antioxidant capacity is attributable to its membrane localization, its ubiquitous and abundant distribution, and its effective reduction to $Q_{10}H_2$ that could be catalysed by several cellular systems. In mitochondria the reduced form $Q_{10}H_2$ is generated directly by the mitochondrial ETC[91]. In addition, in non-mitochondrial biological membranes Q_{10} constantly interchanges between reduced and oxidized forms through the action of the plasma membrane redox system (PMRS)[92]. PMRS includes NAD(P)H dehydrogenases where cytochrome b_5 reductase 3 (CytB$_5$R$_3$) and NAD(P)H:quinone acceptor oxidoreductase 1 (NQO1) are the most important in maintaining $Q_{10}H_2$ levels. PMRS generates

---

* It has been proposed that Q_{10} molecules do not exist in a single homogenous pool in IMM but are segmented into two separate pools, termed Q_{NADH} and Q_{FAD} pool[62]. The Q_{NADH} pool is defined by the supercomplex assembly between CI and CIII, and facilitates electron transfer from NADH via CI and CIII to cyt *c.* The remaining, freely diffusible Q_{10} molecules are part of the Q_{FAD} pool, promoting electron transfer from FADH$_2$ via CII and CIII to cyt *c.* The Q_{FAD} pool also includes Q_{10} molecules that accept electrons delivered from enzymes such as G3PDH, ETF-Q$_0$, DHODH, CHDH, SQOR and PRODH.

$Q_{10}H_2$ by transferring two electrons in a two single-step mechanism ($CytB_5R_3$)[93] or by two-electrons one step quinone reduction (NQO1)[94], where the latter mechanism prevents the formation of a semiubiquinone radical intermediate[92]. Q_{10} plays important roles in preventing lipid peroxidation in biological membranes[35,95] and plasma low density lipoproteins (LDLs)[96,97]. Moreover, the protective effect of Q_{10} against oxidative damage is extended to proteins and DNA[35]. In contrast to other antioxidants, $Q_{10}H_2$ has been shown to hinder both the initiation and progression of oxidative damage by impeding the generation of lipid peroxyl radicals; $Q_{10}H_2$ interacts and reduces perferryl radicals generating ubisemiquinone and H_2O_2[35,91,95]. Additionally, $Q_{10}H_2$ can rescue tocopheryl radicals by their reduction to α-tocopherol (vitamin E), thus slowing down the propagation step of lipid peroxidation. There is also supporting evidence that electron transport across the plasma membrane which relies on Q_{10} can be employed to restore ascorbate (vitamin C) from ascorbyl radical in the extracellular space[42].

Recently it has been proposed that Q_{10} in the plasma membrane aids to prevent ferroptosis[98–100]. Ferroptosis is a type of non-apoptotic cell death triggered by iron-dependent lipid peroxidation[101]. Bersuker *et al.*[98] have shown that CoQ oxidoreductase ferroptosis suppressor protein 1 (FSP1) working in conjunction with glutathione peroxidase 4 (GPX4) inhibits ferroptosis. Doll *et al.*[99] demonstrated that suppression of ferroptosis by FSP1 is mediated by Q_{10}. In this mechanism $Q_{10}H_2$ neutralizes lipid peroxyl radicals responsible for lipid peroxidation, after which FSP1 using NAD(P)H facilitates the regeneration of Q_{10} to its reduced form. Rizzardi *et al.*[100] have demonstrated that exogenous addition of Q_{10} protects membrane lipids from peroxidation and increases cell resistance to ferroptotic stimuli in cultured cells.

A most paradoxical role of Q_{10} is its possible implication in cellular production of ROS. Findings as the one that Q_{10} is adopting three redox states (Figure 1-4) including the semiubiquinone radical as well as the one that major production of ROS in mitochondria occurs in the ETC have raised the question about prooxidant activity of Q_{10} and its possible role in ROS generation during mitochondrial respiration[95]. In mitochondria with abundant succinate supply and therefore high levels of reduced Q_{10}, it is possible to observe a back-flow (RET) of electrons from $Q_{10}H_2$ to NAD^+ through CI, resulting in a burst of ROS and in reduction of NAD^+ to NADH[102]. Q_{10} may act as a prooxidant since the unstable semiquinone radical could react with O_2 generating superoxide radicals ($O_2^{•-}$) and subsequently hydrogen peroxide (H_2O_2). This formation of ROS may not only be harmful for the cells but, on the other side, it may serve as signalling messenger[103].

1.5 Calcium homeostasis in cells

Calcium ions (Ca^{2+}) serve as essential second messengers converting information from both extracellular and intracellular signals into intracellular effects[104]. To fulfil such a complex signalling role, Ca^{2+} concentrations ($[Ca^{2+}]$) in all cellular compartments are tightly regulated to maintain the low intracellular Ca^{2+} concentration, $[Ca^{2+}]_i$[105]. Cellular Ca^{2+} homeostasis is a highly complex and precisely regulated interplay of Ca^{2+} binding proteins, stores, pumps, and channels that cooperatively generate patterns of Ca^{2+} signalling (Figure 1-8). Various mammalian proteins, classified as buffer and trigger proteins, are regulated by Ca^{2+}. Most of these proteins comprise

one or multiple EF-hand motifs for Ca^{2+} binding which are sensitive to global or local changes in $[Ca^{2+}]$. Ca^{2+} binding changes the protein conformation and thereby the functions of these proteins, thus regulating various cellular events such as proliferation, cell death, migration, and immune responses[104,105].

The role of Ca^{2+} in coordinating and regulating different cellular processes extends beyond changes in its cytosolic concentration ($[Ca^{2+}]_c$) and in addition encompasses variations in $[Ca^{2+}]$ within organelles[104–106], therefore affecting organelle-specific metabolic functions as secretion, proliferation, ATP production, and cell mortality[105,107–109].

The intracellular Ca^{2+} concentration is highly variable depending on its location. $[Ca^{2+}]$ in different intracellular compartments is given in Figure 1-8. For instance, $[Ca^{2+}]_c$ is $\sim 10^{-7}$ M under resting conditions, whereas extracellular Ca^{2+} concentration, $[Ca^{2+}]_e$ is $\sim 10^{-3}$ M. In a resting cell, $[Ca^{2+}]$ in the nucleus resembles that of the cytosol. One of the main intracellular Ca^{2+} storage compartment is the endoplasmic reticulum (ER) or in the case of muscle cells the sarcoplasmic reticulum, which accumulates high amounts of Ca^{2+}, $[Ca^{2+}]_{ER}$ is $\sim 10^{-4}$ M^{105}. Additionally, mitochondria and lysosomes (recognized as second largest intracellular storage of Ca^{2+})[110], and the Golgi apparatus can also store significant amounts of Ca^{2+}.
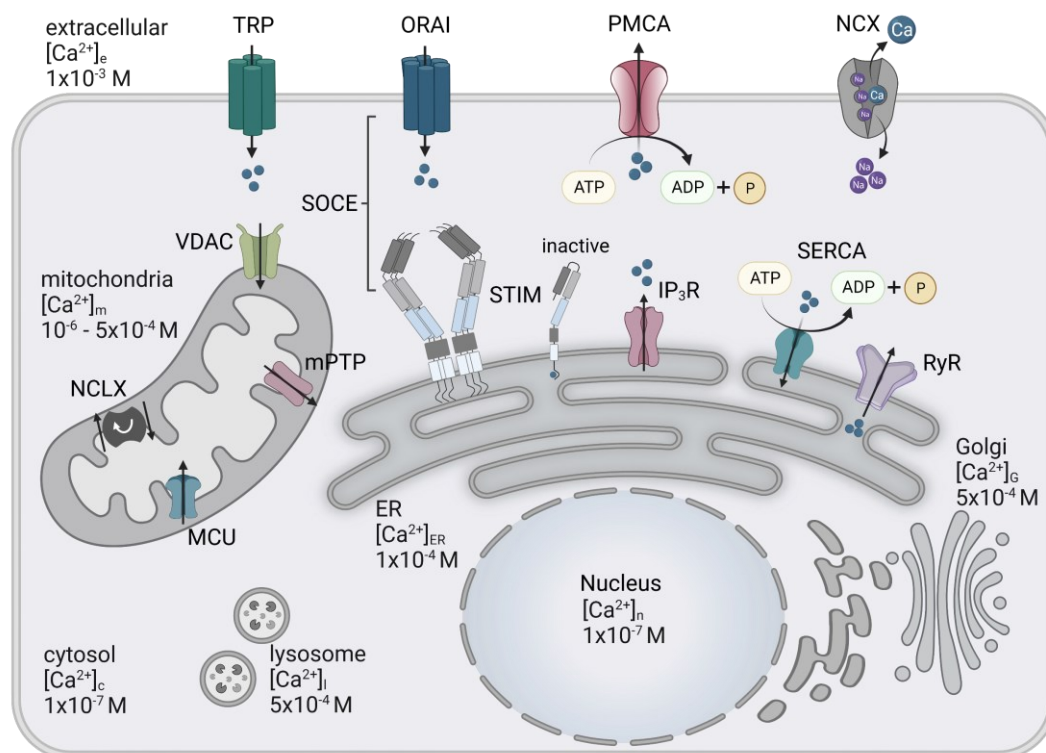
Figure 1-8 Cellular Ca^{2+} homeostasis and signalling. Elevation in cytosolic Ca^{2+} $[Ca^{2+}]_c$ is derived either from the external store (extracellular space) or from internal Ca^{2+} stores (ER, mitochondria, lysosomes, and Golgi apparatus). Ca^{2+} entry from extracellular space is mediated by plasma membrane Ca^{2+} channels or transporters such as TRP channels and Store-Operated Ca^{2+} Entry (SOCE) channels, as major pathways for Ca^{2+} influx into the cytosol. SOCE encompasses STIM and ORAI proteins. Ca^{2+} depletion from ER is sensed by STIM causing dissociation of Ca^{2+} from its EF hand motif followed by movement of STIM to the junctions between the ER and the plasma membrane, where it binds to and opens ORAI channels. Ca^{2+} is exported out of the cell by the action of plasma membrane Ca^{2+} ATPases (PMCA) pumps and the Na^+/Ca^{2+} exchanger (NCX). The levels of Ca^{2+} in the ER are controlled by activity of inositol-1,4,5-trisphosphate receptors (IP₃Rs) and ryanodine receptors (RyRs), which mediate Ca^{2+} release from the ER and sarcoplasmic/endoplasmic reticulum Ca^{2+} ATPases (SERCAs) which are controlling ER Ca^{2+} uptake. Voltage-dependent anion channels (VDACs) and mitochondrial Ca^{2+} uniporters (MCU) are essential for regulating Ca^{2+} influx in mitochondria, whereas Ca^{2+} efflux from mitochondria is mainly regulated by the $Na^+/Ca^{2+}/Li^+$ exchanger (NCLX). Scheme content comprises information from [104,105,107,110,111].

Each organelle exhibits organelle-specific Ca^{2+} channels[104,107,111] crucial for maintaining correct membrane trafficking (Figure 1-8). The low $[Ca^{2+}]_c$ in a resting cell is maintained by the action of the plasma membrane Ca^{2+} ATPases (PMCAs) and the Na^+/Ca^{2+} exchanger (NCX). Upon increase in $[Ca^{2+}]_c$, e.g., by influx of Ca^{2+} from extracellular space, the activity of these channels is complemented by increased activity of sarcoplasmic/endoplasmic reticulum Ca^{2+} ATPases (SERCAs) and to a lesser extent by the mitochondrial calcium uniporter (MCU) complex. ER Ca^{2+} uptake through the action of SERCAs shows buffering effect on $[Ca^{2+}]_c$ ensuring maintenance of resting Ca^{2+} levels in the cell. SERCAs are activated upon increased $[Ca^{2+}]_c$ allowing quick re-uptake of Ca^{2+} by actively pumping two Ca^{2+} ions per ATP molecule against the concentration gradient from the cytosol into the ER. Release of Ca^{2+} from the ER is mediated by inositol-1,4,5-trisphosphate receptors (IP_3Rs) and ryanodine receptors (RyRs). Depletion of Ca^{2+} from the ER stores results in elevated $[Ca^{2+}]_c$ which is sustained by Ca^{2+} influx from the extracellular space through SOCE (store-operated Ca^{2+} entry), a necessary event to refill the intracellular Ca^{2+} stores. The mechanism of SOCE encompasses coordinated activity of two groups of proteins, stromal interaction molecules (STIMs) and Ca^{2+} release-activated Ca^{2+} modulator proteins (ORAIs). Both groups of proteins exist in different isoforms. Briefly, depletion of Ca^{2+} from the ER stores results in the activation of STIM which moves to the junctions between the ER and the plasma membrane, where it binds to and activates the ORAI Ca^{2+} channels, thus inducing Ca^{2+} entry into the cytosol (Figure 1-8)[104]. In addition to SOCE the intracellular Ca^{2+} influx is also mediated by transient receptor potential channels (TRPCs) which comprise a variety of different subtypes[112,113]. It has been observed that upon opening of Ca^{2+} channels at the plasma membrane, mitochondria are transferred to the "mouth" of the channel and take up high amounts of the Ca^{2+} to prevent Ca^{2+} overload of the cytosol[114–117]. Due to the proximity of mitochondria to ER and due to the formation of membrane contact sites[118] most of the Ca^{2+} released from the ER is captured by nearby mitochondria through voltage-dependent anion-selective channel proteins (VDACs) and the MCU complex[104,119]. Excess of Ca^{2+} in the cytosol is actively exported by PMCAs, thus maintaining the $[Ca^{2+}]_c$ at the level for proper cell signalling (Figure 1-8). PMCAs can only compensate for small changes in $[Ca^{2+}]$[105]. Another protein that can carry Ca^{2+} out of the cell is the NCX, which transports one Ca^{2+} out of the cell in exchange with three Na^+ ions into the cell[120]. However, when cytosolic Na^+ concentrations are too high the direction of the transport can be reversed[121]. The NCX, in contrast to the PMCA, has a lower affinity for Ca^{2+} but a tenfold transport rate and thus it can compensate for larger fluctuations in $[Ca^{2+}]$[122].

To reach the mitochondrial matrix (MM) cytosolic Ca^{2+} must cross two membranes, the outer (OMM) and inner (IMM) mitochondrial membranes, both including channels for regulated Ca^{2+} uptake (Figure 1-8)[104]. While the OMM is considered as highly permeable to ions and small molecules due to the presence of VDACs, the IMM is impermeable and specialized channels and carriers are required for their uptake. VDACs form pores in the OMM and mediate flux of ions, nucleotides (ADP and/or ATP) and other metabolites[104]. Transition between open and closed conformation states of VDACs occurs in a voltage-dependent manner. However, VDACs mediate

the flux of Ca^{2+} in both conformations, thereby limiting generation of a Ca^{2+} concentration gradient across the OMM. Ca^{2+} after reaching the intermembrane space (IMS) crosses the IMM mainly through the MCU complex (Figure 1-8). Some of the properties attributed to the MCU are high Ca^{2+} sensitivity, initiation of Ca^{2+} uptake only in stimulated cells (activation only at high $[Ca^{2+}]$) and low affinity for Ca^{2+} (dissociation constant (K_d) of 20-30 μM). Therefore, activity of the MCU depends on mitochondrial membrane potential and $[Ca^{2+}]$ in the vicinity of the MCU[111,123]. Although MCU represents the dominant mechanism of Ca^{2+} entry into MM, additional MCU-independent mechanisms for Ca^{2+} uptake have been suggested. These include an IMM-located pool of RyRs[124], the canonical short transient receptor potential channel 3 ($TRPC_3$)[125], mitochondrial uncoupling proteins 2 (UCP2) and 3 (UCP3)[126], and leucine zipper EF-hand-containing transmembrane protein 1 (LETM1)[127]. Ca^{2+} efflux from MM occurs mainly through $Na^+/Ca^{2+}/Li^+$ exchanger (NCLX) which functions analogously to the NCX in the plasma membrane. Studies suggest that the NCLX cannot be the only pathway for Ca^{2+} efflux from the MM. Moreover, it has been proposed that under certain conditions mitochondrial permeability transition pore (mPTP) could be an alternative for Ca^{2+} efflux[128,129] although other studies question this hypothesis[130].

1.5.1 Oxidative phosphorylation and cellular calcium homeostasis

Mitochondria can take up large amounts of Ca^{2+} thereby acting as an essential modulator of cellular Ca^{2+} homeostasis and Ca^{2+} signalling. Disruptions in mitochondrial Ca^{2+} homeostasis can have an impact on ER Ca^{2+} stores[118] and their replenishment by SOCE[131]. The significance of mitochondrial Ca^{2+} lies in its pivotal role in regulating cell health. This is attributed to its ability to influence cell energetics by triggering oxidative phosphorylation, mitochondrial respiration and consequently ATP synthesis[104,132–134]. In this context, it has been shown that mitochondrial Ca^{2+} accumulation enables activity of mitochondrial respiration and consequently increase in ATP production. Mitochondrial ATP is the main supplier for cellular energy-consuming processes and by that also enables effective functioning of the two major Ca^{2+} pumps, PMCA and SERCA pumps. Nevertheless, an excessive mitochondrial Ca^{2+} influx (Ca^{2+} overload) leads to apoptotic cell death by stimulating mPTP opening and cyt *c* release[135–137].

Intra-mitochondrial Ca^{2+} impacts OXPHOS through different mechanisms. For many years it is known that a rise of mitochondrial Ca^{2+} levels results in activation of four enzymes of TCA cycle: pyruvate dehydrogenase (PDH), FAD-glycerol-3-phosphate dehydrogenase (GPDH), NAD^+-isocitrate dehydrogenase (IDH) and oxoglutarate dehydrogenase (ODH)[133,138–140]. Ca^{2+} from MM regulates the activities of PDH, IDH and ODH, whereas the activity of GPDH is modulated by the cytosolic Ca^{2+}. The effects of Ca^{2+} on GPDH, IDH and ODH includes binding to the enzymes, thus subsequently lowering the K_M (Michaelis constant) for their respective substrates. The activity of PDH is increased by dephosphorylation mediated by Ca^{2+}-sensitive phosphatases[139,140]. Besides modulating the activity of the GPDH, cytosolic Ca^{2+} also regulates activities of Ca^{2+}-binding mitochondrial carriers (CaMCs), mitochondrial glutamate/aspartate carrier[141,142] and ATP-Mg/P_i carrier[143,144], which are located in the IMM. The Ca^{2+} mediated

stimulation of TCA cycle enzymes and mitochondrial carriers leads to increased levels of NADH and FADH$_2$, thus stimulating mitochondrial respiration and increasing ATP production. Furthermore, a direct effect of Ca^{2+} on the ETC and on the activity of F$_1$F$_0$ ATP synthase (complex V, CV) has also been reported[145]. Territo *et al.*[145] proposed that Ca^{2+} directly modulates CV which was followed by another study[146] from the same group describing that an increase in [Ca^{2+}]$_m$ stimulates activity of the ETC by increased electron flow between CI, CII and CIII.

1.6 Research focus

As the most abundant coenzyme Q in humans, Q$_{10}$ and its hydroxylated derivative, HO-Q$_{10}$ have been in the research focus of our group[10,16]. The prominent hydrophobicity of its ten-unit long isoprenoid tail highlights a major limitation of Q$_{10}$ and HO-Q$_{10}$ studies due to its low solubility in numerous solvents. Less hydrophobic but still active derivatives of Q$_{10}$ can be made by replacing the long isoprenoid chain with more water-soluble moieties. Thus, this project was concentrated on *p*-benzoquinones, coenzyme Q$_1$ (Q$_1$) and decylubiquinone (dUQ), as more water-soluble analogues of Q$_{10}$ (Figure 1-9 a, b). Since these Q$_{10}$ analogues bear the same *p*-benzoquinone moiety, they maintain the redox features of Q$_{10}$ but present better water solubility. In contrast to Q$_{10}$, Q$_1$ is much more hydrophilic because it contains only one instead of ten isoprene units in its sidechain (Figure 1-9 a). Due to the very good water solubility of Q$_1$ (~250 mg/L) and the observation that the length of the sidechain does not strongly affect the redox properties of the quinone ring in different Q-compounds[147], Q$_1$ is a valuable model to explore the redox properties of the more lipophilic Q members in aqueous media. On the other hand, dUQ has a decyl hydrocarbon sidechain (Figure 1-9 b) and is incorporating into bio-membranes, particularly of isolated mitochondria[148]. dUQ has a lower solubility in water than Q$_1$, which can be increased by addition of water miscible organic solvent. As a part of another PhD project[149] in our research group, the hydroxylated form of mitoquinone (HO-mQ) was synthesized. Mitoquinone (mQ) is an antioxidant that specifically targets mitochondria. Its structure (Figure 1-9 c) comprises a *p*-benzoquinone moiety and decyl hydrocarbon sidechain connected to a triphenylphosphonium cation (TPP$^+$). What sets mQ apart from Q$_{10}$ and other Q$_{10}$ analogues is its remarkable ability to traverse the highly selective permeable IMM and to accumulate several 100-fold in the MM. This distinct feature is attributable to the TPP$^+$ which utilizes the plasma membrane potential ($\Delta\Psi_p$) to accumulate mQ into the cytosol. Subsequently, driven by the mitochondrial membrane potential ($\Delta\Psi_m$), mQ further accumulates in the MM[150,151].
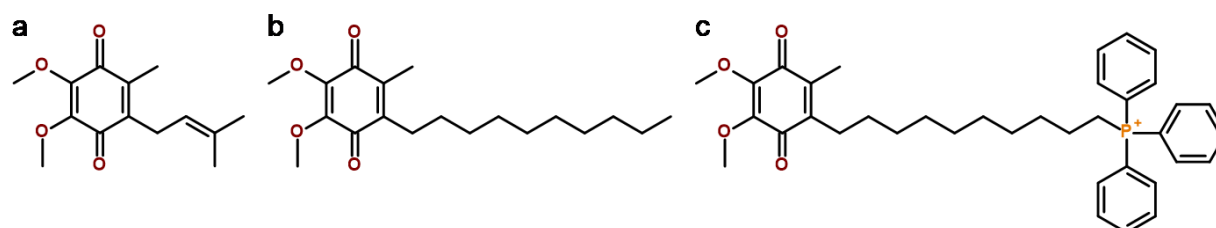
Figure 1-9 Chemical structures of a) coenzyme Q$_1$, b) decylubiquinone, and c) mitoquinone.

My dissertation was designed to achieve three key goals. Firstly, since the hydroxylated forms of Q$_1$ (HO-Q$_1$) and dUQ (HO-dUQ) are commercially not available, they had to be synthesized and

purified in sufficient amounts. Even though the method for synthesis of HO-Q_1 had been established previously by Bogeski *et al*.[10], it had to be scaled up for production of sufficiently large amounts for further isolation and purification. Due to the lipophilic nature of dUQ and to ensure its complete dissolution in aqueous alkaline medium, the procedure for the synthesis of HO-dUQ needed to be established. The structure and purity of the new products were determined by MS and NMR. Secondly, the goal was to gain the first insights into the electrochemical and spectroscopic properties of HO-Q_1 and HO-dUQ. The redox chemistry of Q_1 and dUQ as well as of their hydroxylated derivatives, HO-Q_1 and HO-dUQ, have not been thoroughly examined in the past. For an in-depth study of their basic redox properties with respect to their different solubilities as well as the availability of protons in solution, a broad variation in solvents and solvent compositions was necessary. To this end, voltammetric experiments in unbuffered and buffered aqueous media, in organic protic and aprotic solvents were performed as best suitable for the compounds. Moreover, cyclic and square-wave voltammetric studies were extensively applied to investigate the Ca^{2+} binding properties of the four compounds (Q_1, dUQ, HO-Q_1 and HO-dUQ). Finally, the third aim of this study was to assess potential biological activities of the hydroxylated forms, HO-Q_1, HO-dUQ, HO-Q_{10}, HO-mQ, and their corresponding native compounds. To evaluate the impact of these quinones on the mitochondrial respiration and other cellular functions, the test substances were exogenously applicated to isolated mitochondria from murine heart and to intact culture cells (HEK-293). Cell supplementation by Q_{10} and HO-Q_{10} was greatly limited by their lack of solubility in aqueous media. Consequently, a method for preparation of water-soluble formulations of Q_{10} and HO-Q_{10} had to be established. Thereafter, the content of Q_{10} and HO-Q_{10} was determined before and after treatment of HEK-293 cells with the water-soluble formulations of Q_{10} and HO-Q_{10}. Given that the HO-Q_1, HO-dUQ, and HO-mQ[149] were purified for the first time in our lab, nothing is known about their effects on living cells and potential functions in cellular processes. Moreover, we addressed the question whether Qs and HO-Qs may have toxic effects, even when applied in small amounts. Therefore, after cells treatment with the Qs and their corresponding HO-Qs, besides other metabolic processes, viability of HEK-293 cells was investigated. Since Q_{10} is an essential component of the mitochondrial ETC, which is regulated by mitochondrial $[Ca^{2+}]$, a possible impact of exogenously added Qs and HO-Qs on cellular Ca^{2+} metabolism was tested. For this purpose, cytosolic $[Ca^{2+}]$ was assessed in fura-2 loaded cells. Furthermore, to address the influence of Qs and HO-Qs on the mitochondrial bioenergetics, respiration of freshly isolated mitochondria from murine heart was examined.

Finally, the electrochemical properties of the tested substances as well as the effects on biological samples (intact cells and mitochondria) were compared and evaluated concerning their bio-applicability, especially their possible (long-term) beneficial or toxic effects.

2. Materials

2.1 Chemicals

Table 2-1 List of chemicals and reagents, their corresponding suppliers and product numbers.

Substance	Supplier	Product Number
1,2,4,5-Tetrachloro-3-nitrobenzene	Sigma	40384
2,5-dimethoxy-1,4-benzoquinone	Sigma	R164348
2,5-dimethyl-1,4-benzoquinone	Sigma	39579
2,5-dimethyl-3-hydroxy-1,4-benzoquinone	Sigma	S953199
2-propanol, 99,9% p.a.	Fisher Scientific	10315720
Acetic acid	Carl Roth	3738.5
Acetonitrile, >99,9% Gradient HPLC	Fisher Scientific	10660131
ADP	Sigma	A5285
Aluminium oxide	Alfa Aesar	14558
Ammonia solution, 25%	Merck Millipore	1.05432.1011
Antimycin A, *Streptomyces* sp.	Sigma	A8674
Bovine Serum Albumin, fatty acid free	Sigma	A7030
Calcium chloride-dihydrate	Merck	1.02382
Calcium Green™-5N, Hexapotassium salt	Thermo Fisher	C3737
Calcium perchlorate	Sigma	CDS001586
CCCP	Sigma	C2759
Chloroform	Sigma	24216
Chloroform-d ($CDCl_3$)	Sigma	431915
Chloroform-d ($CDCl_3$) with TMS	Sigma	530735
Cholesterol–PEG 600	Sigma	C1145
Citric acid	Sigma	C0759
Coenzyme Q_1	Sigma	C7956
Coenzyme Q_1	Cayman Chemical	18741
Coenzyme Q_{10}	OMIKRON	101181-5
Coenzyme Q_9	Cayman Chemical	16866
Cytochrome c from equine heart	Sigma	C2506
Decylubiqunone	Sigma	D7911
DMSO	Sigma	D8418
EGTA	Sigma	E4378
Ethanol, >99,8 % absolute, Ph Eur	Fisher Scientific	10437341
Fetal bovine serum (Gibco™)	Fisher Scientific	10270106
Formic acid	VWR	20318.297
Fura-2 AM	Thermo Fisher	F1221
Fura-2, pentapotassium salt	Thermo Fisher	F1200
Gibco™ Trypsin-EDTA (0.05%), phenol red	Thermo Fisher	25300062
Glycerol	Sigma	G5516
HEPES	Sigma	H7523
HO-dUQ	Section 3.1.2, p. 27	-

Substance	Supplier	Product Number
HO-mQ	Katerina Stankoska[149]	-
HO-Q$_1$	Section 3.1.1, p. 27	-
HO-Q$_{10}$	Ewa J. Slowik[16]	-
Hydrochloric acid	Merck	1.00317
Image-iT™ TMRM Reagent	Thermo Fisher	I34361
Ionomycin, Calcium salt, *S. conglobatus*	Merck	407952
ISOTON II diluent	Beckman Coulter Inc.	8448011
L-(−)-Malic acid	Sigma	M1000
Lactobionic acid	Sigma	153516
L-Glutamic acid	Sigma	G1149
Lithium perchlorate	Sigma	634565
Magnesium chloride hexahydrate	Merck	1.05833
Magnesium perchlorate, anhydrous	Alfa Aesar	11636
Methanol, >99,9% p.a.	Fisher Scientific	M/4000/17
Mitoquinone mesylate, >98%	MedKoo Biosciences	317102
n-Dodecyl β-D-maltoside	Sigma	D4641
Oligomycin, *S. diastochromogenes*	Sigma	O4876
Penicillin-Streptomycin	Sigma	P4333
Perchloric acid	Sigma	244252
Potassium chloride	VWR	26764.298
Potassium citrate tribasic monohydrate	Sigma	60153
Potassium hydroxide	J.T. Baker	0385
Potassium phosphate dibasic	Sigma	450200
Potassium phosphate monobasic	Sigma	229806
Proteinase, bacterial Type XXIV	Sigma	P8038
Rompun®, Xylazine Hydrochloride	Bayer	-
Rotenone	Sigma	R8875
Sodium chloride	Millipore	1.37017
Sodium dithionite	Sigma	71699
Sodium hydroxide	Merck	1.09956
Sodium pyruvate	Sigma	P2256
Succinate	Sigma	S2378
Taurine	Alfa Aesar	A12403
Tetrabutylammonium perchlorate	Sigma	86893
Thapsigargin, Invitrogen	Thermo Fisher	T7458
Trizma® base	Sigma	T1503
Ursotamin®, Ketamine Hydrochloride	Serumwerk	-

2.2 Assays

Table 2-2 List of kits and assays.

Kit	Manufacturer	Product Number
CellTiter-Blue® Cell Viability Assay	Promega GmbH	G8081
DC™ Protein Assay Kit II	Bio-Rad Laboratories	5000112
Pierce™ BCA Protein Assay Kit	Thermo Scientific	23225

2.3 Laboratory consumables

Table 2-3 List of laboratory consumables.

Material	Manufacturer	Product Number
1.5 mL clear glass vials, 11.6×32 mm	VWR	548-0029
15 ml polypropylene tubes	Sarstedt	62.554.502
2 mL screw top vials & caps, amber, 12×32 mm	Agilent Technologies	5182-0716
50 ml polypropylene tubes	Sarstedt	62.547.254
Cell culture dishes Ø35×10 mm	Thermo Fisher	353001
Cell culture flask T75	Sarstedt	83.3911.002
Collecting test tubes, 12×48 mm	Agilent Technologies	5022-6534
Falcon 96-well black/clear flat bottom with lid	Corning Incorporated	353219
Glass Pasteur pipettes	VWR	612-1702
Micro reaction tube 1.5 mL	Sarstedt	72.690.001
Microscope cover glasses, Ø12 mm, no. 1.5	neoLab Migge GmbH	MD-0083
Microscope cover glasses, Ø25 mm, no. 1.5	ORSAtec GmbH	O2R2515-D
Polishing set for solid-state electrodes	Metrohm AG	6.2802.000
SafeSeal microtube 2 mL	Sarstedt	72.695.500
SafeSeal SurPhob tips (10 µL; 200 µL; 1250 µL)	Biozym	VT0 103; 143; 173
SafeSeal tube 5 mL	Sarstedt	72.701
Screw caps with central hole Ø6 mm and septa	VWR	548-1502
Serological Pipette (5 mL; 10 mL; 25 mL)	Corning	734-1737; 1738; 1739
Single PCR tubes 0.5 mL	Brand	781310
Tips for Rainin® LTS® pipettes	VWR	613-5786; 5790; 5794
UV-Star® microplates, 96 well, flat bottom	Greiner Bio-One GmbH	655801
Vial insert, 250 µL, pulled point glass, 5.6×31 mm	Agilent Technologies	5183-2085
Viewseal sealer, clear	Greiner Bio-One GmbH	676070

2.4 Buffers and cell culture media

Table 2-4 List of buffers used for electrochemical measurements.

Hydrochloric Acid-Potassium Chloride (HCl-KCl) Buffer (pH range 1.0 – 2.2)

Components	0.2 M KCl		
	0.2 M HCl		
	50 mL of 0.2 M KCl were mixed with indicated volume of 0.2 M HCl and the final volume was adjusted to 200 mL with ddH$_2$O.		
pH	KCl (mL)	HCl (mL)	ddH$_2$O (mL)
1.0	50	97	53
2.0	50	10.6	139.4

Citrate Buffer (pH range 3.0 – 6.2)

Components	0.1 M citric acid ($C_6H_8O_7$)	
	0.1 M potassium citrate ($C_6H_5O_7K_3$)	
	0.1 M $C_6H_8O_7$ were mixed with 0.1 M $C_6H_5O_7K_3$ as indicated below.	
pH	$C_6H_8O_7$ (mL)	$C_6H_5O_7K_3$ (mL)
3.0	82	18
4.0	59	41
5.0	35	65

Phosphate Buffer (pH range 5.8 – 8)

Components	0.2 M KH_2PO_4		
	0.2 M K_2HPO_4		
	0.2 M KH_2PO_4 were mixed with 0.2 M K_2HPO_4 in proportions indicated below and the final volume was adjusted to 200 mL with ddH_2O.		
pH	KH_2PO_4 (mL)	K_2HPO_4 (mL)	H_2O (mL)
6.0	87.7	12.3	100
7.0	39	61	100
8.0	5.3	94.7	100

Carbonate Buffer (pH range 9.2 – 10.8)

Components	0.1 M $NaHCO_3$	
	0.1 M Na_2CO_3	
	0.1 M $NaHCO_3$ were mixed with 0.1 M Na_2CO_3 in proportions indicated below.	
pH	$NaHCO_3$ (mL)	Na_2CO_3 (mL)
9.2	90	10
10.1	40	60
10.8	10	90

Table 2-5 List of buffers and media used for cell culture.

Dulbecco's PBS (DPBS)	Composition	mM	Supplier	Product Number
[-] $CaCl_2$, [-] $MgCl_2$	$CaCl_2$ $MgCl_2$ KCl KH_2PO_4 NaCl Na_2HPO_4	- - 2.67 1.47 137.93 4.29	Sigma	D8537
pH Osmolarity (mOs/kg)			7.1-7.5 275-304	

Dulbecco's PBS (DPBS⁺⁺)	Composition	mM	Supplier	Product Number
[+] $CaCl_2$, [+] $MgCl_2$	$CaCl_2$ $MgCl_2$ KCl KH_2PO_4 NaCl Na_2HPO_4	0.9 0.49 2.67 1.47 137.93 4.29	Sigma	D8662
pH Osmolarity (mOs/kg)			6.9-7.1 275-304	

Gibco™ Minimum Essential Medium (MEM)			Thermo Fisher	31095029
Complete MEM	FCS P/S	10% 0.1%		

Cell Lysis Buffer (LB)	Composition	mM
	Tris	20 mM
	NaCl	100 mM
	Glycerol	10%
	DDM	1%
pH	7.4	

Table 2-6 Buffers used for calcium imaging.

Ringer Ca^{2+}-free Buffer (0 mM Ca^{2+})	Composition	mM
	NaCl	145
	KCl	4
	MgCl$_2$	2
	HEPES	10
	Glucose	10
	EGTA	1
pH	7.4	
Osmolarity (mOs/kg)	310	

Ringer Buffer (0.5, 1 or 2 mM Ca^{2+})	Composition	mM
	NaCl	145
	KCl	4
	MgCl$_2$	2
	HEPES	10
	Glucose	10
	CaCl$_2$	0.5/1/2
pH	7.4	
Osmolarity (mOs/kg)	310	

Table 2-7 Mitochondrial respiration media.

Mitochondrial respiration medium (MiR05)	Composition	mM
	Lactobionic acid	60
	Taurine	20
	D-sucrose	110
	HEPES	20
	MgCl$_2$	3
	KH$_2$PO$_4$	10
	EGTA	0.5
	BSA	0.015
pH (30 °C)	7.1 (5 M KOH)	

Mitochondria isolation solution (MIS)	Composition	mM
	Mannitol	225
	Sucrose	75
	HEPES	2
	EGTA	1
pH	7.4 (Tris base)	

Mitochondria suspension solution (MSS)	Composition	mM
	Mannitol	225
	Sucrose	75
	HEPES	2
pH	7.4 (Tris base)	

Respiration Buffer (0 µM free Ca^{2+}) – RB$_0$	Composition	mM
	KCl	137
	KH$_2$PO$_4$	4
	MgCl$_2$	2.5
	HEPES	20
	EGTA	0.1

Respiration Buffer (0 µM free Ca^{2+}) – RB_0	Composition	mM
pH	7.2 (5M KOH)	

Respiration Buffer (1.227 µM free Ca^{2+}) – $RB_{1.227}$	Composition	mM
	KCl	137
	KH_2PO_4	4
	$MgCl_2$	2.5
	HEPES	20
	EGTA	0.1
	$CaCl_2$	0.1
pH	7.2 (5M KOH)	

Respiration buffers (RB) with defined free Ca^{2+} concentrations were prepared by dilution of $RB_{1.227}$ with RB_0 (table below). Details about the calibration steps and preparation of RBs can be found in doctoral dissertation of Ewa J. Slowik[16]. Briefly, RB with 1 µM free Ca^{2+} was prepared by diluting 0.1 mM CaEGTA ($RB_{1.227}$) to 0.0959 mM CaEGTA with RB_0.

Buffer	free Ca^{2+} (µM)	CaEGTA (mM)
$RB_{1.227}$	1.227	0.1
RB_1	1	0.0959
$RB_{0.5}$	0.5	0.0820

2.5 Cell line and mouse model

2.5.1 Human embryonic kidney (HEK-293) cells

The original human embryonic kidney 293 cell line (HEK-293 cells) was established in 1973 from a kidney of human embryo[152–154]. The HEK-293 cell line was derived by transfection of primary cell cultures of HEK cells with sheared DNA of adenovirus type 5 (Ad5). The cells contain 4 kbp of the viral genome including early region 1 (E1), consisting of two units, E1a and E1b[155]. The products of these two units enable continuous culturing of HEK-293 cells by interfering with the cell cycle control pathways and counteracting apoptosis. The bases from the adenoviral genome are incorporated into human chromosome 19 of the HEK cells[156]. No active viruses are produced. Adherent HEK-293 cells (ATCC® CRL-1573™) were cultured in minimal essential medium (MEM) supplemented with 10% fetal bovine serum (FCS) and 0.1% penicillin/streptomycin (P/S) in humidified incubators kept at 37 °C and supplied with 5% CO_2.

2.5.2 Mouse model

The original C57BL mouse strain was initially established by Clarence Cook Little in 1921. The strain was further separated into two sublines, subline 6 (C57BL/6) and 10 (C57BL/10). From the C57BL/6 strain the two most popular and widely used substrains are C57BL/6J and C57BL/6N, which were developed by the Jackson Institute (JAX, Bar Harbor, Maine, USA) and the National Institutes of Health (NIH, Bethesda, MD, USA), respectively[157,158]. It has been reported[158,159] that there are genetic differences among the C57BL/6 substrains. Unlike C57BL/6N strain, C57BL/6J strain has a deletion in the nicotinamide nucleotide transhydrogenase (Nnt) gene. Since the Nnt gene is important for glucose homeostasis and controls insulin secretion, the C57BL/6J mice lacks these functions[158,160]. All experiments in this thesis were carried out with C57BL/6NCrl mice strain, purchased from Charles River Laboratories (Strain #005304).

2.6 Technical equipment

Table 2-8 List of used devices and their main components.

Laboratory equipment	Manufacturer	Product Number
Metrohm/Eco Chemie Autolab PGSTAT12 Potentiostat/Galvanostat Electrochemical System	Eco Chemie B. V., Netherlands	
equipped with:		
Titration vessel with thermostat jacket	Metrohm	6.1418.110
Ag/AgCl (3 M KCl) reference electrode	Metrohm	6.0726.107
Ag/Ag$^+$ reference electrode for non-aqueous solution	ALS Co., Ltd	012171
Pt-wire electrode (auxiliary electrode)	Metrohm	6.0301.100
Glassy carbon (GC) electrode (Ø2 mm)	Metrohm	6.1204.600
Magnetic stirrer MR 1000	Heidolph Instruments GmbH	503.02000.00
Agilent 1260 Infinity II Series HPLC System	Agilent Technologies, Inc., Germany	
equipped with:		
1260 Infinity II Vialsampler	Agilent	G7129A
1260 Infinity II Quaternary Pump	Agilent	G7111B
1260 Infinity II Thermostatted Column Compartment	Agilent	G1316A
1260 Infinity II Diode Array Detector WR	Agilent	G7115A
1260 Infinity II Fraction Collector Analytical Scale	Agilent	G1364C
1290 Infinity Thermostat	Agilent	G1330B
Poroshell 120 EC-C18, 4.6×100 mm, 2.7 µm	Agilent	695975-902T
Poroshell 120 EC-C18, 9.4×250 mm, 2.7 µm	Agilent	Custom
Oxygraph-2k Series G (O2k)	Oroboros Instruments Corp., Austria	
equipped with:		
O2k-Core	Oroboros	10000-02
O2k-Chambers (Duran® glass polished), 2 mL	Oroboros	23100-01
OroboPOS (polarographic oxygen sensor)	Oroboros	26000-01
OroboPOS-Service Kit	Oroboros	20610-03
OroboPOS-Membrane Ring	Oroboros	26120-01
OroboPOS-O-ring Viton®, 8×1 mm	Oroboros	26130-01
Stirrer Bar, 15×6 mm	Oroboros	23210-01
Stopper, black PEEK, conical shaft, central port	Oroboros	24000-01
Volume-Calibration Ring	Oroboros	2432A/B-01
O-ring Viton® for stopper, 12×1 mm	Oroboros	24310-01
Stopper Cover-Slip	Oroboros	24411-01
O2k-Titration Set	Oroboros	20820-03
Integrated Suction System (ISS)	Oroboros	20810-02
Axio Observer 7	Carl Zeiss Microscopy, Germany	
equipped with:		
Objective EC Plan Neofluar, 10x/0.30 M27	Zeiss	420340-9901-000
Objective Fluar, 20x/0.75 M27	Zeiss	420150-9900-000
Light Source HXP 120 V (LEJ, Jena)	Zeiss	423013-9010-000
Heating insert P S1 (PeCon®)	PeCon GmbH	130-800 005

Axio Observer 7	Carl Zeiss Microscopy, Germany	
Filter Set 21 HE	Zeiss	489021-0000-000
Prime 95B sCMOS-Camera	Photometrics	-
Vacuum suction pump (Schego M2K3)	Schego	740229FRO

Table 2-9 List of other used devices.

Device	Manufacturer
Analytical Balance AW-224	Sartorius AG
Centrifuge Universal 30 R	Hettich
CLARIOStar Microplate Reader	BMG LabTech
Culture CK30 Inverted Microscope	Olympus Corporation
Culture Microscope B201	Olympus Corporation
Dionex UltiMate 3000 RSLC System with Accucore PhenylHexyl column (2.1×100 mm, 2.6 µm)	Thermo Fisher Scientific
Heracell™ 150i CO_2 Incubator	Thermo Fischer Scientific
HI2211 pH/mV benchtop meter with HI1131 pH Electrode	Hanna Instruments Inc.
HI2211 pH/mV benchtop meter with HI1332 pH Electrode	Hanna Instruments Inc.
Infinite M200 PRO Microplate Reader	Tecan Trading AG
Milli-Q® Reference A+ Water Purification System	Merck Millipore
Monoshake Microplate Shaker	Thermo Fisher Scientific
NMR spectrometer, Avance I 500	Bruker BioSpin GmbH
Pipetboy acu 2	Integra Biosciences
Tissue grinder, borosilicate glass, Ø8 mm, 120 mm	Witeg Labortechnik GmbH
Pestle, PTFE head, stainless steel shaft, 230 mm	Witeg Labortechnik GmbH
Q-Exactive Plus Mass Spectrometer	Thermo Fisher Scientific
RV 8 V Rotary Evaporator: • HB 10 digital heating bath • PC 3001 VARIOpro Vacuum Pump • CVC 3000 vacuum controller	IKA®-Werke GmbH IKA®-Werke GmbH Vacuubrand GmbH
Schallsonic 900 Ultrasound Cleaner	Schalltec GmbH
Sonorex Super RK 1028H Ultrasonic bath	BANDELIN electronic GmbH
Sterile workbench HERAsafe™ KS	Thermo Fisher Scientific
Thermomixer Univortemp (1.5 mL)	Universal Labortechnik GmbH
UV-Visible Spectrophotometer Ultrospec™ 2100 pro; High Precision Cuvette (Quartz Suprasil®); opt. path 1 cm	GE Healthcare Life Sciences Hellma Analytics
WiseStir® Homogenizer HS-30E, 200-5000 U/min	Witeg Labortechnik GmbH
Z 32 HK High speed centrifuge with refrigeration system	HERMLE Labortechnik GmbH
Z-Serie Coulter Counter	Beckman Coulter Inc.

2.7 Software

Table 2-10 List of used software.

Software	Version	Manufacturer
Accelrys Draw 4.1	4.1 .NET	Accelrys, Inc.
BioRender.com		
CLARIOStar® Mars Data Analysis Software	3.42 R3	BMG LabTech
General Purpose Electrochemical System (GPES)	4.9	Eco Chemie B. V.
IgorPro	6.3.7.2	WaveMetrics, Inc.

Software	Version	Manufacturer
MarvinSketch	23.7.0	ChemAxon Ltd.
Mendeley Reference Manager	2.62.0	Mendeley Ltd. (Elsevier)
OpenLab CDS ChemStation (offline)	2.16.12	Agilent Technologies
OpenLab CDS ChemStation (online)	2.16.12	Agilent Technologies
OriginPro	2022	OriginLab Corp.
SWIFT II Wavescan		GE Healthcare Life Sciences
TopSpin	4.1.3	Bruker
Word 2019	16.0.14729.20260	Microsoft
Xcalibur™ 4.3	4.3.73.11	Thermo Fisher Scientific
ZEN (blue edition) 2.6 (Acquiring Data)		Carl Zeiss Microscopy
ZEN (blue edition) 3.3 (Data Analysis)	3.3.89	Carl Zeiss Microscopy

3. Methods

3.1 Synthesis of hydroxylated forms of coenzyme Q$_1$ and decylubiquinone

Since the hydroxylated forms of Q$_1$ and dUQ are not commercially available, the initial phase involved synthesis and purification of these substances in sufficient amounts.

3.1.1 Synthesis of hydroxylated form of coenzyme Q$_1$

20 mg of coenzyme Q$_1$ (Q$_1$) were dissolved in 40 mL of 0.1 M NaOH (pH = 13). The reaction was carried out at room temperature (RT) in a round bottom flask and protected from light. After 90 minutes, the reaction was stopped by neutralization with 5 M hydrochloric acid (HCl). The aqueous phase was removed by rotary evaporation and the sodium chloride from the neutralization reaction was removed by washing the reaction mixture with chloroform. The washing step was performed 3 times with 10 mL chloroform. The reaction mixture was reconstructed in a small volume of ethanol and aliquoted in autosampler vials. Ethanol was evaporated under a stream of nitrogen at RT and any residual ethanol was removed in a desiccator under vacuum. The vials containing the reaction products were stored at −20 °C.

3.1.2 Synthesis of hydroxylated form of decylubiquinone

1 mM decylubiquinone (dUQ) in methanol was mixed with the same volume of 0.2 M NaOH (1:1 v/v, final concentration of NaOH was 0.1 M). The reaction was carried out at RT in a round bottom flask protected from light. After 2 hours of incubation at RT, the reaction was stopped by neutralization with 5 M HCl. Solvent was removed by rotary evaporation and the sodium chloride from the neutralization reaction was removed by washing the reaction mixture with chloroform (3 times with 10 mL chloroform). The reaction mixture was dissolved in a small volume of methanol and aliquoted in autosampler vials. Methanol was evaporated under a stream of nitrogen at RT, followed by total removal of residual methanol in a desiccator under vacuum. The vials with reaction products were stored at −20 °C.

3.1.3 Spectrophotometric analysis of the synthesis reaction course

Principle. Spectroscopy is a technique used for measurement and analysis of spectra arising from the interaction of electromagnetic (EM) radiation with matter. EM radiation can have different energies and dependent on that energy different molecular features can be probed. EM radiation is composed of electric and magnetic field vectors directed perpendicular to each other and perpendicular to the direction of propagation (Figure 3-1 a). It can be described in terms of wavelength (λ) defined as distance between two consecutive peaks and frequency (v) defined as number of oscillations per second (1 s^{-1} = 1 Hz). The relationship between λ and v is given by:

$$\lambda = \frac{c}{v}$$

<div align="right">Eq. 3-1</div>

where λ is wavelength (m), v is frequency (s^{-1}) and c is the velocity of light (3·10^8 m·s^{-1}). Electromagnetic radiation carries a certain amount of energy, the photon energy E, which is related to the frequency or wavelength by

$$E = hv = \frac{hc}{\lambda}$$

Eq. 3-2

where h is *Planck*'s constant. It is apparent that the shorter the wavelength or the greater the frequency, the greater the energy will be[161].
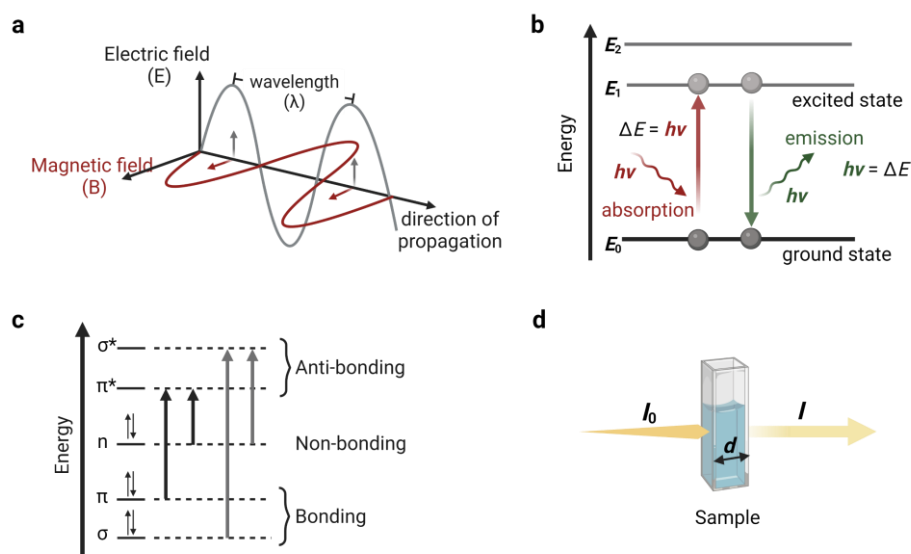
Figure 3-1 Principles of UV-Vis Spectroscopy. a) Illustration of an electromagnetic radiation which is plane-polarized and propagates along the *x*-axis. The electric (E) and magnetic (B) fields are directed perpendicular to each other and to the direction of propagation. b) An energy diagram depicting the absorption and emission of a photon by an atom or a molecule; when an incoming photon with energy hv (red colour) interacts with the atom or molecule, absorption can take place if the energy difference ΔE between the ground (E_0) and the excited state (E_1) matches the energy of the photon. An atom or molecule in E_1 can transition back to E_0 by emitting a photon with energy hv (green colour) which corresponds to the energy difference ΔE between the two states. c) Scheme of possible molecular electronic transitions. The length of the arrows indicates the energy for various transitions. Black arrows represent transitions achievable with energies from the UV-Vis spectrum, whereas the transitions indicated by grey arrows demand higher energies such as X-rays. d) Absorption of radiation by a sample in a cuvette. Intensity of incident radiation (I_0), intensity of transmitted radiation (I) and pathlength (d).

When EM radiation is passing through a sample, some of the radiation (energy) will be absorbed, while the remaining is transmitted. The absorption of energy by a molecule can result in rotational, vibrational, and electronic transitions depending on the frequency of the EM radiation. Spectroscopy in the ultraviolet (UV) and visible (Vis) regions of the EM spectrum involves observation of transitions in electronic energy levels. Despite being termed UV-Vis spectroscopy, the wavelength scale that is typically used ranges from 180-380 nm (near-ultraviolet), 380-780 nm (visible) up to 1100 nm in the near-infrared region of the EM spectrum. Electrons within atoms or molecules are distributed across multiple energy levels, primarily occupying the levels with lowest energy (ground state, E_0). An electron will jump to a higher-energy level (excited state, E_1) only if photon energy hv is equivalent to the energy difference (ΔE). The ΔE is defined by the difference in energies between the final (excited, E_1) and the starting (ground, E_0) state as $\Delta E = E_1 - E_0 = hv$ (Figure 3-1 b). Excited states typically have very short lifespans ranging from femtoseconds to microseconds due to the instability of the higher-energy state. The excess energy is dissipated through relaxation processes (emission) (Figure 3-1 b). These emission processes can occur in several ways: (i) production of heat, (ii) emission of radiation with the same energy (spontaneous emission) or with a lower energy than that of the absorbed radiation (fluorescence, phosphorescence), and (iii) photochemical processes (photoinduced reaction leading to internal structural change like ionization, cleavage, etc.)[161,162].

In an absorption spectrum the measured absorption is plotted against wavelength. In the simpler case of single atom, electronic transitions lead to line spectra. In contrast, spectra of molecules are usually observed as band spectra attributable to a broader distribution of energy levels and hence, of more possible electronic transitions. The electronic transitions in molecules can be categorized based on the molecular orbitals involved in the transitions (Figure 3-1 c). Among the four potential transitions ($\sigma \rightarrow \sigma^*$, $n \rightarrow \sigma^*$, $\pi \rightarrow \pi^*$ and $n \rightarrow \pi^*$) only two can be induced by UV-Vis radiation: $\pi \rightarrow \pi^*$ and $n \rightarrow \pi^*$. The $\sigma \rightarrow \sigma^*$ and $n \rightarrow \sigma^*$ transitions require higher energy that cannot be provided by UV-Vis radiation.

UV-Vis spectroscopy can be used in both qualitative and quantitative analysis. Qualitatively, it is used to identify functional groups or validate the identity of a compound by comparing its absorption spectrum to that of a known compound. In a quantitative manner, it is used to determine the concentration of the analyte using the *Lambert-Beer* law which relates absorbance to analyte concentration as given by Eq. 3-3:

$$A = d \cdot c \cdot \varepsilon$$

<div align="right">Eq. 3-3</div>

where d (cm) is the path length of the light through the sample, c (mol/dm^3) the molar concentration, ε (dm^3/mol·cm) is the molar absorption coefficient, and A is the absorbance of the sample which is detected by the spectrophotometer (Figure 3-1 d)[161,162].

Experiment. To follow the changes in the absorption spectra during the chemical reaction over time, aqueous solutions of Q_1 or ethanolic solution of dUQ were added in 0.1 M NaOH in a final concentration of 0.05 mM Q_1 or dUQ. Measurements were performed in sealed quartz cuvettes for a wavelength range from 200−900 nm, a scan speed of 1800 nm/min and scan step of 1 nm.

3.2 Separation and purification of the hydroxylated forms of coenzyme Q_1 and decylubiquinone by high-performance liquid chromatography (HPLC)

Principle. Reversed-Phase High-Performance Liquid Chromatography (RP-HPLC) is the most popular and widely used analytical technique for separation of substances. The term reversed-phase arises from the fact that separation is based on differences in analyte (sample) partitioning between a polar mobile phase (solvent, eluent) and a non-polar stationary phase (column packing material). Mobile phase consists of solvents that give an overall greater polarity compared to the stationary phase. The polarity of the mobile phase can be changed by changing the solvent composition. Most used components for the mobile phase are water and water-miscible solvents (methanol, ethanol, acetonitrile, etc.). The stationary phase consists of hydrophobic ligands (n-alkyl hydrocarbon groups: octyl group, octadecyl group, etc.) chemically bound to a porous insoluble core, typically silica core (Figure 3-2, a and b). The stationary phase must be chemically and mechanically stable. Hydrocarbon groups are generally coupled to the silica core via silanol groups (−Si−OH) on its surface (Figure 3-2 a).

HPLC involves injection of a small volume of liquid analyte (mixture of at least two compounds) into a column, where individual components of the analyte are moved down the column with a mobile phase (Figure 3-2 c). The mobile phase together with the analyte are forced through the

column by high pressure delivered by a pump. The retention time of each component in the injected analyte depends on its chemical structure and intermolecular interactions with the column packing material. Generally, retention increases with increasing size and/or hydrophobicity of the sample resulting in a faster elution of polar molecules (Figure 3-2 c). Therefore, different components of the analyte are eluted at distinct time points, achieving separation of the mixture (Figure 3-2 c). Subsequently, a detection device (UV detector, MS detector, etc.) identifies the compounds upon exiting the column. The resultant plot is termed chromatogram, where the x-axis represents the analysis time and y-axis displays the intensity of the signals as recorded by the detector (Figure 3-2 c). Following detection, the mobile phase can be further passed on to additional detection devices, a fraction collection system or disposed as waste[163].
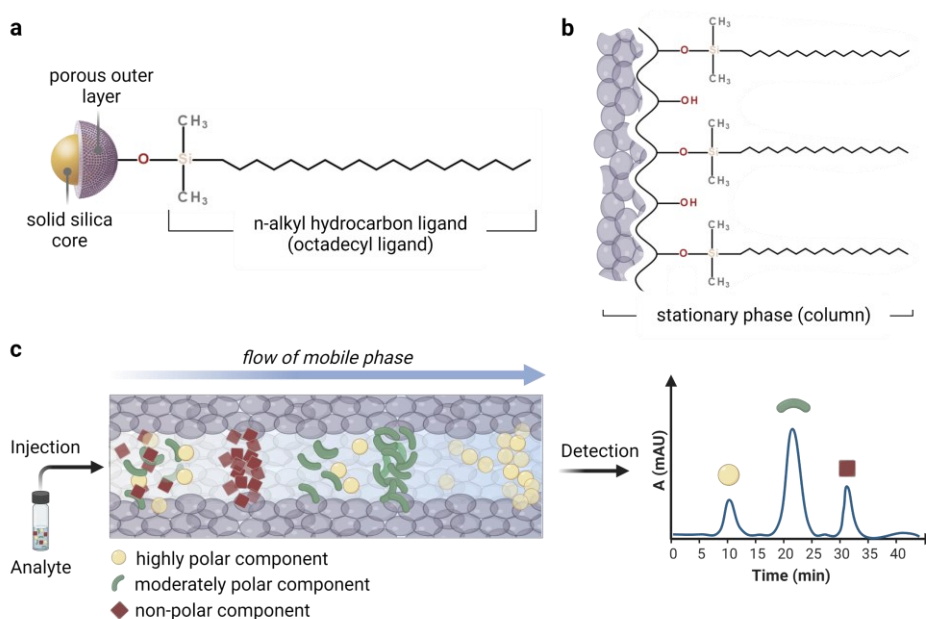
Figure 3-2 Schematic diagram of reverse-phase chromatography separation. a) *InfinityLab* Poroshell 120 EC-C18 particle composition: octadecyl group chemically bound to the surface of the solid silica core. b) Structure of *InfinityLab* Poroshell 120 EC-C18 column. c) Principle of RP-HPLC: The separation is based on the interaction between the components of the injected analyte and the stationary phase. The stationary phase is non-polar and exhibits a high affinity for non-polar molecules (red) slowing down their progression. The mobile phase is polar, resulting in faster elution of the polar components (yellow – highly polar) in the analyte. The moderately polar molecules (green) are eluted by the mobile phase faster than non-polar (red) molecules, but slower than highly polar molecules (yellow). The output of the separation is chromatogram in which x-axis displays the analysis time and y-axis shows the intensity of the signals.

The purpose behind the HPLC approach can be analytical or (semi)preparative. Analytical HPLC is used to separate the ingredients of a sample mixture and the observed chromatogram generally provides the starting point for a preparative separation. On the other hand, the (semi)preparative HPLC is used for isolation and purification of reasonably sufficient quantities of a specific substance(s) from the sample[164].

3.2.1 Analysis of the reaction mixture and method development for purification of the reaction products by analytical HPLC

The reaction mixture samples obtained as described in sections 3.1.1 and 3.1.2 were analysed by HPLC. The stationary phase consisted of a C−18 silica-based column (*InfinityLab* Poroshell 120 EC-C18), with dimensions: 4.6 x 100 mm, 2.7 µm. The column was washed and equilibrated with the mobile phase. The mobile phase was a mixture of either 52:48 (v/v) acetonitrile (ACN)

and water containing 0.1% HCOOH for the reaction mixture of Q_1 or a mixture of 84:16 (v/v) methanol (MeOH) and water containing 0.1% HCOOH for the reaction mixture of dUQ. The dried reaction mixture was dissolved in the corresponding mobile phase. The isocratic program was run with a flow rate of 0.5 mL/min at column temperature of 40 °C (Table 3-1). The detection was performed with a UV detector at 275 nm which is characteristic absorbance of the quinone ring. In order to determine the retention time and distinguish between peaks from the products and the parental quinone, solutions of commercially available Q_1 and dUQ were chromatographed under identical analytical conditions.

3.2.2 Purification of the reaction products by semi-preparative HPLC

Using the analytical isocratic HPLC methods developed in section 3.2.1, the separation was scaled to the preparative C−18 column (Poroshell 120 EC−C18, with dimensions: 9.4 x 250 mm, 2.7 µm). The column for semi-preparative HPLC was designed and produced in a way to meet our needs. The packing was produced using the same particle and bonding technology as in the *InfinityLab* Poroshell 120 EC−C18 column used for analytical scale analysis (Figure 3-2 a and b). This enables direct scale-up of separations from analytical to preparative proportions with little modifications. The column was washed and equilibrated between runs with 30 volumes from the mobile phase. The flow rate was 2.5 mL/min at column temperature of 40 °C (Table 3-1). The dried reaction mixture was dissolved in the corresponding mobile phase. Per each run, 100 µL of the reaction mixture (3 mg/mL) was injected into the sample loop (100 µL), which prevented dilution of the injected sample with the mobile phase. The compounds were collected in fractions using peak-based trigger mode. To eliminate collection of impurities the lower threshold was set to 750 mAU for the reaction mixture of Q_1 and 1000 mAU for the mixture of dUQ. The needle was rinsed between collection of each peak in the chromatogram. The purified peaks were collected in 4.5 mL glass vials and the temperature of the fraction collector was kept at 4 °C. At the end of the working day, the purified fractions were dried and stored at −20 °C. After separation and purification of the new products in sufficient amounts, the fractions from different days were mixed and dried by rotary evaporation. The yield of the new products was 78% for HO-Q_1 and 25% for HO-dUQ. The products were aliquoted in glass autosampler vials and stored at −20 °C.

Table 3-1 Conditions for separation and purification of the new products by HPLC. ACN, acetonitrile; MeOH, methanol; HCOOH, formic acid.

	Q_1 reaction		dUQ reaction	
	Analytical HPLC	Preparative HPLC	Analytical HPLC	Preparative HPLC
Column dimensions	4.6 x 100 mm, 2.7 µm	9.4 x 250 mm, 2.7 µm	4.6 x 100 mm, 2.7 µm	9.4 x 250 mm, 2.7 µm
Mobile phase	ACN:H_2O = 52:48, v/v, 0.1% HCOOH		MeOH:H_2O = 84:16, v/v, 0.1% HCOOH	
Flow rate	0.5 mL/min	2.5 mL/min	0.5 mL/min	2.5 mL/min
Injection volume	10 µL	100 µL	10 µL	100 µL
Column temperature	40 °C			
Detection	275 nm			
Fraction collector	4 °C			

3.3 Structural analysis of the reaction products

3.3.1 Liquid Chromatography - Mass spectrometry

Principle. Liquid Chromatography - Mass spectrometry is a powerful technique that couples two independent analytical systems and their functions: the resolving power of liquid chromatography (LC) with the detection sensitivity of mass spectrometry (MS). LC-MS involves use of LC wherein the analyte is passing through chromatographic column resulting in separation of individual components of the analyte. As the mobile phase is eluted from the column, it passes through an MS interface (Figure 3-3) where the mobile phase is nebulized into an aerosol (Figure 3-3, step 1), its separated components are ionized (Figure 3-3, step 2) and then transferred to the mass analyser and detector (Figure 3-3, steps 3 and 4). The mass analyser separates the generated ions under vacuum according to their mass to charge (*m/z*) ratios and quantifies the intensity of each ion. The resulting mass spectrum is a graphical representation of the relative ion intensities against *m/z* values and provides structural data for eluted components (Figure 3-3, step 4)[165–167]. All mass spectrometers have three fundamental components: an ion source (ionization), a mass analyser (separation) and a detector (Figure 3-3).
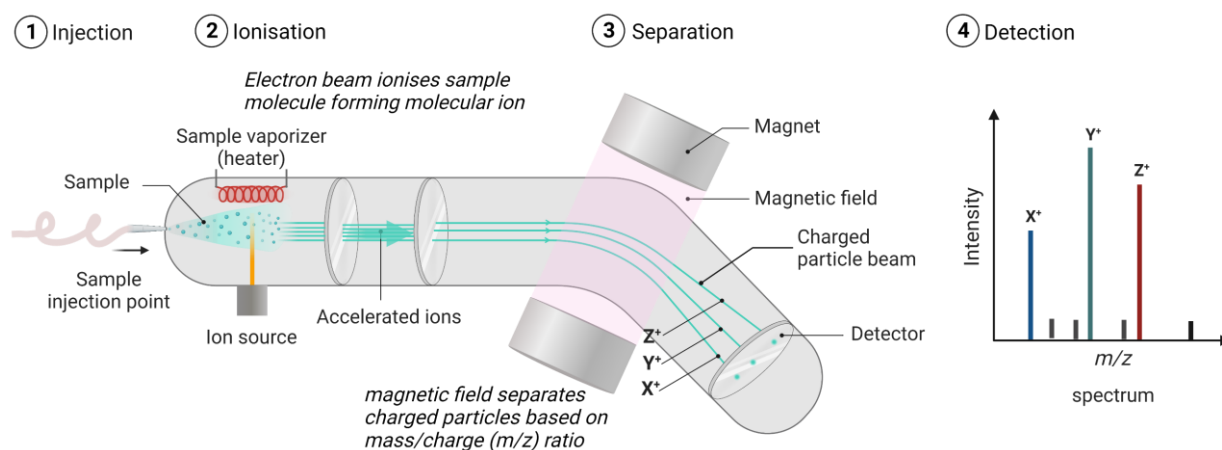
Figure 3-3 Schematic illustration of mass spectrometer. 1) In the initial step a liquid sample, often obtained from a liquid chromatography, is injected into the mass spectrometer. Via a charged needle and nebulizer gas a fine aerosol is formed and sprayed into a high-vacuum environment. 2) Thereafter, the sample is vaporized and ionized which is typically achieved through an electron beam. The resulting ions are then accelerated towards a magnetic field. 3) Within the field the ionized particles are effectively separated by the *Lorentz*-force according to their mass-to-charge (*m/z*) ratio before reaching the detector. 4) From the detector data a mass spectrum is generated, plotting the intensity of each detected ion over *m/z*. Figure is adapted from BioRender (2021) and comprises information from [165–167].

For MS analysis the sample need to be ionisable and its ions must be sufficiently stable in gas-phase environment under high vacuum. Several ionization techniques are used in MS to produce ions according to the physical state of the sample: (i) gas, (ii) liquid or dissolved sample, or (iii) solid substance or dry material on a target. Electron ionization (EI) and chemical ionization (CI) represent conventional examples of gas-phase ionization techniques and are commonly applied in gas chromatography-mass spectrometry (GC-MS). Electrospray ionization (ESI), which is extensively used in LC-MS, is a liquid-phase ionization technique. Matrix-assisted laser desorption/ionization (MALDI) and desorption electrospray ionization (DESI) exemplify solid-phase ionization techniques. In the mass analyser ions are sorted and separated according to their *m/z* ratios. There are multiple varieties of mass analysers including quadrupole, ion trap, time of flight, magnetic sector, electrostatic sector, and ion cyclotron resonance[167].

For the experiments in this thesis, ESI was used as an ionization technique with orbitrap (ion trap) mass analyser. A brief description of each is included below.

Electrospray ionization (ESI)

In electrospray ionization (ESI) an electrical field is applied to convert the sample in solution into ions in gas-phase prior to their analysis by the MS analyser. The conversion of sample in solution into ions in the gas-phase consists of three successive steps. Initially, a continuous stream of sample in solution is passed through a capillary maintained at high voltage (Figure 3-3, step 1). By application of nebulizing gas (nitrogen) the flow rate of the sample is increased. Due to the electrical field an aerosol of highly charged droplets (with same polarity as the capillary voltage) is produced at the exit of capillary tip. Next, a heat source and/or an extra stream of nitrogen promotes evaporation of the solvent, so that the charged droplets are shrinking in size. This process results in an enhancement of the surface charge density and the ions contained in the droplets are ejected into gas-phase and subsequently accelerated into the mass analyser for analysis (Figure 3-3, step 2)[165,167,168]. In most cases, either a proton is added to the analyte (M) resulting in molecular ion $[M+H]^+$ (when the ion source is operated in positive ionization mode) or a proton is lost generating $[M−H]^-$ ion (when ion source is operated in negative ionization mode). Furthermore, other adduct (quasi-molecular) ions such as $[M+Na]^+$, $[M+K]^+$, $[M+NH_4]^+$, $[M+HCOO]^-$, $[M+CH_3COO]^-$ can be generated as well (or instead).

Orbitrap Mass Analyzer

Ions generated in the ion source are transferred to the mass analyser region along a potential gradient. The orbitrap mass analyser is an ion trap mass analyser that consist of two outer electrodes that have shape of cups facing each other to form a barrel-like enclosure and a central spindle-like electrode that holds the trap (barrel) together. By applying voltage between the outer and the central electrodes an electric field is generated. Ions are injected into the volume between the central and the outer electrodes where the electric field traps them. Ions rotate about the central electrode and oscillate harmonically with a frequency characteristic of their *m/z* values, inducing current on the outer electrodes. The detection is performed by recording the induced current over time followed by a fast conversion of the recorded time-domain signal in a *m/z* spectrum by applying a Fourier transform algorithm (Figure 3-3, step 4)[169].

Experiment. The LC-MS measurements were established and performed by Prof. Dr. Markus R. Meyer (Department of Experimental and Clinical Toxicology, Saarland University) using modified published protocols[170–172].

Sample Preparation: Q_1, HO-Q_1, DUQ and HO-DUQ were prepared freshly by dissolving in methanol to yield concentration of 1 mM. The samples were kept in a glass autosampler vials closed with a silicon-sealed screw cap, protected from light, and stored at 4 °C.

Measurement parameters: The samples were analysed using a Dionex UltiMate 3000 RS system (degasser, quaternary pump, UltiMate autosampler) coupled to a Q-Exactive Plus system equipped with a heated electrospray ionization (HESI-II) system (Table 2-9). Autosampler temperature was set at 4 °C and 1 µL sample was injected into the column. As a stationary phase

an Accucore PhenylHexyl column with dimensions 2.1 x 100 mm, 2.6 µm was used. Elution was performed using a gradient at a flow rate of 0.5 mL/min. The composition of the mobile phase, together with the gradient elution method is given in Table 3-2.

Table 3-2 Composition of the mobile phase and the timeline for the gradient elution used for LC-MS. HCOONH₄, ammonium formate; aq., aqueous solution; ACN, acetonitrile; HCOOH, formic acid; MeOH, methanol; H_2O, water.

Mobile phase composition		Gradient elution method		
Eluent A (water-based)	Eluent B (organic-based)	Time (min)	Eluent A (%)	Eluent B (%)
HCOONH₄, 2 mM (aq.)	HCOONH₄, 2 mM	0.0 − 10.0	99.5 to 0.5	0.5 to 99.5
ACN, 1% (v/v)	ACN:MeOH = 1:1 (v/v)	10.0 − 10.1	0.5 to 99.5	99.5 to 0.5
HCOOH, 0.1% (v/v)	H_2O, 1% (v/v)	10.1 – 12.1	99.5	0.5
pH = 3	HCOOH, 0.1% (v/v)			

Mass calibration was done prior to measurements following manufacturer's recommendations employing external mass calibration[170–172]. Conditions for HESI-II source were set as follows: ionization mode, positive and negative alternating; spray voltage, ± 3.50 kV; sheath gas, 53 AU; auxiliary gas, 14 AU; sweep gas, 3 AU; heater temperature, 438 °C; ion transfer capillary temperature, 269 °C; and S-lens RF level, 60.0. Mass spectrometry was performed using full scan data. The settings for full scan data acquisition were as follows: resolution, 70000; automatic gain control target, $3x10^6$; maximum injection time, 200 ms; microscans, 1; scan range, *m/z* 50 – 750. Data analysis was performed using *Xcalibur Qual Browser* software.

3.3.2 Nuclear magnetic resonance spectroscopy

Principle. Nuclear magnetic resonance (NMR) spectroscopy is a technique that has the specific advantage to simultaneously assess the chemical structure for identification and the purity/impurity ratios of the compounds. NMR is based on the principle that a paramagnetic nucleus of an atom placed in a strong magnetic field is resonating at a specific frequency when exposed to EM radiation. Similar to the other spectroscopic techniques, the interaction of EM radiation with atoms or molecules triggers transition of entities from lower- to higher-energy states (e.g., electrons in UV-Vis spectroscopy, Figure 3-1 b)[173]. In NMR these entities are the atomic nuclei which follow quantum chemical rules to occupy specific energy levels. After a certain period, the nuclei will relax from the higher-energy state to the lower one. An atomic nucleus can be detected by NMR only when possessing a spin state, which generates its own nuclear magnetic moment. In general, nuclei composed of an odd number of protons (^1H and its isotopes, ^{14}N, ^{19}F and ^{31}P) or an odd number of neutrons (^{13}C) have a spin, thus they have magnetic moment and are considered as NMR-active nuclei. When the number of protons and neutrons are both even (^{12}C or ^{16}O) the nuclei have no spin and therefore are not NMR-active[173–175].

Proton NMR (^1H NMR)

The nucleus of hydrogen (^1H) is a spinning particle with a local magnetic field (µ). In the absence of an external magnetic field the nuclear magnetic moment is oriented in random directions (Figure 3-4). However, when an external magnetic field is applied, the nucleus aligns either with

(α state) or against (β state) the field of the external magnet. The α spin state is lower in energy than the β spin state. The energy difference (ΔE) represents the difference in energy between α and β spin state and it depends on the strength of the applied magnetic field (Figure 3-4). With no applied field, there is no energy difference between the spin states. The greater the strength of the applied magnetic field, the larger is ΔE between the spin states. A transition from lower to higher energy state and vice versa can be triggered by using EM radiation. Since the ΔE between the spin states is small, the energy transition occurs at a wavelength that corresponds to the radio frequency (RF) range of the EM spectrum. The frequency of radiation absorbed by a proton during a spin transition in an NMR experiment is called its resonance frequency[174].
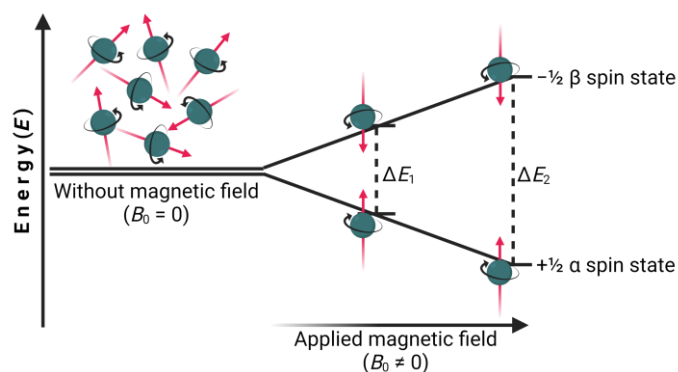
Figure 3-4 Magnetic properties of atomic nuclei with a nuclear spin ½. With no applied magnetic field ($B_0 = 0$), the nuclei are randomly orientated and there is no energy difference ($\Delta E = 0$) between the spin states. In the presence of external magnetic field ($B_0 \neq 0$), nuclei exist in two nuclear spin states (α and β states) of different energy. As the strength of the applied magnetic field is enhanced, the energy difference between spin states increases and therefore a higher frequency is required to cause the spin-flip.

Every atom is surrounded by electrons, which orbit the nucleus and will create a magnetic field that is felt by nucleus. Due to the electronic clouds surrounding the nucleus, the effective magnetic field that is experienced by the nucleus differs from that of the applied magnetic field, an effect known as nuclear shielding. Depending on the shielding effect, different frequencies are required to excite the spin flip of the nucleus in the applied magnetic field. The greater the electron density (electronegativity) around the proton, the larger is the effect of shielding and the proton is less susceptible to the applied magnetic field. Thus, less energy is taken (lower RF) to flip that proton. In contrast, when the electron density around the proton is lower (deshielded proton), the exposure of the proton to the applied magnetic field is higher. Therefore, more energy is needed (higher RF) to flip it. That creates a set of peaks in the NMR spectrum where each peak corresponds to protons with distinct chemical environment (non-equivalent protons). In some compounds, protons in a molecule can be equivalent. Chemically equivalent protons are protons that have the same chemical environment (same electron density, same distance, and type of a bonding to all the other atoms in the molecule).

Since the different proton frequencies are depending on the strength of the applied magnetic field and NMR instruments may have different field strengths, the resonance frequencies would differ accordingly. Therefore, frequencies are not reported as absolute values in Hz, but rather as values relative to the frequency of a defined reference compound. The difference between the position of the signal of interest and that of the reference is termed chemical shift. To remove the dependence of the chemical shift on the strength of applied magnetic field and therefore operating

frequency, the chemical shift is expressed as parts per million (ppm) and defined by the following equation:

$$\delta_{sample}(ppm) = \frac{v_{sample} - v_{reference}}{v_{reference}} \times 10^6$$

<div align="right">Eq. 3-4</div>

where δ_{sample} is the chemical shift, v is the frequency (Hz) of the sample and reference compound, respectively, and the factor 10^6 is introduced to present the chemical shift value in ppm.

In ^{1}H and ^{13}C NMR spectroscopy, tetramethylsilane (TMS) is mostly employed as internal standard to determine the chemical shift of the sample (δ_{TMS} = 0 ppm). Since TMS contains twelve equivalent and highly shielded protons it gives only a single sharp peak, located at the right end of the spectrum, which is well separated from most of the other signals normally observed for organic compounds. TMS is chemically inert and can be easily removed from the sample due to its low boiling point[174–176].

The features of ^{1}H NMR spectrum provide the following insights into the molecular structures:

- number of signals: reveals the number of non-equivalent (different types) protons.
- position of signals: indicates the chemical environment (shielding and deshielding).
- intensity of signals: integration of the signals gives the number of equivalent protons.
- spin-spin coupling (splitting) of the signals: protons on adjacent carbons will interact and split each other's resonances into multiple peaks following the n + 1 rule.

Quantitative NMR (qNMR)

Although NMR spectroscopy is mainly used as a qualitative method for structural elucidation of chemical compounds, its quantitative use has gained increasing importance over the past years[177–179]. The crucial feature of quantitative NMR (qNMR) is that the signal response (integrated signal area) is directly proportional to the number of nuclei. Despite that the NMR spectrum of a single compound usually consists of several signals (resonance lines), it is sufficient to select a single signal specific for the sample composition. Quantitative data is obtained from a direct comparison of NMR signal intensities of the compound of interest with the intensities of a reference compound. The reference compound can be used as an internal or an external standard. Utilization of an internal standard involves adding the reference compound directly to the sample. Thus, the reference compound must meet several criteria including availability in high-purity form, stability, chemically unreactive, soluble, weighable, non-volatile as well as having a straightforward NMR spectrum that does not overlap with signals of the sample[180]. The purity of the sample P_x (%), when an internal standard is used, can be calculated using the formula (Eq. 3-5)[177]:

$$P_x = \frac{I_x}{I_{std}} \times \frac{N_{std}}{N_x} \times \frac{M_x}{M_{std}} \times \frac{m_{std}}{m_x} \times P_{std}$$

<div align="right">Eq. 3-5</div>

where I_x and I_{std} are the integrated signal area of NMR line of the sample and the standard, respectively; N_x and N_{std} correspond to the number of spins of the sample and standard, respectively; M_x and M_{std} are the molar masses of the sample and the reference compound,

correspondingly; m_x the weighed mass of the sample; m_{std} and P_{std} are the weighed mass and the purity of the reference compound.

qNMR can also be carried out by calibration with external standard, meaning that the sample and the standard are separated from each other in different solutions. External standards are used mainly for biological samples, where the sample contamination must be avoided. One approach for using external calibration is ERETIC method (***E**lectronic **RE**ference **T**o access **I**n vivo **C**oncentrations*)[181]. In this method an electronic pulse device is employed to create an artificial reference signal. The operator has control over various parameters of this signal such as frequency and magnitude. Additionally, this signal is calibrated against known concentrations of an external standard solution. The ERETIC signal provides a pseudo-FID (Free Induction Decay) that has all the characteristics of an authentic NMR signal and which after *Fourier* transformation is transformed into a frequency line within the NMR spectrum. Consequently, the resulting NMR spectrum of the studied sample features an extra line alongside those corresponding to the sample itself[180,181]. The concentration of the sample solution is determined by using the formula below:

$$[sample] = k[ERETIC]\frac{A_{sample}}{A_{ERETIC}}$$

Eq. 3-6

where *k* considers the number of protons per chemical group; A_{sample} is the area of the NMR signal to be quantified; A_{ERETIC} is the area of the ERETIC peak; [*sample*] is the concentration of sample; [*ERETIC*] is the concentration of the ERETIC signal determined after a calibration against known concentration of external standard solution by the following formula:

$$[ERETIC] = [reference]\frac{A_{ERETIC}}{A_{reference}}$$

Eq. 3-7

where [*reference*] is the concentration of the external standard solution and $A_{reference}$ is the area of the calibration peak[181].

Experiment. NMR experiments were recorded and analysed by Dr. Josef Zapp (Department of Pharmaceutical Biology, Saarland University).

Sample preparation for ^{1}H-NMR. NMR spectroscopy detection was performed on *Bruker AVANCE I 500 MHz* spectrometer equipped with a 5 mm double resonance broad band BBO probe. The samples were measured in tightly capped NMR tubes at room temperature. Dried samples (Q_1, HO-Q_1, dUQ, HO-dUQ), around 5.0 - 5.5 mg, were accurately weighed and prepared by dissolving them in 750 µL deuterochloroform ($CDCl_3$) containing 0.03% TMS (v/v) as internal standard.

Analysis of ^{1}H-NMR. NMR data was processed in *TopSpin*. For graphical representation, data were exported as JACMP-DX file and further analysed in *OriginPro*. The peak of the TMS was set to chemical shift δ = 0 ppm. Using *OriginPro*, the absolute frequency was calculated with the formula:

$$absolute\ frequency\ (Hz) = (number\ of\ intervals - measured\ interval) \times$$

$$\left(\frac{pulse\ width}{number\ of\ intervals}\right) + \left(sending\ frequency - \frac{pulse\ width}{2}\right)$$

where the number of intervals corresponds to the total number of rows in the exported file subtracted by 1; measured interval represents specific number of a row subtracted by 1; pulse width is the first listed frequency (maximal frequency); sending frequency is taken from the measurement parameters in *TopSpin* for each experimental set. The calculated absolute frequency was transformed into chemical shift (ppm) using Eq. 3-4, where as a v_{sample} is taken the absolute frequency and $v_{reference}$ is found within measurement parameters in *TopSpin* for each experimental set.

Sample preparation for qNMR. NMR spectra were recorded on a *Bruker AVANCE III HD 700 MHz* spectrometer equipped with a 5 mm triple resonance TCI probe. The samples were measured in tightly capped NMR tubes at room temperature. Dried samples (Q$_1$, HO-Q$_1$, dUQ, HO-dUQ), around 5.0 - 5.5 mg, were accurately weighed and prepared by dissolving them in 750 µL CDCl$_3$ (containing 0.03% TMS). Calibration of ERETIC peak was performed using 1,2,4,5-tetrachloro-3-nitrobenzene (TCNB) as external standard (Eq. 3-6 and Eq. 3-7). Standard solution of TCNB was prepared by dissolving 64 mg TCNB in 10 mL CDCl$_3$ (containing 0.03% TMS).

Analysis of qNMR. The qNMR was carried out employing the ERETIC method. The purity (*P*) of the sample was calculated in % using the following formula:

$$\%P_{sample} = \frac{[sample]_{experimental} - [sample]_{calculated}}{[sample]_{calculated}} \times 100$$

where [sample]$_{calculated}$ is the concentration of the investigated sample calculated from the weighed mass of the sample; [sample]$_{experimental}$ is the measured concentration of the sample, determined with formula (Eq. 3-6). The molar masses are 260.89 g/mol, 250.29 g/mol, 236.26 g/mol, 322.44 g/mol and 308.41 g/mol for the standard TCNB, Q$_1$, HO-Q$_1$, dUQ and HO-dUQ, respectively.

3.4 Electrochemical characterization of quinones and their hydroxylated forms

Principle. Electrochemistry is a subfield of physical chemistry that studies the connection of electricity and chemistry. Electrochemical techniques are used to measure electrical parameters such as current, potential or charge and their correlation to chemical features.

Electrochemistry is divided in two major categories, bulk electrochemistry and interfacial electrochemistry. Bulk electrochemistry investigates properties of the whole solution, i.e., measurement of the conductivity of a solution. Interfacial electrochemistry comprises electrochemical methods where the resulting signal is a function of phenomena occurring at the interface between a conductor (electrode) and the solution (electrolyte). Based on the absence or presence of current (*I*) flow, interfacial methods are further divided into two main groups, static

and dynamic techniques. In static (equilibrium) methods, the current is zero ($I = 0$), no net reaction occurs and consequently concentrations of the species remain unchanged, or static (e.g., potentiometry applied in pH glass electrodes). In dynamic (transient) interfacial methods a net reaction occurs and measurable currents flow ($I > 0$). Depending on the experimental conditions, these methods can be additionally divided in controlled–current and controlled–potential (potentiostatic) techniques[182].

Voltammetry encompasses all controlled-potential methods where non-spontaneous, interfacial charge transfer processes are driven by an externally applied potential and a resulting current is measured. Applied potentials can be perceived as "electron pressure" compelling the chemical species to either acquire or lose electrons leading to reduction or oxidation, respectively. Consequently, the resulting current reflects the rate at which electrons traverse the interface[183]. The nature and magnitude of the current is used to study the sample. The unique advantage of electrochemistry is that the redox equilibrium (thermodynamics) and the rate of the electrode reaction can be affected by alteration of the electrode potential.

Before targeting the principles of the two voltammetric techniques used in this project, cyclic and square-wave voltammetry, an overview of fundamental aspects common for all voltammetric methods will be given.

The core of the voltammetric methods is the electrode|electrolyte interface, where an electrochemical (redox) reaction takes place with electrons being exchanged between an electrode[*] and the analyte present in the solution. Thus, the redox reaction is termed electrode reaction. While the analyte is present in the solution, the other participant in the reaction, i.e., electrons, reside in a different phase (electrode), so that this reaction is a heterogenous electron transfer[†] process. Simple electrode reactions can be described by the general reduction (forward, left to right) and oxidation (backward, right to left):

$$Ox_{(aq)} + ne^-_{(s)} \underset{k_b}{\overset{k_f}{\rightleftarrows}} Red_{(aq)} \qquad\qquad E^{\theta\prime} \qquad\qquad \text{Eq. 3-10}$$

where Ox and Red are the oxidized and reduced forms, respectively, n the stoichiometric number of electrons e^-, k_f and k_b the forward and backward heterogeneous rate constants, respectively, $E^{\theta\prime}$ the formal potential of the redox couple Ox/Red and the abbreviations (aq) and (s) indicate solution phase and the electrode as source of electrons, correspondingly.

Considering the reduction half-reaction in Eq. 3-10, at the start of an experiment at positive potential relative to the formal potential, it is assumed that only Ox species are present in the electrolyte solution at a bulk concentration $[Ox]_b$, whereas the Red form is absent ($[Red]_b = 0$). In the course of the experiment the potential of the electrode is gradually decreased triggering a shift in the electrode reaction towards the Red form, consequently causing a current to flow within the electrochemical cell. The current attributable to the change in oxidation state of redox-active

---

[*] When referring to "electrode", it denotes the working electrode as it is the site where the reaction of interest occurs.

[†] Correspondingly, homogeneous electron transfer occurs between species in the same phase.

species is termed as faradaic current since it obeys *Faraday*'s law[*] and its magnitude depends on the concentration of the analyte in the region of the electrode surface. The faradaic[†] current is a direct measure of the rate of the electrode reaction. The generation of faradaic currents requires Ox and Red species to reach the electrode surface and establish certain concentrations at the electrode|electrolyte interface. The concentrations of Ox and Red species at the interface are termed surface concentrations, $[Ox]_s$ and $[Red]_s$ respectively, and they differ from the corresponding bulk concentrations, $[Ox]_b$ and $[Red]_b$[183,184].

Faradaic processes which involve charge transfer at the electrode interface (e.g., reaction in Eq. 3-10) represent just one aspect of current generation in voltammetry. Concurrently, an interfacial phenomenon termed as non-faradaic processes take place. Although these processes do not involve an interfacial charge transfer, they still contribute to overall current. Both faradaic and non-faradaic processes occur during electrode reactions and they are closely linked to the formation of an electric double layer (EDL) at the electrode|electrolyte interface[184].
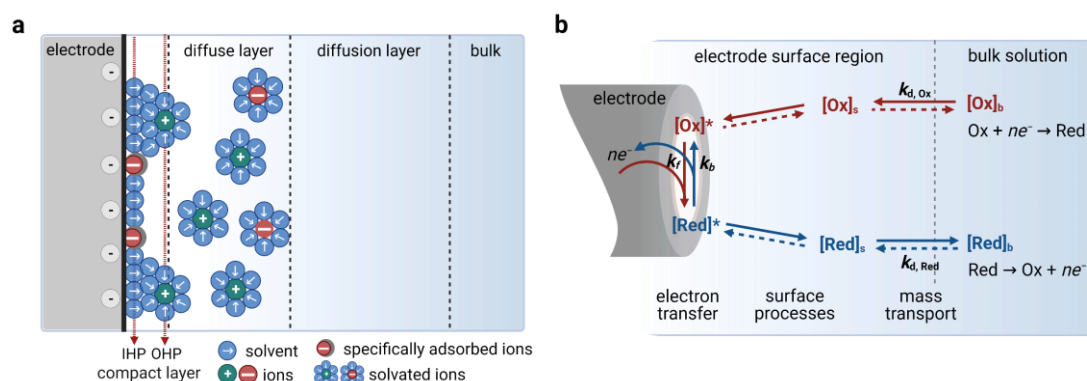
Figure 3-5 Schematic representations of an electric double layer and electrode reaction. a) Scheme of the composition of the electric double layer (EDL) at the electrode|electrolyte interface. The compact layer is closest to the electrode surface characterized by the inner *Helmholtz* plane (IHP) representing the specifically adsorbed ions and the outer *Helmholtz* plane (OHP) embodying non-specifically adsorbed counterions. OHP is the region where diffuse layer begins. b) Schematic pathway of the electrode reaction composed of simultaneous and consecutive steps: mass transfer with respective coefficient k_d, surface processes, e.g., chemical reactions and electron transfer. Ox and Red are the oxidized and reduced species, respectively; subscripts b and s indicate bulk and surface concentrations of the species, correspondingly; superscript * indicates different species after the surface processes.

The formation of a microscopic EDL (Figure 3-5 a) occurs as a result of an excess of charge at the electrode surface and the subsequent arrangement of the charged particles at the side of the electrolyte solution in response to the charge surplus. Such a layer is made of ions of opposite sign to that of electrode, i.e., negatively charged electrode attracts positive ions and vice versa. Figure 3-5 a illustrates the complex structure of EDL which consists of several distinct parts. The compact layer is the layer closest to the electrode, where ions are strongly adsorbed at the electrode surface. It comprises specifically adsorbed species (molecules or ions of the solvent, reactants, products or intermediates of the reaction) on the electrode surface and non-specifically adsorbed ions drawn to the electrode surface by electrostatic forces. The inner (IHP) and outer (OHP) *Helmholtz* plane are used to discriminate between the two categories of adsorbed species. IHP is defined as a plane passing through the centres of the specifically adsorbed ions which are

---

[*] *Faraday*'s law states that the quantity of reacted species is directly proportional to the current passing through the cell.

[†] The faradaic current is not the sole source of current in voltammetry. In addition, a small non-faradaic current can be measured.

not fully solvated allowing to get closer to the electrode, while OHP reflects the plane passing through the centres of non-specifically adsorbed solvated counterions at their closest approach to the electrode. The OHP is also the plane where a three-dimensional region of scattered ions termed as diffuse layer begins. The total charge of the compact and diffuse layer equals and is opposite in sign to the net charge on the electrode. The established microscopic EDL functions as a capacitor holding significant capacitance due to very small distance between the two oppositely charged layers. Accordingly, formation of the EDL is associated with the current flow referred to as charging current (I_c). The I_c interferes with the faradaic one as both are contributing components of the overall resulting current. Although the faradaic current is usually of primary interest in the study of an electrode reaction, the effects of the charging (capacitive) current must be considered when using electrochemical measurements to obtain data about the charge transfer[182–185].

The schematic pathways of electrode reactions are shown in Figure 3-5 b. Generally, the mechanism of electrode reactions (Eq. 3-10) consists of several different steps which happen in a sequence: (i) mass transport of the analyte from the bulk solution to the electrode surface, (ii) an electron transfer at the electrode surface, (iii) a chemical reaction preceding or following the electron transfer in the vicinity of the electrode and (iv) other surface processes such as absorption, desorption or crystallization. The slowest step in this sequence is the rate determining step. The rate of electrode reaction (υ_{net}) in terms of current (I) is described with the equation:

$$\upsilon_{net} = \frac{I}{nFA} \qquad \text{Eq. 3-11}$$

where A (m^2) is the area of the electrode, n the stoichiometric number of electrons transferred in the reaction, F is the *Faraday* constant (96487 C/mol).

Mass transfer occurs before the charge transfer step. Since both processes are always taking place, the slower of the two processes will be the rate determining step, i.e., the net rate of the electrode reaction, and consequently the measured current can be limited either by the mass transport of the analyte or by the rate of the electron transfer[183].

Mass transport process

The transport of redox species to and from the electrode surface can be accomplished only by mass transport. The rate at which reactants and products are moved to and from the electrode surface is predisposed by three modes of mass transport[183]:

- Diffusion – is a spontaneous mass transfer under the influence of concentration gradient (from region with high to region with low concentration). Diffusion occurs due to the difference in the concentration of the redox species at the electrode surface and bulk solution.

- Migration – is a movement of ions along an electrical field (potential gradient). When a potential is applied at the electrode, the electrode|electrolyte interface becomes charged and ions near that interface will be either attracted or repelled from it by electrostatic forces.

- Convection – is a mass transport caused by an external mechanical force, e.g., stirring of the solution.

For electrode reactions where the mass transport is the slowest step in the sequence (Figure 3-5 b), the net rate (υ_{net}) is governed totally by the rate at which the redox species are brought to the surface by mass transfer (υ_{mt}). Therefore, from Eq. 3-11 follows

$$\upsilon_{net} = \upsilon_{mt} = \frac{I}{nFA}$$
<div align="right">Eq. 3-12</div>

The measure for the rate of mass transport (υ_{mt}) is flux (J) defined as the number of molecules passing through a unit area over time (mol/m^2·s). The flux to an electrode which includes the three modes of mass transport is described by the *Nernst–Planck* equation:

$$J(x,t) = \underbrace{-D \cdot \frac{\partial c(x,t)}{\partial x}}_{diffusion} \underbrace{- \frac{zFDc}{RT} \cdot \frac{\partial \phi(x,t)}{\partial x}}_{migration} \underbrace{+ c(x,t) \cdot v(x,t)}_{convection}$$
<div align="right">Eq. 3-13</div>

where D is the diffusion coefficient (m^2/s), $\frac{\partial c(x,t)}{\partial x}$ the concentration gradient, z is the charge (dimensionless), c is the concentration of the reagent (mol/dm^3), R is the universal gas constant (8.314 J/K·mol), T (K) is the temperature, $\frac{\partial \phi(x,t)}{\partial x}$ the potential gradient, and υ is the velocity of the solution (m/s). In Eq. 3-13, the first term contains the diffusion (concentration gradient), the second one expresses the migration (potential gradient), and the third term describes the convection. An accurate mathematical solution of Eq. 3-13 generally becomes very complex when the three processes happen simultaneously. The situation is greatly simplified when an inert supporting electrolyte is added to the media at a concentration much higher than that of the analyte and when solution remains unstirred. This allows the effects of migration and convection processes to be considered negligible compared to the diffusion effect. Hence, the electrode reaction is limited only by the diffusion process and Eq. 3-13 can be simplified to Eq. 3-14, known as *Fick*'s first law, according to which the rate of diffusion (J) is directly proportional to the slope of the concentration gradient:

$$J(x,t) = -D \cdot \frac{\partial c(x,t)}{\partial x}$$
<div align="right">Eq. 3-14</div>

Combination of Eq. 3-12 and Eq. 3-14 yields a general expression for the I response in diffusion limited systems:

$$I = -nFAD \frac{\partial c(x,t)}{\partial x}$$
<div align="right">Eq. 3-15</div>

Considering once again Eq. 3-10, as reduction of Ox progresses, the Ox form is consumed and is depleted in the vicinity of the electrode. Figure 3-6 shows the evolution of the concentration profiles of Ox and Red with time. Since Ox is present in high concentration in the bulk solution, a concentration gradient is created which triggers fresh Ox to diffuse from bulk solution to the interface. On the other hand, Red that is generated at the electrode surface will diffuse towards bulk solution. The region of the solution where these changes in concentration take place is defined as the diffusion layer and will grow with time. The rate of its growth depends on the diffusion coefficients (D) of the species. The thickness of the diffusion layer (δ) grows with time,

while the concentration gradient (the steepness of concentration vs. distance function) will decrease with time (brighter red and dotted lines in Figure 3-6)[182–184].
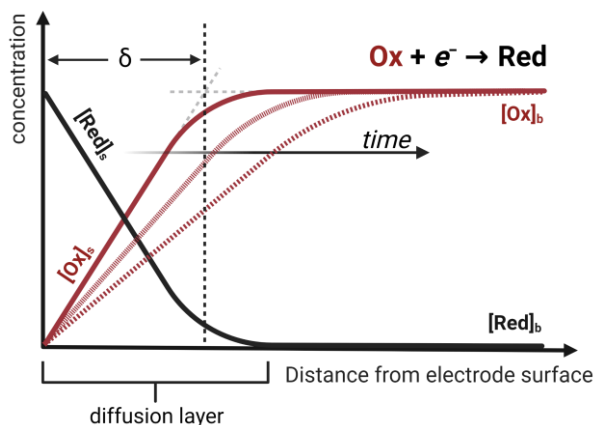
Figure 3-6 Diffusion layer and evolution of the concentration profiles of Ox and Red forms with time. Ox form undergoes reduction, resulting in depletion of its concentration and production of Red form at the vicinity of the electrode. δ is the thickness of the diffusion layer where the concentration changes and is increasing with time (intersection of dashed grey lines of Ox concentration).

The rate of mass transport is measured by the coefficient k_d defined as:

$$k_d = \frac{D}{\delta}$$

Eq. 3-16

where D (m²/s) is the diffusion coefficient and δ (m) the thickness of the diffusion layer.

Clearly, because the concentration gradient decreases with time, the current also drops with time (Eq. 3-15). When diffusion is the rate determining step, the current decay for planar electrode and unstirred solution is given by the *Cottrell* equation (Eq. 3-17) according to which the current decreases with $t^{1/2}$ [183]:

$$I = nFAc\sqrt{\frac{D}{\pi t}}$$

Eq. 3-17

Electron transfer process

For electrode reactions with sufficiently fast mass transport, the generated current is controlled by the rate of electron transfer (υ_{ct}). Kinetics of the electron transfer describes the electrode reaction with respect to potential and concentration. Considering redox reaction (Eq. 3-10) and equation for the net rate of the electrode reaction (Eq. 3-11), the rate of the forward (reduction) reaction (υ_f) and the rate of the backward (oxidation) reaction (υ_b) are expressed as:

$$\upsilon_f = \frac{I_f}{nFA} = k_f[Ox]_s$$

Eq. 3-18

$$\upsilon_b = \frac{I_b}{nFA} = k_b[Red]_x$$

Eq. 3-19

where k_f and k_b are the forward and backward heterogeneous rate constants, respectively. The dependence of these constants upon the applied potential is described by an exponential relationship:

$$k_f = k°\,exp\left[\frac{-\alpha nF\left(E - E^{\theta'}\right)}{RT}\right]$$

Eq. 3-20

43

$$k_b = k^{\circ} exp\left[\frac{(1-\alpha)nF\left(E - E^{\theta'}\right)}{RT}\right]$$

Eq. 3-21

where k° is the standard heterogeneous rate constant (m/s) and α is the transfer coefficient which varies between 0 and 1.

The net (overall) current (I_{net}) for the electrode reaction (Eq. 3-10) is given by the difference between the forward (I_f) and backward current (I_b):

$$I_{net} = I_f - I_b$$

Eq. 3-22

By reorganizing Eq. 3-18 and Eq. 3-19 to express I_f and I_b and by substituting the expressions for k_f and k_b, given by Eq. 3-20 and Eq. 3-21 respectively, I_{net} is given with the following equation:

$$I_{net} = nFAk^{\circ}\left\{[Ox]_s exp\left[\frac{-\alpha nF\left(E - E^{\theta'}\right)}{RT}\right] - [Red]_s exp\left[\frac{(1-\alpha)nF\left(E - E^{\theta'}\right)}{RT}\right]\right\}$$

Eq. 3-23

Eq. 3-23 describes the current-potential relationship for electrode reactions controlled by the rate of electron transfer.

When the equilibrium between Ox and Red forms is rapidly established at the electrode|electrolyte interface, i.e., when charge transfer is faster than mass transport, the relationship between the potential of the electrode (E) and the concentration of the redox couple Ox/Red is given by the *Nernst* equation:

$$E = E^{\theta'} + \frac{RT}{nF} ln\frac{[Ox]_s}{[Red]_s}$$

Eq. 3-24

where $E^{\theta'}$ (V) is the formal potential for the redox couple Ox/Red, $[Ox]_s$ and $[Red]_s$ (mol/dm^3) are surface concentrations of the oxidized and reduced forms. R, T, n and F have their already defined meaning[182,183].

The *Nernst* equation describes an equilibrium situation, and hence an electrode reaction in which the redox species reach equilibrium concentrations at the interface for any potential of the electrode is termed reversible reaction. Oppositely, when the charge transfer process is slower than the mass transport, the equilibrium cannot be established with a sufficient rate and such electrode reactions are termed irreversible reactions[182,183].

Electrochemical cell

Voltammetric measurements are performed in an electrochemical cell with a three-electrode set-up consisting of working electrode (WE), reference electrode (RE) and counter electrode (CE). They are immersed in an electrolytic (ionic) solution containing the sample of interest (Figure 3-7). While the WE is the electrode at which the reaction of interest (charge transfer process) occurs, the RE provides a reference potential against which the potential of the WE is measured. Thus, the RE should be robust with a constant chemical composition preserving a stable, reproducible, and constant potential, i.e., the RE must behave as an ideally non-polarizable electrode. Such shielding against changes in RE potential is achieved by a reversible redox process of its redox couple at a very high rate, which enables rapid adjustment to changes in the

ion concentrations in the vicinity of RE interface[186]. Commonly used reference electrode in aqueous media is the silver-silver chloride (Ag/AgCl) electrode in a saturated chloride (e.g., 3M KCl) solution. In non-aqueous solvents, usually pseudo-reference electrodes based on Ag/Ag^+ couple are employed, consisting of a silver wire immersed in a solution of silver salt, e.g., $AgNO_3$. Current should never pass through the RE since it can cause damage of the electrode and change its potential. The third electrode CE is used to complete the electrical circuit carrying the current generated by the processes proceeding at the WE, and ensuring that the generated current does not flow through the RE. The CE must be substantially larger in area size than the WE so that the current density at its surface is small (negligible) and the processes occurring at CE do not affect the current signal generated at the WE[186]. The CE is generally chosen to be inert under the reaction conditions, e.g., platinum wire or carbon. The WE may be constructed from a broad variety of materials such as noble metals, carbon, liquid metals etc. Additionally, its surface can be modified to increase its sensitivity toward specific species, e.g., chemical sensors. The liquid phase typically consists of a solvent containing the dissolved sample and a supporting electrolyte salt to achieve the required conductivity, thus enabling a continuous current flow in solution. The supporting electrolyte is composed of non-reactive ionic salts or ionisable compounds. It is used in much higher concentration than the analyte to minimize the solution resistance and to prevent migration of charged species caused by the electric field[186,187].
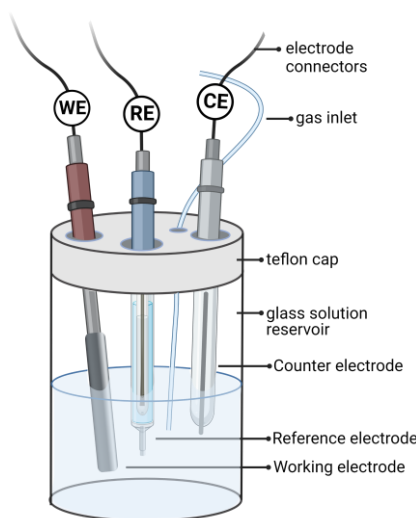
Figure 3-7 Electrochemical cell with three-electrode set-up. Working electrode (WE); reference electrode (RE); counter electrode (CE); gas inlet (e.g., N_2) for degassing the solution. Electrodes are immersed in the electrolyte solution containing the sample.

The potential on the WE is controlled relative to the RE and the current between the WE and the CE is measured with the aid of a potentiostat.

Cyclic voltammetry

Cyclic voltammetry (CV) is the most commonly used electroanalytical technique for obtaining data about electrochemical processes[183,184]. CV provides fast and direct insights into thermodynamics of electrode reactions and kinetics of heterogeneous electron transfer processes as well as data on coupled chemical reactions (reaction preceding and/or following the electron transfer) or adsorption processes. During a CV experiment, the potential of a stationary WE is scanned linearly over time using a triangular potential waveform (Figure 3-8 a).

The CV response can be fragmented into two linear potential scans, one in positive (anodic) potential direction and the other in negative (cathodic) potential direction. The potential is swept between two values, initial potential E_1 and end (switching) potential E_2 (Figure 3-8 a), starting from E_1. When the potential reaches E_2 the scan is reversed and swept back to E_1. Applied potential is changed linearly as a function of time at a defined rate termed as scan rate (v) in V/s. The potentiostat measures the current as a function of the applied potential and the resulting plot of current (I) vs. potential (E) is called cyclic voltammogram (Figure 3-8 b)[183,184].

Considering redox reaction (Eq. 3-10) and assuming that only the Red form is present at the beginning of the experiment, a positive potential scan is chosen for the first half cycle starting from a value (E_1) where no oxidation occurs and no faradaic current flows. As the applied potential approaches the $E^{\theta\prime}$ for the redox couple (Ox/Red), oxidation (anodic) current begins to increase until a maximum peak current ($I_{p,a}$) at a given potential ($E_{p,a}$) is achieved (Figure 3-8 b). When the switching potential E_2 is reached, the scan direction of the potential is reversed, and the potential is scanned in negative direction. During the reversed half cycle, Ox products generated in the first half cycle and accumulated near the WE surface are reduced back to Red, resulting in an increase of the reduction (cathodic) current and a new peak current ($I_{p,c}$) at a certain potential, $E_{p,c}$ (Figure 3-8 b). By convention, the oxidation (anodic) current (I_a) and reduction (cathodic) current (I_c) are assigned with a positive and negative sign, respectively[184,187].
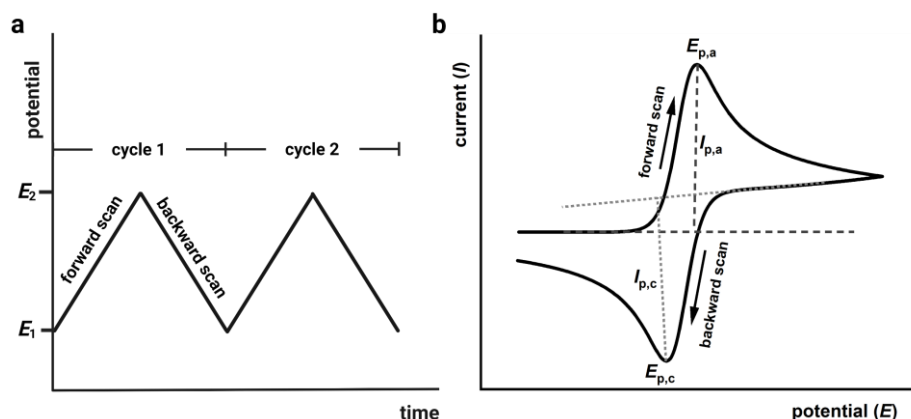
Figure 3-8 Waveform and response in cyclic voltammetry. a) Triangular potential-time signal in cyclic voltammetry. b) Typical cyclic voltammogram for a reversible redox process, where $I_{p,a}$, $E_{p,a}$, $I_{p,c}$ and $E_{p,c}$ are the anodic and cathodic peak currents and peak potentials, respectively. Dashed lines show the method used for extracting the current values from the voltammogram. The baseline currents are extrapolated and the peak currents are measured vertically from the peak down or up to the associated extrapolated baselines. Figure modified from [184].

The characteristic "duck" shaped cyclic voltammograms are a consequence of the formation of the diffusion layer near the electrode surface (Figure 3-6)[183,184,187]. The concentrations of Ox and Red near the WE surface are dependent on (i) the applied potential (Eq. 3-24) and (ii) on mass transport, i.e., how the species move from the bulk solution to the electrode and vice versa (Eq. 3-14). The continuous change in [Ox]$_s$ and [Red]$_s$ is coupled with an expansion of the diffusion layer thickness (Figure 3-6), and the resulting current peaks reflect a continuous change of the concentration gradient over time. Hence, the increase in the current resembles the achievement of diffusion control (new material reaching electrode surface), whereas the current drop (decaying tail of the voltammogram) exhibits a $t^{1/2}$ dependence (Eq. 3-17) and reflects the mass transport in the expanding diffusion layer[183,184,187].

The key features of the cyclic voltammogram are the peak current (I_p) and the peak potential (E_p) of both, reduction (cathodic) and oxidation (anodic) scan. These parameters can be directly obtained from the cyclic voltammogram as shown in Figure 3-8 b. By detailed assessment of the interrelation of peak currents and peak potentials as a function of the scan rate (v), information regarding thermodynamics and kinetics of the electrode reaction as well as the mechanism of the electron transfer process can be acquired[184].

In Figure 3-9 three different heterogenous electron transfer processes are shown associated to reversible, quasi-reversible and irreversible processes, each giving rise to a unique voltammetric profile. As mentioned previously, electrochemical reversibility depends on the rate of electron transfer process and on the rate of mass transport. Fast kinetics of the electron transfer ($k^0 \gg k_d$) causes a reversible process, while a slow electron transfer ($k^0 \ll k_d$) shows irreversibility. In the case of a quasi-reversible process, the rate of electron transfer becomes comparable to the rate of mass transport and the current is controlled by both processes[182].
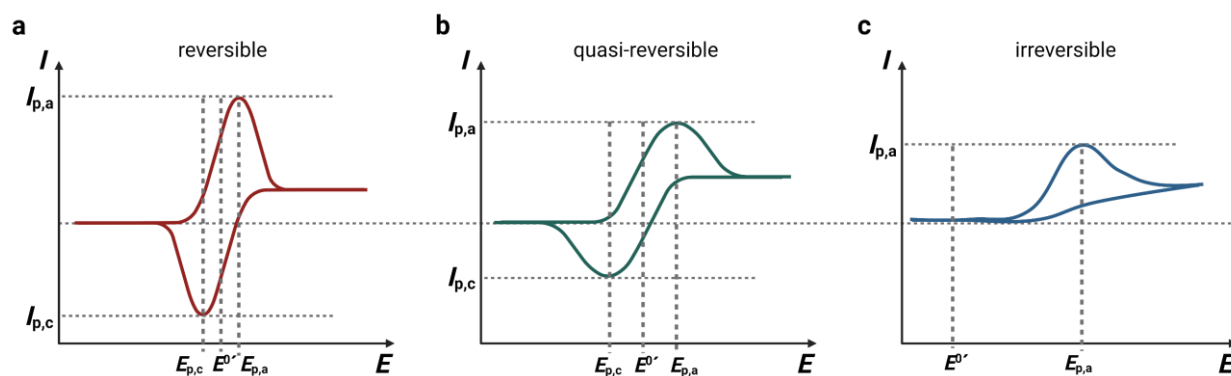
Figure 3-9 Cyclic voltammogram shapes for: a) reversible, b) quasi-reversible and c) irreversible redox reaction.

Varying experimental scan rate (v) provides the crucial diagnostic tool to distinguish between these three processes. With different v, the mechanism of the electrode reaction is affected by changing the diffusion layer thickness. For a reversible and an irreversible electrode reaction, the link between the applied v and peak current I_p is given by the *Randles−Ševčík* equations:

$$\text{Reversible} \qquad I_p = \pm 0.446 nFAc \sqrt{\frac{nFvD}{RT}} \qquad \text{Eq. 3-25}$$

$$\text{Irreversible} \qquad I_p = \pm 0.496 nFAc \sqrt{\frac{\alpha nFvD}{RT}} \qquad \text{Eq. 3-26}$$

where the ± sign is used to indicate oxidation (+) or reduction (−), A (m^2) is the electrode area, D the diffusion coefficient (m^2/s) and v the scan rate (V/s). Parameters n, F, α, R, T and c have their usual meaning. According to the *Randles−Ševčík* equations the current is directly proportional to the concentration and to the square root of the applied scan rate.

Several criteria can be utilized to identify a reversible electrode reaction:

(i) For a fully reversible process, anodic and cathodic peak currents are equal in magnitude and their ratio $I_{p,a}/I_{p,c}$ equals 1.

(ii) The formal reduction potential ($E^{\theta\prime}$) for a reversible redox couple is centred between $E_{p,a}$ and $E_{p,c}$ and can be calculated for the midpoint (half-wave) potential $E_{p,mid}$:

$$E_{p,mid} = \frac{E_{p,a} + E_{p,c}}{2}$$

Eq. 3-27

(iii) Another parameter as a criterion for reversibility is the peak separation between the peak potentials of the anodic and cathodic scan:

$$\Delta E_p = E_{p,a} - E_{p,c} = \frac{0.059}{n}$$

Eq. 3-28

For a reversible one-electron transfer reaction, ΔE_p is 0.059 V and independent of the applied v, i.e., the positions of both, anodic and cathodic peak potentials are not shifted for different scan rates. For a quasi-reversible reaction, the peak-to-peak separation increases with increasing v. Quasi-reversible processes appear reversible at slow v and shift to irreversible behaviour with increasing v. For irreversible processes the individual peaks are widely separated and reduced in size. The peak current, defined in Eq. 3-26, is still proportional to the concentration of the species, but is characterized by a lower height, depending on the value of electron transfer coefficient α. The peak current for an irreversible reaction is about 80% of the peak current for reversible process[183,184].

Square-Wave Voltammetry

Square-wave voltammetry (SWV) belongs to the group of pulse voltammetric techniques and is one of the most advanced methods[183,184,188]. It is characterized by high sensitivity because it is able to diminish the contribution of the charging current. As discussed previously, this current is a result of discharging the electrical double layer and is measured simultaneously with the faradaic current and may easily mask the faradaic values. The ability to discriminate between these two currents is achieved by replacing the continuous potential ramp (Figure 3-8 a) in CV with a staircase potential function combined with small potential pulses (Figure 3-10 a). By sampling the current at the end of each pulse, the contribution of charging current is significantly omitted, so that the resulting current is mainly faradaic[184,188]. Consequently, the sensitivity and quality of the voltammetric data are greatly improved.
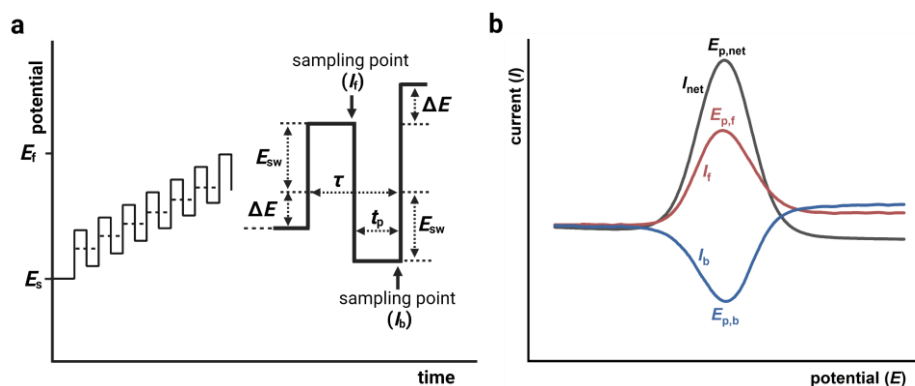
Figure 3-10 Waveform and response in square-wave voltammetry. a) Potential modulation and single potential cycle in square-wave voltammetry. E_{sw} is the square-wave amplitude; ΔE the scan increment; τ duration of one potential step; I_f and I_b, sampling points where the current is measured. b) Typical square-wave voltammogram for a reversible electrode reaction. I_{net}, net peak current; $E_{p,net}$, net peak potential; I_f and $E_{p,f}$ forward peak current and peak potential, respectively; I_b and $E_{p,b}$, backward peak current and peak potential, respectively. Figure adapted from [184].

The SWV waveform is a square wave which is placed over a potential staircase as presented in (Figure 3-10 a). During a single potential step, two brief and oppositely oriented potential pulses are applied. These two pulses share the same duration which is defined as $t_\mathrm{p} = \tau/2$, where τ represents the duration of a single potential step. The key parameters of the SW potential modulation include the scan increment (ΔE) of the staircase ramp, the height of a single pulse known as square-wave amplitude (E_sw) and the duration of the potential pulse (t_p) (Figure 3-10 a). From t_p the SW frequency (f) is defined as:

$$f = \frac{1}{2t_p}$$

<div align="right">Eq. 3-29</div>

A potential cycle consists of two contiguous and oppositely oriented potential pulses termed as forward and backward pulse which drive the electrode reaction to both, anodic (oxidation) and cathodic (reduction) directions. This procedure is repeated at each potential step starting from certain potential E_s to end potential E_f resulting in potential modulation given in Figure 3-10 a, and thus avoiding the necessity to reverse the overall potential scanning as in CV. The current is measured twice during each potential cycle, once at the end of the forward pulse and once at the end of the backward pulse. Current measured during the forward pulse is termed forward current (I_f), whereas the one measured during the opposing pulse is the backward current (I_b)[184,188].

A typical SW voltammogram encompasses three current (I) vs. potential (E) curves (Figure 3-10 b), two experimentally measured currents I_f (red curve) and I_b (blue curve), and a third net current I_net (black curve) which is calculated by subtracting the I_b from the I_f:

$$I_{net} = I_f - I_b$$

<div align="right">Eq. 3-30</div>

Since I_net is calculated as the difference between I_f and I_b, it is larger than either the forward or backward current.

In general, net SW voltammogram (I_net vs. E curve) is a well-defined peak (black curve, Figure 3-10 b) enabling precise determination of the position, i.e., the net peak potential (E_p) and the net peak current ($I_\mathrm{p,net}$). The overall shape of the forward and backward components in SWV (Figure 3-10 b) is similar to the shape of CV (Figure 3-8 b) offering comparable insights into the electrode reaction. All three components of the SW voltammogram are important in an analytical context as they provide measurable parameters like peak heights and peak positions.

The net peak current, $I_\mathrm{p,net}$ has a linear dependence on the square root of the frequency (f):

$$I_{p,net} = nFAc\Psi_{(\varphi)}\sqrt{Df}$$

<div align="right">Eq. 3-31</div>

where $\Psi(\varphi)$ is the dimensionless net response which can be revealed only through mathematical modelling and simulations[188]. It depends on the amplitude E_sw and scan increment ΔE. The symbols n, F, A, c, f and D represent the same parameters as defined previously in the text[183,184,188].

Experiment. Cyclic and square-wave voltammetric measurements were performed using a potentiostat/galvanostat (Table 2-8) controlled by GPES software.

All experiments were conducted with a three-electrode set-up (working, reference and counter electrode) in a one compartment electrochemical cell (5 mL) placed in a *Faraday* cage to minimize any external interference. A platinum wire was applied as a counter electrode. As a working electrode a glassy carbon electrode (GCE) with 2 mm diameter was used. Once activated, the surface of the GCE is very reactive and often is contaminated during use with products of the electrode reactions or any impurities present in the solvent. Hence, the GCE was polished prior to each measurement by using an aluminium oxide powder (grain size 0.3 µM). Polishing cloth was fixed on a flat surface, i.e., the bottom of 35 mm *Petri* dish and a small amount of aluminium oxide powder and distilled water were mixed to form a thick pulp. The electrode tip was polished by hand with figure-eight motions for approximately 10 s, rinsed thoroughly with distilled water and sonicated in an ultrasonic bath for 5 s to remove any leftovers of the powder. Afterwards it was rinsed again with distilled water and used for the next experiment.

Two different reference electrodes were used depending on the solvent in the cell to avoid/reduce formation of junction potential. The experiments in aqueous media were performed with Ag/AgCl (3M KCl) reference electrode, while the measurements in organic solvents with a non-aqueous Ag/Ag$^+$ reference electrode. The latter consists of a silver wire immersed in acetonitrile (ACN) containing 0.01 M AgNO$_3$ and 0.1 M tetrabutylammonium perchlorate (internal solution). The non-aqueous reference electrode was assembled on the day of the experiments following the manufacturer's recommendations. This included immersing the sample holder in ACN for at least one hour, rinsing of the Ag wire with acetone, carefully filling the sample holder with internal solution (without forming air bubbles), immersing the Ag wire in the solution inside the holder and sealing the Teflon cap with parafilm to avoid evaporation of the inner solution. When not used the electrode was kept in ACN containing only 0.1 M tetrabutylammonium perchlorate. The potential of the Ag/Ag$^+$ reference electrode can fluctuate between experiments due to variations in concentration of silver ions, electrolyte or solvent used. To circumvent this, all non-aqueous measurements were performed with ferrocene as internal standard. Ferrocene was added to the measuring solution at the end of each experiment.

Compositions of the supporting electrolyte solutions used in the present study:

- 0.1 M solution of KCl in *Millipore* water was used for the measurements in unbuffered aqueous media.
- Buffers used for the studies in buffered aqueous environment are listed in Table 2-4.
- 0.1 M solution of LiClO$_4$ in methanol, ethanol and 2-propanol was applied for measurements in organic protic solvents.
- 0.1 M solution of tetrabutylammonium perchlorate (TBAP) in ACN was utilized for experiments in organic aprotic solvents.

Stock solutions of Q$_1$, HO-Q$_1$, dUQ and HO-dUQ were prepared freshly by dissolving them in corresponding solvents (water, alcohol, or acetonitrile) to yield a concentration of 10 mM each. Stock solutions were kept in a glass autosampler vials closed with a silicon-sealed screw cap, protected from light at room temperature. For individual voltammetric experiment samples were diluted to 0.5 mM in the corresponding electrolyte solution.

Measurements were carried out in de-aerated solutions (N_2 atmosphere) at room temperature under quiescent conditions.

Cyclic voltammetry parameters were as follows: scan rate v = 10 mV/s; ΔE = 1 mV; start, first vertex and second vertex potential are given in the table below:

media	Qs			HO-Qs		
	Start E (V)	1st vertex E (V)	2nd vertex E (V)	Start E (V)	1st vertex E (V)	2nd vertex E (V)
Buffered	0.4	0.4	−0.6	0.25	0.25	−0.75
Unbuffered	0.2	0.2	−0.75	0.2	0.2	−1.0
ACN	−0.25	−0.25	−2.0	−0.25	−0.25	−2.0

Square-wave voltammetry parameters: frequency, f = 8 Hz; square-wave amplitude, E_{sw} = 25 mV; ΔE = 1 mV; initial and end potentials were chosen depending on the used solvent and are listed in the table below:

media	Qs		HO-Qs	
	Initial E (V)	End E (V)	Initial E (V)	End E (V)
Buffered	0.4	−0.75	0.2	−1.0
Unbuffered	0.2	−0.8	0.1	−1.0
Alcohols	−0.2	−1.2	−0.1	−1.50
ACN	−0.6	−2.0	0.0	−2.0

Analysis. The key parameters from cyclic and square-wave voltammograms were extracted with *GPES* software and analysed in *OriginPro*. The establishment of a correct baseline is essential for the accurate measurement of peak currents and peak potentials. The peak current was measured vertically from the peak down to the extrapolated baseline current as shown in the Figure 3-8 b.

3.5 Preparation of water-soluble formulations of quinone derivatives

Principle. Since Q_{10} application to living cells is challenging and greatly limited by its lack of solubility in aqueous media, finding a reliable dissolution method was essential step for biological experiments. To enhance the solubility and bioavailability of poorly water-soluble Q_{10}, water-soluble (WS) formulations have been prepared by solubilization of Q_{10} with the carrier conjugate Cholesterol-PEG 600 (PCS)[*] following the Borowy-Borowski[189] method[†]. It works by transforming cholesterol to an amphiphilic self-emulsifying molecule of PCS (polyoxyethanyl-cholesteryl sebacate). PCS has been synthesized by conjugation of polyethylene glycol-600 (hydrophilic part) to cholesterol (hydrophobic part) via the aliphatic linker sebacic acid (Figure 3-11 a)[189,190]. To achieve a water-dispersion Q_{10} is subjected to the micellization procedure creating stable non-covalent complexes (nanomicelles) that contain the two components Q_{10} and PCS combined at a molar ratio of 1:2. WS formulations can be prepared via the direct melt method and the auxiliary solvent method. Preparation by the direct melt method involves direct mixing of Q_{10} and PCS in

---

[*] Polyoxyethanyl-cholesteryl sebacate (PCS); CAS number 69068-97-9.
[†] US patents: 6,045,826; 6,191,172 B1 and 6,632,443.

a 1:3 (wt/wt) and subsequent heating above their melting points to form a clear melt. The melted mixture can then be diluted with aqueous solution (water, saline, PBS, etc.) to a desired concentration of an active ingredient. In the case of the auxiliary solvent method solubilization is achieved by dissolving Q_{10} and PCS in a water miscible organic solvent (e.g., THF) and then diluting the resulting solution with water. The organic solvent is then removed and the volume can be adjusted to achieve the required concentration.

For the present studies, WS formulations of Q_{10} have been prepared via the direct melt method (Figure 3-11 c). This method is simpler and avoids the use of organic solvents. The use of organic solvents can be disadvantageous since complete removal of the solvent may not always be possible.
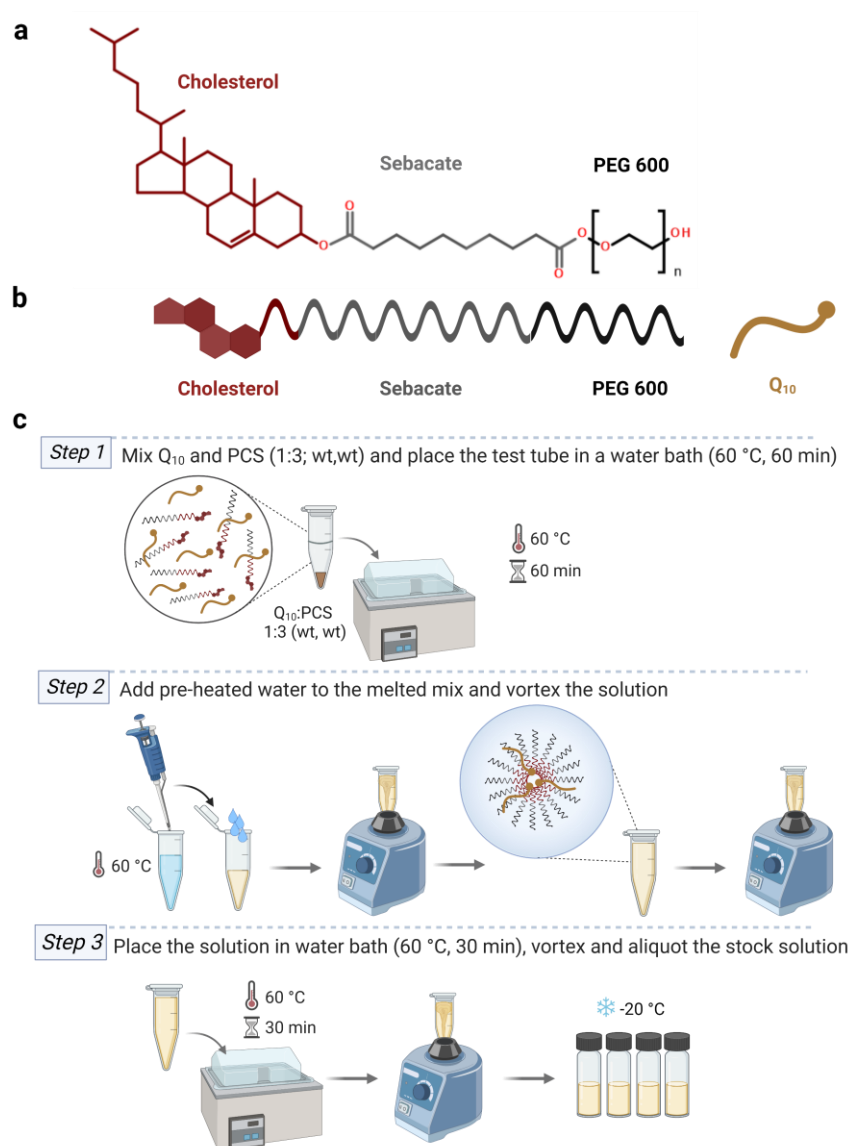
Figure 3-11 Preparation of an aqueous solution of Q_{10} using Cholesterol-PEG 600. a) Chemical composition of Cholesterol-PEG 600 (PCS): cholesterol, sebacate as a linker and PEG 600 (polyethylene glycol with an average molecular weight of 600 u, *n* around 13 units); b) Schematic representation of PCS and Q_{10} molecules; c) Schematic illustration of the procedure for preparing water-soluble formulations of Q_{10} by the direct melt method.

Experiment. *Sample preparation*: 12.95 mg Q_{10} and 38.85 mg PCS (1:3, wt/wt) were placed in a test tube and melted at 60 °C using a water bath for 1 hour (Step 1, Figure 3-11 c). 3 mL water, pre-heated at 60 °C, was added to the test tube with melted mixture of Q_{10} and PCS and mixed thoroughly until complete dissolution (Step 2, Figure 3-11 c). To assure total solubilization, the

prepared solution was reheated to 60 °C in a water bath and mixed by ultrasonication for additional 30 minutes (Step 3, Figure 3-11 c). The procedure from Borowy-Borowski[189] to enclose Q_{10} in nanomicelles formed with PCS was adapted for preparation of WS formulations of HO-Q_{10}, Q_1, HO-Q_1, dUQ, HO-dUQ, mQ and HO-mQ. Quinones and PCS were used in a weight ratio of 1:3 and merged by the direct melt method. Aliquots of the respective stock solution were stored in vials with silicon-sealed lids at −20 °C. Before use solutions were thawed at RT, mixed and reheated to ensure solubilization. During the experiments the samples were incubated at 37 °C.

Determination of the quinone concentration in WS formulations by UV-Vis spectroscopy

Dilution series (5-100 µM) of Qs-PCS were prepared in three different solvents: water, ethanol, and 2-propanol. The final volume was 0.5 mL. Absorbance of the dilutions was measured in closed quartz cuvettes with optical path of 1 cm at 275 nm wavelength where Qs display highest absorbance. Concentrations of the Qs in the WS formulations were calculated using the *Lambert-Beer* equation (Eq. 3-3). The literature values of the molar extinction coefficients (ε) for the Qs used in this research are given in Table 3-3.

Table 3-3 Molar absorption coefficient (ε) of used quinones at λ = 275 nm in ethanol.

compound	Molar absorption coefficient (ε) $dm^3/mol \cdot cm$
Q_{10}	14 200[191]
Q_1	13 700[192]
dUQ	14 000[192]
mQ	10 400[150]
Q_9	14 700[191]

3.6 Treatment of HEK-293 cells with quinone derivatives

Adherent HEK-293 cells were cultivated in 75 cm^2 flasks (T75) in Minimum Essential Media (MEM) with 10% Fetal Calf Serum (FCS) and 0.1% Penicillin/Streptomycin (P/S) under standard culture conditions (37 ºC, 5% CO_2). The cells were passaged twice a week with growth patterns of 1:4 and 1:3. For this purpose, the old medium was removed, the cells were rinsed with DPBS and detached from the bottom of the flask by adding 1 mL trypsin-EDTA (0.05%). After 1 minute incubation with trypsin, 5 mL of complete MEM (Table 2-5) were added to the cells to block the action of trypsin. Cells were spun down at 300*g* for 5 minutes. The supernatant was discarded, and the pellet was re-suspended in fresh complete MEM. The cells were counted with a *Z-Serie Coulter Counter* and seeded onto a new flask or *Petri* dish.

3.6.1 Control of cellular uptake of the applied quinones

3.6.1.1 *Exogenous supplementation of HEK-293 cells with water-soluble formulations of Q_{10} and HO-Q_{10}*

HEK-293 cells were grown to approximately 75% confluency in T75 flasks as described above. Prior to the treatment with the quinones (Qs and HO-Qs), cells were rinsed with DPBS and fresh complete MEM was added. Stock solutions of the quinones were preincubated at 37 ºC for 30 minutes to ensure dissolution. Water-soluble formulations of the quinones (Q-PCS/HO-Qs-PCS)

or the solubilizing agent PCS (control) were added directly to the flasks with cells to final concentrations of 20 µM. Treated cells were incubated for 30 minutes at 37 ºC in 5% CO_2 (step 1, Figure 3-12).
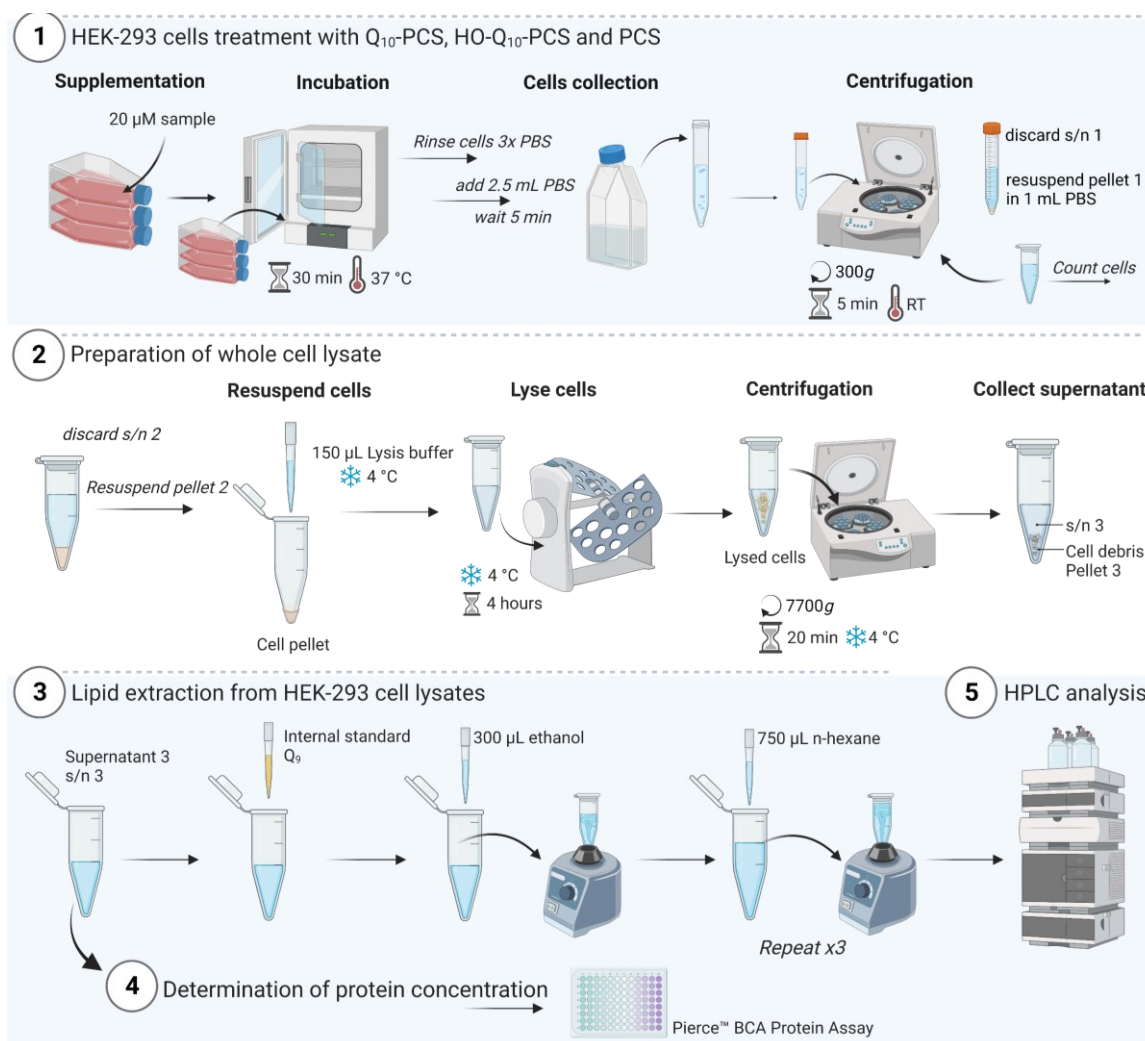
Figure 3-12 Detailed schematic illustration of the experimental workflow for monitoring the cellular uptake of the applied quinones including 1) cell treatment, 2) cell lysis, 3) lipid extraction, 4) determination of protein concentration and 5) chromatographic separation.

3.6.1.2 Preparation of whole HEK-293 cell lysates

After the incubation of the cells with the samples, the following protocol was used to prepare whole cell lysates (follow the steps in Figure 3-12):

- Cells were carefully washed with DPBS three times to assure total removal of the samples present in the media. DPBS was placed on the side wall of the flask, then the flask was rolled two times followed by removal of the buffer (step 1, Figure 3-12).

- Next, 2.5 mL of DPBS were added to the flask for 5 minutes to ensure that all cells have dissociated from the flask bottom (step 1, Figure 3-12).

- The respective cell suspensions were transferred to centrifuge tubes; additional DPBS was used to harvest all cells from the flask (step 1, Figure 3-12).

- Cell suspensions were centrifuged for 5 min at 300*g*, RT. The *supernatant 1* of all suspensions was discarded and the respective pellet was resuspended in 1 mL DPBS. 10 µL of this cell suspension was added to 10 mL *ISOTON II* diluent and cells were counted (step 1, Figure 3-12).

- The rest of the cell suspension was centrifuged for 5 minutes at 300*g*. The *supernatant 2* was tossed and the pellet was resuspended in 150 µL ice-cold lysis buffer (Table 2-5). Next steps

were done at 4 ºC by keeping the samples on ice throughout the procedure (step 2, Figure 3-12).

- Cells were lysed by agitation at 4 ºC on a tube roller for 4 hours (step 2, Figure 3-12).

- Lysates were centrifuged at 7700*g*, 4 ºC for 20 minutes. The resulting pellets contained the nuclei and were discarded (step 2, Figure 3-12). *Supernatant 3* (plasma membrane, cytoplasm and mitochondria) was used in the next steps for protein concentration determination and extraction of the quinones.

3.6.1.3   Determination of protein concentration

Protein concentration of the lysate sample (*Supernatant 3*) was determined using *Pierce™ BCA Protein Assay* with the microplate procedure as described by the manufacturer guideline[193]. Standard bovine serum albumin (BSA) solutions of a defined concentrations were loaded as duplicates and the sample (lysates) solutions were loaded as triplicates in a 96-well plate (step 4, Figure 3-12).

The standard curve was generated by plotting the absorbance versus known concentrations (0, 0.01, 0.02, 0.04, 0.06, 0.08 and 0.1 mg/mL) of BSA. Three different dilutions of the lysates and lysis buffer were prepared in the range of the standard curve. 25 µL of BSA standards, lysate solutions and lysis buffer solutions were pipetted into a 96-well plate followed by addition of 200 µL from BCA reagent. BCA reagent was prepared by mixing reagent A and reagent B from the kit in a 1:50 (v/v) ratio.

The plate was incubated for 45 minutes at 60 °C with shaking on a plate shaker. Thereafter, the plate was cooled down to RT before measuring the absorbance. The absorbance was measured at 562 nm using plate reader. The absorbance values of the pure lysis buffer solutions were subtracted from the absorbance values of the dilutions of the lysates (similarly diluted), followed by correction with the dilution factor. Protein concentration was calculated as an average of the triplicate measurements.

3.6.1.4   Lipid extraction of Q_{10} and HO-Q_{10} from HEK-293 cell lysates

First, as an internal standard 1 µM Q_9 (in ethanol) was added to *supernatant 3*. Thereafter, extraction of Q_{10} and HO-Q_{10} from the lysates was performed as described by Takada *et al*.[194]. 150 µL of *supernatant 3* were mixed with 300 µL ethanol and after rapid shaking 750 µL of *n*-hexane were added and the samples were vigorously mixed. Lipids were recovered within the upper hexane phase and this extraction step was repeated twice (step 3, Figure 3-12). Hexane phases were pooled and the extracts were dried by evaporation of the solvent under a stream of nitrogen at room temperature. After evaporation extracts were dissolved in 100 µL of ethanol for HPLC analysis.

3.6.1.5   Measurement of extracted Q_{10} and HO-Q_{10} from HEK-293 cells by HPLC

Standard Curve. The individual stock solutions were prepared by dissolving pure Q_9, Q_{10} and HO-Q_{10} in ethanol. The concentration of the stock solutions was then checked and calculated (Eq. 3-3) by reading the absorbance on a UV-Vis spectrophotometer (at 275 nm; quartz cuvette 1 cm), using a molar absorptivity (ε) for Q_{10}, HO-Q_{10}, and Q_9 given in Table 3-3. The individual stock solutions were combined to prepare the working standard for the calibration curve. The final

concentrations of the quinones in the working standard were 1 µM. A sequence of 15 different dilutions of the working standard (ranging from 10 to 1000 nM) was used to establish the standard curve. Since each quinone is present in the working standard, three calibration curves result from the injections, one curve for each component. The calibration curve was created by plotting the integrated peak area against known concentrations of the quinones.

HPLC analysis. HPLC analysis (step 5, Figure 3-12) was carried out with a HPLC System connected to an UV detector (Table 2-8). The chromatographic separation was performed with an *InfinityLab Poroshell* 120 EC-C18 column with dimensions: 4.6 x 100 mm, 2.7 µm. The mobile phase was composed of ethanol and water 91:9 (v/v) containing 0.1% HCOOH. The program was run with the following parameters: injection volume of 100 µL, a flow rate of 0.5 mL/min, isocratic elution at 37 ºC and detection at 275 nm.

Analysis. The analysis of the chromatograms was performed by integration of the peak area, normalized with the correspondent standard curve and internal standard, by referring to the amount of protein of each sample calculated previously with a *Pierce™ BCA Protein Assay*.

3.6.2 Determination of cell viability in quinone-treated HEK-293 cells

Principle. The here used *CellTiter-Blue™ Cell Viability Assay* is a fluorometric method for monitoring viability and metabolic activity of cells[195,196]. The *CellTiter-Blue™* reagent is a buffered solution containing highly purified resazurin (7-hydroxy-10-oxidophenoxazin-10-ium-3-one) which can easily penetrate cells. The assay is based on the ability of living cells to convert the redox dye resazurin (non-fluorescent dye, blue) into the end product resorufin (fluorescent dye, pink) that is released from cells into the surrounding medium. The reduction of resazurin to resorufin inside living cells[196] is mediated by intracellular diaphorase enzymes (like NAD(P)H dehydrogenase) which transfer an electron to resazurin generating resorufin[197]. Viable cells have an active metabolism and thus the ability to irreversibly reduce resazurin into fluorescent resorufin (Figure 3-13 a). In contrast, non-viable cells experience a rapid loss of their metabolic activity, consequently failing to reduce resazurin and to produce a fluorescent signal. Accordingly, the fluorescence output is directly correlated to the number of viable cells. The level of reduction can be quantified by measuring fluorescence at λ_{ex} = 560 nm and λ_{em} = 590 nm. Fluorescence excitation and emission spectra for resorufin are shown in Figure 3-13 b.
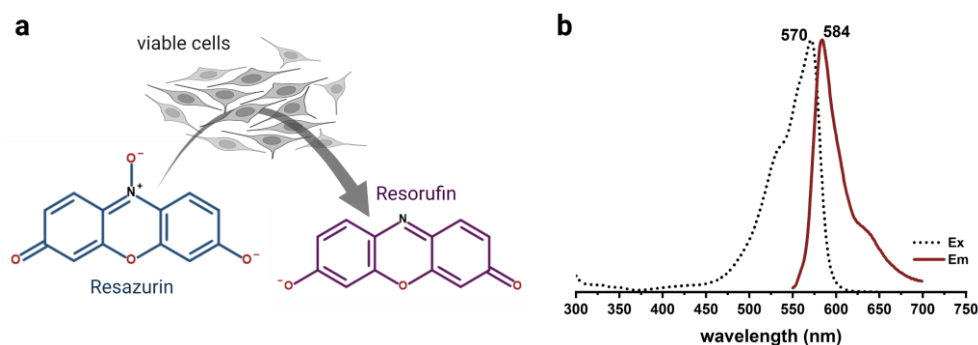
Figure 3-13 Principle of the *CellTiter-Blue™ Cell Viability assay.* a) Representative scheme of the conversion of resazurin to resorufin by metabolically active (viable) cells. Resazurin, a non-fluorescent dye with blue colour is reduced to resorufin, a pink fluorescent product. The fluorescence (resorufin) produced is proportional to the number of viable cells. b) Fluorescence excitation and emission spectra for resorufin obtained from *https://www.fpbase.org/,* accessed November 2022.

The *CellTiter-Blue™* reagent is designed for use as an endpoint assay rather than as a kinetic approach for tracking cell growth over time. This method does not directly assess cell proliferation. For example, increase in the fluorescence signal may suggest that the cell number has increased due to cell proliferation. Alternatively, another reason may be a decline in cell mortality. Furthermore, a higher signal because of increased enzymatic activity (high rate of reduction of resazurin) within a group of cells may suggest either increased proliferation or it could indicate improved metabolic activity of non-proliferating cells[195–197].

Experiment. HEK-293 cells were plated in 96-well black, clear flat-bottom with lid microplates, at a density of 5000 cells per well in 100 μL complete MEM and cultured for 24 hours (37 ºC, 5% CO_2). Thereafter, old medium was exchanged with fresh complete MEM and cells were treated with the water-soluble formulations of the quinones (Qs-PCS/HO-Qs-PCS, final concentration 20 μM). The stock solutions of Qs-PCS and HO-Qs were preincubated at 37 °C. Wells containing only complete MEM were prepared as a negative control to determine background fluorescence that may be present. Additionally, two controls for untreated cells were included: (i) only HEK-293 cells in complete MEM and (ii) HEK-293 cells in complete MEM with addition of water as the solvent control. The sample distribution for a 96-well plate is given in Figure 3-14.
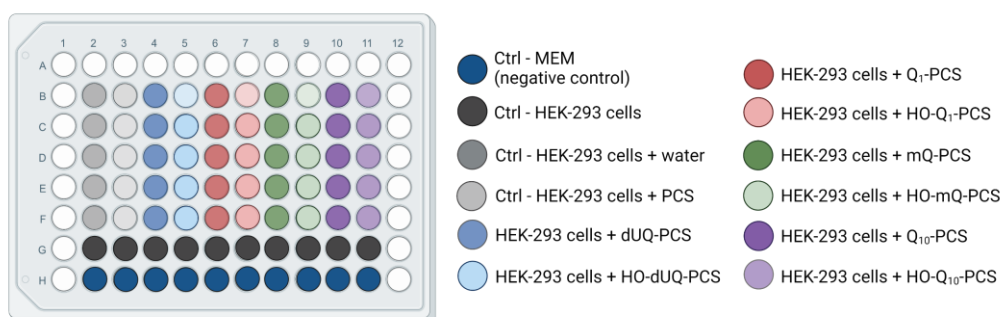
Figure 3-14 96-well plate scheme used for the *CellTiter-Blue™ Cell Viability Assay*. White wells represent culture medium alone; dark blue wells (10 replicates) symbolize the negative control containing culture medium with *CellTiter-Blue™* reagent (no-cell control); black wells (10 replicates) represent only HEK-293 cells in culture medium (untreated cells). Tested quinones were studied in 5 replicates.

The cells were incubated under standard cell culture conditions and the cell viability was assessed after 2, 24 and 48 hours following manufacturer's instructions[198]. The *CellTiter-Blue™* reagent was thawed at room temperature and kept in a water bath at 37 °C, protected from light at all times, before being added to the cells in each well. At the desired time point (2, 24 and 48 hours) medium was removed and cells were washed two times with DPBS++ to assure total removal of the test compounds and to avoid interference with the fluorescence of the *CellTiter-Blue™* reagent. 100 μL fresh complete MEM and 20 μL *CellTiter-Blue™* reagent were added to each well. The plate was mixed for 10 seconds on a plate shaker and incubated for 4 hours under standard cell culture conditions. The fluorescence was measured with a 545±20 nm excitation filter, 600±40 nm emission filter and 567.5 nm dichroic filter in a temperature-controlled (37 °C) *CLARIOstar®* microplate reader. Before the measurement, the plate was shaken for 10 s followed by resting time of 60 s to settle down the cells. The fluorescence was detected using bottom reading, 50 flashes per well, and the values were obtained from spiral averaging in a diameter of 4 mm per well.

Analysis. The average of the relative fluorescence units (RFU) values of the no-cell control was subtracted from all RFU values of the other wells. The average of RFU values (10 replicates) of the untreated cells control (only HEK-293 cells in complete MEM) was taken as 100% viability and the difference (%) between treated and untreated cells, based on RFU values was calculated using the formula below:

$$ \% = \frac{RFU_{treated}}{RFU_{untreated}} \times 100 $$

<div align="right">Eq. 3-32</div>

where $RFU_{treated}$ are fluorescence values of the cells treated with the different Qs-PCS/HO-Qs-PCS, $RFU_{untreated}$ are fluorescence values of the untreated cells (HEK-293 cells in complete MEM). RFU values were calculated as an average of 10 replicates for the negative control and untreated cell control and average of 5 replicates for the treated cells with different Q-PCS/HO-Qs-PCS. The results are the means of three independent experiments using HEK-293 cells with passage numbers: 18, 25 and 34.

3.6.3 Calcium measurements in quinone-treated HEK-293 cells

Principle. There are various approaches for investigating Ca^{2+} metabolism in living cells. In addition to the electrophysiological patch clamp technique in which the currents flowing through ion channels are directly measured, another convenient method is fluorescent dye based Ca^{2+} imaging. For those methods several dyes are available which provide information for the global cytosolic or compartment specific Ca^{2+} concentrations ($[Ca^{2+}]$). By using the dye fura-2 in the present studies mainly cytosolic $[Ca^{2+}]$ could be monitored directly in the cells. However, conclusions on compartment residing Ca^{2+} as well as Ca^{2+} channels and pumps activities could be drawn indirectly.

There are two forms of the fura-2 dye available designed specifically for either extracellular or intracellular measurements[199]. Fura-2 free acid is a charged molecule with carboxylic acid groups chelating Ca^{2+}. This form is membrane impermeant because the negatively charged carboxyl groups prevent the passage of the dye through biological membranes. The cell-permeant version, fura-2 pentaacetoxymethyl ester (fura-2 AM), is created by masking the carboxyl groups with acetoxymethyl (AM) ester which reduces hydrophilicity of the molecule and allows it to traverse the plasma membrane by passive diffusion. Once inside the cell, the AM groups are cleaved by cellular esterase enzymes liberating the carboxylic groups and leaving fura-2 free acid trapped inside the cell where it binds Ca^{2+}. Fura-2 is a ratiometric dual-excitation Ca^{2+} indicator[200]. In the absence of Ca^{2+} or at very low $[Ca^{2+}]$ fura-2 shows an excitation spectrum between 300 and 400 nm with a maximum at approximately 380 nm (black dashed line, Figure 3-15). In the presence of high $[Ca^{2+}]$ the excitation peak of fura-2 increases in intensity and shifts further into the UV region of the spectrum with a maximum at 340 (red dashed line, Figure 3-15). In each case the emission occurs at 510 nm (Figure 3-15). By exciting the dye sequentially at 340 and 380 nm, the ratio of the respective emission signals is employed for monitoring the $[Ca^{2+}]$[201]. Ratiometric measurements offer multiple advantages as the ratio remains unaffected by factors such as dye concentration, illumination intensity or the length of the optical path. Such factors are particularly

important in imaging of cytosolic [Ca^{2+}] where the illumination intensity and the optical path vary across the field of view or loss of the dye during experiments could happen due to photobleaching or extrusion by the cell.
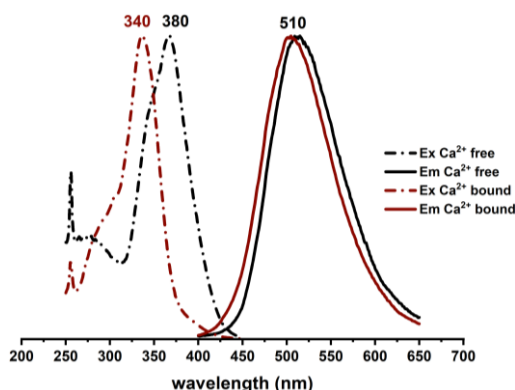
Figure 3-15 Ca^{2+} free and Ca^{2+} bound excitation and emission spectra of fura-2. In the absence of Ca^{2+} fura-2 excitation spectrum is obtained at 380 nm (black dashed line). The excitation spectrum is shifted to the left (340 nm) by an increase in Ca^{2+} concentration (red dashed line). In both cases emission occurs at approximately 510 nm. Spectra obtained from *https://www.fpbase.org/*, accessed May 2023.

The fluorescence ratio of fura-2 at 340/380 is proportional to the intracellular [Ca^{2+}] ([Ca^{2+}]$_i$). Therefore, by following the 340/380 ratio, the change in the [Ca^{2+}]$_i$ can be tracked over time. As described by Grynkiewicz *et al.*[201] the conversion of the ratios into [Ca^{2+}]$_i$ could be performed if the minimal and maximal [Ca^{2+}]$_i$ values using the cell type under study are determined by *in vitro* calibration using the following equation:

$$\left[Ca^{2+}\right]_i (nM) = K_d \times \left(\frac{R - R_{min}}{R_{max} - R}\right) \times \frac{S_f}{S_b}$$

Eq. 3-33

where K_d is a Ca^{2+} dissociation constant for fura-2; R stands for 340/380 ratio value, background corrected and measured from cells during the experiment; R_{min} and R_{max} are determined with *in vitro* calibration. R_{min} is 340/380 ratio in the absence of extracellular Ca^{2+} and under conditions where all intracellular Ca^{2+} stores are depleted by thapsigargin and ionomycin, whereas R_{max} is 340/380 ratio at 20 mM extracellular [Ca^{2+}]. S_f and S_b are baseline fluorescence at 380 nm under Ca^{2+} free (S_f) and Ca^{2+} bound (S_b) conditions.

Experiment. HEK-293 cells used for Ca^{2+} imaging with fura-2 AM were prepared 24 hours before the measurements. 1 mg/mL stock solution of fura-2 AM was prepared by dissolving 50 µg fura-2 AM in 50 µL DMSO (stored at −20 °C and protected from light). Adherent HEK-293 cells cultured in complete MEM in T75 flasks were trypsinated, washed, quantified, and plated on Ø25 mm cover slips placed in Ø35 mm *Petri* dishes supplemented with 2 mL complete MEM. The volume from the cell suspension was calculated such that the cell density reaches approximately 100 000 cells per dish within 24 hours. Prepared *Petri* dishes with cells were incubated under standard cell culture conditions for 24 hours to assure cell adherence on the cover slips.

To prepare the cells for Ca^{2+} imaging, growth medium was removed and carefully replaced (by slowly pipetting on the walls of the *Petri* dish) with fresh 1 mL complete MEM containing 1 µg/mL fura-2 AM. Then the cells were incubated for 30 min at RT, protected from light. Thereafter, the cover slip was washed with 0.5 mM Ca^{2+} *Ringer* buffer and placed in an imaging chamber.

The chamber (Figure 3-16 a) consists of a nest (chamber holder) in which all parts fit in, perfusion chamber (with perfusion inlet port and suction port) and top ring. The Ø25 mm cover slip was placed on the bottom of the chamber holder and the edges were sealed with silicone paste on the side facing away from the cells. The top of the cover slip (side with adherent cells) was covered with the perfusion chamber and carefully sealed with silicon. A second cover slip (Ø12 mm) was used to close the perfusion chamber, sealed with silicone and held down by a top ring fixed with two screws. The chamber was placed in the prewarmed (37 °C) microscope stage. Henceforward, an appropriate area of the specimen was determined: the cells were marked as regions of interest (ROIs) and a background ROI was defined, necessary for the automatic background correction included in the microscope's software. Furthermore, the excitation ratio of the Ca^{2+}-free and Ca^{2+}-bound fura-2 (340/380 nm) was directly calculated by the *Zen Blue 2.6* software.
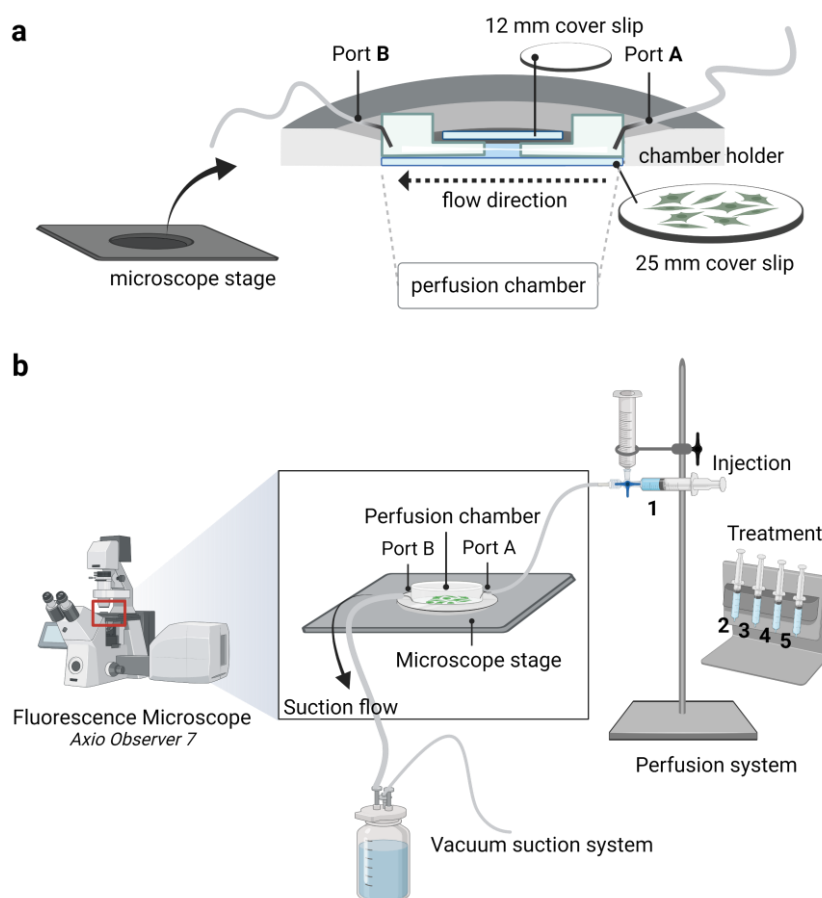
Figure 3-16 Diagram of the perfusion system for Ca^{2+} imaging experiments. a) Assembly of the perfusion chamber. A Ø12 mm and a Ø25 mm cover slip are mounted and sealed to the top and the bottom of the chamber by silicone paste. HEK-293 cells were grown attached on the chamber-facing side of the 25-mm cover slip. Solutions enter from port A and exit from port B. b) Solution from the syringe is directed to the perfusion chamber through the port A. Waste is removed from the chamber at port B by vacuum suction system. The perfusion chamber is placed in the preheated (37 °C) microscope stage and the 25-mm cover slip is positioned next to the lens of an inverted fluorescence microscope for image acquisition.

The cells were perfused by manual injection of the solutions (Figure 3-16 b). Thin-walled silicone tubes were used due to their flexibility and easiness to wash away any salt blockages. A vacuum suction system was used to remove perfused solutions. To facilitate sterilization of the perfusion system and to avoid building up of deposits, tubes were washed with 70% ethanol and ddH$_2$O before and after each measurement. Prior to the start of each experiment, tubes and solution

flow were checked to ensure absence of blockages or bubbles. A schematic overview of the perfusion system is shown on Figure 3-16 b. The solutions were held in 5 mL syringes. The perfusion setup enables exchange of the solutions surrounding the cells, and by using successive perfusion steps and/or specific solutions, 340/380 ratio could be monitored over time.

To measure store-operated Ca^{2+} entry (SOCE), the so-called "Ca^{2+} re-addition standard protocol"[202] was employed (Table 3-4, measurements at 37 °C). The measurements started with perfusion of the cells with 0.5 mM Ca^{2+} *Ringer* buffer to assure basal levels of $[Ca^{2+}]_i$. After 2 minutes, cells were perfused with 0.5 mM Ca^{2+} *Ringer* buffer containing the sample (Qs-PCS or HO-Qs-PCS) or control (PCS) and basal levels of $[Ca^{2+}]_i$ in presence of the sample/control were measured for 10 minutes. Starting from this time point, the tested Qs/HO-Qs were consistently added to the imaging buffers throughout the subsequent steps. The external solution was then replaced with a nominally Ca^{2+}-free solution for 2 minutes. Next, Ca^{2+}-free solution containing 1µM thapsigargin (Tg) was perfused which causes a depletion of the ER Ca^{2+} stores by irreversibly inhibiting the SERCA pumps. Because of their blockage by Tg, the $[Ca^{2+}]_i$ first rises and thereafter declines due to extrusion of Ca^{2+} out of the cell by plasma membrane Ca^{2+} pumps. The ΔTg peak is obtained by subtracting the last value before Tg application from the maximum $[Ca^{2+}]_i$ value following Tg application. The ER store depletion step was followed by perfusion of the cells with 2 mM Ca^{2+} *Ringer* buffer. Under physiological conditions, this results in Ca^{2+} influx through SOCE into the cells. In this phase, the parameters Ca^{2+} influx rate (slope of increase), $ΔCa^{2+}$-peak (maximum value) and Ca^{2+}-plateau (mean value over several minutes) can be determined. The final perfusion step was performed with a Ca^{2+}-free solution to observe termination of the influx. The chemical compositions of the buffers used for Ca^{2+} imaging are listed in Table 2-6.

Table 3-4 "Calcium re-addition standard protocol" used to measure store-operated Ca^{2+} influx (SOCE). Upper row: perfusion steps; *Ringer* buffers (Table 2-6) containing different $[Ca^{2+}]$; Tg, thapsigargin (1 µM final concentration). S, sample (water-soluble formulations of the Qs and HO-Qs; 20 µM final concentration). Samples: PCS (control), Q_1-PCS, HO-Q_1-PCS, Q_{10}-PCS, HO-Q_{10}-PCS, dUQ-PCS, HO-dUQ-PCS, mQ-PCS and HO-mQ-PCS. Second row: 1-425, number of cycles, 1 cycle = 5 s.

0.5 mM Ca^{2+}	0.5 mM Ca^{2+}+S	0 mM Ca^{2+}+S	0 mM Ca^{2+}+ Tg+S	2 mM Ca^{2+}+S	0 mM Ca^{2+}+S
1-25	30-150	155-180	185-270	275-390	395-425
Basal $[Ca^{2+}]_i$ in resting cells.	$[Ca^{2+}]_i$ in cells supplemented with 20 µM Qs-PCS/HO-PCS.	Ca^{2+} is pumped out of the cells and chelated by EGTA contained in the buffer.	Tg irreversible inhibiths SERCA pumps, resulting in ER depletetion. Momentary increase in $[Ca^{2+}]_i$ is detected.	Ca^{2+} influx through SOCE.	Termination of Ca^{2+} influx.

Ca^{2+}-imaging measurements were performed using an inverted epifluorescence microscope *Axio Observer 7* (configuration described in Table 2-8) equipped with a 20x objective and Prime 95B sCMOS-Camera. The microscope was adjusted to the following settings: Zeiss 21 HE filters set was used for excitation channels with intensity between 43%-58% and exposure time of 25 ms. The binning was 1×1 and images were taken every 5 s. The measurements were recorded and analysed using the *Zeiss Zen Blue 2.6* software.

Analysis. Quantification of 340/380 nm signal ratio was performed using *IGOR Pro* software. For graphical representation data were exported and further analysed in *OriginPro.* Analysed parameters include the average basal Ca^{2+} signal, the maximum peak induced by Tg (ΔTg), the maximum (ΔPeak), the plateau (ΔPlateau) signals, and the influx rate after re-addition of 2 mM [Ca^{2+}]. To determine the Δ values, the minimal signal before the addition of Tg or 2 mM [Ca^{2+}] was subtracted from the Tg peak or Ca^{2+} peak/plateau, respectively. Per experiment, n = 30-50 cells from the same dish were measured and the results were averaged. Further, the averages of at least 8 independent experiments (N = 8-15) were averaged and data shown represents the average of averages. Data are presented as mean±SEM.

3.6.4 Determination of the mitochondrial membrane potential in quinone-treated cells

Principle. Mitochondrial membrane potential ($\Delta\Psi_m$) was determined using an assay with the fluorescent dye tetramethylrhodamine methyl ester (TMRM) and following the general procedures and recommendations given in Perry *et al.*[203]. Under basal physiological conditions in most cells, the plasma membrane potential ($\Delta\Psi_p$) ranges from -30 to -80 mV[204] against the extracellular space and mitochondrial membrane potential ($\Delta\Psi_m$) ranges from -120 to -160 mV[203] compared to the cytosol. Since these potentials are additive, mitochondria are between 150-260 mV more negative than the extracellular space, thus providing a strong driving force for accumulation of cations in the mitochondrial matrix (MM). TMRM (Figure 3-17 a) is a lipophilic fluorescent dye that accumulates within the MM in a $\Delta\Psi_m$-dependent manner. Due to the lipophilic solubility, TMRM can enter living cells passing through the plasma membrane and mitochondrial membranes. TMRM has a delocalized positive charge dispersed throughout its molecular structure which enables TMRM driven by the negative $\Delta\Psi_m$ to enter MM and accumulate there.

TMRM can be used in quenching or non-quenching mode[203,205]. In the quenching mode, relatively high concentration of TMRM (0.2$-$20 μM) are utilized, followed by accumulation of high amounts of the dye in the mitochondria. Consequently, aggregates are formed and the fluorescence signal of TMRM is quenched (auto-quenching). Under these conditions, a subsequent mitochondrial depolarization will lead to release of TMRM which will unquench the dye and increase the fluorescence signal. Contrarywise, mitochondrial hyperpolarization will trigger more dye to accumulate in mitochondria leading to further quenching of the dye and decrease in the signal[203]. In the non-quenching mode, a lower concentration of TMRM is used (0.5$-$100 nm), therefore dye aggregation and quenching in mitochondria do not occur. When using non-quenching mode, depolarized mitochondria accumulate a lower amount of TMRM and will exhibit lower

fluorescence, while hyperpolarized mitochondria will accumulate higher amounts of the dye, hence manifesting higher fluorescence. TMRM dye is maximally excited at 552 nm and exhibits emission maximum at 577 nm (Figure 3-17 b).
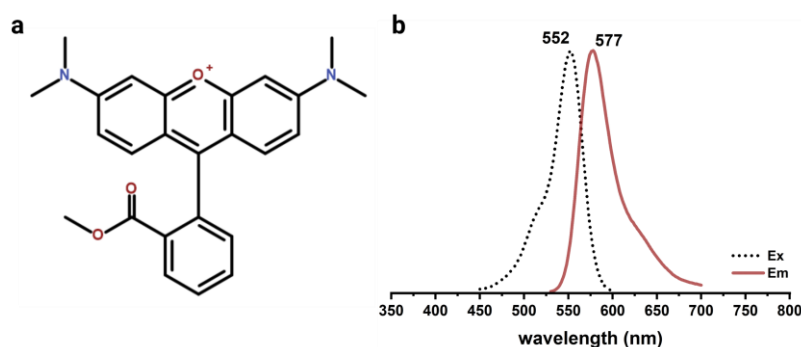
Figure 3-17 a) Chemical structure of TMRM; b) Fluorescence spectrum of TMRM.

TMRM is loaded into the cell over the plasma membrane and subsequently it is taken up by the mitochondria as the most negatively charged part of the cell. Therefore, changes in $\Delta\Psi_p$ could affect the TMRM fluorescence and thereby falsify the results. This is controlled by additional measurements with uncoupling agents such as carbonyl cyanide *m*-chlorophenyl hydrazone (CCCP) or carbonyl cyanide *p*-trifluoromethoxyphenyl-hydrazone (FCCP). CCCP and FCCP are ionophores that prevent mitochondrial ATP synthesis by transporting protons across the inner mitochondrial membrane (IMM) into the MM causing quick reduction of the electrochemical potential and thereby mitochondrial depolarization[206,207]. The difference of the fluorescence intensity of TMRM before and after applying the ionophore specifically corresponds to the $\Delta\Psi_m$.

Experiment. HEK-293 cells were plated at a density of 5000 cells/well in 96-well black, clear flat-bottom with lid microplates. After culturing overnight (24 hours) in complete MEM under standard culture conditions, the culture medium in each well was replaced with 1 mM Ca^{2+} *Ringer* buffer and 20 µM water-soluble formulations of the quinones (Q-PCS and HO-Qs-PCS). The stock solutions of Q-PCS and HO-Qs-PCS were preincubated at 37 °C. After incubation for 30 minutes under standard culture conditions with the test compounds, TMRM was added to each well to a final concentration of 150 nM. Following 15 minutes incubation with TMRM under standard cell culture conditions, the cells were washed three times with DPBS[++] to assure removal of the free TMRM dye and test compounds that may interfere with the analysis. After the last wash, 200 µL of 1 mM Ca^{2+} *Ringer* buffer were added to each well. Additionally, three sets of controls were run. Negative controls consisted of: (i) no-cell control for determination of background fluorescence and (ii) untreated cells (cells were not exposed to the test compounds). In parallel, positive controls with CCCP were run for each condition mentioned above. For this purpose, HEK-293 cells were treated with corresponding solvent control or test compound (water, PCS, Qs-PCS or HO-Qs-PCS) and incubated for 30 minutes under standard culture conditions. Afterwards, cells were exposed to 20 µM CCCP for 10 minutes incubated under standard cell culture conditions and subsequently incubated with 150 nM TMRM for 15 minutes under standard cell culture conditions. Cells were then washed three times with DPBS[++], supplemented with 200 µL 1 mM Ca^{2+} *Ringer* buffer and the fluorescence was measured. The sample distribution on a 96-well plate is given in Figure 3-18.
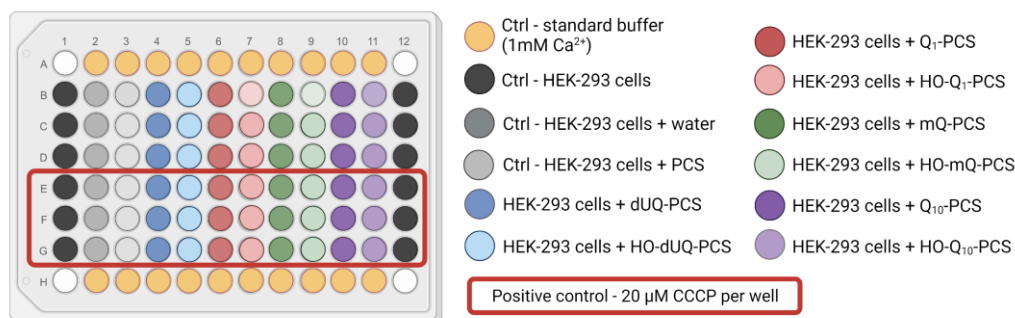
Figure 3-18 Working map of the 96-well plate for measuring mitochondrial membrane potential ($\Delta\Psi_m$) in HEK-293 cells using TMRM.

The fluorescence was measured in a temperature controlled (37 °C) *CLARIOstar®* microplate reader. Filters with an excitation wavelength of 535±20 nm and an emission wavelength of 585±30 nm were used to record the fluorescence. A 570 nm dichroic filter was applied to cut off any plate noise from the excitation signal. The fluorescence in each well was recorded using a bottom reading mode with 50 flashes per well.

Analysis. The average of the relative fluorescence units (RFU) values of the negative no-cell control was subtracted from all RFU values of the other wells. The percentage of the TMRM fluorescence signal, based on RFU values was calculated using the formula below:

$$(\%)TMRM_{fluorescence} = \frac{RFU_{treated}}{RFU_{untreated}} \times 100 \qquad \text{Eq. 3-34}$$

where $RFU_{treated}$ are fluorescence values of the cells treated with test compounds (water, PCS, Qs-PCS and HO-Qs-PCS) and $RFU_{untreated}$ are fluorescence values of the untreated cells. The results are the means of three independent experiments performed in triplicates using HEK-293 cells with passage numbers 16, 20 and 34. All data are expressed as mean±SEM.

3.7 Assessment of mitochondrial respiration in murine heart mitochondria

3.7.1 Isolation of murine heart mitochondria

Animal experiments were approved by the local animal ethics committee and conducted in compliance with guidelines from Society of Laboratory Animal Science (GV-SOLAS). Mitochondria isolation protocol was developed from previously published protocols by Wei *et al*.[208] and Nickel *et al*.[209] and it was standardized in our laboratory[16]. It was performed in collaboration with Prof. Dr. Leticia Prates-Roma (Center for Integrative Physiology and Molecular Medicine (CIPMM), Saarland University).

C57BL/6NCrl mice (20-30 weeks old) were euthanized by intraperitoneal injection of a xylazine/ketamine mixture (1:2, v/v; 0.01 mL per g bodyweight). Before starting the incision to expose the heart, the animal was wetted and cleaned with 70% ethanol. The heart was extracted by ventral incision along the median followed by cutting in cranial direction through the ribcage to expose the heart. The explanted heart was placed in a *Petri* dish with ice-cold DPBS (Figure 3 19, step 1). All subsequent steps were performed on ice. The chemical composition of the used solutions is given in Table 2-7.

1. *Harvesting of the mice heart tissue* (Figure 3-19*, step 1*):

Working solutions as well as the tissue grinder were kept ice-cold during the whole procedure.

- The beating heart was transferred in 5 mL DPBS in a Ø35 mm *Petri* dish on ice. The heart was pressed with tweezers to remove the blood. Connected lung tissue, vessels and residual blood were removed by opening both ventricles.

- Heart tissue was moved to a separate *Petri* dish with fresh DPBS (5 mL) and it was chopped into fine pieces with scissors.

- Minced tissue was transferred into a *Potter-Elvehjem* glass grinder with 0.5 mL mitochondria isolation solution MIS (containing 0.16 mg/mL proteinase and 3.6 mg/mL bovine serum albumin, fatty acid free (BSA)) and it was disrupted with 10 motorized strokes. At this point, homogenate should not contain any visible tissue pieces. Additional 0.5 mL MIS were added and the sample was further homogenized with 5 additional strokes.

- The homogenate was transferred to a 2 mL test tube and the glass grinder was washed with additional 0.5 mL MIS (0.16 mg/mL proteinase and 3.6 mg/mL BSA) to ensure transfer of residual homogenate.
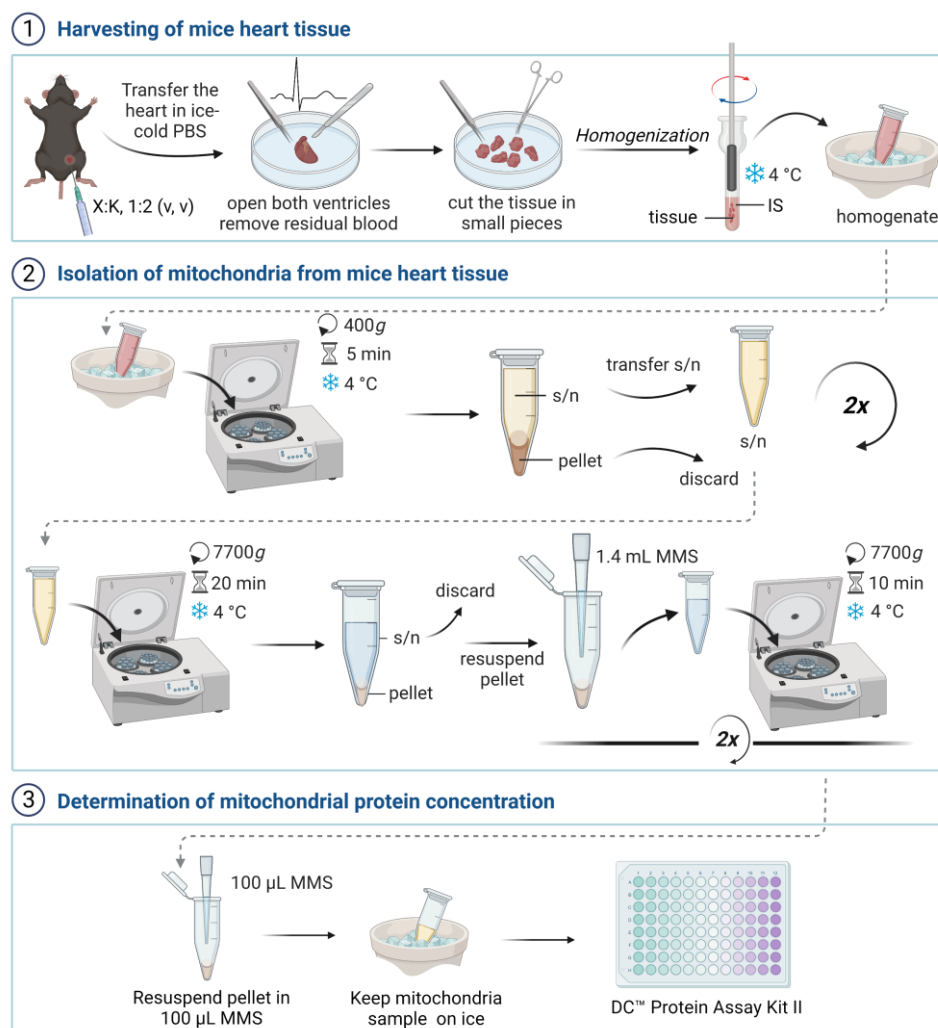
Figure 3-19 Schematic workflow for isolation of mitochondria from murine heart tissue. 1) Extraction of the heart from the mouse and preparation of homogenate. 2) Centrifugation steps to pellet mitochondria. 3) Quantification of isolated mitochondrial protein.

2. *Isolation of mitochondria from mice heart tissue* (Figure 3-19*, step 2 and step 3*):

- The homogenate was centrifuged at 400g for 5 minutes at 4 °C. The resulting supernatant (s/n) was moved to a new 2 mL tube and the centrifugation (400g, 5 minutes, 4 °C) was repeated. The resulting pellet was discarded, while the s/n was collected in a new 2 mL tube.

- From the collected s/n mitochondria were pelleted at 7700g for 15 minutes at 4 °C.

- The s/n was discarded, while the pellet was washed with 1.4 mL mitochondria suspension solution (MSS) and centrifuged at 7700g for 10 minutes at 4 °C. The washing step of the pellet was performed 2 times, each with 1.4 mL MSS.

- The pellet was reconstructed in 100 µL MSS yielding mitochondrial protein concentrations of 15-25 mg/mL.

- Isolated mitochondria were kept on ice and the experiments were performed on the same day.

3. *Determination of mitochondrial protein concentration* (Figure 3-19*, step 3*)

Mitochondrial protein concentration was quantified using *DC™ (detergent compatible) Protein Assay Kit II* with the microplate protocol as described by the manufacturer guideline[210]. The principle of the assay is adapted from the method of Lowry[211] and it is based on the reaction of protein with an alkaline copper tartrate solution and subsequent reduction of *Folin* reagent by the copper-treated protein. The resulting reduced species have a characteristic blue colour with maximum absorbance at 750 nm. The standard curve was generated by plotting the absorbance versus known concentrations (0, 0.025, 0.125, 0.25, 0.5, 0.75, 1, 1.5 and 2 mg/mL) of BSA. Three different dilutions of the sample (mitochondrial protein) and control (MMS) were prepared in the range of the standard curve. 5 µL of BSA standards, diluted samples (mitochondrial protein) and diluted MSS (control) solutions were pipetted as triplicates into a 96-well plate. 25 µL of the working solution (mixture of reagent A and reagent S, 50:1, v/v) were added to each well followed by addition of 200 µL from Reagent B. The plate was incubated for 15 minutes at RT, protected from light. After incubation, the absorbance was measured at 750 nm using a plate reader. The absorbance of the diluted MSS solutions was subtracted from the absorbance of the diluted samples (similarly diluted). The values were corrected using the dilution factor and the mitochondrial protein concentration was calculated as an average of the dilutions.

3.7.2 Mitochondrial respiration measurements by high-resolution respirometry

The effects of Qs and HO-Qs on mitochondrial oxygen consumption were analysed by high-resolution respirometry (HRR).

Principle. The principle of respirometry is based on monitoring oxygen concentration ($[O_2]$) in a closed chamber over time by *Clark*-type polarographic oxygen sensors[212–214]. The high-resolution Oxygraph-2k (O2k)[213] is one of the devices that allows monitoring O_2 consumption with high accuracy, resolution and sensitivity. The O2k consists of two independent glass chambers placed in a stainless-steel housing equipped with an integrated *Peltier* temperature regulator (2−45 °C, ±0.001 °C), stirrer controller and barometric pressure transducer crucial for accurate O_2 calibration. The cylindrical glass chambers are closed with cone-shaped stoppers. The stoppers have injection ports for extrusion of gas bubbles and insertion of a titration needle. Each chamber is equipped with a *Clark*-type[212] polarographic oxygen sensor (POS) and a magnetic stirrer. Angular insertion of the POS into the cylindrical glass chamber places the POS into an optimum position for stirring. POS consists of two electrodes, a platinum or gold cathode that serves as a working electrode and a silver anode coated with silver chloride Ag/AgCl as a reference electrode, both immersed in concentrated electrolyte solution (1 M KCl) and separated from the sample solution by a gas-permeable membrane. The membrane is highly permeable for O_2 and impermeable for other redox-active molecules present in the sample solution. Dissolved O_2 diffuses from the sample solution through the membrane to POS where on the surface of the cathode is reduced (Eq. 3-35) by accepting electrons due to applied negative potential. At the

same time, oxidation takes place at the anode that provides the electrons for reduction of O_2 on the cathode (Eq. 3-36)[213].

$$O_2 + 2\ H_2O + 4\ e^- \rightarrow 4\ OH^- \qquad E^0 = -0.401\ V \qquad \text{Eq. 3-35}$$

$$4\ Ag \rightarrow 4\ Ag^+ + 4\ e^- \qquad E^0 = +0.210\ V \qquad \text{Eq. 3-36}$$
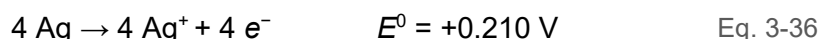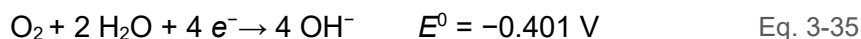
The detection method used in HRR is amperometry. The sensor measures the current over time that flows as a result of the electrochemical reactions (Eq. 3-35 and Eq. 3-36), while the potential between the electrodes is held constant. The measured current (µA) is the primary signal in HRR and it is proportional to the partial pressure of O_2 (pO_2) in the solution. $[O_2]$ in µM is calculated (automatically by the instrument software) as a function of the recorded signal, O_2 solubility factor of the medium, temperature and barometric pressure. During the measurement, $[O_2]$ and O_2 flux (negative time derivative of $[O_2]$) per chamber volume or per amount of the sample are displayed and followed simultaneously on-line. Since the reduction of O_2 at the cathode is a fast process, the $[O_2]$ in the vicinity of the electrode is changing and it might not reflect the $[O_2]$ in the working solution. To overcome this problem and obtain a homogenous system, the solution is constantly stirred at high-speed providing fresh material at the cathode.

Functional measurements of cellular respiration provide important insights into respiratory capacity of the mitochondrial electron transfer chain (ETC), mitochondrial membrane integrity and energy metabolism. HRR records cellular respiration in real time, by titrating various substrates, uncouplers, and inhibitors during the experiment (Table 3-5). Respiratory assays are conducted by addition of these substances in a certain order (titration regimes) known as SUIT (**S**ubstrate-**U**ncoupler-**I**nhibitor Titrations) protocols[213,215]. Generally, mitochondria are added first followed by substrate and then ADP titration.

Table 3-5 Substrates and inhibitors for the respiratory chain complexes I-V used in SUIT protocols.

Complex	Substrate	Inhibitor
I	pyruvate (P) malate (M) glutamate (G)	rotenone (r)
II	succinate (S)	malonate (Mna) atpenin A5 (AA5)
III	duroquinol	antimycin A (Ama)
IV	TMPD (Tm) ascorbate (As)	cyanide (KCN)
ATP synthase	ADP	oligomycin (Omy)

Chance and Williams[216–220] introduced five classical states of mitochondrial respiration, which are still extensively employed with minor adjustments[221]. Mitochondria added to air-saturated respiration buffer containing inorganic phosphate (P_i) but in absence of exogenously added fuel substrates and ADP exhibit state 1 respiration. State 1 is characterized with very slow O_2 consumption rate (OCR). In the original protocol by Chance and Williams[216–220], mitochondria exhibit state 2 respiration by addition of high concentrations of ADP in absence of exogenous fuel

substrates. This results in stimulation of mitochondrial respiration based on endogenous fuel substrates and only small portion of the added ADP being phosphorylated to ATP. Nowadays, an alternative approach to induce state 2 respiration is applied. It involves titration of fuel substrates prior to the titration of ADP. Once the fuel substrate(s) is/are added, the mitochondria enter state 2 (LEAK) respiration where the OCR should increase noticeably. State 2 respiration can be achieved via three different pathways:

- NADH (N)-pathway (Complex I-linked pathway) is induced by addition of substrates (or their combination) such as pyruvate, malate or glutamate. These substrates are (indirectly) linked to complex I (CI) by generating NADH which transfers electrons to CI.

- Succinate (S)-pathway (Complex II-linked pathway) is prompted by addition of succinate and rotenone (inhibitor of CI). When succinate is added without rotenone, oxaloacetate* is formed from malate and accumulates, causing inhibition of CII. Under these conditions, reverse electron flow from CII to CI is triggered resulting in ROS production.

- NS pathway (CI- and CII-linked pathway) is stimulated by addition of NADH-substrates in combination with succinate.

Upon addition of ADP, mitochondria enter state 3 (OXPHOS) respiration leading to a significant increase in OCR. In state 3, ADP is phosphorylated by ATP synthase driven by proton translocation from the intermembrane space to the matrix. Under not saturating concentrations of ADP, the added ADP will be fully converted to ATP and mitochondria will enter state 4 (LEAK state). Nevertheless, state 3 can be restored by subsequential addition of ADP followed by transitions from State 3 to 4 as long as there is available O_2 in the closed chamber. Under saturating concentrations of ADP, state 4 can be prompted by titrating oligomycin (inhibitor of ATP-synthase) and the remaining mitochondrial respiration is attributed to the proton leak. State 5 respiration is related to complete O_2 depletion in the closed chamber. Alternatively, before complete exhaustion of O_2 in the chamber and by titrating antimycin A and rotenone, residual oxygen consumption (ROX) can be obtained. ROX can be used as a baseline to correct respiration measured in defined states. ROX is related to non-respiratory side reactions[221].

Experiment. O_2 consumption was measured with the Oxygraph O2k (Table 2-8) controlled by *DatLab 7* software. Two measurements were run in parallel in two separate *Duran* glass chambers (2 mL volume). Each chamber was equipped with POS composed of a gold cathode with 2 mm diameter and a silver anode with larger surface area. As electrolyte a 1 M KCl solution was used, enclosed by a fluorinated ethylene propylene (FEP) membrane with 25 µm thickness. The O2k limit of detection is: $[O_2]$ = 0.005 µM and O_2 flux of 1 pmol/s·cm^3 or 0.001 µM/s.

The instrument parameters were set as follows: polarization voltage of POS, + 0.800 V; stirrer speed, 750 rpm; temperature, 37 °C; solubility factor of O_2 in the medium F_M, 0.92 (recommended by the manufacturer); gain, 1; and data recording interval, 2s.

Quality check of the POS and air calibration of the set-up were performed daily before starting the experiments. According to the manufacturer's guideline[222,223], POS are calibrated by a two-point calibration: (i) at air saturation (R_1) and (ii) at zero O_2 concentration (R_0) using the desired

---

* Oxaloacetate is a more potent competitive inhibitor of CII than malonate even at low concentrations.

respiration medium. Air saturation was performed by adding 2.25 mL respiration buffer (RB) into each chamber. The stoppers were fully inserted and the excess of the RB was siphoned off to achieve an exact volume of 2 mL in the volume-calibrated chambers. Using the stopper-spacer tool, the stoppers were lifted to the stopper spacer position for final air equilibration. The following quality controls need to be performed accurately to ensure a high standard in respirometer performance:

- Stirrer test – stirrer is switched off for 30 seconds. Upon its restart, the signal should show a rapid and mono-exponential increase.

- $[O_2]$ of air saturated RB is between 160 and 200 µM corresponding to an O_2 signal (R_1) of 1−3 V with a slope uncorrected of O_2 change close to zero (± 1 pmol/s·cm³) and a noise of ± 2 pmol/s·cm³ (max. ± 4).

- After closing the chambers, the values of the O_2 slope negative should not be higher than 4 pmol/s·cm³. Higher values may indicate contamination and the buffer needs to be replaced by a freshly thawed aliquot.

- zero O_2 condition of the chamber (R_0) was determined from the first experiment when O_2 was completely depleted (R_0 should be <5% of R_1).

If one of the above conditions showed any deviations from the acceptable level, POS-Service[224] was executed including cleaning of the gold cathode and the silver anode. After cathode/anode cleaning cycle, the electrode was coated with 1 M KCl solution and mounted with FEP membrane. Next, an instrumental background test was performed following the manual[223,225] instructions: 20 mg $Na_2S_2O_4$ were dissolved in 2 mL MiR05[226] (Table 2-7) in a 2-mL test tube to minimize air exposure. The potency of the stock solution was determined by adding a small volume (1 µL) of the solution into both chambers, observing the change in $[O_2]$ and calculating the change per µL of $Na_2S_2O_4$. A step-by-step titration with $Na_2S_2O_4$ was performed manually using a 50-µL *Hamilton* microsyringe. The background O_2 flux was measured at four consecutively selected $[O_2]$: initial point air saturation (~ 180 µM) following < 100 µM, < 50 µM, < 23 µM (each level was maintained for 15 minutes) and 0 µM for 5 minutes. Excess of $Na_2S_2O_4$ (100 µL) was added to establish the zero O_2 condition.

Composition of the buffers used for the mitochondrial respiration assays are given in Table 2-7. Before each measurement 2.25 mL respiration buffer (RB_0 or RB_1) were added into each chamber, the stoppers were closed and excessive buffer was siphoned off leaving 2 mL in the chamber. As soon as the buffer has equilibrated to 37 °C and the slope of O_2 change reached a stable signal of less than 4 pmol/s·cm³ (approximately 30 minutes), a new measurement was started.

Mitochondria (isolation procedure in section 3.7.1) were stored on ice and prediluted shortly prior to the measurement by transferring 240 µg mitochondria into 240 µL ice-cold RB (mitochondrial protein concentration 1 mg/mL). A 1:1 mixture of pyruvate (1 M in RB) and malate (1 M in H_2O) was prepared freshly and kept on ice. Succinate, ADP and cytochrome *c* were thawed and preserved on ice. Rotenone solution was unfrozen and kept protected from light at room temperature. 1 mM stock solutions of Qs and HO-Qs (preparation given in section 3.5) were protected from light and stored at room temperature. Mitochondria, substrates, inhibitors and

samples were applied by using *Hamilton* syringes through the injection port of the stopper at defined times. In Table 3-6 are given the substrates and inhibitors used for the measurements.

Table 3-6 Substrates and inhibitors used for mitochondrial respiration measurements and their stock solutions concentrations, storage temperature and abbreviations. RB, respiration buffer; DMSO, dimethyl sulfoxide; 1 M HCl or 5 M KOH used to adjust pH to 7.4; f. p., freshly prepared.

Substance	Abbreviation	Stock concentration (M)	Solvent	Storage (°C)
pyruvate	P	1	RB	f. p.
malate	M	1	RB	f. p.
succinate	S	1	H_2O (1 M HCl)	−20
glutamate	G	1	H_2O (5 M KOH)	−20
cytochrome *c*	c	0.0005	H_2O	−20
ADP	A	0.5	H_2O (5 M KOH)	−80
rotenone	r	0.0001	DMSO	−20

Details about the added volume, concentrations (stock and final), and times of addition for the corresponding substances are given in Table 3-7 for cytochrome *c* test, Table 3-8 for Complex I-linked respiration and Table 3-9 for Complex II-linked respiration. Measurements were stopped after fully depleting O_2 in the chambers. Each experiment was repeated at least 3 times using three different preparations of mitochondria.

Table 3-7 Addition of substances for determination of outer mitochondrial membrane integrity in isolated murine heart mitochondria. MHM, mouse heart mitochondria; abbreviations of substances in Table 3-6; [stock], concentration of stock solutions of substances; [final], final concentrations of substances in each chamber.

Mitochondrial outer membrane integrity (cytochrome *c* test)					
substance	[stock]	added volume (µL)	[final] (in 2mL)	Time (s) 1st chamber	Time (s) 2nd chamber
MHM	1 mg/mL	100	50 µg/mL	180	240
PM	0.5 M	20	5 mM	360	420
A	0.5 M	4	1 mM	540	600
c	5 mM	4	10 µM	720	780
G	1 M	30	15 mM	900	960
S	1 M	20	10 mM	1080	1140

Table 3-8 Addition of substances for Complex I-linked respiration in murine heart mitochondria. MHM, mouse heart mitochondria; PM, pyruvate/malate; A, ADP; sample, Qs-PCS or HO-Qs-PCS; [stock], concentration of stock solutions of substances; [final], final concentrations of substances in each chamber.

Complex I-linked respiration					
substance	[stock]	added volume (µL)	[final] (in 2mL)	Time (s) 1st chamber	Time (s) 2nd chamber
MHM	1 mg/mL	100	50 µg/mL	180	240
PM	0.5 M	20	5 mM	360	420
A	0.5 M	4	1 mM	540	600
sample	1 mM	20	10 µM	720	780

Table 3-9 Addition of substances for Complex II-linked respiration in murine heart mitochondria. MHM, mouse heart mitochondria; r, rotenone; S, succinate; A, ADP; sample, Qs-PCS or HO-Qs-PCS; [stock], concentration of stock solutions of substances; [final], final concentrations of substances in each chamber.

Complex II-linked respiration					
substance	[stock]	added volume (µL)	[final] (in 2mL)	Time (s) 1ˢᵗ chamber	Time (s) 2ⁿᵈ chamber
MHM	1 mg/mL	100	50 µg/mL	180	240
r	1 mM	1	0.5 µM	360	420
S	1 M	20	10 mM	540	600
A	0.5 M	4	1 mM	720	780
sample	1 mM	20	10 µM	900	960

Analysis. $[O_2]$ in the chamber declines during respiration as O_2 is consumed by mitochondria. The experimental data of $[O_2]$ as well as the O_2 flux per chamber volume is displayed over time [h:min] by the *DatLab 7* software. Both signals are recorded in real-time allowing the experimenter to follow respiration of biological samples while experiment is still running. The oxygen consumption rate (OCR) is calculated automatically by the software from the slope of O_2 concentration (first derivative of the O_2 concentration) over time and expressed in picomole per second per mL (pmol/(s·mL)).

For an accurate analysis, the slope smoothing points were marked down by applying the *Savitzky-Golay* smoothing filter of 5 data points (i.e., 10 seconds interval). Average OCRs for each condition were calculated as the mean within 10 seconds before the subsequent addition of the substances.

The damage of the mitochondrial outer membrane (attributed mainly to the isolation process) is defined as percent of increase in the OCR after addition of exogenous cytochrome *c*, when both ADP and substrates are present. The percentage of the increase in the OCR due to damage of the membrane is calculated with the formula below:

$$OCR(\%) = \left(\frac{flux\ per\ volume_{after\ cyt\ c} - flux\ per\ volume_{after\ ADP}}{flux\ per\ volume_{after\ ADP}} \right) \times 100 \qquad \text{Eq. 3-37}$$

CI- and CII-linked respiration results are reported as OCR in percentage normalized to ADP respiration rate (taken as 100%), calculated with formula Eq. 3-38. Percentage data of the reproduced experiments were combined and displayed as mean±SEM.

$$OCR(\%) = \frac{flux\ per\ volume_{after\ sample}}{flux\ per\ volume_{after\ ADP}} \times 100 \qquad \text{Eq. 3-38}$$

4. Results

4.1 Synthesis of hydroxylated forms of coenzyme Q_1 and decylubiquinone

Since the hydroxylated forms of coenzyme Q_1 (HO-Q_1) and decylubiquinone (HO-dUQ) are commercially not available, the initial tasks were synthesis and purification of the substances in sufficient amounts. The chemical structure and purity of the new products were determined using mass spectrometry (MS) and nuclear magnetic resonance (NMR) spectroscopy.

The method for synthesis of HO-Q_1, described in section 3.1.1, was adapted from Bogeski *et al.*[10], and scaled for production of sufficiently large amounts for further isolation and purification. Due to the lipophilic nature of dUQ and to ensure its complete dissolution in aqueous alkaline medium, the procedure for the synthesis of HO-dUQ was slightly modified. Briefly, dUQ was dissolved in methanol as a water miscible organic solvent and the reaction was started by adding 0.2 M NaOH to the methanolic solution of dUQ (1:1, v/v) (detailed procedure in section 3.1.2).

The course of the reaction between Q_1 and HO^- could be followed by a significant colour change of the solution, as shown in Figure 4-1 a. Q_1 dissolved in water exhibited a yellow colour (left flask, Figure 4-1 a), which after addition of NaOH changed to amber (Q_1 dissolved in NaOH after 5 min, middle flask) and as the reaction proceeded the colour changed to intensively violet (right flask). Although UV-Vis spectroscopy conveys limited information on the structure of the species involved in a reaction, it is yet the most commonly used technique to follow structural and electronic variations associated with chemical transformation over time. Consistent with the colour impression, UV-Vis spectroscopic data revealed time dependent spectral changes which are related to the chemical transformation of Q_1. The spectrum of Q_1 (Figure 4-1 b, black line) is characterized by typical absorption for aromatic ring at 280 nm which is assigned to π-π^* electron transitions of the carbonyl group and the aromatic ring and weak absorption band at 416 nm attributed to an n-π^* transitions of the oxygen lone (unshared) pair of electrons. Addition of Q_1 to NaOH solution showed clear time dependent changes in the absorption bands (Figure 4-1 b, c). As the reaction proceeded, the absorption band at 280 nm from the initial UV-Vis spectrum decreased over time (Figure 4-1 c, d) and one additional shoulder at 335 nm appeared, which increased over time (Figure 4-1 b, c, d). The weak absorption band at 416 nm (black line, Figure 4-1 b) showed bathochromic shift of around 100 nm (530 nm, red line in Figure 4-1 b). This bathochromic displacements of the bands from the initial UV-Vis spectrum of Q_1 to longer wavelengths are typical for introduction of hydroxyl group to an aromatic ring[227]. The broad absorption band centred at 530 nm is assigned to n-π^* transitions of an unshared pair of electrons on oxygen atom and electrons from the aromatic ring. Although the hydroxyl group is auxochrome, i.e., it lacks absorption characteristics, it exerts a profound impact on systems to which it is bonded by providing additional possibilities for charge delocalization. This increases the resonance stability by interaction of the lone pair of electrons on oxygen atoms with the π-electrons of the aromatic ring, thus lowering the energy needed for electron transition from ground to excited states (Figure 3-1 b, c). Therefore, the improved resonance stability increases the absorption of light and shifts the absorption bands to longer wavelength (bathochromic

displacement)[2,227,228]. At a wavelength of 291 nm the absorption was constant over time (Figure 4-1 c). This isosbestic point is typical for 1-to-1 chemical reaction indicating direct transformation of reactant to product.

Observed spectral changes are consistent with a hydroxyl group in the structure of the new product and a different electronic structure compared to the parent compound Q_1. By following the absorption intensity of the bands located at 280, 335 and 530 nm over time (Figure 4-1 d), it is noticed that the chemical reaction of Q_1 and OH^- anions is completed in approximately 100 minutes.

Figure 4-1 Reaction of Q_1 with HO^- ions. a) 25 mg of Q_1 dissolved in water (left flask), in 0.1 M NaOH for 5 min (middle flask) and for 60 min (right flask). b) UV-Vis spectra of 100 µM Q_1 in water (black line) and dissolved in 0.1 M NaOH for 120 min, reaction quenched by neutralization with 5 M HCl to pH~7 (red line). c) Time evolution of the UV-Vis spectra of 100 µM Q_1 dissolved in 0.1 M NaOH for 480 min. d) Absorption changes at 280, 335 and 530 nm due to incubation of 100 µM Q_1 in 0.1 M NaOH for 480 min. UV-Vis conditions: wavelength range, 200 - 900 nm; scan speed, 1800 nm/min; scan step, 1 nm.

As shown in Figure 4-2, a similar behaviour was observed when dUQ was mixed with NaOH solution (pH=13). dUQ dissolved in methanol had a yellow colour (left flask in Figure 4-2 a) which changed to dark violet (right flask) after mixing it with NaOH solution. The UV-Vis spectrum of dUQ showed the typical band for aromatic ring at 281 nm and the broad shoulder at 410 nm (Figure 4-2 b, black line). From Figure 4-2 c it is evident that addition of dUQ to NaOH solution triggered time dependent changes in the absorption bands which are related to the formation of the new product. The absorption band at 281 nm from the initial UV-Vis spectrum of dUQ decreased over time while the shoulder at 410 nm shifted to 540 nm (bathochromic shift) and increased over time (Figure 4-2 c, d). As it was discussed above, this shift to the visible region is indicative for the presence of a hydroxyl group in the structure. The presence of an isosbestic point at 297 nm (Figure 4-2 c) indicates 1-to-1 chemical reaction, i.e., direct transformation of reactant to product. Analysis of the intensity of the absorption bands at 281 and 540 nm over time showed that the chemical reaction between dUQ and OH^- anions is completed in approximately 120 minutes and the new product is stable in the measured time (360 minutes).
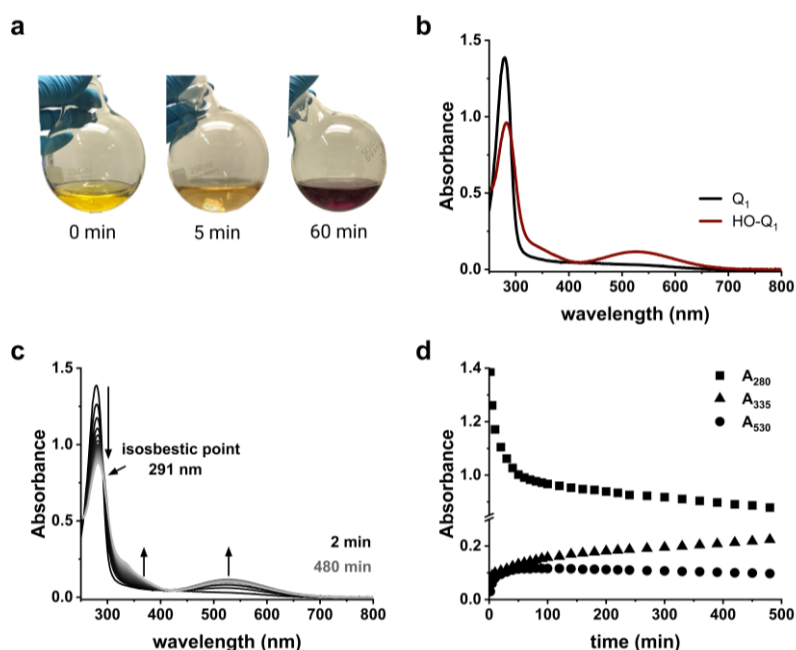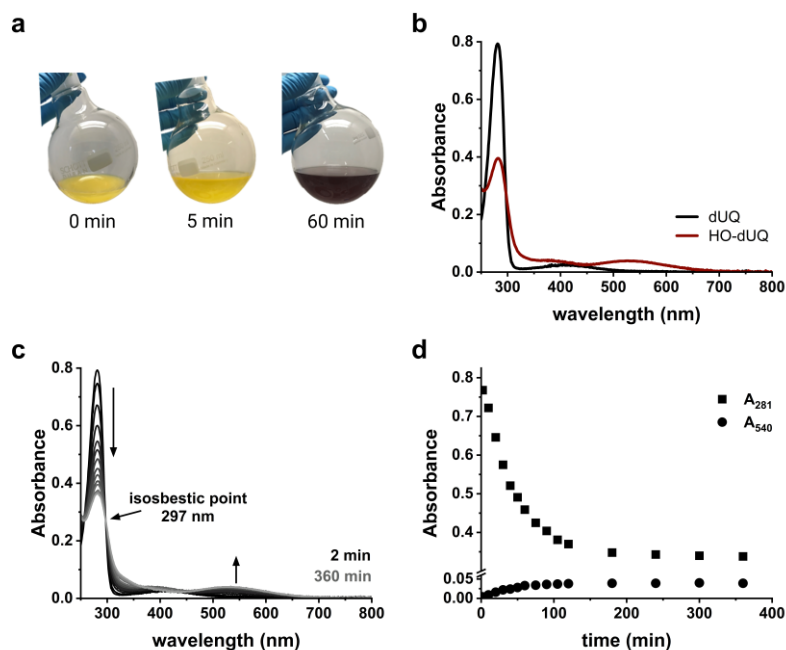
Figure 4-2 Reaction of dUQ with HO⁻ ions. a) 20 mg of dUQ dissolved in methanol (left flask), 0.1 M NaOH for 5 min (middle flask) and for 60 min (right flask). b) UV-Vis spectra of 50 µM dUQ in methanol:water (50:50, v/v) (black line) and dissolved in 0.1 M NaOH for 120 min and neutralized with 5 M HCl to pH 7 (red line). c) Time evolution of the UV-Vis spectra of 50 µM dUQ dissolved in 0.1 M NaOH for 360 min. d) Absorption changes at 281 and 540 nm due to incubation of 50 µM dUQ in 0.1 M NaOH for 360 min. UV-Vis conditions are same as in Figure 4-1.

Additionally, the chemical transformation of Q_1 in a strong alkaline solution (pH=13) was studied by cyclic voltammetry (CV) and square-wave voltammetry (SWV). Figure 4-3 shows time evolution of the cyclic (panel a) and square-wave (panel c) voltammograms of Q_1 dissolved in NaOH. As shown in Figure 4-3 a, two reversible-like redox processes were observed, whose intensities were significantly changed over time. The intensity of the first pair of peaks at more positive potentials and originating from Q_1 (marked with Q_1, Figure 4-3 a) decreased with time, while the height of the second pair of peaks at more negative potentials associated with the new product increased considerably (marked with HO-Q_1, panel a). The individual voltammograms at 5 min (black line, Q_1) and at 120 min (red line, OH-Q_1) after starting the reaction are shown in Figure 4-3 b. After 5 min some portion of Q_1 was already converted to OH-Q_1 causing the additional waves at lower potentials of the black line. These waves grew on expense of the Q_1-peaks and finally gave the red voltammogram. Because the intensity of the peak potentials (peak current) is proportional to the concentration of electrochemical species (Eq. 3-25), the observed voltammetric responses implicated that after about 2 hours the reaction between Q_1 and NaOH was greatly shifted toward the product, HO-Q_1, which then was the prevalent fraction in the solution. The mid-peak potential ($E_{p,mid}$) which is related to the thermodynamic features of the redox process[10] differed significantly between the two responses. Calculated mid-peak potential for the redox process of Q_1 was $E_{p,mid}$ = −0.3519 V and for that of the new product $E_{p,mid}$ = −0.5864 V which further implied that they originate from different species. The results obtained with SW voltammetry (Figure 4-3 c, d) were in complete agreement with CV data. The SW voltammograms consisted of two voltammetric responses whose intensities were changing over time (Figure 4-3 c). The peak current of the voltammteric response at more positive potentials assigned to Q_1 decreased with time, while the peak current of the second voltammetric response at more negative potentials attributed to the product HO-Q_1 increased.

Reaction of Q$_1$ with HO$^-$ ions
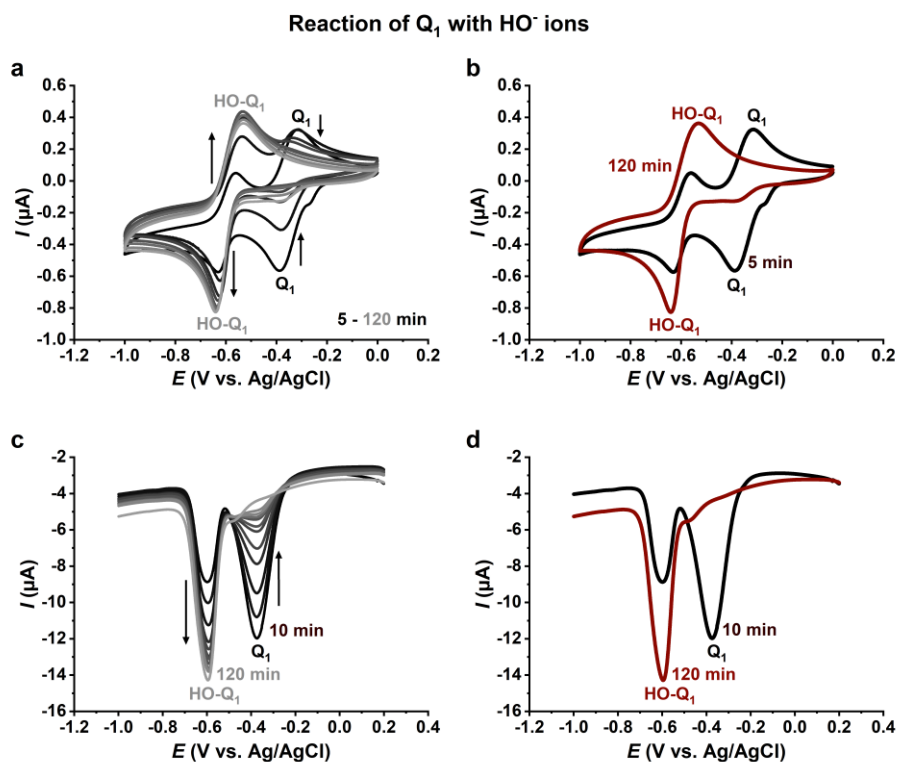
Figure 4-3 Time-dependent changes of the voltammetric response of Q$_1$ dissolved in strong alkaline solution. a) Time evolution of cyclic voltammograms (CVs) of 0.5 mM Q$_1$ dissolved in 0.1 M NaOH (black line, 5 min after mixing Q$_1$ and NaOH; light grey line, 120 min after the start of the reaction). b) Comparison of CVs of 0.5 mM Q$_1$ incubated with 0.1 M NaOH for 5 min (black line) and 120 min (red line). Conditions for CV: scan rate 20 mV/s; ΔE = 1 mV. c) Time evolution of square-wave voltammograms (SWVs) of 0.5 mM Q$_1$ dissolved in 0.1 M NaOH (black line, 10 min after dissolving Q$_1$ in NaOH; light grey line, 120 min after the start of the reaction). d) Comparison of SWVs of Q$_1$ incubated with 0.1 M NaOH for 10 min (black line) and 120 min (red line). Conditions for SWV: f = 8 Hz; E_{sw} = 50 mV; ΔE = 1 mV.

As it is evident from Figure 4-4, an analogous behaviour was obtained for the reaction of dUQ with HO$^-$ ions followed by SWV. The SW voltammograms consisted of two voltammetric responses whose intensities were time dependent. The peak current at more positive potentials (dUQ, Figure 4-4 a) resulting from the redox process of dUQ decreased with time. The intensity of the peak at more negative potentials (HO-dUQ, Figure 4-4 a) increased at the expense of the dUQ-peaks over time indicating that the product was becoming the dominant redox species in the solution. In contrast to the reaction of Q$_1$ (Figure 4-3 c, d), the conversion of dUQ was not fully completed after 120 minutes as inferred from the peak intensities in Figure 4-4 b (red line). Obviously, dUQ had a slower reaction kinetics than Q$_1$ for hydroxylation.

Reaction of dUQ with HO$^-$ ions
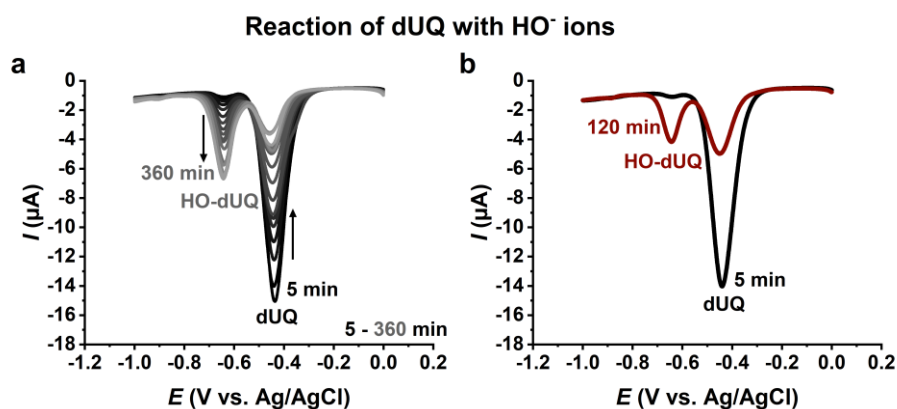
Figure 4-4 Time-dependent changes of the square-wave voltammetric response of dUQ dissolved in strong alkaline solution. a) Time evolution of square-wave voltammograms (SWVs) of 0.5 mM dUQ dissolved in 0.1 M NaOH (dUQ dissolved in methanol and mixed with 0.2 M NaOH in ratio 1:1, v/v); black line, 5 min after mixing dUQ and NaOH; light grey line, 360 min after the start of the reaction. b) Comparison of SWVs of 0.5 mM dUQ incubated with 0.1 M NaOH for 5 min (black line) and 120 min (red line). Conditions: f = 8 Hz; E_{sw} = 50 mV; ΔE = 1 mV.

4.1.1 Isolation and purification of the new hydroxylated products

The reaction mixtures were further analysed by reversed-phase high-performance liquid chromatography (RP-HPLC) in order to separate and characterize the products of the chemical transformations of Q_1 and dUQ in NaOH solution. Separation of the different products was the first step and crucial for method development for further purification and characterization of the targeted compounds. In this course, HPLC protocols for isolation and purification of the hydroxylated products of Q_1 and dUQ from the reaction mixture have been developed and applied to produce sufficient material for further studies. A detailed overview of the used methods is given in Table 3-1. To minimize the consumption of samples and solvents, separation methods were first developed on a small (analytical) scale column and later transferred to a larger (preparative) scale column.

After choosing the appropriate column, the next crucial step in developing a separation protocol was to optimize the composition of the mobile phase and the mode of elution (gradient or isocratic elution). Application of isocratic mode (constant composition of the mobile phase) for product elution has several advantages over the gradient elution (gradually changed composition of the mobile phase over time). In terms of finding adequate separation within an acceptable analysis time, the optimization of gradient elution presents a bigger challenge than that of isocratic elution since numerous variables have impact on the selectivity. Even though gradient elution generally gives better sensitivity and much narrower chromatographic peaks, optimization of isocratic elution is considerably easier and faster. Gradient elution is a slower technique than isocratic because it requires flushing and equilibrating of the column with a minimum of ten column volumes of the starting eluent before achieving reliable retention in the subsequent run[229]. In isocratic mode the composition of the mobile phase is constant over time, thus no equilibration is needed between consecutive injections resulting in greatly shorter time of the analysis. Additionally, isocratic elution does not depend on the dimensions of the column making the transfer of the method between columns, instruments and laboratories significantly easier than the transfer of a gradient elution method. Since our goal was isolation and purification of bulky amounts of the hydroxylated derivatives of Q_1 and dUQ, development of an isocratic separation method for the reaction products was more advantageous.

To achieve a good peak separation and peak resolution for each compound of the reaction mixtures, several compositions of the mobile phase such as methanol-water, acetonitrile-water, with or without different concentrations of formic acid (HCOOH) were tested. Additionally, various flow rates, temperature and elution modes were used. The test results showed that good and satisfactory separation in isocratic mode was achieved with a mobile phase of 52:48 (v/v) acetonitrile and water containing 0.1% HCOOH for the reaction mixture of Q_1 and mixture of 84:16 (v/v) methanol and water containing 0.1% HCOOH for the reaction mixture of dUQ. The UV detector was set to measure the absorbance at 275 nm since at that wavelength the typical band for the aromatic ring (which should be intact in both reactants and products) is located (Figure 4-1 b and Figure 4-2 b). With such conditions (detailed overview in Table 3-1) a good

separation of the compounds in the reaction mixtures was achieved (Figure 4-5). The peaks of native compounds in the chromatograms were identified by a comparison of the retention times of the individual parent compounds Q_1 and dUQ, applying identical chromatographic conditions (red lines in Figure 4-5). In addition, spiking of the reaction mixtures with the respective native compounds Q_1 and dUQ identified the portion of native material after reaction. Because hydroxylated derivatives of Q_1 and dUQ should be more polar than the parent compound due to the insertion of hydroxyl groups in their structure, their elution will happen before the parent compound. In absence of a reference compound for the new products to determine the elution times of the compounds the changes in the chromatographic peaks over time were followed (Figure 4-6) and preliminary mass spectrometric experiments on the reaction mixture were performed to check for the mass to charge ratio (*m/z*) corresponding to each peak. As shown in Figure 4-5 a, HPLC analysis of reaction mixture of Q_1 revealed three main chromatographic peaks with retention times (t_R) 6.2, 8.4 and 10.3 minutes, that were tentatively attributed by preliminary MS experiments to mono-hydroxylated form of Q_1, HO-Q_1 (t_R = 6.2 min), a byproduct B (t_R = 8.4 min) where the hydroxyl group is attached to the methyl group at position 5 of aromatic ring, and pure (unreacted) Q_1 (t_R = 10.3 min). HPLC (Figure 4-5 b) and preliminary MS analysis of the reaction mixture of dUQ, showed that the peak with t_R = 9.9 min corresponded to the new mono-hydroxylated product of dUQ (HO-dUQ), while the peak at 13.8 minutes is arising from pure (unreacted) dUQ.
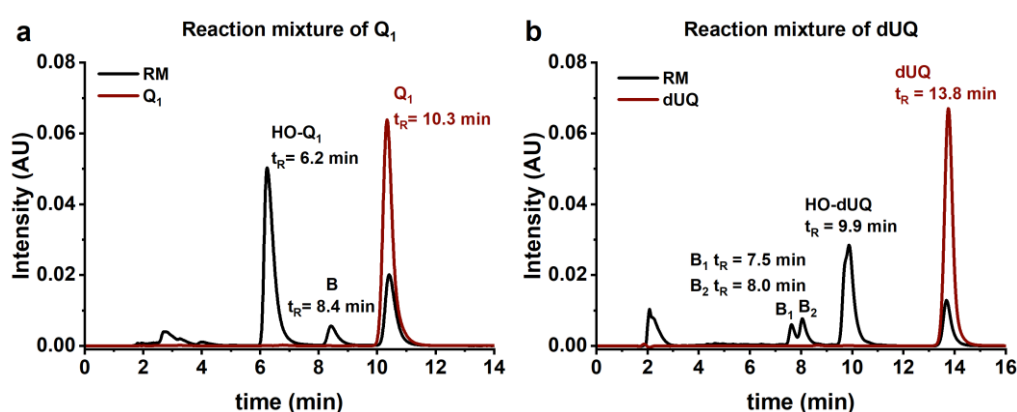
Figure 4-5 Analytical HPLC chromatograms of reaction mixture of Q_1 and dUQ. a) Reaction mixture (RM) of Q_1 (black line) shows elution peak of HO-Q_1 at shorter retention time (t_R) than t_R of Q_1 (red line) as well as an additional product B (black line). b) Reaction mixture (RM) of dUQ (black line) shows four main elution peaks, byproducts B_1 and B_2, product of interest HO-dUQ and native unreacted dUQ (black line). Red line represents HPLC chromatogram of pure dUQ. Experimental HPLC conditions are given in Table 3-1.

HPLC analysis (Figure 4-6) of reactions time evolution showed that the reaction between the quinones and HO⁻ happened very fast in the first 120 min and even before the reactant (parent compound) was consumed, the synthesis of the product was saturated. This is consistent with the time evolution of UV-Vis (Figure 4-1 d and Figure 4-2 d) and voltammetric (Figure 4-3 b, d and Figure 4-4 b) time evolution data of the reaction. Longer incubation times did not enhance the yield of the hydroxylated form of the corresponding quinone, but led to more byproducts associated with the chromatographic peak B with t_R = 8.4 min for the reaction mixture of Q_1 (Figure 4-6 a, b) and peaks B_1 and B_2 with t_R of 7.5 and 8 minutes for the reaction mixture of dUQ (Figure 4-6 c, d).
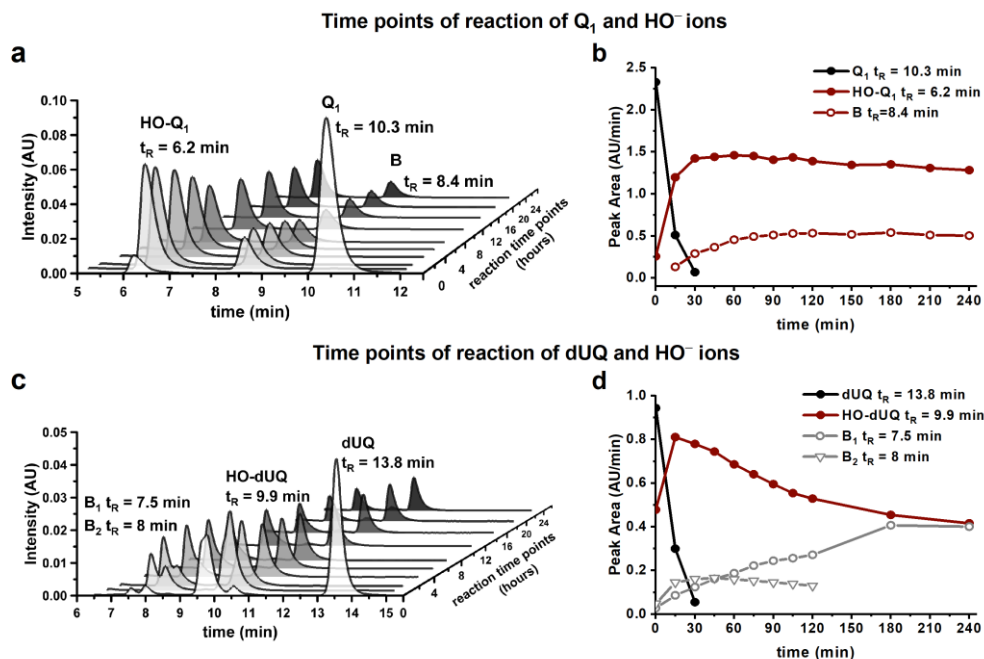
Figure 4-6 Time evolution of the HPLC chromatograms and peak area due to reaction between quinones and HO⁻. Elution profiles of 100 µM reaction mixture of a) Q_1; elution peak at 10.3 min corresponds to the native Q_1, peak at 6.2 min belongs to the product of interest HO-Q_1 and peak at 8.4 min arising from a byproduct B. b) Time evolution of peak areas over 240 min; longer incubation times did not improve the yield of the product. c) dUQ; elution peak at 13.8 min arising from the native unreacted dUQ, peak at 9.9 min corresponding to hydroxylated product HO-dUQ, and elution peaks at 7.5 and 8 min arising from additional products. d) Time evolution of peak areas over 240 min for the reaction mixture of dUQ, reaction proceeds very fast and longer incubation times result in production of byproducts B_1 and B_2.

In a next step, the analytical separation of the reaction mixtures of Q_1 and dUQ was successfully transferred to a preparative scale (Figure 4-7) for purification and isolation of the compounds (detailed experimental conditions for the preparative separation are given in Table 3-1).

From the reaction mixture of Q_1, two fractions, HO-Q_1 at t_R = 18.5 min and Q_1 at t_R = 34.8 min of a preparative run were collected as shown in Figure 4-7 a and were further analysed by LC-MS and NMR to identify the chemical structure of the collected material. From the reaction of dUQ, four fractions (B_1, B_2, HO-dUQ and dUQ, Figure 4-7 b) were collected. Collected amounts from chromatographic peaks B_1 and B_2, with t_R = 17.3 min and t_R = 18.3 min correspondingly, were very low and sufficient only for MS analysis but not for NMR. The yield of hydroxylated product from the reaction of Q_1 and NaOH was 78%, and only 25% for the reaction of dUQ with NaOH.
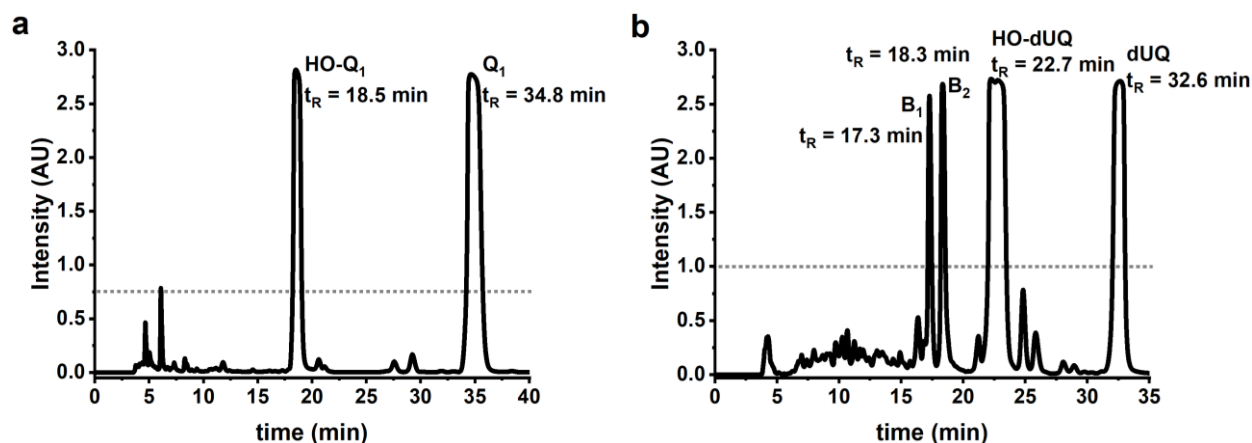
Figure 4-7 Isolation of hydroxylated products by preparative HPLC coupled to an UV detector. a) Isolation of the products from 2 mg reaction mixture of Q_1; collection started after absorption reached value of 0.75 AU (dashed line); elution peak of the new product HO-Q_1 at retention time 18.5 min and unreacted native Q_1 at 34.8 min. b) Elution profile of 3 mg reaction mixture of dUQ, elution peaks of byproducts B_1 and B_2, product of interest HO-dUQ and dUQ. Collection of the peaks started after absorption reached 1 AU (dashed line). Detailed reactions and experimental HPLC conditions are given in section 3.1 and 3.2, respectively.

4.1.2 Structural characterization of the new hydroxylated products

LC-MS analysis (Figure 4-8) of collected material for chromatographic peak HO-Q$_1$ (Figure 4-7 a) of the reaction mixture of Q$_1$ revealed a single chromatographic peak with retention time 5.95 min (Figure 4-8 e), associated with a molecular ion peak at a mass to charge (*m/z*) ratio of 237.1117 obtained with electrospray ionization in positive mode (Figure 4-8 f) and *m/z* 235.0974, when negative mode of the electrospray ionization was used (Figure 4-8 g). These molecular ions corresponded to a molecular weight reduction of 14 units (one CH$_2$ group) with respect to the mass of native Q$_1$ (Figure 4-8 c and d). This implied a substitution of one methoxy group with a hydroxyl group, so that the detected *m/z* represented the mono-hydroxylated form of Q$_1$ (HO-Q$_1$). For the second collected peak, marked as Q$_1$ (Figure 4-7 a) a molecular ion [M+H]$^+$ at *m/z* 251.1272 was found originating from the native unreacted Q$_1$ (Figure 4-8 a, b and c).
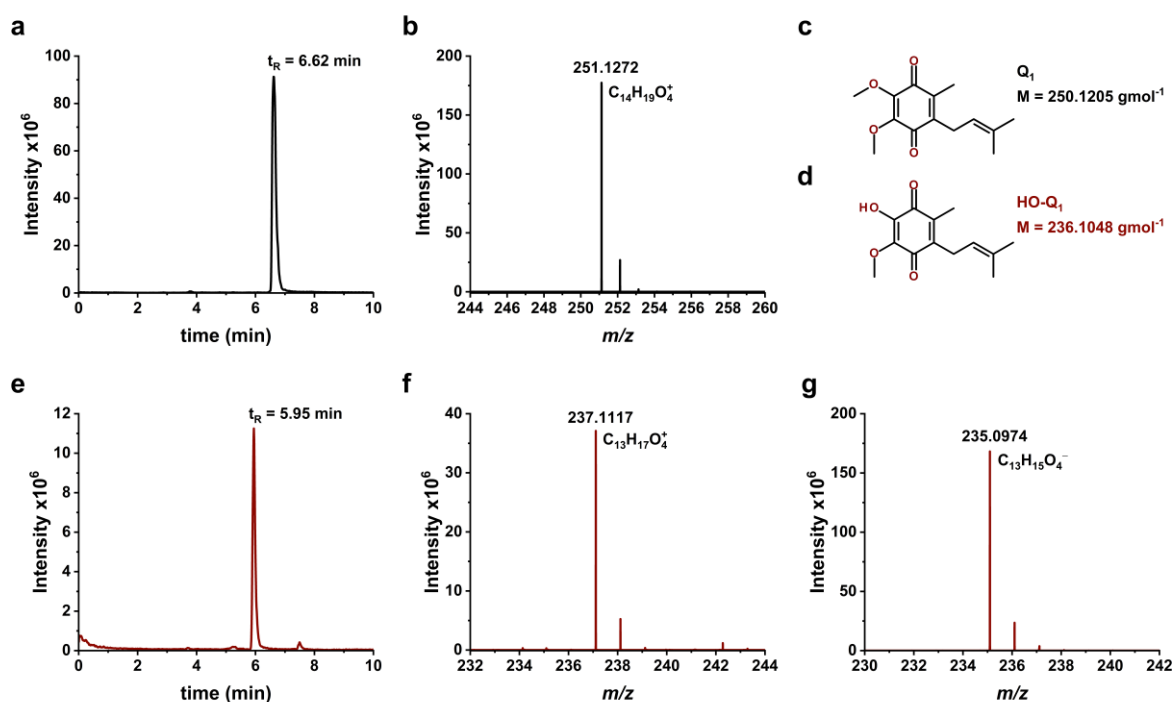
Figure 4-8 LC-MS analysis of isolated and purified material from reaction mixture of Q$_1$. a) LC analysis of chromatographic peak Q$_1$ (Figure 4-7 a); b) Mass spectrum of Q$_1$, obtained with positive ionization mode showing [M+H]$^+$ of Q$_1$; c) Structure and exact molar mass (M) of Q$_1$; d) Structure and exact molar mass (M) of HO-Q$_1$; e) LC analysis of chromatographic peak HO-Q$_1$ (Figure 4-7 a); Mass spectrum of HO-Q$_1$ obtained with ionization f) in positive mode, resulting in [M+H]$^+$ and g) in negative mode, giving [M-H]$^-$.

Furthermore, LC-MS analysis was performed for the four collected peaks from the reaction mixture of dUQ, which is compiled in Figure 4-9. Collected material from peak HO-dUQ at retention time 22.7 min (Figure 4-7 b) showed one chromatographic peak with retention time 7.89 min (Figure 4-9 e) related with a molecular ion peak at *m/z* 309.2073 in positive mode electrospray ionization (Figure 4-9 f) and *m/z* 307.1916 with ionization in negative mode (Figure 4-9 g). These molecular ions again corresponded to the mono-hydroxylated form of dUQ (HO-dUQ), where one methoxy group is substituted with a hydroxyl group compared to the mass of dUQ (Figure 4-9 c and d). LC-MS analysis of collected material from peak dUQ (Figure 4-7 b) revealed a molecular ion peak [M+H]$^+$ at *m/z* 323.2213 (Figure 4-9 b) with t_R = 8.73 min (Figure 4-9 a) corresponding to the native unreacted dUQ (Figure 4-9 c). The LC-MS analysis of collected material from peak B$_1$ at retention time 17.3 minutes (Figure 4-7 b) showed a *m/z* ratio of

323.1865 corresponding to a structure that contains a hydroxyl group replacing one methoxy group and an additional hydroxyl group attached to the methyl group (at position 5) of the quinone ring. LC-MS of peak B_2 at t_R = 18.3 min (Figure 4-7 b) gave a *m/z* ratio of 339.2178 which probably arises from the attachment of a hydroxyl group either to the methyl group at position 5 of the quinone ring or to the methyl group at the end of the sidechain of dUQ.
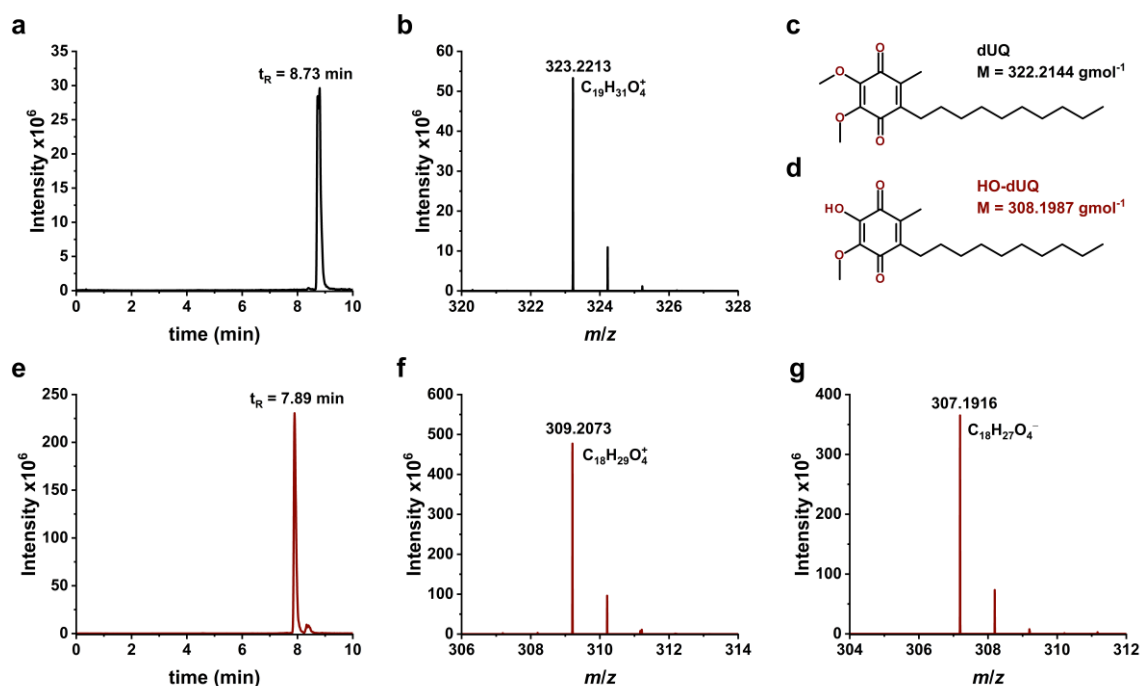
Figure 4-9 LC-MS analysis of isolated and purified material from reaction mixture of dUQ. a) LC analysis of chromatographic peak dUQ (Figure 4-7 b); b) Mass spectrum of dUQ, obtained with positive ionization mode showing [M+H]$^+$ of dUQ; c) Structure and exact molar mass (M) of dUQ; d) Structure and exact molar mass (M) of HO-dUQ; e) LC analysis of chromatographic peak HO-dUQ (Figure 4-7 b); Mass spectrum of HO-dUQ acquired with ionization f) in positive mode, resulting in [M+H]$^+$ and g) in negative mode, giving [M-H]$^-$.

Isolated and purified material from both reactions was further examined with ^{1}H-NMR and quantitative NMR (qNMR) to identify the compounds, to gain better insight into their structures and to determine the purity of isolated compounds. Assignment of the signals of the NMR spectra was made in collaboration with Dr. Josef Zapp (Department of Pharmaceutical Biology, Saarland University) and by comparison with previously performed NMR experiments of our group for Q_{10}/HO-Q_{10}[16] and mQ/HO-mQ[149]. These results clearly showed the change of the substituents at the quinone ring and confirmed the insertion of a hydroxyl group.

Figure 4-10 b and Figure 4-11 b show the respective ^{1}H NMR spectra of Q_1 and dUQ and their hydroxylated forms, HO-Q_1 and HO-dUQ, correspondingly, whose resonances extended from about 1.00 to 7.00 ppm. Panels c-h show the individual regions of ^{1}H signals. The resonance at 7.26 ppm, present in all four spectra, was a residual peak of CHCl$_3$ in the solvent CDCl$_3$ and was used for calibration of the chemical shift.

The NMR spectrum of native Q_1 (Figure 4-10 panels b-h, black line) showed resonances at δ 1.67 and 1.74 ppm (panel h) from the protons of methyl (−CH$_3$) groups at the end of the sidechain (position 10 and 11, Figure 4-10 a, left structure), δ 2.02 ppm (panel e) was assigned to the protons of −CH$_3$ group at ring position 5, peaks at δ 3.98 and δ 3.996 ppm (panel c) to methoxy (−OCH$_3$) groups at position 2 and 3, the signals around δ 3.17 ppm (panel f) to the protons of the

first methylene (−CH₂−) group of the sidechain (position 7) and signal at δ 4.93 ppm (panel g) corresponded to the vinyl proton at position 8 (−CH=).
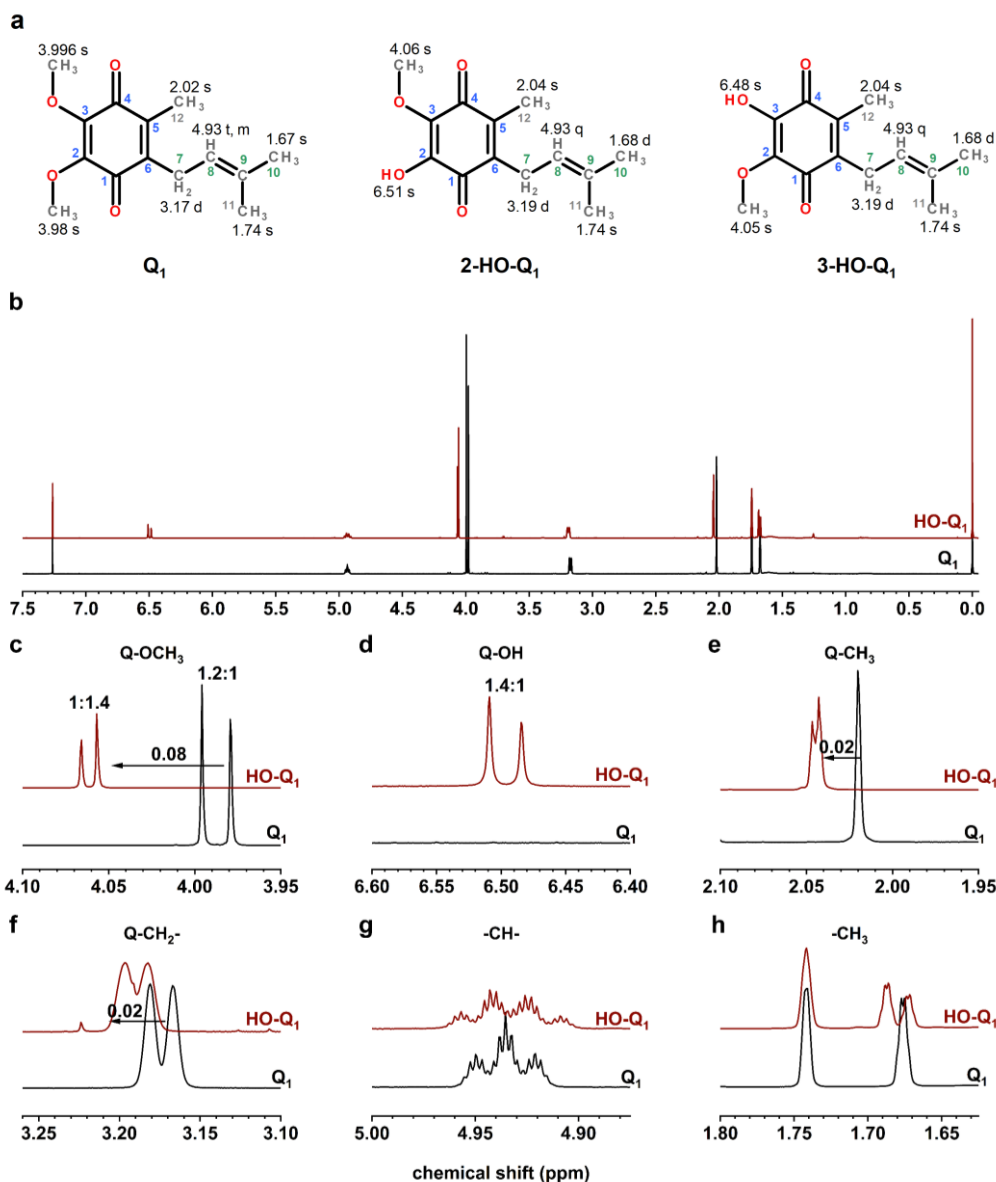
Figure 4-10 ¹H-NMR spectra of Q₁ and isolated product HO-Q₁. a) Structure and ¹H-NMR signal assignment of the native Q₁ (left structure) and the two isomers of the product with −OH group at position 2 (middle structure) and −OH group at position 3 (right structure); multiplicity: s, singlet; d, duplet; t, triplet and m, multiplet. b) Comparison of the spectra between Q₁ (black) and HO-Q₁ (red). Individual regions of ¹H signals of c) methoxy groups (−OCH₃) at position 2 and 3; d) hydroxyl group (−OH) attached to the ring Q at position 2 or 3; e) methyl group (−CH₃) attached to Q at position 5; f) first methyl group (−CH₂−) of the side chain at position 7; g) vinyl group (−CH=) of the side chain at position 8; and h) −CH₃ groups of the side chain at position 10 and 11. Arrows in c, e and f indicate the shift of the signals in the product; ratio of the signal integrals is specified in c and d; Q stands for quinone ring.

From Figure 4-10 b it is noticeable that the signal patterns of Q₁ (black line) and the hydroxylated product (red line) were similar in shape, intensity, and position. However, the resonance signals at δ 3.98 ppm and δ 3.996 ppm (black trace, panels b and c), corresponding to the −OCH₃ groups at position 2 and 3 (left structure, Figure 4-10 a) were smaller and shifted by 0.08 ppm downfield in the spectrum of HO-Q₁ (red line, panels b and c in Figure 4-10) indicating the presence of an electronegative atom in the structure. Additionally, two new signals at δ 6.51 and δ 6.48 ppm in the NMR spectrum of HO-Q₁ (red line, Figure 4-10 b and d) corresponded to the proton of hydroxyl groups with a typical downfield position. Both peaks also integrated to one proton (Table 4-1) supporting this assignment. Additionally, a smaller shift of 0.02 ppm was detected for the

protons in direct vicinity to the aromatic ring (Figure 4-10 panel e, −CH$_3$ group at position 5, and panel f, first −CH$_2$− of the sidechain at ring position 6). On the other hand, the proton signals obtained from the isoprene chain were not shifted but changed their apparent multiplicity or line width (panel g, −CH= group at position 8, and panel h, −CH$_3$ groups of the sidechain at position 10 and 11). Therefore, the new product contained an intact sidechain and it was chemically modified only at the positions of the methoxy groups.

Integration of the signals (Table 4-1) showed that total proton count was only changed for the signals arising from the protons of −OCH$_3$ groups, while the total proton count of the other signals was not changed, which indicated the replacement of one −OCH$_3$ group from Q$_1$ with one hydroxyl group in the structure of the new product. The two shifted signals of −OCH$_3$ groups in the product (red line, Figure 4-10 c) showed a peak intensity ratio of 1:1.4, whereas the new signals arising from the proton of the hydroxyl group had a ratio of 1.4:1 (red line, Figure 4-10 d). Therefore, the analysis of the ^{1}H-NMR data suggested that the purified product contained two molecules (isomers) that were hydroxylated either at position 2 or 3 of the quinone ring (middle and right structure, Figure 4-10 a). This observation was consistent with the NMR data of the mono-hydroxylated product of Q$_{10}$ (HO-Q$_{10}$)[16] and the mono-hydroxylated product of mitoQ (HO-mQ)[149]. A detailed comparison of the chemical shifts, relative line intensities and proton counts of HO-Q$_{10}$ for protons in the vicinity of the quinone ring with those of HO-Q$_1$ revealed nearly identical behaviour and parameters. This finding justified to transfer the assignment of 2-HO-Q$_{10}$ and 3-HO-Q$_{10}$ signals, which were based on ^{1}H and ^{13}C heteronuclear 2-D NMR, to define and separate the 2-HO-Q$_1$ and 3-HO-Q$_1$ isomer signals. The assignment to OH-Q$_1$ isomers, their chemical shifts, multiplicities, coupling constants and integration of the signals are compiled in Table 4-1 together with values for native Q$_1$.

Table 4-1 ^{1}H-NMR signal assignments, chemical shifts, and proton count for Q$_1$ and HO-Q$_1$. For atom numbering (position) see Figure 4-10 a; multiplicity: *s*, singlet; *d*, doublet; *t*, triplet; and *m*, multiplet; coupling constant (*J*) is given in Hz. Proton (H) count is obtained in *TopSpin* by integration of each signal from the NMR spectrum (Figure 4-10 b).

position	Q$_1$ δ (ppm)	Q$_1$ H count	2-HO-Q$_1$ δ (ppm)	2-HO-Q$_1$ H count	3-HO-Q$_1$ δ (ppm)	3-HO-Q$_1$ H count
2-OCH$_3$	3.98 *s*	2.9184	-	-	4.05 *s*	2.9933
2-OH	-	-	6.51 *s*	1	-	-
3-OCH$_3$	3.996 *s*	2.8941	4.06 *s*	2.9933	-	-
3-OH	-	-	-	-	6.48 *s*	1
7	3.17 *d* (7 Hz)	2.0078	3.19 *d* (7 Hz)	1.9928	3.19 *d* (7 Hz)	1.9928
8	4.93 *t, m* (7 Hz)	1	4.93 *q***	1.0030	4.93 *q***	1.0030
10	1.67 *s*	3.1079	1.68 *d***	3.1245	1.68 *d***	3.1245
11	1.74 *s*	3.0439	1.74 *s*	3.0955	1.74 *s*	3.0955
12	2.02 *s*	3.0030	2.04 *s***	2.9987	2.04 *s***	2.9987

* Apparent quartet and doublet caused by the two isomers hydroxylated at position 2 or 3.

Because of the excellent resolution, particularly of the isoprenoid protons, of Q$_1$ and HO-Q$_1$ compared to dUQ (Figure 4-11 panels b and g) and Q$_{10}$[16], an apparent change of the multiplicity of signals of protons at position 8 (vinyl proton, Figure 4-10 g) and position 10 (methyl protons,

Figure 4-10 h) could be observed, while the proton count remained constant (Table 4-1). This could be explained by the presence of two isomers, 2-HO-Q_1 and 3-HO-Q_1, with a slightly different electronic distribution (and therefore shifts) in the structurally asymmetric Q_1-molecule. Consequently, protons at position 8 gave an apparent quartet (Figure 4-10 g) from two superimposing triplets and the singlet methyl-resonance of position 10 changed to two signals (Figure 4-10 h). Moreover, the appearance of two barely resolved resonances of the −CH_3 group bound to the ring (protons at position 12, Figure 4-10 e) was in line with two isomers.
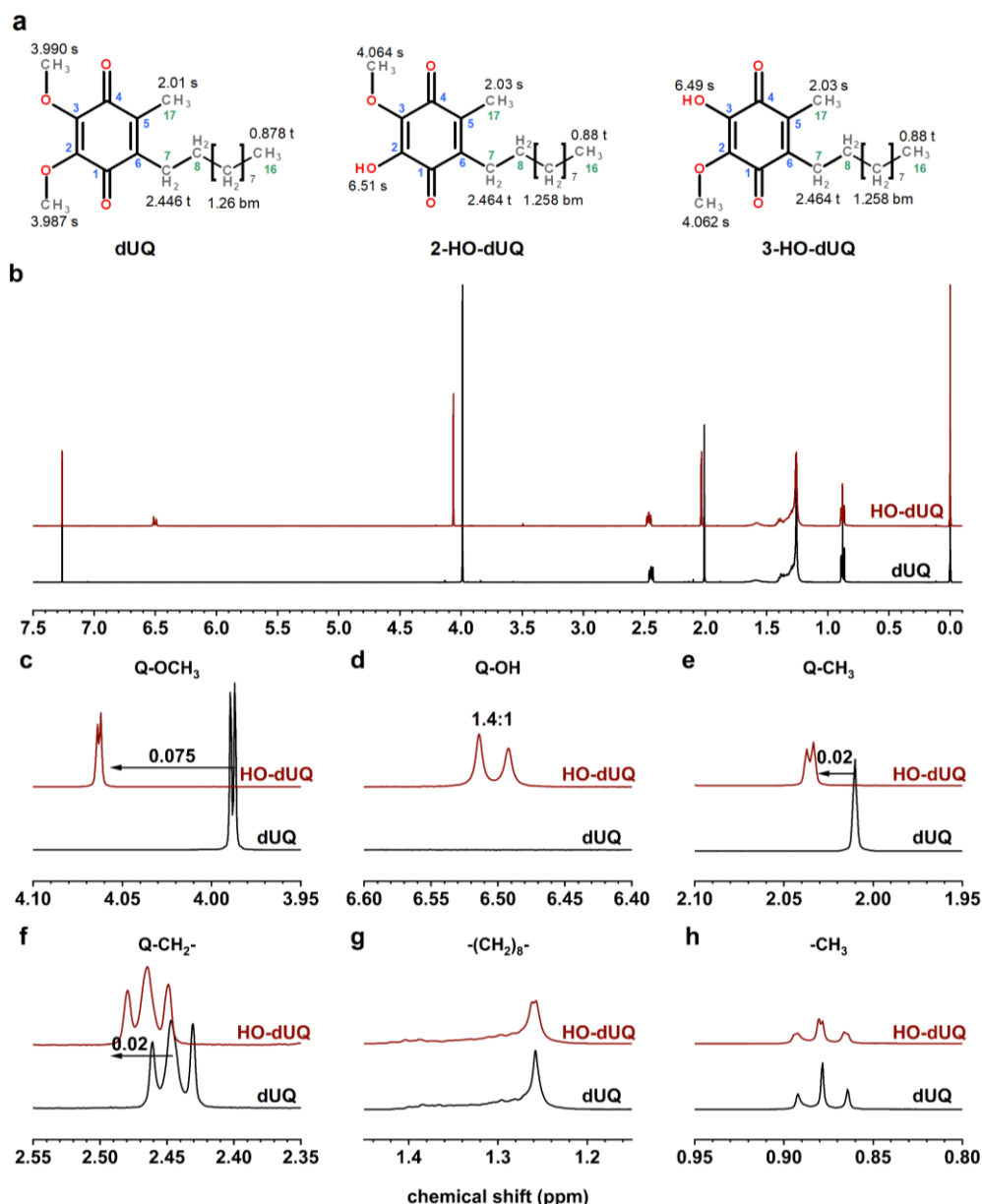
Figure 4-11 ^{1}H-NMR spectra of dUQ and isolated product HO-dUQ. a) Structure and ^{1}H-NMR signal assignment of the native dUQ (left structure) and the two isomers of the product with −OH group at position 2 (middle structure) and −OH group at position 3 (right structure); b) Comparison of the spectra between dUQ (black) and HO-dUQ (red). Individual regions of ^{1}H signals of c) methoxy groups (−OCH_3) at position 2 and 3; d) hydroxyl group (−OH) attached to the ring Q at position 2 or 3; e) methyl group (−CH_3) attached to Q at position 5; f) first methyl group (−CH_2−) of the side chain at position 7; g) −CH_2− groups of the sidechain position 8-15; and h) −CH_3 of the sidechain at position 16. Arrows in c, e and f indicate the shift of the signals in the product; ratio of the signal integrals is specified in d. Meaning of the symbols in panel a is same as in Figure 4-10.

The ^{1}H-NMR spectrum of dUQ (Figure 4-11 panels b-h, black line) showed resonances around δ 0.88 ppm (panel h) from the protons of −CH_3 group at the end of the sidechain (position 16, Figure 4-11 a, left structure), at δ 1.26 ppm (panel g) a broad multiplet signal from the protons of the

decyl-sidechain ($-(CH_2)_8-$), at δ 2.01 ppm (panel e) from the protons of $-CH_3$ at ring position 5, at δ 3.987 and 3.990 ppm (panel c) from the $-OCH_3$ groups at ring position 2 and 3 (left structure, panel a) and signals around δ 2.45 ppm (panel f) from the protons of the first $-CH_2-$ group of the sidechain (position 7, left structure in panel a).

It is evident from Figure 4-11 b and Table 4-2, that very similar ^{1}H-NMR signal patterns to those of Q_1/HO-Q_1 (Figure 4-10 and Table 4-1) were recorded for dUQ and its hydroxylated derivative HO-dUQ. As a dominant feature, HO-dUQ showed a comparable chemical shift (0.075 ppm) of the less well resolved peaks of the $-OCH_3$ group protons (Figure 4-11 c) and the same chemical shift (0.02 ppm) of the protons associated with the quinone ring (Figure 4-11 panel e, $-CH_3$ at ring position 5 and panel f, first $-CH_2-$ group of the sidechain at position 7). Additionally, the total proton count of methoxy groups resonance in the product decreased from 6 to 3 protons (Table 4-2), while the proton count of the other signals remained unchanged. Similar to HO-Q_1, the hydroxyl protons in HO-dUQ were well resolved at δ 6.51 and δ 6.49 ppm (red line, Figure 4-11 d) with a ratio of 1.4:1 for the two isomers of mono-hydroxylated dUQ at position 2 or 3 (Figure 4-11 a, middle and right structure) and total proton count of 1 (Table 4-2).

Referring again to the 2D-heteronuclear NMR of Q_{10}/OH-Q_{10}[16], the assignment of resonances to both isomers 2-HO-dUQ and 3-HO-dUQ was feasible (Table 4-2). In analogy to Q_1/HO-Q_1, the proton signals obtained from the isoprene chain in both native dUQ and HO-dUQ (Figure 4-11 g, $-(CH_2)_8-$ chain, and h, $-CH_3$ group at the end, position 16 of the sidechain) were only slightly affected and showed small splitting compatible with two isomers. ^{1}H-NMR of the native dUQ and the product, HO-dUQ, gave clear evidence for a hydroxylation at position 2 and 3 of the quinone ring and loss of one $-OCH_3$ group.

Table 4-2 ^{1}H-NMR signal assignments, chemical shifts, and proton count for dUQ and HO-dUQ. For atom numbering (position) see Figure 4-11 a; multiplicity: *s*, singlet; *d*, doublet; *t*, triplet; and *m*, multiplet; b, broad signal; coupling constant (*J*) is given in Hz. Proton count is gained by integration of each signal from the spectrum (Figure 4-11 b).

	dUQ		2-HO-dUQ		3-HO-dUQ	
position	δ (ppm)	H count	δ (ppm)	H count	δ (ppm)	H count
2-OCH₃	3.987 *s*	3	-	-	4.062 *s*	2.9812
2-OH	-	-	6.51 *s*	1	-	-
3-OCH₃	3.990 *s*	3	4.064 *s*	2.9812	-	-
3-OH	-	-	-	-	6.49 *s*	1
7	2.446 *t* (7 Hz)	1.9915	2.464 *t* (7 Hz)	2.0223	2.464 *t* (7 Hz)	2.0223
8-15	1.26 b*m**	16.3690	1.258 b*m**	16.2816	1.258 b*m**	16.2816
16	0.878 *t* (7 Hz)	3.0722	0.88 *t*** (7 Hz)	3.2159	0.88 *t*** (7 Hz)	3.2159
17	2.01 *s*	3.0079	2.03 *s***	3.0162	2.03 *s***	3.0162

* broad signal expanding from 1.4 ppm to given value; ** small splitting due to isomers.

The characteristic intensity ratios of the methoxy and hydroxyl protons of HO-Q_1 and HO-dUQ allowed to estimate the relative portion of isomers in the isolated product. Signal integration of the well separated hydroxyl peaks yields in both cases 58% for the 2-HO- and 42% for the 3-HO-isomer. This result is again like the ratios found in HO-Q_{10} (64% vs. 36%)[16].

In the final step, the purities of the isolated products, HO-Q_1 and HO-dUQ were determined by quantitative NMR using as a reference the first −CH_2− group of the sidechain at position 7 (at δ 3.19 ppm for HO-Q_1, Figure 4-10 a; at δ 2.46 ppm for HO-dUQ, Figure 4-11 a). Calculated purities were 89% for HO-Q_1 and 81% for the HO-dUQ.

4.2 Electrochemical studies on coenzyme Q_1, decylubiquinone, and their mono-hydroxylated derivatives HO-Q_1 and HO-dUQ

The studies of the redox chemistry of quinones (Qs) have spanned over seven decades, revealing a depth of complexity that continues to intrigue researchers to this day. Despite initially being perceived as exhibiting straightforward redox behaviour, Qs have proven to engage in intricate electrochemical processes with multiple pathways for their reactions to progress. Through extensive investigation, particularly on the voltammetric features of Qs, it has become evident that the electrochemical behaviour of Qs is significantly influenced by surrounding solvent medium, the presence of protons in the system, pH of the solution as well as the formation of inter- and intramolecular hydrogen bonds and ion pairs[230]. In general, the reduction of Qs always entails the transfer of two electrons which can occur sequentially, one after the other, or simultaneously in a single step depending on the environment. The most straightforward redox mechanism for Qs is observed in organic aprotic solvents (Figure 4-12, red coloured top horizontal reaction). In this scenario, Qs undergo a two-step process involving one-electron reduction in each step, leading to the formation of a quinone dianion (Q^{2-}). During the first step, the Q undergoes reduction to generate the semiquinone radical anion ($Q^{\bullet-}$). Subsequently, with the second electron transfer the $Q^{\bullet-}$ is further reduced yielding the Q^{2-}. These two consecutive electron transfers are well-separated and clearly defined because adding an extra electron to already negatively charged molecules ($Q^{\bullet-}$) requires a substantial amount of potential energy to overcome the energy barrier caused by the electrostatic repulsion between charges.

In aqueous buffered solutions (Figure 4-12, diagonal blue coloured reaction), the reduction of Qs is characterized as a unified two-electron, two-proton ($2e^-/2H^+$) process leading to the formation of hydroquinone (quinol, QH_2). While the theoretical mechanism of this reaction encompasses two distinct, independent one-electron transfers, each followed by a protonation step, experimental observations indicate that both electrons and protons are effectively transferred in a single kinetic step. This intriguing phenomenon is attributed to the protonation of the semiquinone radical anion. The creation of a neutral radical species ($QH^{\bullet}$) results in an immediate and simultaneous transfer of both electrons. This is due to the fact that $QH^{\bullet}$ is more readily reducible compared to the Qs with the potential of the second reduction being more positive than that of the first ($E_{QH^{\bullet}/QH_2} > E_{Q/QH^{\bullet}}$)[230]. The most comprehensive description of the reaction pathways in aqueous environments, where protonation occurs rapidly and remains at equilibrium, is provided by the nine-membered square scheme (Figure 4-12) proposed by Jacq[231]. This scheme elucidates that in aqueous media Qs may undergo either one-electron or two-electron transfer (ET) steps, which could be accompanied by up to two proton transfer (PT) reactions. Electron transfer (ET) processes are typically coupled to the transfer of positively charged entities

such as protons or metal ions to prevent formation of unstable states. The ET that is linked to a transfer of proton is termed proton-coupled electron transfer (PCET)[232]. Analogously to the PCET, the term metal ion-coupled electron transfer (MCET)[233] has been used when ET is coupled to the transfer of redox-inactive metal ions.
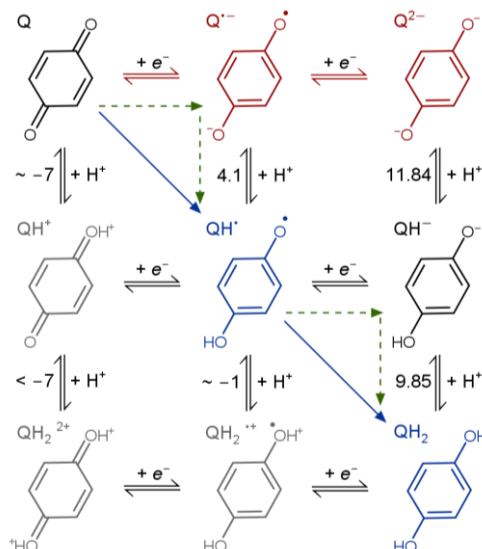
Figure 4-12 Nine-membered square scheme for redox reactions of quinones showing the electron transfer (ET) processes (horizontal arrows), proton transfer (PT) processes (vertical arrows), proton (H+) dependent stepwise (green dashed line), H+-independent stepwise (red arrows) and concerted (blue line) PCET pathways. At neutral pH, redox species QH+, QH$_2$$^{2+}$ and QH$_2$$^{•+}$ (grey structures) do not exist in cationic form but rather in dissociated form. Numbers present known and estimated pK_a values[234] of the redox species. Scheme adapted from Quan *et al.*[235].

PCET is classified as either stepwise where the electron and proton are transferred one at a time separately, or concerted where electron and proton transfers occur simultaneously in a single step. In the scheme (Figure 4-12) the horizontal reactions correspond to electron transfer (ET) processes, whereas the vertical processes involve proton transfer (PT), and they represent the stepwise ET and PT, respectively. The diagonal blue arrow represents the concerted way of PCET. The specific pathway by which PCET proceeds, and consequently, the involvement of protons in the redox process depends on the specific pK_a values of the given hydroquinone as well as the pH of the solution. In acidic conditions, up to a pH approximately equal to the first pK_a value of the hydroquinone species (p$K_{a,1}$ (QH$_2$)), the reduction reaction involves two protons (2e$^-$/2H$^+$). As the pH increases beyond this range, when the p$K_{a,1}$(QH$_2$) < pH < p$K_{a,2}$(QH$^-$), the reaction transforms into a two-electron, one-proton (2e$^-$/1H$^+$) process. In highly alkaline environments where the pH surpasses the p$K_{a,2}$ value, pH > pK$_{a,2}$(QH$^-$), protons do not play a role in the redox reaction (2e$^-$/0H$^+$).

Since PCET reactions involve protons in the redox transformation, the equilibrium potential E of the redox reaction depends on the pH of the solution according to the *Nernst* equation:

$$E = E^{\theta'} - \frac{m}{n} \cdot 0.059 \cdot pH - \frac{0.059}{n} \cdot log \frac{[Red]}{[Ox]} \qquad \text{Eq. 4-1}$$

where $E^{\theta'}$ is the formal potential of the redox couple Ox/Red, n is the number of electrons and m the number of protons involved in the overall redox reaction. From the *Nernst* equation follows that the observed redox potential E for a 2e$^-$/2H$^+$ reduction of the Qs at room temperature, will be shifted by 59 mV per pH unit[236].

Analogously to the PCET processes, in MCET, where redox-inactive metal ions influence the ET, binding of the metal ion brings about a positive shift in the potential, *E*:

$$E = \frac{x}{n} \cdot 0.059 \cdot log[M^{z+}] + const.$$ Eq. 4-2

where *n* is the number of electrons, *x* the number of metal ions, *z* the charge of the metal and *M* the symbol for the metal ion.

A linear dependence is generally found when the potential is plotted over pH or the logarithm of the concentration of metal cations. The associated *Nernst* factor reflects the number of protons or cations transferred per electron and is close to 60 mV for a 1:1 ratio (30 mV for 1:2 ratio).

4.2.1 Electrochemistry of Q_1, dUQ, HO-Q_1 and HO-dUQ in different media

Cyclic and square-wave voltammetry were applied to study the redox behaviour, pH dependence and Ca^{2+} binding properties of the four compounds, native Q_1 and dUQ as well as their purified hydroxylated derivatives, HO-Q_1 and HO-dUQ. Compounds Q_1/OH-Q_1 were examined in all types of solvents, whereas dUQ/OH-dUQ could be best studied in organic protic and aprotic solvents.

4.2.1.1 Buffered aqueous media

In HEPES buffer with pH 7.4 (Figure 4-13), Q_1 exhibited one pair of well-defined peaks (I_c and I_a) with a midpoint peak potential, $E_{p,mid}$ of −0.094 V (vs. Ag/AgCl) in the cyclic voltammogram (CV) (panel a) and one sharp and well-defined peak with net peak potential $E_{p,net}$ of −0.177 V (vs. Ag/AgCl) in the square-wave voltammogram (SWV) (panel b).
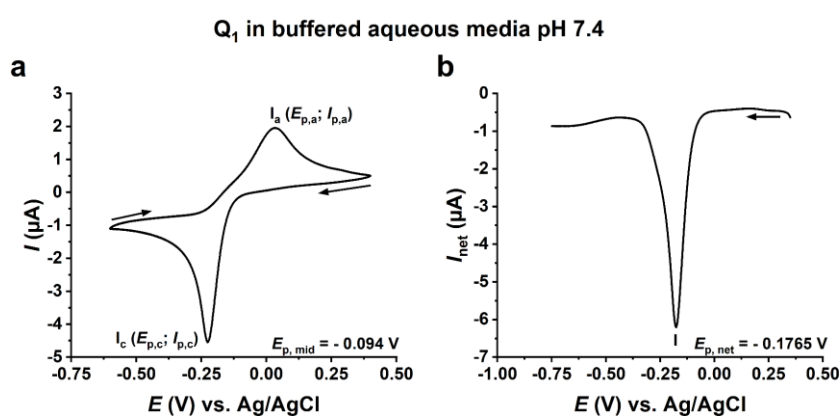
Figure 4-13 Redox reaction of Q_1 in buffered aqueous media at pH 7.4. a) Cyclic voltammogram of 0.5 mM Q_1 in HEPES buffer (pH = 7.4). Redox process of Q_1 exhibited one pair of well-defined peaks, I_a and I_c, corresponding to oxidation and reduction reaction, respectively. $E_{p,a}$, anodic peak potential; $I_{p,a}$, anodic peak current; $E_{p,c}$, cathodic peak potential; $I_{p,c}$, cathodic peak current; $E_{p,mid}$, mid-peak potential; arrows indicate the direction of the potential variation. Conditions: v = 20 mV/s, ΔE = 1 mV. b) Square-wave voltammogram of 0.5 mM Q_1 in HEPES buffer (pH = 7.4). $E_{p,net}$, net peak potential. Arrow indicates direction of the potential variation. Conditions: f = 8 Hz, E_{sw} = 25 mV, ΔE = 1 mV.

The large peak-to-peak separation, $\Delta E_p = E_{p,a} - E_{p,c}$ = 288 mV and the ratio of the anodic and cathodic peak currents, $I_{p,a}/I_{p,c}$ = 0.53 in CV (Table A - 1 in Appendix A), indicated a behaviour different from that of a reversible process where ΔE_p = 60 mV and $I_{p,a}/I_{p,c}$ = 1. To assess the mechanism of the redox reaction of Q_1 at glassy carbon (GC) electrode in HEPES buffer at pH 7.4, scan rate (*v*) studies were performed. In Figure 4-14 the effect of *v* on the voltammetric response of Q_1 is shown. The difference of the peak potentials (peak-to-peak separation, ΔE_p) was significantly bigger than 59 mV and the separation of the two signals increased at faster scan rates (panel b). The $E_{p,a}$ were shifted to more positive values with increasing *v*, while the $E_{p,c}$ were shifted in the opposite direction (panels a and b). The ΔE_p in CVs (panels a and b) of more than

200 mV as well as the $I_{p,a}/I_{p,c} \neq 1$ over the whole scan range (panel c) indicated that the redox process of Q_1 in neutral buffered media exhibits some kinetic hindrances, i.e., slow electron transfer step limits the reaction rate. Therefore, the redox reaction of Q_1 at GC electrode in buffered solution at pH 7.4 was characterized as a quasi-reversible process. Anodic ($I_{p,a}$) and cathodic ($I_{p,c}$) peak currents increased with an increase in the v and gave a good linear dependence of the I_p over the square root of the applied scan rates, consistent with a diffusion-controlled processes (panel c). The slope (panel c) allowed to estimate the diffusion coefficient (D) of Q_1 molecules with the *Randles−Ševčík* equation (Eq. 3-25). The voltammetric peaks during the forward scan (negative polarization) were used to calculate the diffusion coefficient as $D = 6.449 \cdot 10^{-6}$ cm^2/s.
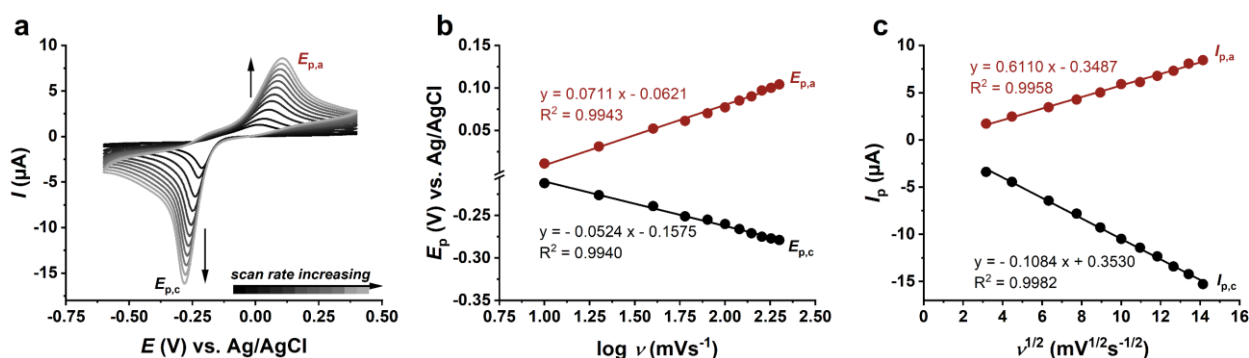
Figure 4-14 Scan rate analysis of Q_1 redox behaviour in buffered aqueous solution at pH 7.4. a) Effect of different scan rates (v) to the features of cyclic voltammograms of 0.5 mM Q_1 in HEPES buffer (pH 7.4) at glassy carbon electrode. Anodic ($I_{p,a}$) and cathodic ($I_{p,c}$) peak currents and the peak-to-peak separation, ΔE_p increased with an increase in the v. b) Variations of the anodic ($E_{p,a}$) and cathodic ($E_{p,c}$) peak potentials vs. logarithm of v. c) Dependence of the peak currents, $I_{p,a}$ and $I_{p,c}$, on the square root of v.

Cyclic (CVs) and square-wave (SWVs) voltammograms of 0.5 mM Q_1 were recorded in buffered media with pH ranging from 1 to 11 (Figure 4-15). Reduction of Q_1 in aqueous solution consumes protons so that the position of the $E_{p,mid}$ in CV (Figure 4-15 a) and $E_{p,net}$ in SWV (Figure 4-15 b) for Q_1 were sensitive to pH changes. As predicted by the *Nernst* equation (Eq. 4-1), with increasing the pH (decrease in proton concentration) of the solution the $E_{p,a}$ and $E_{p,c}$ (panel a), consequently $E_{p,mid}$, for the redox reaction of Q_1 were shifted to more negative values. The pH dependence of the net peak potential, $E_{p,net}$ is shown in Figure 4-15 b and indicates two different slope segments. In the pH interval 1 to 6 the $E_{p,net}$ of the redox reaction were shifted by 58 mV per pH unit, while in the pH range from 8 to 11 $E_{p,net}$ were shifted by 28 mV/pH. Knowing that $2e^-$ are always required for the reduction of the quinones (Figure 4-12), the reduction of Q_1 in the pH region 1-7 where the slope is 58 mV/pH is described as $2e^-/2H^+$ process to generate the hydroquinone Q_1H_2. In the pH range 8-11 where the slope is 28 mV/pH the reaction proceeds with two electrons and one proton ($2e^-/1H^+$) reaction pathway, generating Q_1H^-. Additionally, these results implied that $pK_{a,1}(QH_2)$ has a value lower than 8, while the $pK_{a,2}$ for (QH^-) has a value bigger than 11. When the pH surpasses the $pK_{a,2}$ value, Q^{2-} becomes the thermodynamically favoured product. In this pH range, a slope of 0 mV/pH is expected, indicating a change in the reduction mechanism that is independent of the presence of protons, involving only two electrons $2e^-/0H^+$. The dependence of the peak potentials on the pH in the studied pH region (1-11) was not lost, i.e., a slope of 0 mV/pH was not observed, indicating participation of

protons in the overall reduction of Q_1. Unfortunately, solutions with pH higher than 11 could not be applied due to the instability of Q_1 in strong alkaline media, which resulted in substitution of a methoxy group with a hydroxyl group as shown previously. The estimated values for the pK_a were comparable to reported values for some *p*-benzoquinones[234].
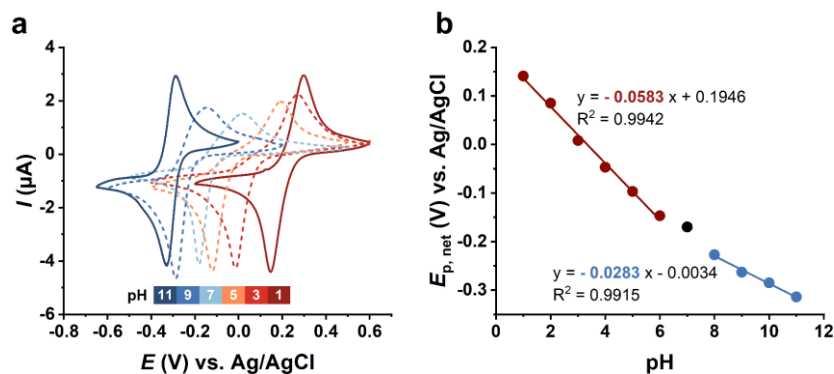
Figure 4-15 pH dependence of the voltammetric response of Q_1 in buffered solutions with different pHs. a) Cyclic voltammograms of 0.5 mM Q_1 recorded in 0.1 M buffer solutions with pH ranging from 1 -11. Anodic and cathodic peak potentials were shifted to more negative potentials with increase in pH. Conditions: v = 20 mV/s, ΔE = 1 mV. b) pH dependence of the net peak potentials ($E_{p,net}$) of 0.5 mM Q_1 which showed two different slope regions, 58 mV in pH range 1-6 (red) and 28 mV in pH range 8-11 (blue) recorded by square-wave voltammetry. Conditions: f = 8 Hz, E_{sw} = 25 mV and ΔE = 1 mV. The chemical composition of the buffers is given in Table 2-4.

In summary, the redox transformation of Q_1 in buffered aqueous solution at pH 7.4 is a one-step reaction involving $2e^-$ and $2H^+$, giving hydroquinone (Q_1H_2) as final product.

Analysing the mono-hydroxylated Q_1 (HO-Q_1), a single redox process was observed in the CV and SWV in buffered aqueous solution (HEPES buffer) at pH 7.4 (red traces, Figure 4-16). Redox transformation of HO-Q_1 exhibited well-defined reversible-like pair of peaks (I_a and I_c) in CV (red trace, panel a) with $E_{p,mid}$ = −0.23 V and one sharp and well-defined peak in SWV (red trace, panel b) with $E_{p,net}$ = −0.272 V.
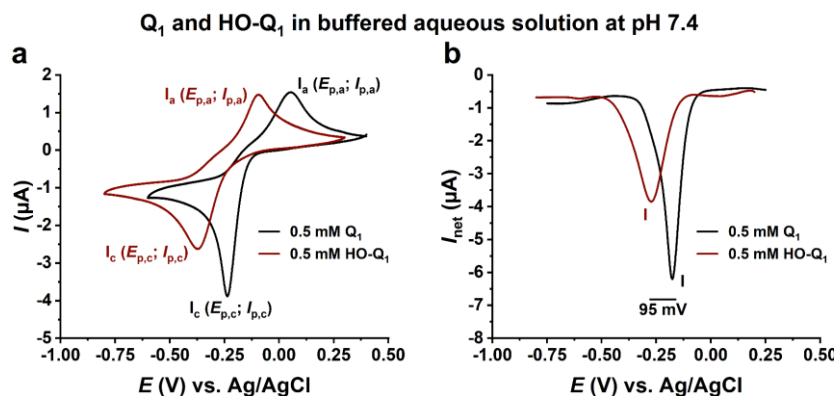
Figure 4-16 Comparison of voltammetric responses of Q_1 and HO-Q_1 in buffered aqueous solution at pH 7.4. a) Cyclic voltammograms and b) square-wave voltammograms of 0.5 mM Q_1 (black) and 0.5 mM HO-Q_1 (red) in 0.1 M HEPES buffer (pH 7.4). $E_{p,a}$ and $I_{p,a}$, anodic peak potential and current, respectively; $E_{p,c}$, and $I_{p,c}$, cathodic peak potential and current, correspondingly.

The observed peak potentials for HO-Q_1, $E_{p,mid}$ and $E_{p,net}$, were ~90 mV more negative compared to that of native Q_1, and indicated that the reduced form of HO-Q_1 is a stronger antioxidant than Q_1. Moreover, the peak-to-peak separation for HO-Q_1, albeit still large (ΔE_p = 270 mV), was lower than the ΔE_p observed for Q_1 (Table A - 1). The $I_{p,a}/I_{p,c}$ ratio of HO-Q_1 was calculated to be 0.94 (Table A - 1), a value close to that for a reversible process. These parameters indicated that the redox transformation of HO-Q_1 shows better reversibility than the redox process of Q_1.

To get more insight into the kinetics of the electrode reaction of HO-Q_1 in neutral buffered solutions, the effects of scan rate (v) variations on peak potentials and currents were studied. Figure 4-17 panel a shows CVs of a 0.5 mM HO-Q_1 in 0.1 M HEPES solution (pH 7.4) at scan rates between 10 and 200 mV/s. With increasing scan rates, the anodic peak potentials ($E_{p,a}$) were shifted to more positive and the cathodic peak potentials ($E_{p,c}$) to more negative values, resulting in an expansion of the peak-to-peak separation. The cathodic-to-anodic peak separation increased exponentially with faster v (panel b) indicating that the redox process of HO-Q_1 in neutral buffered media exhibits some kinetic barriers, which are linked to a slow electron transfer step. Consequently, the redox reaction of HO-Q_1 at GC electrode in buffered solution at pH 7.4 is characterized as quasi-reversible reaction, a similar finding as for native Q_1. Moreover, the redox transformation of HO-Q_1 is a diffusion-controlled process as demonstrated by the linear dependence of the peak currents of both cathodic and anodic peaks on the square root of the applied scan rates (panel c). Using the fitted slopes (panel c) and the *Randles−Ševčík* equation (Eq. 3-25), the diffusion coefficient of HO-Q_1 molecules could be estimated as $D = 3.287 \cdot 10^{-6}$ cm^2/s, which is about half of the D value for the native Q_1.
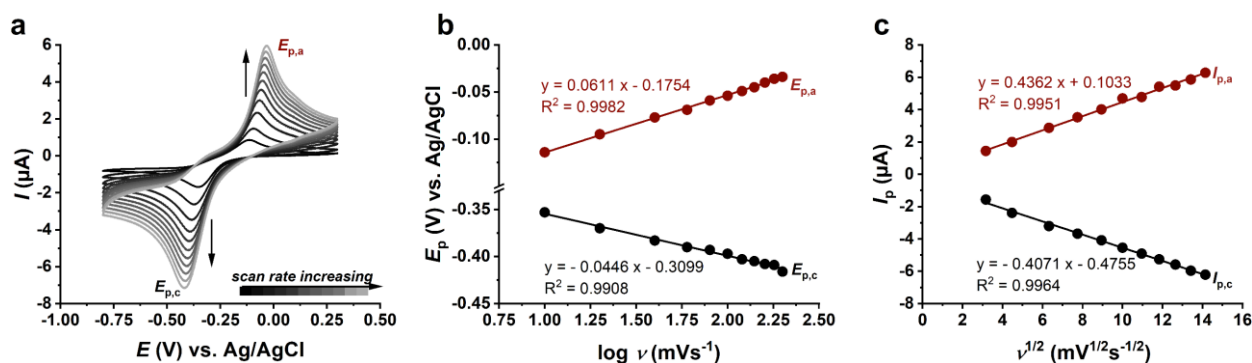
Figure 4-17 Scan rate analysis of HO-Q_1 redox behaviour in buffered aqueous solution at pH 7.4. a) Effects of different scan rates (v) on the features of cyclic voltammograms of 0.5 mM HO-Q_1 in 0.1 M HEPES buffer (pH 7.4) at glassy carbon electrode. Anodic ($I_{p,a}$) and cathodic ($I_{p,c}$) peak currents and the peak-to-peak separation increased with an increase in the v. b) Variations of the anodic ($E_{p,a}$) and cathodic ($E_{p,c}$) peak potentials vs. logarithm of the v. c) Dependence of the peak currents, $I_{p,a}$ and $I_{p,c}$, on the square root of v.

For a more detailed analysis of the redox reaction of HO-Q_1 in buffered aqueous media, a series of CV and SWV measurements in the pH range 1-11 were carried out and are shown in Figure 4-18. Similarly to the redox behaviour of Q_1, the voltammetric responses of HO-Q_1 were also sensitive to pH changes of the solution. With decreasing the pH (increase in proton concentration) of the solution, the anodic and cathodic peak potentials in the CVs (panel a) for the redox reaction of HO-Q_1, subsequently $E_{p,mid}$, were shifted to more positive potential values. The pH-dependence of the net peak potentials ($E_{p,net}$) in SWV showed three linear regions (panel b). The slope of 64 mV/pH in the pH range 3-7 (orange, panel b) implied that an equal number of electrons and protons are involved in the redox transformation of HO-Q_1. Since 2e^- are always involved in the redox reaction of quinones (Figure 4-12), the reduction of HO-Q_1 in the pH range 3-7 involved 2e^- and 2H$^+$. In the pH range 9-11 the slope was 35 mV/pH (blue, panel b) indicative for participation of 2e^- and 1H$^+$ in the reaction. Additionally, these data allowed estimation of the p$K_{a,1}$ and p$K_{a,2}$ values for the reduced HO-Q_1 (HO-Q_1H_2 and HO-Q_1H^-), indicating similar range as for Q_1. The observed slope of 94 mV/pH for HO-Q_1 in the lower pH range suggests that the reduction

of HO-Q$_1$ follows a mechanism involving 2e^-/3H$^+$ (red, panel b). Since the concentration of protons is exceptionally high in this pH range, it is plausible that a third proton is being consumed by the hydroxyl group located at the α-position (position 2- or 3-) on the quinone ring. However, for a final conclusion the pH dependence over smaller pH-intervals in this range should be studied. The theoretically calculated p$K_{a,3}$ value for the α-hydroxyl group present in HO-Q$_1$ was approximately 5.4[*], indicating that at physiological pH (7.4) most HO-Qs molecules (98%) exist in a deprotonated form ($^-$O-Qs). Although the precise values of pK_a could not be determined accurately from the experimental data, the estimated values for the pK_a were agreed with reported values for some *p*-benzoquinones[18,234] and α-hydroxylated *p*-benzoquinones[18].
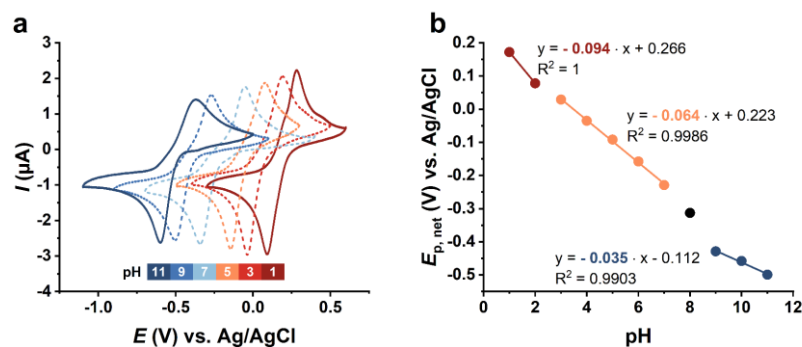
Figure 4-18 Voltammetric response of HO-Q$_1$ in buffered solutions with different pHs. a) Representative cyclic voltammograms of 0.5 mM HO-Q$_1$ recorded in 0.1 M buffer solutions with pH ranging from 1-11. Anodic and cathodic peak potentials were shifted to more negative potentials with increase in pH. Conditions: *v* = 20 mV/s, Δ*E* = 1 mV. b) pH dependence of the net peak potentials (*E*$_{p,net}$) in square-wave voltammograms of 0.5 mM HO-Q$_1$ which showed three different slope regions, 94 mV in pH range 1-2 (red), 64 mV in pH range 3-7 (orange) and 35 mV in pH range 8-11 (blue). SWV conditions: *f* = 8 Hz, *E*$_{sw}$ = 25 mV and Δ*E* = 1 mV. The chemical composition of the buffers is given in Table 2-4.

Summing up, the redox reaction of HO-Q$_1$ in buffered aqueous solution at pH 7.4 is a one-step reaction involving 2e^- and 2H$^+$, giving hydroquinone ($^-$O-Q$_1$H$_2$) as final product in which the hydroxyl group at position 2-(3-) on the quinone ring is deprotonated.

4.2.1.2 Unbuffered aqueous media

The electrochemical behaviour of Q$_1$ and HO-Q$_1$ in aqueous media was studied in 0.1 M HEPES buffer with pH 7.4 as a buffered and in 0.1 M KCl with the same pH as an unbuffered solution. One redox reversible-like wave is observed in the corresponding cyclic voltammograms for both, Q$_1$ and HO-Q$_1$, for buffered as well as unbuffered aqueous conditions (Figure 4-19). Presence of only one cathodic (reduction) peak in the CVs of both solutions indicated that regardless of the buffering capacity, reduction of Q$_1$ and HO-Q$_1$ in aqueous solutions (pH 7.4) always happens in one step. However, it is obvious that different redox chemistry occurred under unbuffered and buffered conditions. Figure 4-19 illustrates significant differences in the redox behaviour of Q$_1$ (panel a) and HO-Q$_1$ (panel b) in unbuffered (darker line) and buffered (lighter line) aqueous solution with identical pH. In unbuffered solution a single reversible looking redox process was observed for Q$_1$ with a midpoint peak potential, *E*$_{p,mid}$ = −0.244 V, significantly lower than in buffer, *E*$_{p,mid}$ = −0.094 V (panel a). Similarly, for the redox reaction of HO-Q$_1$ in unbuffered solution *E*$_{p,mid}$ = −0.416 V was observed, which was more negative than in buffered solution *E*$_{p,mid}$ = −0.230 V

---

[*] p$K_{a,3}$ values calculated with MarvinSketch: 2-HO-Q$_1$ p$K_{a,3}$ = 5.46 (98.20%, pH=7.4); 3-HO-Q$_1$ p$K_{a,3}$ = 5.48 (98.11%, pH=7.4)

(panel b). Compared to the unbuffered conditions, the $E_{p,mid}$ of the redox reactions of Q_1 and HO-Q_1 in buffered solutions were shifted to more positive values by about 150 mV and 186 mV, correspondingly. Additionally, there was also a large increase in the peak-to-peak separation ($\Delta E_p = E_{p,a} - E_{p,c}$) from 84 mV in unbuffered to 288 mV in buffered aqueous media for Q_1 and from 168 mV to 270 mV for HO-Q_1 (Table A - 1 and Table A - 2 in Appendix A). These changes are a clear indication that fundamentally different redox transformations of Q_1 and HO-Q_1 were happening under buffered and unbuffered conditions. The shift of the $E_{p,mid}$ to more positive values for the potential in buffered solution indicated that the reduction was thermodynamically easier in buffered media. However, the increase in peak-to-peak separation indicated that the overall reaction was kinetically much slower in buffered media than in unbuffered. Similar behaviour was found when phosphate buffer as a buffered and NaCl as an unbuffered solution were applied (data not shown), revealing that these effects were not attributable to the chemical composition of the solutions. Quan *et al.*[235] observed a similar behaviour for the redox reaction of 1,4-benzoquinone and 2-anthraquinone sulfonate as well as Gulaboski *et al.*[12] for the coenzyme Q_0, which implies that these effects are not unique for Q_1.
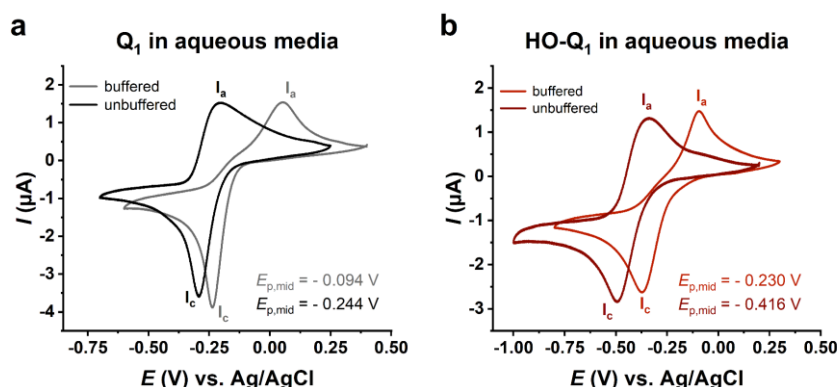
Figure 4-19 Voltammetric responses of Q_1 and HO-Q_1 in buffered and unbuffered aqueous solution at pH 7.4. Cyclic voltammograms of a) Q_1 and b) HO-Q_1 at pH = 7.4 in 0.1 M HEPES buffer as a buffered (lighter-coloured traces) and in 0.1 M KCl as an unbuffered aqueous solution (darker-coloured traces). CV parameters: v = 20 mV/s, ΔE = 1 mV.

Two electrons are always involved in the redox reaction of Qs, and the number of transferred electrons remained the same as evidenced by similar cathodic peak heights (I_c) under both conditions (Figure 4-19). Therefore, the fundamental difference in the overall redox reactions in buffered and unbuffered aqueous solutions arises from the protonation step and the state of the resulting reduced product. The change of the reduction mechanism of Q_1 and HO-Q_1 in unbuffered media is further supported by comparing their voltammetric curves obtained in unbuffered media with those recorded in buffered solutions at high pH of 11 (black trace, Figure 4-19 a and blue trace in Figure 4-15 a for Q_1; dark red trace in Figure 4-19 b and blue trace in Figure 4-18 a for HO-Q_1). The voltammetric responses under these conditions showed similarities in terms of improved reversibility and faster reaction rates. The analysis of the dependence of peak potentials on pH (Figure 4-15 b and Figure 4-18 b) revealed a shift of the mechanism from $2e^-/2H^+$ to $2e^-/1H^+$ with increasing pH of the buffers. This further supports the change of the mechanism of the redox behaviour of Q_1 and HO-Q_1 observed in unbuffered media with those recorded in buffered solutions. In line with this, Quan *et al.*[235] have reported similar behaviour for the redox reaction of some *p*-benzoquinones. Additionally, in-depth electrochemical study by

Gulaboski *et al.*[12] revealed much more complex transformations of Q_0 under unbuffered conditions across a wide pH range. Both studies[12,235] suggested that the redox transformation of the *p*-BQ in unbuffered media is influenced by the pH of the solutions, pK_a values of the *p*-BQ and the ratio of the concentrations of the quinones ([*p*-BQ]) and protons ([H^+]). According to these studies, in an unbuffered medium where the [H^+] >> [Q] (strong acidic pH) the redox reaction proceeds by $2e^-/2H^+$ ECEC (E, electron transfer step; C, chemical (protonation) step) mechanism. When the [Q] approaches or exceeds the [H^+], redox transformation of the *p*-BQ proceeds via EECC mechanism. Hence, the redox reaction of quinones in media where the [Q] ≥ [H^+] (unbuffered aqueous solutions with pH ≥ 7 or organic protic solvents) is a two-electron reduction resulting in an equilibrium mixture of reduced species. This mixture includes monoanionic (QH^-) and dianionic (Q^{2-}) species as major products, and hydroquinone QH_2 as a minor product, where QH^- and Q^{2-} are stabilized by hydrogen bonding with solvent molecules[12,235]. Based on the above, the primary reduced products of the Q_1 reduction in unbuffered aqueous media must be either anion (Q_1H^-) or dianion (Q_1^{2-}), and the Q_1H_2 is most likely a minor product. Due to the presence of the α-hydroxyl group in HO-Q_1, the products of its reduction under unbuffered conditions would exist in a mixture of at least four reduced species: hydroquinone (HO-Q_1H_2) and anions as monoanion (HO-Q_1H^-/$^-$O-Q_1H_2), dianion (HO-Q_1^{2-}/$^-$O-Q_1H^-) or trianion ($^-$O-Q_1^{2-}). Nonetheless, since the composition of this mixture depends on the [Q], acid-base properties (pK_a) of the reduced species and the pH around the electrode, theoretical calculations are needed to predict the exact distribution of the species.

4.2.1.3 Non-aqueous protic media

In the next step, the aqueous phase was replaced with non-aqueous (organic) protic solvents (methanol, ethanol, 2-propanol) which are weaker acids than water with higher pK_a-values (>15.5)[237,238], meaning that proton dissociation is much less pronounced, but hydrogen bonding is still possible. Alcohols are polar organic solvents that engage in hydrogen bonding due to the presence of the −OH functional group. The strength of hydrogen bonding depends on the polarity of the alcohols, their pK_a values as well as that of the hydrogen bond acceptors. Moreover, alcohols exhibit characteristics of weak acids and therefore could also dissociate depending on their pK_a. Table 4-3 provides the pK_a values for the alcohols used in this study. Notably, alcohols featuring shorter aliphatic chains display more potent hydrogen bonding capabilities and exhibit higher acidity.

Table 4-3 pK_a values of water and different alcohols in water and DMSO.

Solvent	Structure	pK_a in water	pK_a in DMSO[239]
Water	H_2O	14	31.4
Methanol	CH_3OH	15.5[238]	29.0
Ethanol	CH_3CH_2OH	15.9[240]	29.8
2-Propanol	$(CH_3)_2CHOH$	17.1[240]	30.3

Figure 4-20 shows SWV of Q_1, dUQ and their corresponding hydroxylated forms, HO-Q_1 and HO-dUQ, recorded in organic protic solvent. As expected for a protic solvent, a single peak for the

reduction of Q_1 (black line, Figure 4-20 a) and dUQ (black line, Figure 4-20 b) was observed, indicating that the reduction happens in one step. Considering the high pK_a value of 2-propanol (Table 4-3), the concentration of protons in the solution would be very low. As a result, protons would not be involved in the reduction of Q_1 and dUQ. Consequently, under these conditions, Q_1 and dUQ undergo 2e^- reduction, yielding Q^{2-} hydrogen bonded with 2-propanol molecules as a final product. Taking the mentioned effects of low H^+ concentration into account, the electrode mechanism of Qs in 2-propanol and similar lower aliphatic alcohols is expected to closely resemble the reaction pathway observed in unbuffered aqueous solutions (Figure 4-19).
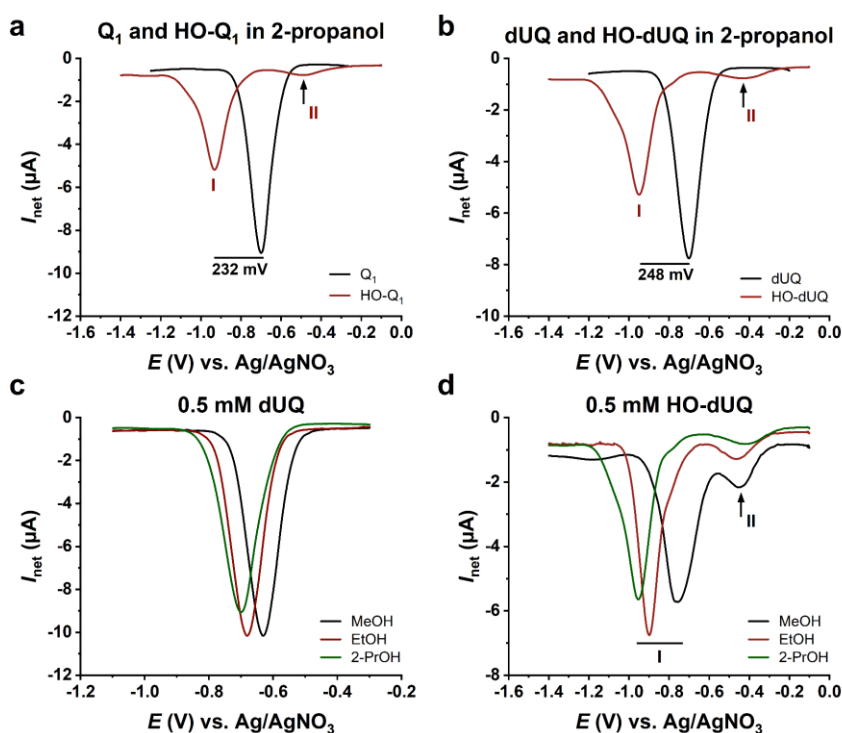
Figure 4-20 Reduction of Q_1, HO-Q_1, dUQ and HO-dUQ in organic protic solvents. Comparison of square-wave voltammograms (SWVs) of 0.5 mM a) Q_1 (black) and HO-Q_1 (red) and b) dUQ (black) and HO-dUQ (red) recorded in 2-propanol. Comparison of SWVs of 0.5 mM c) dUQ and d) HO-dUQ recorded in methanol (black), ethanol (red), and 2-propanol (green). Numbers in mV (panel a and b) show the potential difference between the $E_{p,net}$ of the native Q and major peak I of HO-Q. Arrows indicate the new weaker peak II of HO-Qs. All voltammograms were recorded at GC electrode with 0.1 M LiClO$_4$ as electrolyte. Conditions: f = 8 Hz; E_{sw} = 50 mV; ΔE = 1 mV.

In all applied alcohols only one voltammetric peak correlated to the 2e^- reduction was observed for Q_1 and dUQ as demonstrated for dUQ in Figure 4-20 c. Voltammetric curves for HO-Q_1 and HO-dUQ (red traces, panels a and b in Figure 4-20, respectively) were characterized with two distinct peaks. One intense peak (I) at about −0.933 V due to 2e^- reduction of HO-Qs, and one weaker peak (II) at about −0.500 V (marked with an arrow, panels a, b and d). Besides the intermolecular bonding with the alcohol molecules, HO-Qs might form an intramolecular hydrogen bond between the hydrogen of the -OH (at position 2 or 3) and the oxygen atom of the neighbouring carbonyl group, leading to a five-membered ring structure. As previously reported in the literature for other α-hydroxy-*p*-benzoquinones[241–245], the presence of an intramolecular bond in the HO-Q molecule would have an impact on its redox potential by stabilizing negative charges in the reduced forms. Therefore, under the same conditions the reduction potential of HO-Q is expected to be more negative than that of the corresponding Q without α-hydroxyl group in the structure. Moreover, in methanol which is a stronger acid than 2-propanol (Table 4-3), consequently having higher $[H^+]$, peak II exhibited an increased intensity (black vs. green traces,

respectively, Figure 4-20 d), thereby supporting the intramolecular stabilization of HO-Qs molecules.

It is worth mentioning that HO-Qs showed more negative redox potentials than the corresponding native Qs, independently of the used alcohol for the measurements (Table 4-4). The net peak potentials, $E_{p,net}$, for OH-Q$_1$ and HO-dUQ in 2-propanol, were shifted by 232 mV and 248 mV, respectively, to more negative values being the stronger reductants (Table 4-4 and Figure 4-20 a and b, red curves) when compared to Q$_1$ and dUQ.

Table 4-4 Summary of the net peak potentials ($E_{p,net}$) of Qs and HO-Qs in different alcohols. ΔE is the potential difference between the peaks of the parental quinone and the major peak I of the mono-hydroxylated species. Square-wave voltammograms were recorded in 0.1 M solution of LiClO$_4$ as electrolyte at GCE. Conditions: f = 8 Hz, E_{sw} = 25 mV and ΔE = 1 mV. All potentials are given in V. MeOH, methanol; EtOH, ethanol; 2-PrOH, 2-propanol.

	Q$_1$	HO-Q$_1$			dUQ	HO-dUQ		
solvent	$E_{p,net}$	$E_{p,net}$ (I)	$E_{p,net}$ (II)	$\Delta E_{Q1/HO-Q1(I)}$	$E_{p,net}$	$E_{p,net}$ (I)	$E_{p,net}$ (II)	$\Delta E_{dUQ/HO-dUQ(I)}$
MeOH	−0.652	−0.813	−0.515	−0.161	−0.636	−0.760	−0.441	−0.124
EtOH	−0.681	−0.895	−0.486	−0.214	−0.687	−0.900	−0.460	−0.213
2-PrOH	−0.701	−0.933	−0.474	−0.232	−0.702	−0.950	−0.428	−0.248

4.2.1.4 Non-aqueous aprotic media

In the aprotic solvent acetonitrile, Q$_1$ and dUQ exhibited an electrochemical behaviour which is characteristic for other quinones reported in literature. As shown in Figure 4-21, Q$_1$ and dUQ underwent two step one–electron transfers in acetonitrile, generating two reversible-like voltammetric responses. The peaks labelled I$_c$ and I$_a$ (panel a) correspond to the reduction and re-oxidation reaction between the neutral quinone and the semiquinone radical anion Q$^{\bullet-}$. The second pair of peaks that are labelled II$_c$ and II$_a$ (panel a) correspond to the reduction and re-oxidation reaction between the radical anion Q$^{\bullet-}$ and the quinone dianion Q^{2-}. Analogously, the peak labelled I in the square-wave voltammogram (panel b) corresponds to the reduction reaction of the Q to the Q$^{\bullet-}$, while the second peak II corresponds to the reduction of the Q$^{\bullet-}$ to the Q^{2-}. The first wave (I), showed almost reversible behaviour, $I_{p,a}/I_{p,c}$ = 0.99 and ΔE_p = 70 mV, whereas second wave (II) showed quasi-reversible features, $I_{p,a}/I_{p,c}$ = 0.91 and ΔE_p = 90 mV (Table 4-5).
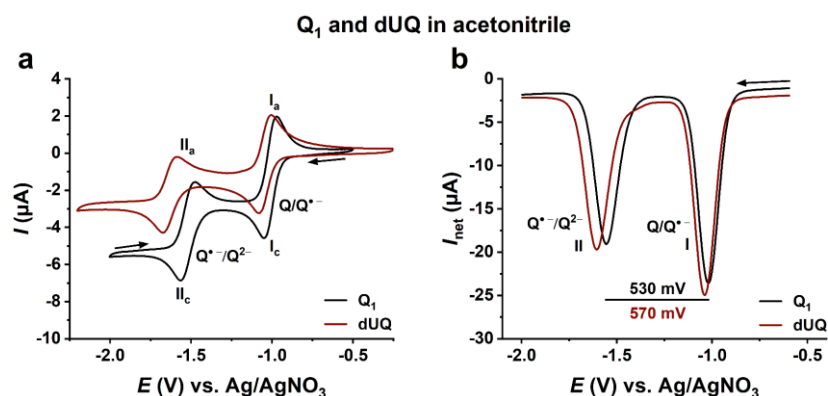
Figure 4-21 Redox reaction of Q$_1$ and dUQ in organic aprotic solvent. a) Cyclic voltammograms of 0.5 mM Q$_1$ (black) and dUQ (red) in acetonitrile with 0.1 M TBAP as electrolyte. The peaks labelled I$_c$ and I$_a$ correspond to the reduction and re-oxidation reaction between the neutral Q and the semiquinone radical anion Q$^{\bullet-}$; the peaks labelled II$_c$ and II$_a$ represent reduction and re-oxidation reaction between the Q$^{\bullet-}$ and the quinone dianion Q^{2-}. Conditions: v = 20 mV/s, ΔE = 1 mV. b) Square-wave voltammograms of 0.5 mM Q$_1$ (black) and dUQ (red) in acetonitrile with 0.1 M TBAP as electrolyte. Peak I correspond to the reduction reaction of the Q to the Q$^{\bullet-}$; Peak II shows the reduction of the Q$^{\bullet-}$ to the Q^{2-}; arrows indicate the direction of the potential variation. Conditions: f = 10 Hz, E_{sw} = 50 mV, ΔE = 1 mV.

The fundamental feature governing the redox chemistry of compounds, which can lead either to a single voltammetric response or two responses in the voltammograms, is the potential difference between the two steps of electron transfer. In aprotic solvents this potential difference is significantly large, so that two well-defined pairs of peaks in CV (comparably, two well-defined peaks in SWV) are observed (Figure 4-21). In aqueous solution, these values are sufficiently close, so that the two electron transfers merge into one pair of peaks (Figure 4-13 and Figure 4-19). The reduction of Qs in aqueous solutions follows a sequence starting with a one-electron reduction (E), followed by protonation (C), then by another reduction and protonation (ECEC mechanism). The overall process occurs in a single step because the protonation of the radical anion leads to a neutral radical (QH$^\bullet$) which easily accepts another electron without a coulombic energy barrier and provides a half-empty orbital for electron pairing. On the other hand, during the reduction of quinones in aprotic organic solvents such as acetonitrile, the protonation step does not occur due to the absence of protons, resulting in radical anions (Q$^{\bullet-}$) as intermediates and quinone dianions (Q^{2-}) as final products of the reduction (EE mechanism). Therefore, in aprotic solvent the insertion of an electron to a species already bearing a negative charge is more challenging as this process demands a higher potential energy. In contrast, adding an electron to an uncharged species is easier since there is no energy barrier.

While the native Qs, Q$_1$ and dUQ, showed only two well-resolved and well-separated consecutive voltammetric signals (Figure 4-21), their hydroxylated derivatives HO-Q$_1$ and HO-dUQ presented a more complicated reduction mechanism (red trace, Figure 4-22). Since both, HO-Q$_1$ and HO-dUQ showed similar electrochemical behaviour in acetonitrile, only data of HO-dUQ are displayed and the general symbol HO-Qs is used in the next paragraphs. The experimental results for HO-Q$_1$ (Figure A - 1) are given in the Appendix A to this chapter. The parameters extracted from cyclic voltammograms for HO-Qs as well as for the corresponding Qs are given in Table 4-5.

Unlike Qs, HO-Qs contain an acidic proton from the −OH group in α-position on the quinone ring, whose presence leads to a behaviour that significantly deviates from the redox transformation of the Qs in aprotic media.

Table 4-5 Electrochemical parameters from the cyclic voltammograms of Qs and HO-Qs measured in aprotic solvent. Peak I and II (black colour) correspond to the voltammetric responses of dUQ and Q$_1$; peak I′ and II′ (red colour) correspond to the voltammetric responses of HO-dUQ and HO-Q$_1$; $E_{p,a}$, anodic peak potential; $E_{p,c}$, cathodic peak potential; $I_{p,a}$, anodic peak current; $I_{p,c}$, cathodic peak current; $\Delta E_p = E_{p,a} - E_{p,c}$, peak-to-peak separation; $E_{p,mid} = (E_{p,a} - E_{p,c})/2$, midpoint peak potential.

	I (I′)					II (II′)				
	$E_{p,a}$	$E_{p,c}$	ΔE_p	$E_{p,mid}$	$I_{p,a}/I_{p,c}$	$E_{p,a}$	$E_{p,c}$	ΔE_p	$E_{p,mid}$	$I_{p,a}/I_{p,c}$
	V	V	mV	V		V	V	mV	V	
dUQ	−1.01	−1.08	70	−1.05	0.99	−1.59	-1.68	90	−1.64	0.91
Q$_1$	−0.99	−1.06	70	−1.03	0.99	−1.54	−1.63	90	−1.59	0.96
HO-dUQ	−0.55	−0.79	240	−0.67	0.74	−1.69	−1.76	70	−1.73	0.88
HO-Q$_1$	−0.55	−0.78	230	−0.66	0.80	−1.65	−1.72	70	−1.69	0.90

As shown in Figure 4-22 (red traces), the redox transformation of HO-dUQ in acetonitrile resulted in two voltammetric pair of peaks (marked I′ and II′) and a weaker irreversible peak (III$_c$′). The first

pair of peaks (I_c' and I_a') showed large peak-to peak separation $\Delta E_p = E_{p,a}(I_a') - E_{p,c}(I_c') = 240$ mV and $I_{p,a}/I_{p,c} \sim 0.7$, indicating a quasi-reversible behaviour (Table 4-5). The second pair of peaks (II_c' and II_a') exhibited characteristics close to reversible redox reaction with $\Delta E_p = 70$ mV and $I_{p,a}/I_{p,c} = 0.90$ (Table 4-5). The large peak-to-peak separation for the voltammetric signal I' suggested quasi-reversibility in the system, features consistent with a mechanism involving electron transfer processes coupled with a chemical reaction.
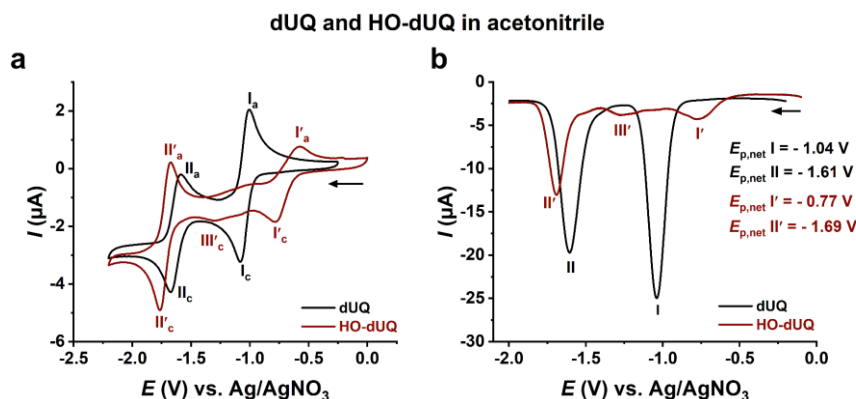
Figure 4-22 Redox reaction of dUQ and HO-dUQ in organic aprotic solvent. a) Cyclic voltammograms and b) square-wave voltammograms of 0.5 mM of dUQ (black) and HO-dUQ (red) in acetonitrile with 0.1 M TBAP as electrolyte at glassy carbon electrode. The subscripts c and a in the peak descriptions (e.g., I_c, I_a) indicate cathodic (reduction) and anodic (oxidation) reaction. Arrows indicate the direction of the applied potential. CV parameters: $v = 20$ mV/s, $\Delta E = 1$ mV; SWV parameters: $f = 10$ Hz, $E_{sw} = 50$ mV, $\Delta E = 1$ mV.

As previously reported in several studies[241–245], the reduction mechanism of α-HO-Qs involves self-protonation processes and it could be described through a series of consecutive proton and electron transfer reactions, given by the equations below:

$$HO - Q + e^- \rightleftarrows HO - Q^{\bullet -} \qquad \text{Eq. 4-3}$$

$$HO - Q^{\bullet -} + HO - Q \rightleftarrows HO - QH^\bullet + {}^-O - Q \qquad \text{Eq. 4-4}$$

$$HO - QH^\bullet + e^- \rightleftarrows HO - QH^- \qquad \text{Eq. 4-5}$$

$$\text{or} \qquad HO - QH^\bullet + HO - QH^\bullet \rightleftarrows HO - Q + HO - QH_2 \qquad \text{Eq. 4-6}$$

$$HO - QH^- + HO - Q \rightleftarrows HO - QH_2 + {}^-O - Q \qquad \text{Eq. 4-7}$$

I_c' $$\qquad 3HO - Q + 2e^- \rightleftarrows HO - QH_2 + 2\,{}^-O - Q \qquad \text{Eq. 4-8}$$
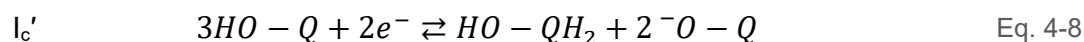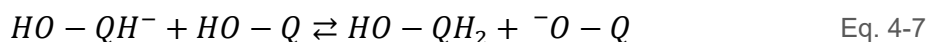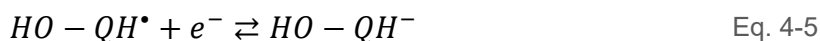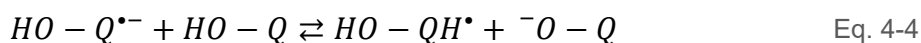
The initial reduction peak (I_c') is accompanied by self-protonation reaction (due to the acidity properties of α-hydroxyl group), and corresponds to the overall reaction (Eq. 4-8) where HO-Q is reduced by $2e^-$ per each three molecules of HO-Qs yielding the hydroquinone $HO-QH_2$ and its conjugated base, ^-O-Q. In these reactions, one molecule of HO-Qs is used in the redox reactions (Eq. 4-3 and Eq. 4-5) and two molecules are used in the protonation steps (Eq. 4-4 and Eq. 4-7). The neutral semiquinone radical, $HO-QH^\bullet$ produced in Eq. 4-4 could be further reduced either by heterogeneous electron transfer step (Eq. 4-5) or by homogeneous electron transfer reaction (Eq. 4-6). The later reaction decreases the amount of $HO-QH^\bullet$ transformed into $HO-QH^-$ in the redox reaction, consequently (as given by Eq. 3-25) decreasing the peak current (peak height). Hence, occurrence of a homogenous electron transfer reaction (Eq. 4-6) explains the observed decrease of the peak current of I_c' in the CV of HO-Q (red trace, Figure 4-22 a and Figure A - 1 a) compared to the peak current of I_c in the CV of Q (black traces). Identical behaviour was observed for the magnitudes of peaks I' and I in the SWV of HO-Q and Q, respectively (Figure 4-22 b and Figure

A - 1 b). The cathodic peak potentials ($E_{p,c}$) for the first reduction peak (I_c') of HO-Qs are less negative than those (I_c) of the corresponding Qs (Table 4-5) implying that the first electron transfer during the reduction of HO-Qs (Eq. 4-3) requires less energy than the first electron transfer step for Qs. Due to the presence of intramolecular hydrogen bonding between the −OH group in α-position on the quinone ring and the adjacent carbonyl group, the electron density of the quinone ring in HO-Qs is more delocalized than in Qs, resulting in higher stabilization of radical anions of HO-Qs compared to that of Qs.

The intermediates generated during the sequence of the reactions (Eq. 4-3 to Eq. 4-7) indicate that at negative potentials, where the second reduction peak (II_c') appears ($E_{p,c}$ (II_c') ~ −1.7 V, Figure 4-22 and Figure A - 1), the only species that are most likely present at the electrode surface are deprotonated HO-Qs, i.e., the conjugated base $^-$O-Q, produced in the self-protonation processes (Eq. 4-4 and Eq. 4-7). Therefore, the second reduction wave (II_c') corresponds to one electron reduction of $^-$O-Q (Eq. 4-9), generating the radical dianion of HO-Qs ($^-$O-Q$^{\bullet-}$).

$$II_c' \qquad\qquad ^-O - Q + e^- \rightleftarrows {}^-O - Q^{\bullet-} \qquad\qquad \text{Eq. 4-9}$$
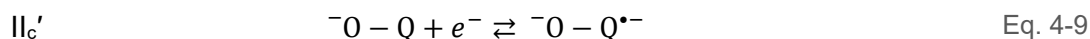
At this point, it is important to highlight that the second reduction step of α-HO-Qs has received much less attention in the literature compared to the first reduction step and thus there is still controversy and debate on the identification of the electrochemical reactions that underline its appearance. One of the reasons is the complexity of the reaction sequence (self-protonation processes) of the first reduction and the generated species during this sequence. Therefore, relying solely on voltammetric data is insufficient to reach a conclusion for the second reduction step of HO-Qs. A coupled approach including electrochemical and EPR experiments could be utilized for a more comprehensive understanding.

The intermediate shoulder peaks labelled with III_c' in CV and III' in SWV of both, HO-dUQ and HO-Q$_1$ (Figure 4-22 and Figure A - 1, respectively), showed features of an irreversible process and most likely arose from reduction of hydrogen-bonded complexes formed due to dimerization of HO-Qs molecules. It is well established that the reduction potential of a sample that participates in dimerization falls within the range of potential values found for its fully protonated and non-protonated forms[246].

4.2.2 Calcium affinity of Q$_1$, dUQ, HO-Q$_1$ and HO-dUQ in different media

After having analysed the redox processes depending on the availability of protons, we turn to the interaction with metal ions. Hence, cyclic and square-wave voltammetry were extensively applied to study the Ca^{2+} binding properties of the four compounds, parental compounds Q$_1$ and dUQ as well as their mono-hydroxylated derivatives HO-Q$_1$ and HO-dUQ.

4.2.2.1 Calcium affinity of Qs and HO-Qs in aqueous solutions

Figure 4-23 shows the responses of Q$_1$ (panels a, b and c) and HO-Q$_1$ (panels d, e and f) to Ca^{2+} in unbuffered aqueous solution (0.1 M KCl, pH 7.4). Addition of Ca^{2+} up to 100 mM bulk concentration produced a small potential shift of +28 mV for Q$_1$ (panels a and b) and +31 mV for OH-Q$_1$ (panels d and e). Since the reduction of Q$_1$ and HO-Q$_1$ in aqueous solution consumes protons, the redox mechanism in unbuffered media is additionally affected by pH changes in the

vicinity of the working electrode. Hence, it was essential to control the pH of the solution before and after addition of 100 mM Ca^{2+}, which gave a pH decrease by −0.85 units. The observed potential shift of Q_1 and OH-Q_1 in presence of Ca^{2+} in unbuffered aqueous solution was consistent with the pH change of the solution (shift to more positive values as predicted by the *Nernst* equation (Eq. 4-1)). However, this was not purely a pH effect since the decrease of pH by −0.85 should cause a shift of + 51 mV (Eq. 4-1), i.e., the smaller potential shifts after addition of Ca^{2+} to Q_1 and HO-Q_1 were most probably due to an overlaid effect of pH change and Ca^{2+} interactions with the Qs. Generally, the slope associates the number of the electrons exchanged in the electrode reaction with the number of protons or Ca^{2+} participating in the reaction, so that the values of 15 mV and 16 mV would indicate a formal 1:4 ratio for the Ca^{2+}-quinone interaction. However, the merging effects on the potential change are impairing a clear interpretation. The electrochemical behaviour of quinones in unbuffered aqueous solutions is a subject of many disagreements, mainly due to the rather complex electrochemical mechanism under these conditions. Additionally, reduction of the quinones in aqueous media consumes protons and if the pH of the solution is not well buffered, the concentration of protons near the surface of the working electrode could be different from that in the bulk solution making accurate measurements of the potentials very difficult. Furthermore, addition of salts (here, $CaCl_2$ as a source for Ca^{2+}) to unbuffered aqueous solutions influences the acid-base equilibrium of the solution, thereby affecting its pH. All these facts inevitably led to the conclusion that pH buffered solutions or organic solutions should be used.
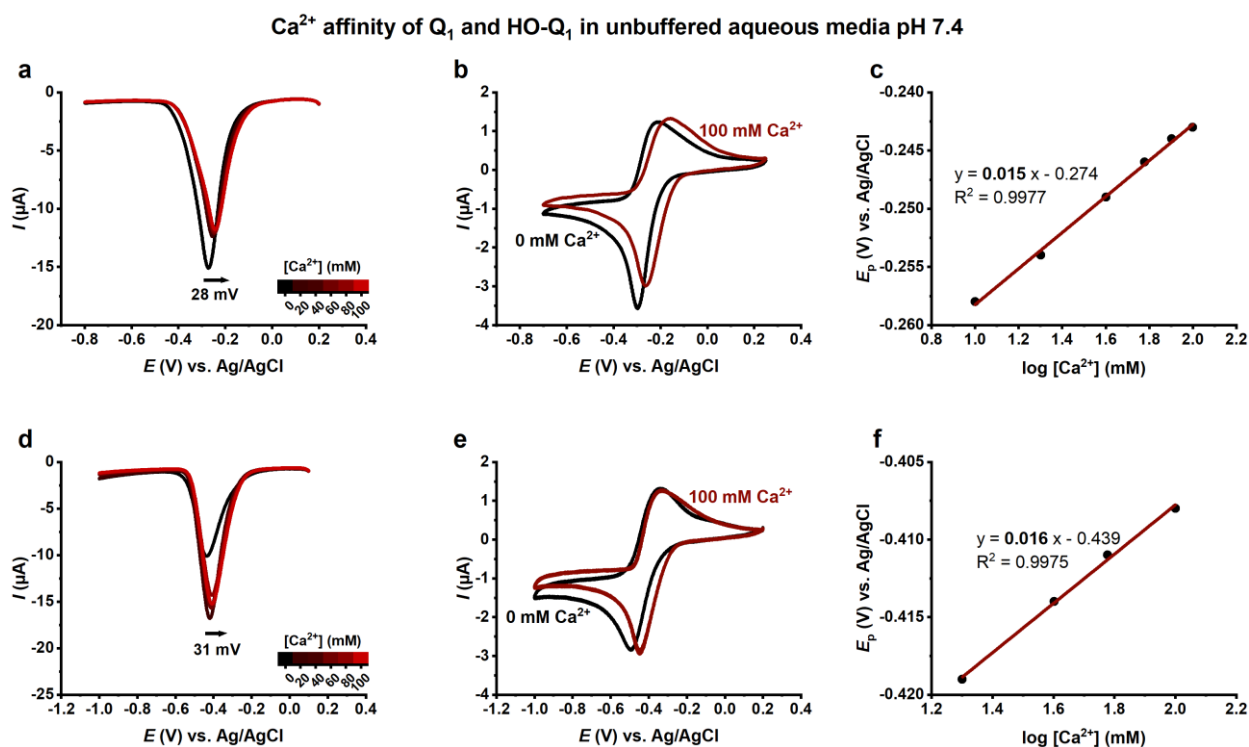
Figure 4-23 Effects of Ca^{2+} on the voltammetric responses of Q_1 and HO-Q_1 in unbuffered aqueous media. a) Square-wave voltammograms of 0.5 mM Q_1 in absence (black) and presence of different concentrations of Ca^{2+} up to 100 mM (red line). b) Cyclic voltammograms of 0.5 mM Q_1 in absence (black) and presence of 100 mM Ca^{2+} (red). c) Dependence of the net peak potentials ($E_{p,net}$) of Q_1 on logarithm of [Ca^{2+}] from panel a. Panels d and e show the same features as panel a and b for 0.5 mM HO-Q_1. f) Dependence of $E_{p,net}$ of HO-Q_1 on logarithm of [Ca^{2+}] from panel d. CV parameters: v = 10 mV/s, ΔE = 1 mV; SWV parameters: f = 8 Hz, E_{sw} = 25 mV, ΔE = 1 mV.

Performing the same experiments in buffered solution (0.1 M HEPES, pH 7.4) no influence on the redox potential of Q_1 was observed for any concentration of Ca^{2+} (Figure 4-24 a and b). Additionally, the minor shift (-35 mV) for OH-Q_1 (Figure 4-24 c, d and e) with increasing concentration of Ca^{2+} was in the opposite direction of what is expected for the interaction and predicted by Eq. 4-2. These observations indicated that binding of Ca^{2+} to the reduced forms of Q_1 and HO-Q_1 in unbuffered (Figure 4-23) and buffered (Figure 4-24) aqueous solutions is weak. As previously shown (section 4.2.1.1), the overall redox transformation of Qs in buffered solutions (pH~7) always proceeds via $2e^-/2H^+$ mechanism with QH_2 as a final product. Most likely, Ca^{2+} cannot compete with H^+ when the latter are present in sufficient concentration. In buffers the concentration of protons is 10^{-3} to 10^{-1} M in the order of Q_1 (10^{-3} M) and HO-Q_1 (10^{-3} M) and Ca^{2+} (10^{-2}-10^{-1} M), so that protons cannot be replaced by the cation. This indicated that the applied voltammetric approach did not allow to directly monitor Ca^{2+} affinity of Q_1 and HO-Q_1 in aqueous solutions presumably because of competition with protonation and/or hydrogen bonding.

Ca^{2+} affinity of Q_1 and HO-Q_1 in buffered aqueous media pH 7.4
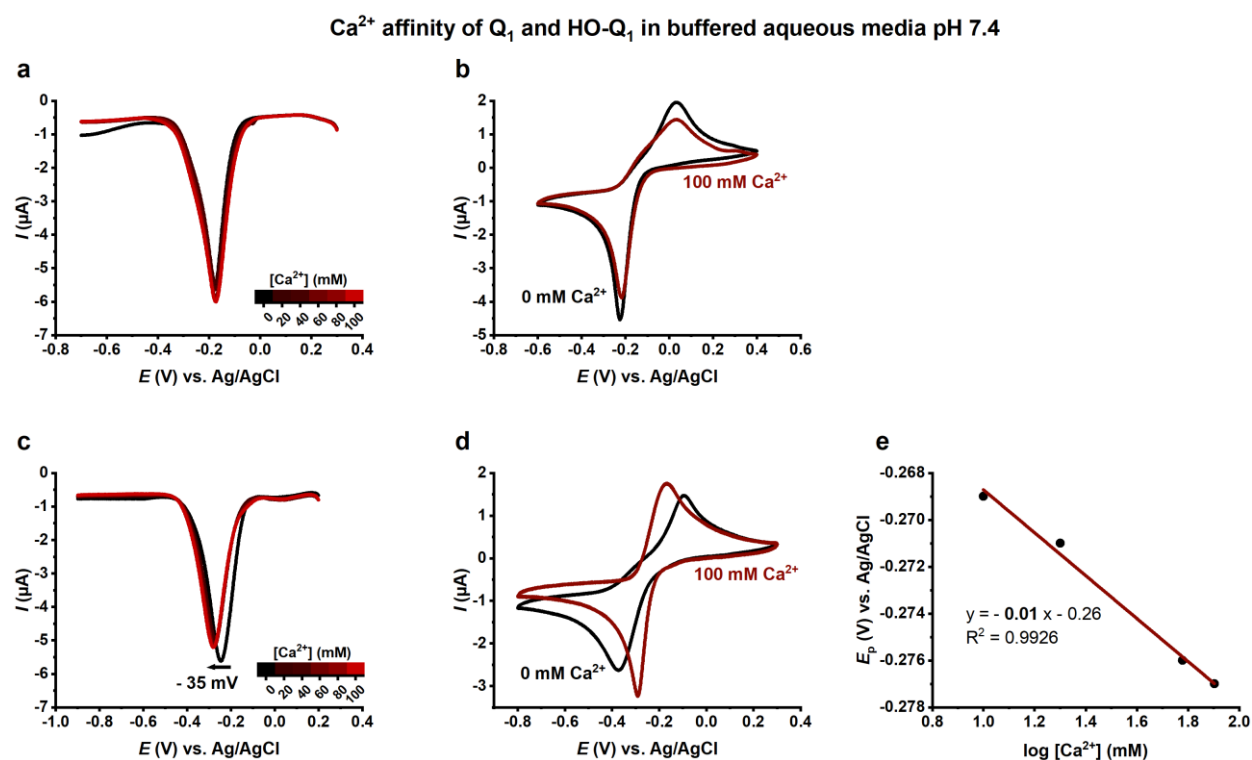
Figure 4-24 Effects of Ca^{2+} on the voltammetric responses of Q_1 and HO-Q_1 in buffered aqueous media at pH 7.4. a) Square-wave voltammograms of 0.5 mM Q_1 in absence (black) and presence of different concentrations of Ca^{2+} up to 100 mM concentration of Ca^{2+} (red line). b) Cyclic voltammograms of 0.5 mM Q_1 in absence (black) and presence of 100 mM Ca^{2+} (red). Panels c and d show the same features as panel a and b for 0.5 mM HO-Q_1. e) Dependence of the net peak potentials ($E_{p,net}$) of HO-Q_1 on logarithm of [Ca^{2+}] from panel c. CV parameters: v = 10 mV/s, ΔE = 1 mV; SWV parameters: f = 8 Hz, E_{sw} = 25 mV, ΔE = 1 mV.

4.2.2.2 Calcium affinity of Qs and HO-Qs in non-aqueous protic solutions

Replacing the aqueous phase with alcohols had a two-fold effect for the experiments. Because they are weaker acids than water with higher pK_a values (Table 4-3), proton dissociation is much less pronounced, but hydrogen bonding is still possible. Moreover, Q_1 and the more lipophilic dUQ as well as their hydroxylated forms are much better soluble in alcohols than in water. In addition, $Ca(ClO_4)_2$ which was used as a source of Ca^{2+} is sufficiently soluble in alcohols (~50 mM). With these prerequisites, SWV experiments were performed in bulk solution.

Addition of different [Ca^{2+}] to Qs and HO-Qs in 2-propanol, ethanol, and methanol induced very similar peak potential ($E_{p,net}$) alterations for the compounds. For that reason, only data in 2-propanol are exemplified in the next paragraphs. The experimental results for ethanol and methanol are given in the Appendix B to this chapter. The complete data set is compiled in Table 4-6. Due to the observed analogue behaviour of the compounds, the results will be categorized into two groups: native quinones (Q) including Q_1 and dUQ and mono-hydroxylated forms (HO-Q), namely HO-Q_1 and HO-dUQ.

For [Ca^{2+}] below those of Qs (< 0.5 mM) a continuous shift of the $E_{p,net}$ to more positive values was observed up to equimolar concentrations in 2-propanol (Figure 4-25, b and e), which further proceeded for higher [Ca^{2+}] up to 10 mM (Figure 4-25 a and d). This finding suggests that the reduction of the Qs is coupled to a chemical step (EC mechanism), i.e., as given by Eq. 4-10, first the Q is reduced to Q^{2-} (electron transfer step, E) which further interact with Ca^{2+} (chemical step, C). Interaction with Ca^{2+} leads to energetic stabilization of Q^{2-}, thereby $E_{p,net}$ shifted to more positive values.
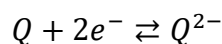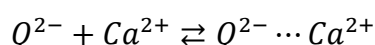
Electron transfer step (E) $$Q + 2e^- \rightleftarrows Q^{2-}$$
Chemical step (C) $$Q^{2-} + Ca^{2+} \rightleftarrows Q^{2-} \cdots Ca^{2+}$$ Eq. 4-10
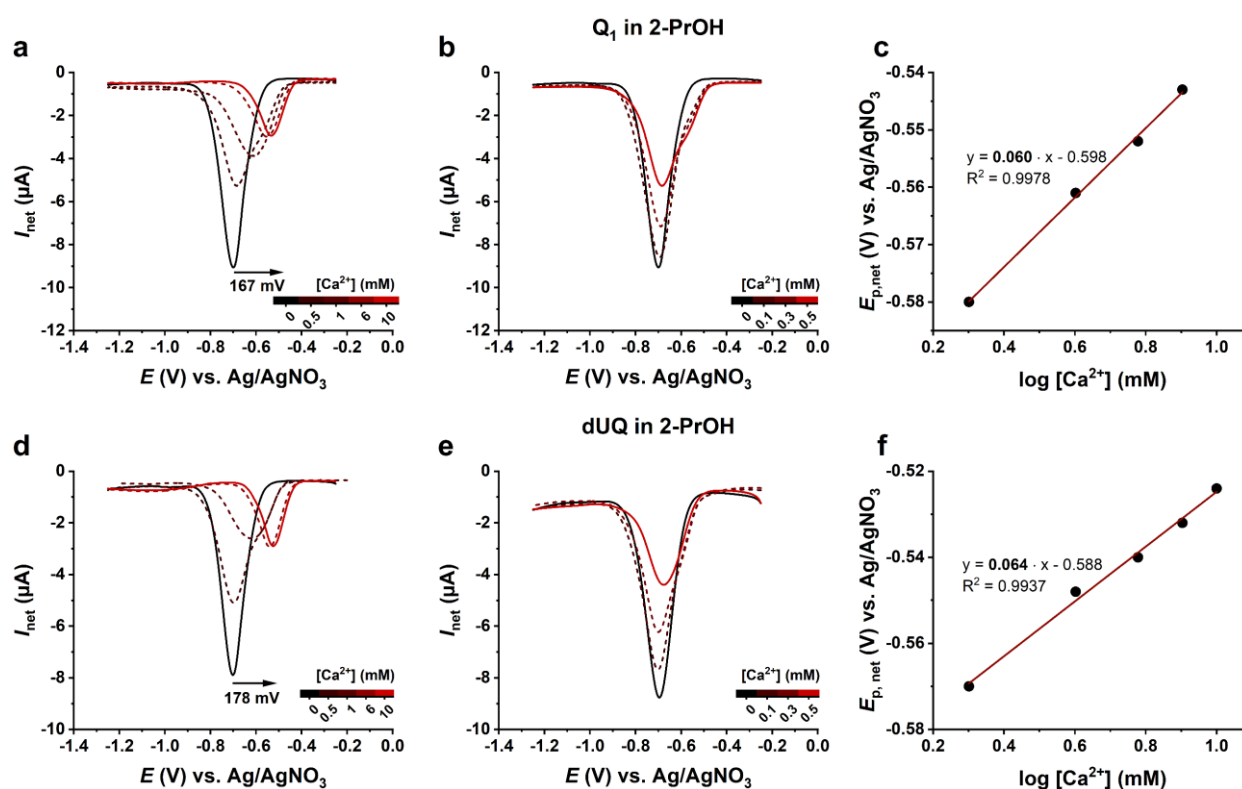
Figure 4-25 Effects of Ca^{2+} on the voltammetric responses of Q_1 and dUQ recorded in 2-propanol. Square-wave voltammograms of 0.5 mM Q_1 (panels a, b) and dUQ (panels d, e) in the absence (black line) and in the presence of different concentrations of Ca^{2+} up to 10 mM (red dashed and solid lines) in de-aerated 2-propanol with 0.1 M LiClO$_4$ as electrolyte at GCE. Dependence of the peak potential ($E_{p,net}$) of c) Q_1 and f) dUQ on the logarithm of concentration of Ca^{2+} from panels a and d, respectively. SWV parameters: f = 8 Hz, E_{sw} = 50 mV, ΔE = 1 mV.

The voltammetric experiments of OH-Qs (Figure 4-20 and Table 4-4) showed about 200 mV more negative redox potentials than Qs. Moreover, the reduction of HO-Qs in SWV was portrayed with two peaks, one intense peak I at about −0.950 V and an additional weaker peak II at around −0.5 V, whereas the reduction of Qs showed only one well-defined peak at −0.700 V (Figure 4-20).

Likewise, a significant difference in Ca^{2+}-interaction between parental compounds, Qs, and their mono-hydroxylated forms was observed. While for Qs an increase in $[Ca^{2+}]$ caused a continuous shift of the peak potential to more positive values (Figure 4-25), the position of peak I associated with reduction of OH-Qs was not affected, but a new peak appeared at about -0.750 V (panels b, e in Figure 4-26). While the intensity of peak I decreased and diminished (at around 1 mM Ca^{2+}), the intensity of the new peak III increased with an increase in $[Ca^{2+}]$. Furthermore, for higher $[Ca^{2+}]$ the peak III was moderately shifted to even more positive potential values (panels a, d, Figure 4-26), indicating energetic stabilization of the reduced species. These comparisons implied that hydroxylated species tend to form an OH-Q-Ca^{2+} ion pairs already in the oxidized state which upon reduction produces the voltammetric peak III at about -0.75 V (CE mechanism, Eq. 4-11). The interaction of Ca^{2+} with the oxidized form of HO-Qs becomes feasible owing to the presence of α-OH group which behaves as a weak acid and HO-Qs are already present in monoanionic form ($^-$O-Q). When $[Ca^{2+}] < [Q]$, the amount of Ca^{2+} is insufficient to bind all HO-Qs molecules, so a portion of HO-Qs remains unbound (presence of peak I, panels b and e in Figure 4-26) while a certain portion associates with Ca^{2+} (peak III, panels b and e).

Chemical step (C)
$$^-O - Q + Ca^{2+} \rightleftarrows\; ^-O - Q \cdots Ca^{2+}$$
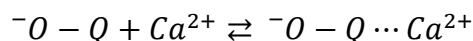
Electron transfer step (E)
$$^-O - Q \cdots Ca^{2+} + 2e^- \rightleftarrows \left(^-O - Q \cdots Ca^{2+} \right)^{2-}$$

Eq. 4-11
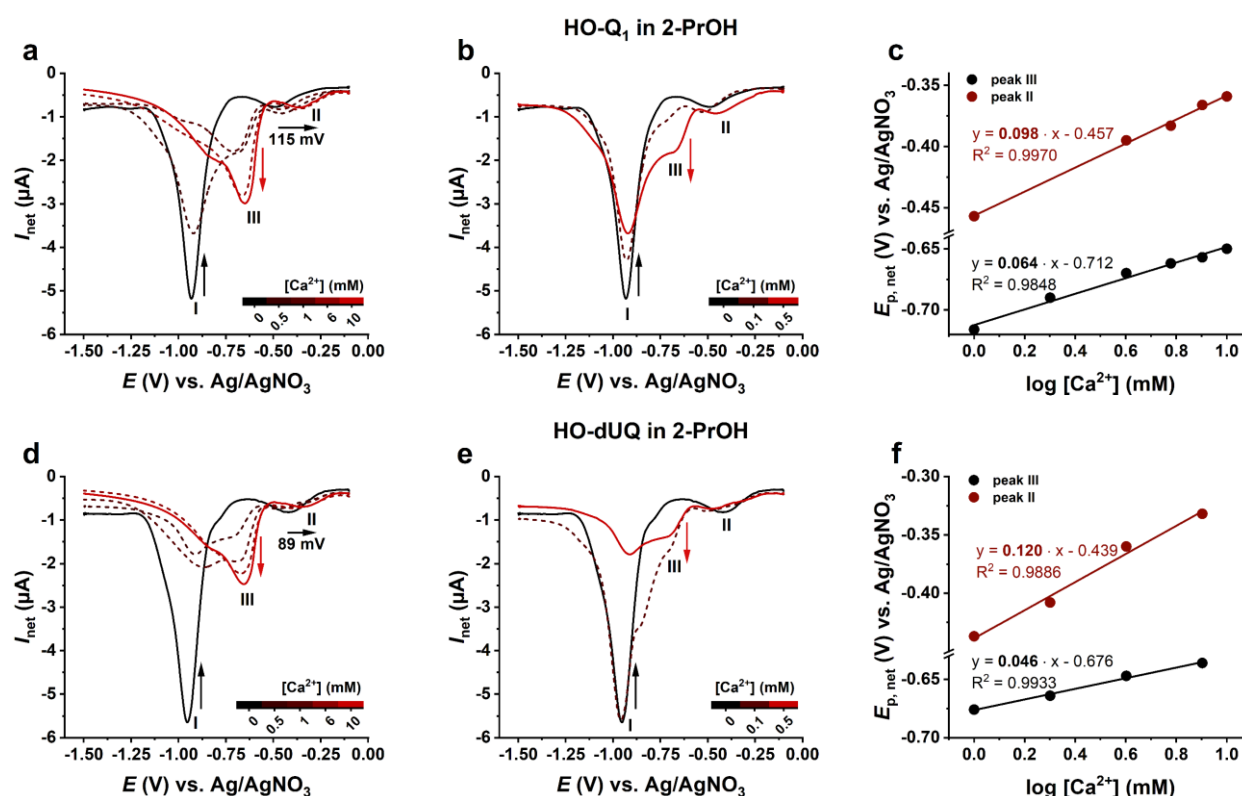
Figure 4-26 Effects of Ca^{2+} ions on the voltammetric responses of HO-Q_1 and HO-dUQ recorded in 2-propanol. Square-wave voltammograms of 0.5 mM HO-Q_1 (panels a, b) and HO-dUQ (panels d, e) in the absence (black line) and in the presence of different concentrations of Ca^{2+} (red dashed and solid lines) in de-aerated 2-propanol solution of 0.1 M $LiClO_4$ as electrolyte at GCE. Dependence of the potential of peak III (black) and peak II (red) of c) HO-Q_1 and f) HO-dUQ on the logarithm of $[Ca^{2+}]$ from panels a and d, respectively. SWV parameters: f = 8 Hz, E_{sw} = 50 mV, ΔE = 1 mV.

The smaller peak (II) in voltammograms of HO-Qs at about −0.5 V was also sensitive to Ca^{2+} and moved to higher (positive) potentials by 115 mV for HO-Q_1 and for 89 mV for HO-dUQ in 2-

propanol (Figure 4-26 panels a and d). The Ca^{2+}-sensitivity of HO-Q_1 and HO-dUQ in ethanol was very similar to that in 2-propanol (Table 4-6, Figure B - 2).

Nevertheless, an interaction of Ca^{2+} with reduced species of Qs and HO-Qs other than anionic forms (Q^{2-} and $^-$O-Q) should not be dismissed. It has been reported that stable $Q^{\bullet-}$ could be formed during the electrochemical reduction of Qs in alcohol solutions[247,248]. Therefore, a formation of ion-pair association between Ca^{2+} and $Q^{\bullet-}$ should be also considered. In line with this, besides the peak potentials ($E_{p,net}$), Ca^{2+} also influenced the peak heights ($I_{p,net}$) of both Q and HO-Qs. For instance, in 2-propanol $I_{p,net}$ was reduced by half in Ca^{2+}-containing compared to Ca^{2+}-free conditions, although identical [Q] were used and the working electrode was cleaned before each measurement. These effects on the $I_{p,net}$ were not observed in ethanol and methanol. Since $I_{p,net}$ is proportional to the number of transferred electrons (Eq. 3-31), this decrease in $I_{p,net}$ could be an indication that only one electron participates in the electrode reaction which will result in $Q^{\bullet-}$ as a product of the reduction.

The HO-Qs generally showed greater affinity for Ca^{2+} than the parental compounds. Comparing the Ca^{2+} induced effect for a concentration ratio [Q]:[Ca^{2+}] = 1:20 in 2-propanol, the peak potential ($E_{p,net}$) shifted by 180 mV for the Qs and by more than 290 mV for the HO-Qs ($\Delta E_{p,net}$ in Table 4-6) which implied a much higher affinity of the OH-Qs for Ca^{2+}. Comparing these shifts for 10 mM Ca^{2+}, corresponding to the ratio [Q]:[Ca^{2+}] = 1:20, the most prominent shift of the peak potential ($\Delta E_{p,net}$) was found in 2-propanol (~170 mV for Qs and ~300 mV for HO-Qs) followed by ethanol (~90 mV for Qs and 170 mV for HO-Qs). The weakest effect was seen in methanol with $\Delta E_{p,net}$ of only ~50 mV for Qs and ~20 mV for HO-Qs (Table 4-6).

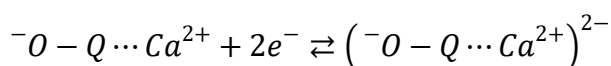Table 4-6 Summary of the net peak potentials ($E_{p,net}$) of Qs and HO-Qs in different alcohols in absence and presence of 10 mM Ca^{2+}. $\Delta E_{p,net}$ represents the potential difference between redox reaction of the respective compound in absence and presence of 10 mM Ca^{2+}.

	2-propanol				ethanol			
Ca^{2+} (mM)	0	10			0	10		
	$E_{p,net}$ (V)	$E_{p,net}$ (V)	$\Delta E_{p,net}$ (mV)	Slope (mV)	$E_{p,net}$ (V)	$E_{p,net}$ (V)	$\Delta E_{p,net}$ (mV)	Slope (mV)
Q_1	-0.700	-0.533	167	60	-0.681	-0.600	81	55
HO-Q_1	-0.941	-0.650	291	64	-0.895	-0.725	170	48
dUQ	-0.702	-0.524	178	64	-0.687	-0.594	93	57
HO-dUQ	-0.957	-0.653	304	46	-0.900	-0.730	170	32

	methanol			
Ca^{2+} (mM)	0	10		
	$E_{p,net}$ (V)	$E_{p,net}$ (V)	$\Delta E_{p,net}$ (mV)	Slope (mV)
Q_1	−0.645	−0.590	55	20
HO-Q_1	−0.820	−0.788	32	-
dUQ	−0.637	−0.593	44	17
HO-dUQ	−0.781	−0.771	10	-

Moreover, a range of *Nernst*-factors (slopes) for Ca^{2+}-binding was observed, which indicated that Ca^{2+} interacted in different modes (stoichiometry) with Qs and HO-Qs (Table 4-6). The square-wave peak potentials ($E_{p,net}$) of Qs shifted linearly with the logarithm of the [Ca^{2+}] in all solvents. In 2-propanol, $E_{p,net}$ shifted to more positive values with a slope of 60 mV for Q_1 and 64 mV for dUQ (Figure 4-25 c and f), of around 55 mV for both, Q_1 and dUQ in ethanol (Table 4-6, Figure B - 1) and with about 20 mV in methanol (Table 4-6, Figure B - 3). These values showed a clear difference in stoichiometry of the ion-pair associations between the Qs and Ca^{2+} in different protic media. The slope of about 60 mV (observed in 2-propanol and ethanol) for the Qs implied an equal number of electrons accepted in the reduction step, and of Ca^{2+} participating in the chemical step of the reaction (Eq. 4-10). The slope of about 20 mV in methanol suggested that, besides Ca^{2+} ions, still competing protons were present or that more methanol molecules were hydrogen bonded to the Qs. Ca^{2+}-induced effect on voltammetric response of HO-Qs in 2-propanol (Figure 4-26) and ethanol (Figure B - 2) resulted in an appearance of a new peak III at more positive potentials. About half the slope (32 mV and 46 mV) was found for HO-Qs in ethanol and 2-propanol (Table 4-6), indicating that two times more electrons than Ca^{2+} participated in the overall process. In contrast, a new peak at a shifted potential was not seen for HO-Qs in methanol, but a continuous shift of the original peak I (at about −0.950 V) to more positive values for the potential was observed for all used concentrations, lower and higher than the concentration of the HO-Qs (Figure B - 4). Moreover, the weaker peak II at about -0.500 V was not affected by increasing [Ca^{2+}] in methanol. Considering the pK_a values of the alcohols (Table 4-3), which indicate the degree of the dissociation, methanol has the highest rate of dissociation and the [H^+] will be higher than in ethanol and 2-propanol. Hence, the weaker peak II in SWV of HO-Qs, arising from an intramolecular hydrogen bonding between the α-OH group and the oxygen atom of the neighbouring carbonyl group, was much better stabilized by protons available in methanol than in ethanol and 2-propanol. Additionally, as a stronger acid (Table 4-3), methanol forms much stronger hydrogen bonds with the reduced forms of Qs and HO-Qs than 2-propanol, which also causes a steric hindrance for the necessary molecular approach to Ca^{2+}. Thus, Q^{2-} would be more stabilized in methanol than in 2-propanol and consequently the interactions with Ca^{2+} and Q^{2-} would be weaker. Oppositely, Qs/HO-Qs are less stabilized by 2-propanol, but more by Ca^{2+}. Likewise, the potential difference of the $E_{p,net}$ measured in absence and presence of 10 mM Ca^{2+} ($\Delta E_{p,net}$ in Table 4-6) was smallest in methanol, followed by ethanol and highest in 2-propanol, a tendency that aligns with the reported pK_a values of the alcohols.

4.2.2.3 Calcium affinity of Qs and HO-Qs in non-aqueous aprotic solutions

As discussed earlier, in aprotic solvents Qs showed two clearly separated one-electron waves at potentials of about -1.0 V and -1.6 V corresponding to $Q/Q^{•-}$ and $Q^{•-}/Q^{2-}$ processes, respectively (black lines, Figure 4-27). This good separation of 530 mV for Q_1 and 570 mV for dUQ allowed following the effects of Ca^{2+} on the reduced forms $Q^{•-}$ and Q^{2-} of the Qs. Addition of Ca^{2+} to an acetonitrile solution of Q_1 and dUQ had a large effect on the peak potentials as shown in Figure 4-27. Increasing [Ca^{2+}] resulted in rapid loss of the transition waves (I and II) and appearance of a new single peak (III) at more positive potential (red solid lines, Figure 4-27). When Ca^{2+} was

titrated in lower concentration (<0.5 mM) than the [Qs], both waves decreased in intensity and disappeared at 0.3 mM Ca^{2+} (dashed lines in panels b and e, Figure 4-27). Furthermore, a new peak III arose at more positive potentials (red solid line, panels b and e). The potential of the wave II at about -1.6 V, associated with the Q$^{\bullet-}$/Q^{2-} process, was slightly shifted to more negative potentials and disappeared after addition of 0.3 mM Ca^{2+} (dashed lines in panels b and e). This negative shift of wave II indicated that the dianion is destabilized in the presence of Ca^{2+}, making the reduction of the Q$^{\bullet-}$ to Q^{2-} more difficult. The net peak potential ($E_{p,net}$) of peak III shifted linearly with the logarithm of the [Ca^{2+}] with a slope of 84 mV for Q$_1$ and 93 mV for dUQ. The slope implied that the ratio of Ca^{2+} and electrons, x/n (Eq. 4-2), involved in the overall process is 1.5 for Q$_1$ and 1.4 for dUQ. These findings can be interpreted by postulating a Ca^{2+}-Q$^{\bullet-}$ association, where the Q$^{\bullet-}$ is much more stabilized in the presence of Ca^{2+}, so that the second electron transfer is happening at roughly the same potential and very fast which finally gives a single peak. Hence, Ca^{2+} is interacting preferentially with the semiquinone radical anion Q$^{\bullet-}$.
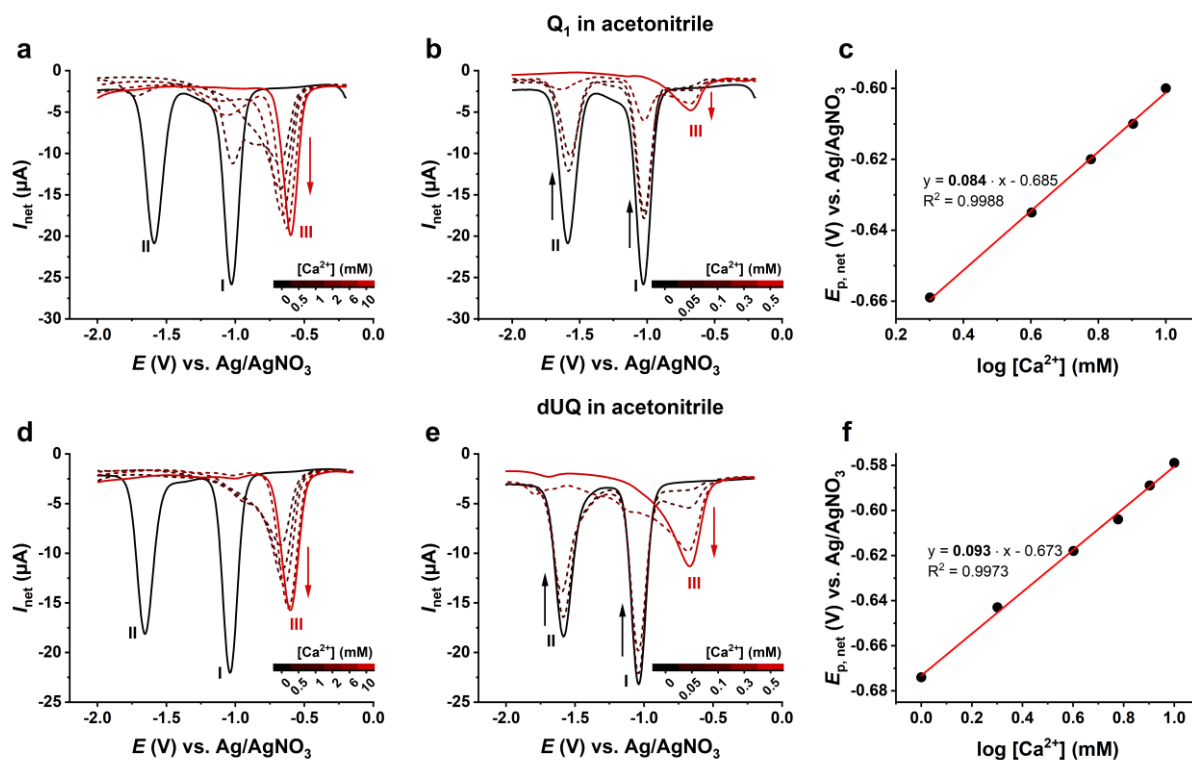
Figure 4-27 Effects of Ca^{2+} on the voltammetric responses of Qs in acetonitrile. Square-wave voltammograms of 0.5 mM Q$_1$ (panels a, b) and dUQ (panels d, e) in the absence (black solid line) and in the presence of different concentrations of Ca^{2+} (dashed and solid red lines) in de-aerated acetonitrile solution of 0.1 M TBAP as electrolyte at GC electrode. Dependence of the net potential of peak III of c) Q$_1$ and f) dUQ on the logarithm of [Ca^{2+}] from panels a and d, respectively. SWV parameters: f = 10 Hz, E_{sw} = 50 mV, ΔE = 1 mV.

In acetonitrile, Qs showed two well-separated one-electron peaks (black lines, Figure 4-27), while their hydroxylated derivatives, HO-Qs (black lines, Figure 4-28) presented more complicated redox mechanism due to the presence of a hydroxyl group in α-position and the possibility of self-protonation reactions (section 4.2.1.4). Addition of Ca^{2+} had a large effect on the net peak potentials of HO-Qs in acetonitrile, as shown in Figure 4-28. Several processes occurred at similar potentials that made the resulting voltammograms hard to be evaluated. Nonetheless, when [Ca^{2+}]>>[HO-Qs] the formation of two distinct ion pairs was observed (red line, Figure 4-28

a and c), which owing to their unique energy state underwent reduction at a different potentials (peaks marked with red arrows, panels a and c).
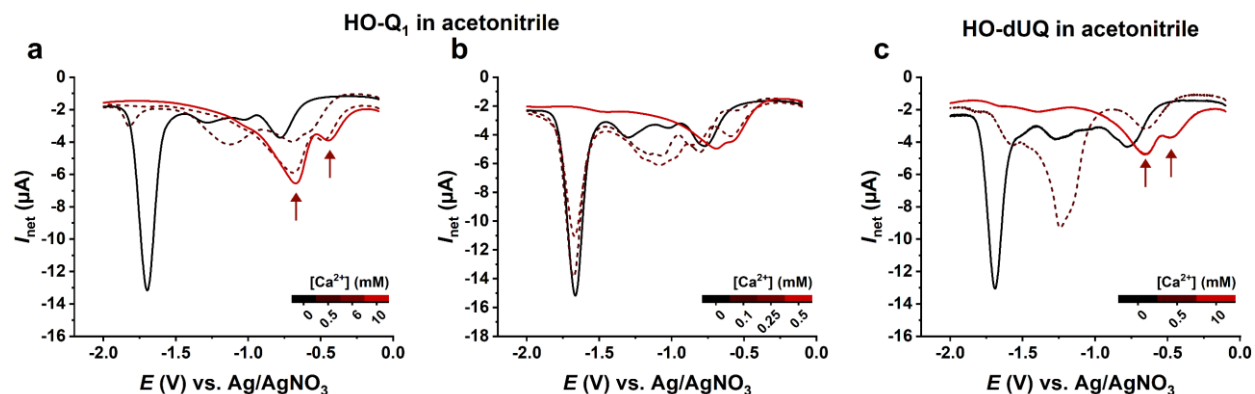
Figure 4-28 Effects of Ca^{2+} on the voltammetric responses of HO-Qs in acetonitrile. Square-wave voltammograms of 0.5 mM HO-Q_1 (panels a, b) and HO-dUQ (panel c) in the absence (black solid line) and in the presence of different [Ca^{2+}] (dashed and solid red lines) in acetonitrile solution of 0.1 M TBAP as electrolyte at GC electrode. SWV parameters: f = 10 Hz, E_{sw} = 50 mV, ΔE = 1 mV.

4.2.3 Hydrogen bonding of the quinones

The Ca^{2+} affinity experiments of Qs and HO-Qs in aqueous solutions and protic organic media strongly suggested that Ca^{2+} and protons were competing for binding to the quinones. To substantiate this hypothesis, a set of experiments was designed to investigate the effect of proton donors and affinity for hydrogen bond formation on the redox processes of the Qs. Protonation and hydrogen–bonding are fundamental factors controlling potentials and mechanisms in the reduction of Qs. In addition, these processes are particularly important in view of the essential biological functions of quinone-based redox couples as electron-proton carriers in oxidative phosphorylation and photosynthesis. Therefore, experiments in acetonitrile as a proton-free solvent were performed by adding variable amounts of hydrogen bond donors.

The voltammetric responses of Q_1 (panels a, b, c) and dUQ (panels d, e and f) in acetonitrile at different concentrations of methanol, ethanol and 2-propanol are shown in Figure 4-29.

Titration of the alcohols to Qs (Q_1 and dUQ) caused the net peak potential ($E_{p,net}$) for the second wave (peak II, $Q^{\bullet-}/Q^{2-}$ process) to shift to more positive values of the potential. The $E_{p,net}$ for the $Q/Q^{\bullet-}$ process (peak I) moved also in the positive direction but by a much smaller amount, indicating that $Q^{\bullet-}$ was obviously much less stabilized by hydrogen bonding. The two waves moved closer together as the protic solvent content was increased, and for larger additions the two waves fully coincided (solid lighter lines in Figure 4-29). It was consistently found that the net peak potentials of the first and second wave were shifted towards more positive values for the potential with a decrease in peak separation and no loss of reversibility as the concentration of the alcohols was increased. Additionally, the two peaks merged for much lower concentration of methanol and ethanol (panels a, b, d and e) than upon titration of 2-propanol (panels c and f). Increasing concentrations of 2-propanol resulted in a smaller shift of the second peak (II) and even for the highest concentration of 10 M 2-propanol both waves were still separated in the voltammograms (panels c and f).

Comparing the effect of all hydrogen bond donors (Figure 4-30), it was observed that the most effective stabilization of the Q^{2-} occurred with methanol, followed by water, ethanol and finally 2-

propanol. The strength of hydrogen bonding depends on the pK_a of the proton donors and proton acceptors as well as possible steric effects for molecular approach. Considering the literature data for pK_a of water and alcohols (Table 4-3), the acidity trend in DMSO is methanol ≥ water > ethanol > 2–propanol. To the best of our knowledge there is no literature data available for the pK_a of these hydrogen bond donors in acetonitrile. Nevertheless, our observation agreed with the sequence of acidity in DMSO.
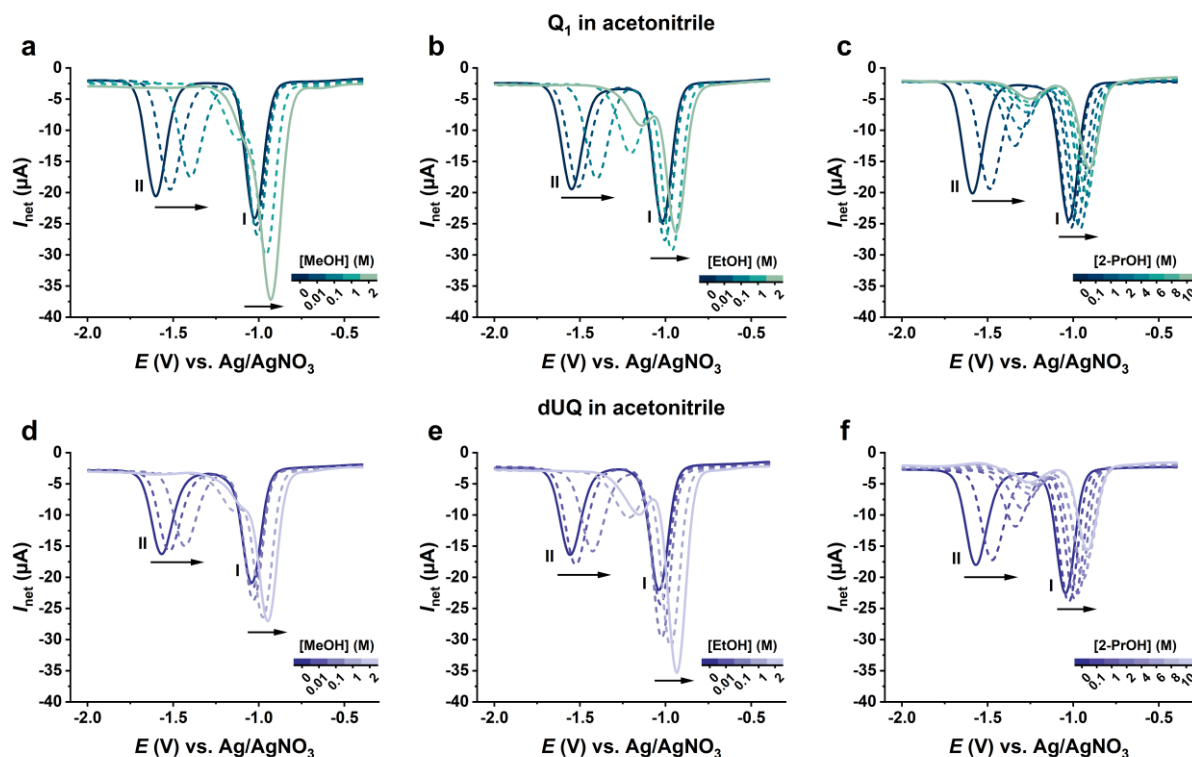
Figure 4-29 Changes of square-wave voltammograms of Q_1 and dUQ in acetonitrile induced by hydrogen bond donors. 0.5 mM Q_1 (panels a, b and c) and 0.5 mM dUQ (panels d, e and f) in acetonitrile with 0.1 M TBAP as electrolyte at GC electrode titrated with different alcohols (MeOH, methanol; EtOH, ethanol; 2-PrOH, 2-propanol). Qs showed two distinct electron transitions in acetonitrile, labelled I and II (darker solid lines), which collapsed to a single peak upon titration with hydrogen bond donating solvents. SWV parameters: f = 10 Hz, E_{sw} = 50 mV, ΔE = 1 mV.

Previous findings[249–251] regarding analogous shifts in the potentials of various quinones resulting from increased content of water and alcohols in aprotic environment have been attributed to the fast protonation of the Q^{2-}. The possibility of protonation of quinone monoanions can be ruled out simply on the basis of the unfavourable pK_a values of the semiquinones, which are lower than the pK_a of water and alcohols[18,238,252–254]. Summing up, hydrogen bonding promotes the stability of the fully reduced quinone (Q^{2-}) more than that of the semiquinone ($Q^{\bullet-}$).
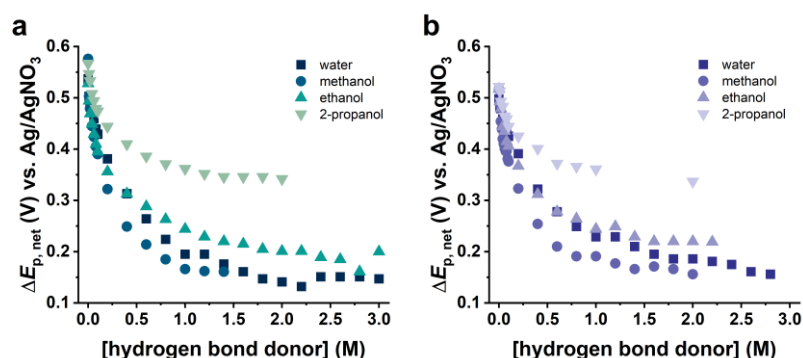
Figure 4-30 Effects of hydrogen bond donors on the peak separation of Qs in acetonitrile. Changes of the peak separation $\Delta E_{p,net} = E_{p,net}$ (II) $- E_{p,net}$ (I) in square-wave voltamograms with increasing concentration of hydrogen bond donors for a) Q_1 and b) dUQ in acetonitrile.

Titration with 2-propanol resulted in a smaller shift of the second peak (II), and even when 90% of the total volume of acetonitrile in the electrochemical cell was replaced with 2-propanol, both waves were still present in the voltammogram (Figure 4-29 c and f). To further understand the reason for this behaviour and considering that the supporting electrolyte can also alter the redox processes by undergoing competitive ion-pairing reactions with the sample, tetrabutylammonium perchlorate (TBAP, 0.1 M) was used as supporting electrolyte in 2-propanol instead of $LiClO_4$. The later (as well as other perchlorates of metal ions as potassium or sodium) is generally used as supporting electrolyte for the experiments in protic organic media since TBAP, among other non-metal perchlorates, is not fully soluble in high concentrations in alcohols, making the preparation of stock solutions (1 M) challenging. However, TBAP showed good solubility in 2-propanol up to 0.1 M and was therefore used as supporting electrolyte for the measurement of the voltammetric response of dUQ in 2-propanol. Figure 4-31 a and b show that with TBAP (red lines) as an electrolyte, two redox processes manifested by two pair of peaks in CV and two peaks in SWV appeared for dUQ in 2-propanol, whereas only one voltammetric process in CV and SWV was observed with $LiClO_4$ as electrolyte. Importantly, when TBAP was replaced with $LiClO_4$ as supporting electrolyte in acetonitrile (Figure 4-31 c and d), only one voltammetric process was observed in the voltammograms (black lines) contrasting the expectation of two separated electron transfer processes (red lines) for aprotic media. This clearly implied that Li^+ most probably interacted with dUQ which prompted us to further study the sensitivity of dUQ towards Li^+.
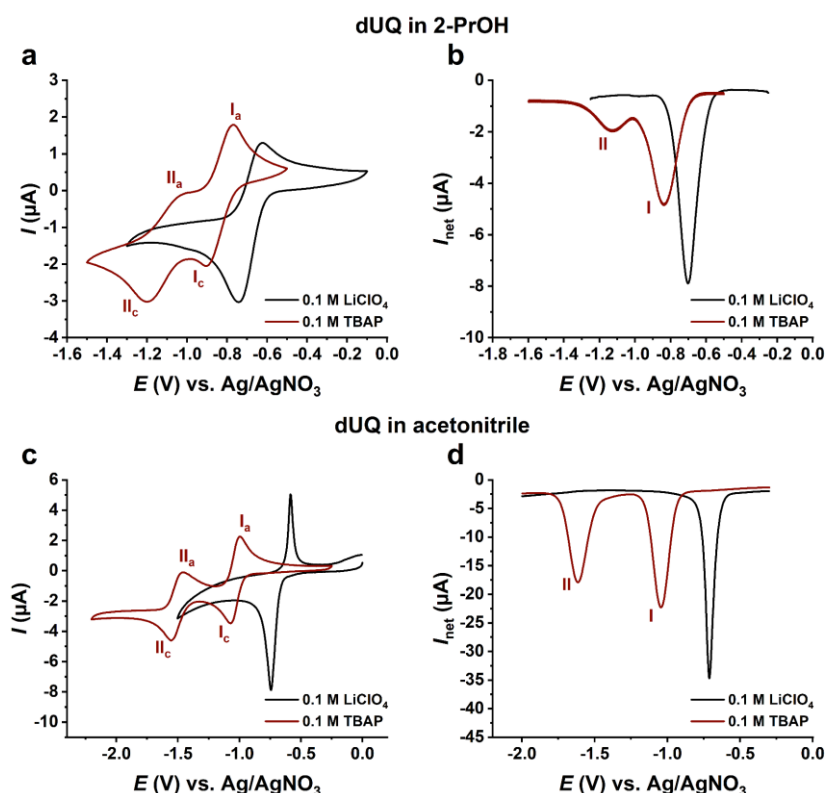
Figure 4-31 The effects of different supporting electrolytes on the voltammetric response of Qs. The effects of lithium perchlorate ($LiClO_4$) and tetrabutylammonium perchlorate (TBAP) on the voltammetric responses of 0.5 mM dUQ in 2-propanol (a, b) and acetonitrile (c, d). CV: v = 20 mV/s, ΔE = 1 mV; SWV: f = 8 Hz, E_{sw} = 50 mV, ΔE = 1 mV.

Figure 4-32 shows the effect of Li^+ concentration on the voltammetric responses of dUQ in acetonitrile with 0.1 M TBAP as supporting electrolyte. Titration of $LiClO_4$ to a de-aerated

acetonitrile solution of dUQ revealed a similar behaviour of the voltammetric response as Ca^{2+} (Figure 4-27) and had a large effect on the peak potentials of dUQ. A 0.5 mM [Li^+] resulted in a complete loss of both transition waves (black solid line, Figure 4-32 a and b) and the appearance of a new single redox peak III at more positive potential which was slightly shifted to more positive potentials as Li^+ concentration was further increased (dashed lines and red solid line, panel a). The new peak III arose at more positive potentials and was present in the voltammogram already at very low concentrations of Li^+ ions (0.1 mM) (dark red dashed line, panel b).

dUQ in acetonitrile
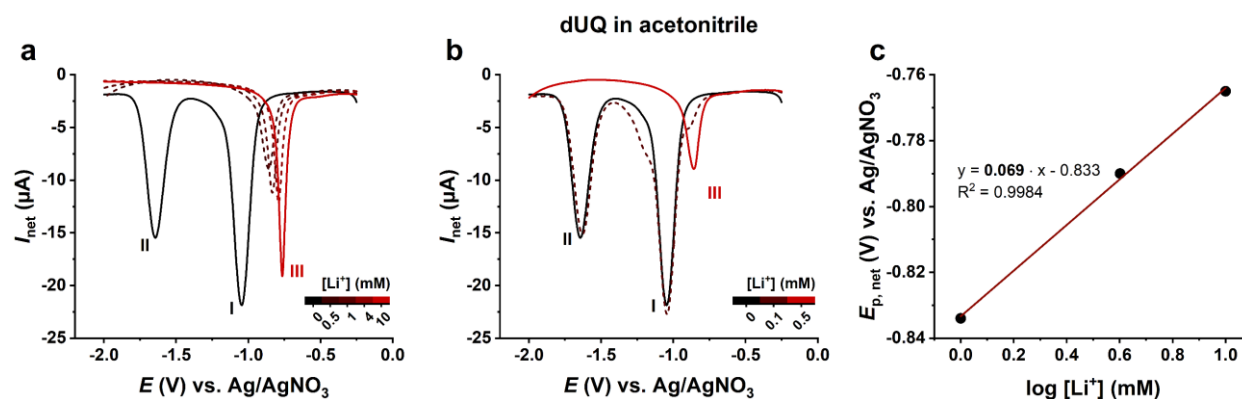
Figure 4-32 Effects of Li^+ on the voltammetric responses of dUQ in acetonitrile. Square-wave voltammograms of 0.5 mM dUQ in the absence (black solid line) and in the presence of a) higher and b) lower concentrations of Li^+ than the concentration of dUQ (dashed lines and solid red line) in de-aerated acetonitrile solution with 0.1 M TBAP as electrolyte at GC electrode. c) Dependence of the net peak potential of III of 0.5 mM dUQ on the logarithm of [Li^+] from panel a.

4.3 Functional studies on the cellular and mitochondrial metabolism in quinone-treated cells and isolated mitochondria

Coenzyme Q_{10} (Q_{10}) is an essential electron carrier and important antioxidant in the inner mitochondrial membrane. Manipulating Q_{10} content within cells and especially in mitochondria may help in understanding functions of the quinone and exploring its therapeutic potential. One way to increase the cellular and mitochondrial concentration of Q_{10} is to administer it to cells or isolated mitochondria. However, the hydrophobicity of Q_{10} and its consequently low solubility in aqueous solutions is limiting this approach. Several attempts to supplement HEK-293 cells with Q_{10} or HO-Q_{10} using solutions with a final concentration of 1% ethanol produced inconsistent results. Under these conditions, most often cells were detaching from the cover slips, impairing the measurements, and additionally, ethanol at concentrations higher than 0.1% is known to interfere with many physiological processes of the cell[255–257]. On the other hand, the use of ethanol as a solvent for stock solutions of quinones limits the maximal concentration in aqueous media to 10 µM and 50 µM for Q_{10} and HO-Q_{10}, respectively[16].

Since cell supplementation by Q_{10} and HO-Q_{10} was greatly limited by their lack of solubility in aqueous media, and more importantly, by the correlated lessened uptake by cells and impeded intracellular distribution, we introduced water-soluble Q_{10} formulations to administer Q_{10} as well as HO-Q_{10} to biological samples.

4.3.1 Preparation of water-soluble formulations of the quinones and mono-hydroxylated derivatives

To enhance the solubility and bioavailability of poorly water-soluble Q_{10}, water-soluble (WS) formulations were prepared by solubilization with the carrier conjugate Cholesterol-PEG 600

(PCS) following the Borowy-Borowski[189] method. This protocol to enclose Q_{10} in nanomicelles formed with PCS was adopted for HO-Q_{10}. In Figure 4-33 a solutions of 10 mM Q_{10}-PCS and HO-Q_{10}-PCS (left panel) and 5 mM Q_{10}-PCS and HO-Q_{10}-PCS (right panel) prepared in water are shown. Q_{10} (left vials) gave a yellow-coloured solution and HO-Q_{10} (right vials) a reddish-brown coloured solution. UV-Vis absorption spectra, displayed in Figure 4-33 b and c, showed that high concentrations (100 µM) in water were reached for both substances. Absorption spectra of Q_{10} (panel b) show the characteristic quinone absorption peak around 275 nm and absorption of visible light around 400 nm. Spectra of HO-Q_{10}, shown in Figure 4-33 c, consisted of the typical quinone absorption peak at 275 nm and the broad absorption band at around 500 nm, characteristic for the HO-Qs. Absorption at 275 nm was increased by a factor of two when concentrations were doubled for both compounds (arrows, Figure 4-33 b and c).
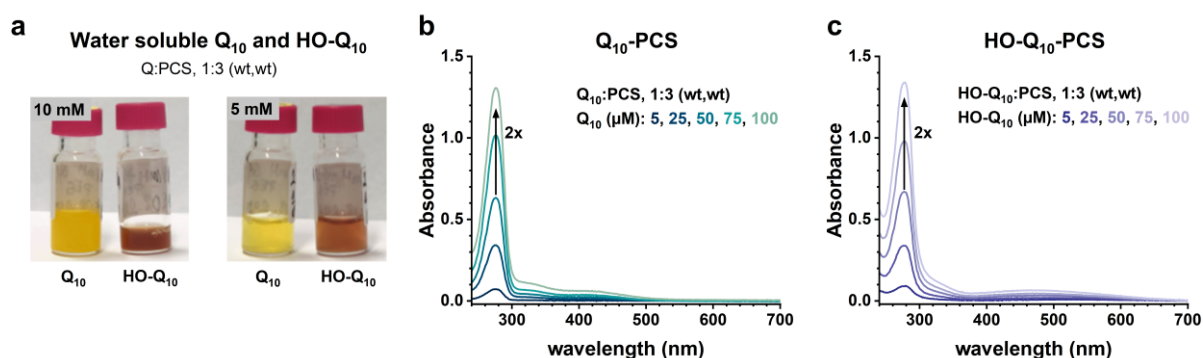
Figure 4-33 Aqueous solutions of Q_{10} and HO-Q_{10} using Cholesterol-PEG 600. a) Stock solutions of 10 mM (left) and 5 mM (right) Q10-PCS (yellow colour, left vial) and HO-Q_{10}-PCS (reddish-brown colour, right vial) in water. Q:PCS, 1:3 (wt/wt). UV-Vis absorption spectra of different concentrations of b) Q_{10}-PCS and c) HO-Q_{10}-PCS in water. Arrows indicate increase in the absorption by a factor of two when concentrations were doubled (50 µM compared to 100 µM).

Following this protocol, aqueous solutions with high concentrations (mM range) of Q_{10} and HO-Q_{10} were successfully prepared. Q_1, dUQ, mQ and their mono-hydroxylated forms are less hydrophobic than Q_{10} and HO-Q_{10}, so that they can be easily dissolved in water in sufficiently high concentrations mixed with very low amounts of organic solvents like ethanol or DMSO. Nevertheless, the procedure from Borowy-Borowski[189] was adapted for preparation of their WS formulations for supplementing endogenous Q levels in whole cells and mitochondria to assure comparable conditions for all studied quinones.

Exact concentrations of the stock solutions of the quinones in the WS formulations were calculated with *Lambert-Beer* equation (Eq. 3-3) by measuring the absorbance at 275 nm and utilizing literature values of the molar extinction coefficients (ε) for the quinones (Table 3-3).

4.3.2 Exogenous supplementation of HEK-293 cells with water-soluble formulations of the quinones and mono-hydroxylated forms

To obtain insights in the effects of the Qs and HO-Qs on the mitochondrial respiratory chain and on the cellular Ca^{2+} homeostasis, the first step was to test how their contents within the cells were affected by exogenous supplementation with Q_{10}-PCS and HO-Q_{10}-PCS. For this purpose, a simple HPLC method has been optimized and applied to determine the content of Q_{10} and HO-Q_{10} in HEK-293 cells. As a first step, concentrations of endogenous Qs had to be measured. Thereafter, we tested whether administered Q_{10} and HO-Q_{10} were taken up by the cells.

Figure 4-34 panel a shows typical chromatograms of the calibration solution (mixture of the three compounds, Q_9, HO-Q_{10} and Q_{10}) at five different concentrations. The HPLC method provided good chromatographic resolution, i.e., well-shaped peaks and very good separation of the three compounds with retention times of 14.66 minutes for Q_9, 16.60 minutes for HO-Q_{10} and 23.28 minutes for Q_{10} (Figure 4-34 a), required for reliable quantification. An excellent linear relationship ($R^2 = 0.99$) was observed between the area of the peak (mAU/min) and the molar concentration of each compound over a wide concentration range from 10 to 1000 nM (Table 4-7). The baseline was clean, and the lower limit of quantification was 10 nM.

Table 4-7 Standard curves for HPLC determination of Q_{10} and HO-Q_{10} content in quinone-treated HEK-293 cells. Summary of linearity (range, slope, intercept and R^2 values) of the calibration solution and analyte retention times.HPLC parameters are given in section 3.6.1.

Analyte	Linearity				Retention time (min)
	Range (nM)	R^2	Slope ± SD	Intercept ± SD	
Q_9	10−1000	0.998	0.1027±0.0002	0.0156±0.246	14.66
HO-Q_{10}	10−1000	0.999	0.1084±0.0006	0.1908±0.282	16.60
Q_{10}	10−1000	0.998	0.1074±0.002	0.7784±1.009	23.28

In the next step, cultured HEK-293 cells were supplemented with 20 µM Q_{10}-PCS and HO-Q_{10}-PCS, respectively for 30 minutes and cell lysates were prepared as described in section 3.6.1.

Determination of the Q_{10} content in biological matrices is hampered by its hydrophobic nature, thus its extraction from biological material is a crucial step that affects the quantitative yield. Due to its hydrophobic nature, Q_{10} dissolves easily in non-polar solvents such as hexane and chloroform, while its solubility in lower alcohols is limited following the order 1-propanol > 2-propanol > ethanol. Thus, the non-polar phase from the cell lysates was selectively extracted using liquid-liquid extraction. Extraction efficiencies of two different solvent mixtures, water/ethanol/hexane (1:2:5) and water/ethanol/chloroform (1:2:5) were evaluated. Hexane proved to be more effective than chloroform resulting in a signal enhancement factor ranging from 2- to 5-fold increase for both Q_{10} and HO-Q_{10} and was consequently selected as solvent for the extraction. Recovery (extraction efficiency) data were obtained by adding known amounts of Q_9 to the cell lysates before extraction steps. Q_9 was selected as standard control due to its structural similarity to the targeted analytes. The extraction efficiency for Q_9 was 89%.
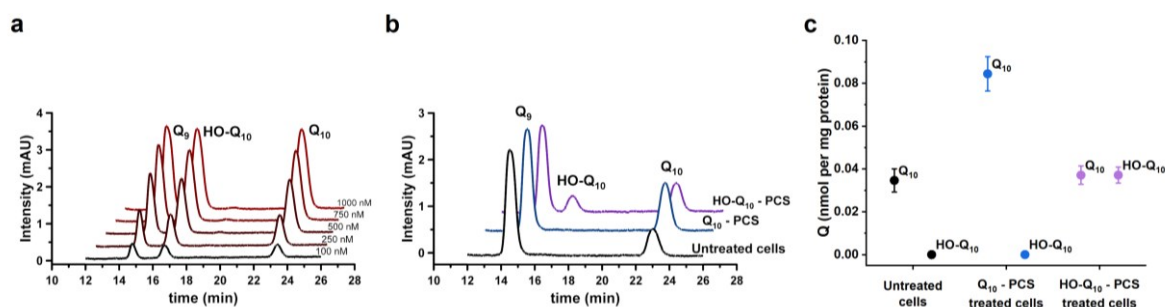
Figure 4-34 HPLC determination of cellular content of Q_{10} and HO-Q_{10} in HEK-293 lysates. a) HPLC chromatograms of 100-1000 nM Q_9, HO-Q_{10} and Q_{10}, used for preparation of standard curves. b) HPLC chromatograms of extracted samples from untreated (control) cells (black; corresponds to intrinsically present Q_{10}), cells treated with 20 µM Q_{10}-PCS (blue) or 20 µM HO-Q_{10}-PCS (purple) for 30 minutes. Q_9 as a standard control for extraction efficiency. c) Intracellular contents of Q_{10} and HO-Q_{10} before (untreated cells, black) and after supplementation with Q_{10}-PCS (blue) or HO-Q_{10}-PCS (purple). Data were normalized to total cellular protein content. Values are mean±SEM, n=5 experiments, each with ~5 x 10^6 cells.

Extracted cell-derived samples were run and analysed by HPLC (Figure 4-34 b). As shown, elution times of Q_9, Q_{10} and HO-Q_{10} from the extracts were identical to their retention times in the chromatogram of calibration solutions (Figure 4-34 a and Table 4-7).

Since Q_{10} is the predominant form of coenzymes Q in human cells, a certain amount of Q_{10} was detected as expected in the untreated HEK-293 cells (black line, Figure 4-34 b). The measured concentration of Q_{10} in control HEK-293 cells was 0.03465 nmol/mg protein (panel c). However, HO-Q_{10} was not detected in the control (black line, panel b) and also not in the sample of cells treated with Q_{10}-PCS (blue line, panel b). Data showed significantly elevated contents of Q_{10} (blue colour, panels b and c) and HO-Q_{10} (purple colour, panels b and c) following 30 minutes of supplementation of the cells with the corresponding compounds. The concentration of Q_{10} after treatment with 20 µM Q_{10}-PCS for 30 minutes was approximately 3-fold higher than the Q_{10} content in control cells (0.03465 nmol/mg protein vs. 0.08444 nmol/mg protein, panel c). The content of Q_{10} was similar in the control cells and cells treated with HO-Q_{10}-PCS (0.03465 nmol/mg protein vs. 0.03712 nmol/mg protein, black- and purple-coloured dots, respectively, panel c). Furthermore, the concentration of HO-Q_{10} after treatment with HO-Q_{10}-PCS was 0.03715 nmol/mg protein (purple colour, panel c), while HO-Q_{10} was not detectable in the control cells (black colour, panels b and c) and in the cells treated with Q_{10} (blue colour, panels b and c). These results demonstrated that Q_{10}-PCS and HO-Q_{10}-PCS efficiently passed through the plasma membrane and were accumulated in the cells.

4.3.3 Cell viability of quinone-treated HEK-293 cells

Given that the hydroxylated forms, HO-Q_1 and HO-dUQ as well as of HO-mQ[149], were for the first time purified in our lab, nothing is known about their potential functions in cellular processes. Moreover, it was questionable whether Qs and HO-Qs may have toxic effects, even when applied in small amounts. It has been shown that embelin (2,5-dihydroxy-3-undecyl-1,4-benzoquinone), a hydroxylated benzoquinone, impairs tumour growth[258] so it was important to evaluate if the hydroxylated as well as the native forms of Qs may influence viability of cells.

After cells treatment with Qs-PCS and HO-Qs-PCS, viability of HEK-293 cells was investigated by the *CellTiter-Blue Assay*. Cholesterol-PEG 600 (PCS), used to prepare water-soluble formulations, was applied as a control. Measurements were conducted at different time points 2, 24 and 48 hours (Figure 4-35). The results showed that there was no difference in viability between untreated controls and HEK-293 cells supplemented with dUQ/HO-dUQ, Q_{10}/HO-Q_{10}, HO-Q_1 or with the control substance PCS (Figure 4-35). Treatment with Q_1 for 2 hours did not influence the cell viability; nevertheless, decline in cellular metabolic activity compared to the controls was observed after 24- and 48-hours treatment with Q_1. In contrast, treatment with mQ showed that viability of the cells was strongly affected and extremely decreased. Around 90% of the cells were lost after 2 hours, indicating a strong cytotoxic effect of mQ when applied at a concentration of 20 µM. Supplementing HO-mQ for 2 hours did not affect viability; however, treatment for 24 hours resulted in reduction of the cellular metabolic activity to 70% compared to

untreated control. A further drop to about 50% was observed after 48 hours. Obviously, HO-mQ was less cytotoxic than mQ.
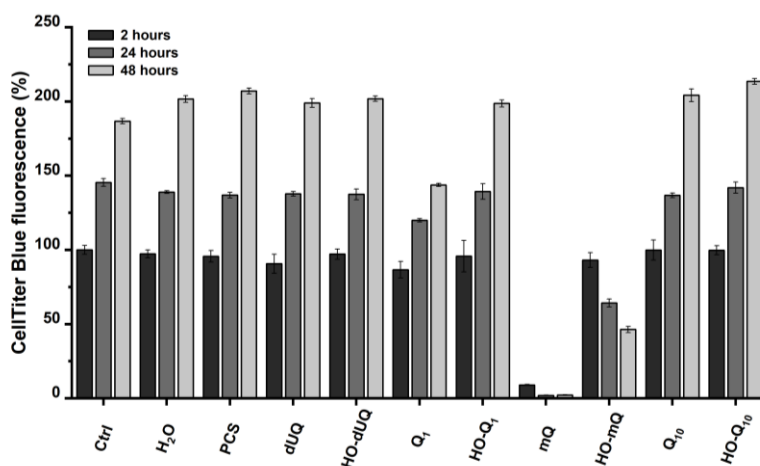
Figure 4-35 Effects of application of quinones and their mono-hydroxylated forms on the viability of HEK-293 cells. Cells were treated with 20 µM dUQ, HO-dUQ, Q_1, HO-Q_1, mQ, HO-mQ, Q_{10} and HO-Q_{10}. Controls included untreated cells, treated cells with water and treated cells with PCS. Resazurin fluorescence was normalized to the signal of untreated cells after 2 hours. Graph shows mean±SEM from 5 replicates of 2 independent experiments.

4.3.4 Calcium measurements in quinone-treated HEK-293 cells

Because Qs are an essential constituent of the mitochondrial respiratory chain and based on the essential role of mitochondrial Ca^{2+} uptake for cells, our interest was to monitor a possible impact of the Qs and particularly HO-Qs on cellular Ca^{2+} homeostasis. As shown by voltammetric experiments, HO-Qs have a higher Ca^{2+} affinity than Qs, which led us to investigate the effects of exogenously supplemented HO-Qs-PCS and Qs-PCS on Ca^{2+} signalling in HEK-293 cells.

First, intracellular Ca^{2+} ($[Ca^{2+}]_i$) was assessed under basal conditions, i.e., in the presence of 0.5 mM Ca^{2+} *Ringer* buffer. Then, in the absence of extracellular Ca^{2+} (Ca^{2+}-free buffer) cells were treated with thapsigargin (Tg), an irreversible inhibitor of the SERCA pumps. This caused release of Ca^{2+} from the ER stores into the cytosol. The elevated $[Ca^{2+}]_i$ activates PMCAs and restores the basal $[Ca^{2+}]$ in the cytosol. Addition of Ca^{2+} to the extracellular buffer (2 mM Ca^{2+} *Ringer* buffer) is then followed by opening of plasma membrane Ca^{2+} channels (ORAI) and influx of Ca^{2+} into the cell (store-operated Ca^{2+} entry, SOCE).

In Figure 4-36 (panels a, c and e) are shown the traces of the ratio of the Ca^{2+} indicator fura-2 signals at 340/380 nm, measured in HEK-293 cells. Black lines show a typical trace for untreated HEK-293 cells, grey lines represent PCS control and coloured traces represent results after cells treatment with Qs/HO-Qs. From these data the following parameters were analysed: the maximum peak induced by Tg (ΔTg Peak), the maximum after addition of 2 mM Ca^{2+} (ΔPeak), plateau (ΔPlateau) and the Ca^{2+} influx rate, as explained in section 3.6.3. As evident from Figure 4-36 a and b, no differences for basal $[Ca^{2+}]_i$ levels and ΔTg Peak were detected between untreated control HEK-293 cells (black line) and cells treated only with PCS (grey line). Likewise, SOCE was restored under both conditions and ORAI-mediated Ca^{2+} influx was not significantly[*] different in ΔPeak, ΔPlateau and in the Ca^{2+} influx rate (panel b, black- and grey-coloured bars).

---

[*] The statistical analysis did not yield significant differences between untreated cells control and PCS-treated cells. To enhance clarity and simplify the graphs, the ns for the controls has been excluded.

Figure 4-36 Effects of Qs and HO-Qs on the intracellular $[Ca^{2+}]$ in HEK-293 cells. Representative traces of fura-2 ratio at 340/380 nm corresponding to cytosolic $[Ca^{2+}]$ levels in HEK-293 cells supplemented with 20 µM a) Q_{10} (dark violet), HO-Q_{10} (light violet), c) Q_1 (dark red), HO-Q_1 (light red), e) dUQ (dark blue), and HO-dUQ (light blue). Cells were perfused with *Ringer* buffer with different $[Ca^{2+}]$ (mM) as indicated above each graph. ER Ca^{2+} release was prompted by 1 µM thapsigargin (arrow; Tg) and Ca^{2+} influx by addition of 2 mM Ca^{2+} in the external solution. S with arrow indicates addition of 20 µM Qs, HO-Qs or control (PCS). Quantification of the changes in the fura-2 ratio b), d), f) of ΔTg peak, ΔPeak, ΔPlateau and Ca^{2+} influx rate calculated from the experimental results in panels a), c) and e), respectively. Statistical test: One-way ANOVA with *Dunnett* multiple comparisons test; ns, $p \geq 0.05$; *, $p < 0.05$; **, $p < 0.01$; ***, $p < 0.001$; ****, $p < 0.0001$. Controls: n = 360; 30 cells/per condition from 12 individual experiments; Qs, HO-Qs: n = 240; 30 cells/per condition from 8 individual experiments.

Additionally, no differences were detected for basal $[Ca^{2+}]_i$ levels for HEK-293 cells supplemented with Q_{10} (panel a), HO-Q_{10} (panel a), Q_1 (panel c), HO-Q_1 (panel c) and dUQ (panel e). Once HO-dUQ was applied, the basal $[Ca^{2+}]_i$ levels started to increase gradually over time compared to the controls (panel e, light blue trace). The ΔTg Peaks reached similar maximum levels for all Qs and HO-Qs compared to the controls. The Ca^{2+} influx peak (ΔPeak) and the plateau (ΔPlateau) as

well as the Ca^{2+} influx rate in the presence of Q_{10}, HO-Q_{10}, Q_1 and HO-Q_1, were similar to those of the control cells (panels b and d, correspondingly). Store-operated Ca^{2+} influx (SOCE) was not detectable after cells treatment with HO-dUQ (light blue colour, panels e and f). On the other hand, in dUQ-treated cells SOCE could be detected, albeit at significantly lower levels compared to the controls (darker blue colour, panels e and f).

Following treatment with HO-dUQ, the basal $[Ca^{2+}]_i$ instantly began to gradually increase over time which was not observed in the control cells. This prompted the investigation of the source of Ca^{2+} into the cytosol, whether it originates from the extracellular buffer solution or from intracellular Ca^{2+} stores. An attempt to monitor the cells for 30 minutes in Ca^{2+}-free solution was unsuccessful since the cells were detaching from the cover slips and flushed away. Alternatively, HEK-293 cells were treated with HO-dUQ and monitored for 30 minutes in constant extracellular $[Ca^{2+}]$ of 0.5 mM (Figure 4-37 a). Again a continuous gradual elevation in $[Ca^{2+}]_i$ was observed. No such behaviour was seen in the control cells or after treatment with Q_{10} or HO-Q_{10} (Figure 4-37 a). If the gradually increasing Ca^{2+} influx originated from the extracellular solution, an equilibrium should be reached within 30 minutes. As this was not the case, most likely intracellular stores could be the source for this Ca^{2+}. Four major intracellular Ca^{2+} stores come into play: ER, mitochondria, Golgi apparatus and lysosomes. To check for the ER, the ER Ca^{2+} stores were depleted with Tg and then HO-dUQ was added in Ca^{2+}-free conditions for 10 minutes (Figure 4-37 b). Once again, a gradual increase of the cytosolic Ca^{2+} signals was observed. Since Ca^{2+} influx from extracellular solution (Ca^{2+}-free buffer) could be excluded, Ca^{2+} most probably originates from another intracellular Ca^{2+} store than ER. Mitochondria, Golgi apparatus and lysosomes, which can accumulate significant amounts of Ca^{2+}, are candidates for further investigation. To empty all Ca^{2+} stores, ionomycin (Im) was used (Figure 4-37 b). Im caused immediate increase of $[Ca^{2+}]_i$ under control and HO-dUQ conditions. The above-mentioned organelles showed to contain enough Ca^{2+} to function as possible sources for HO-dUQ-induced Ca^{2+} release. Moreover, the Im-induced Ca^{2+} peak declined to basal $[Ca^{2+}]_i$, showing that the activities of the PMCAs and NCXs are not affected by Im and HO-dUQ. Consequently, one can assume that the HO-dUQ-induced increase of Ca^{2+} would be even higher if the activities of PMCAs and NCXs would not counteract it.
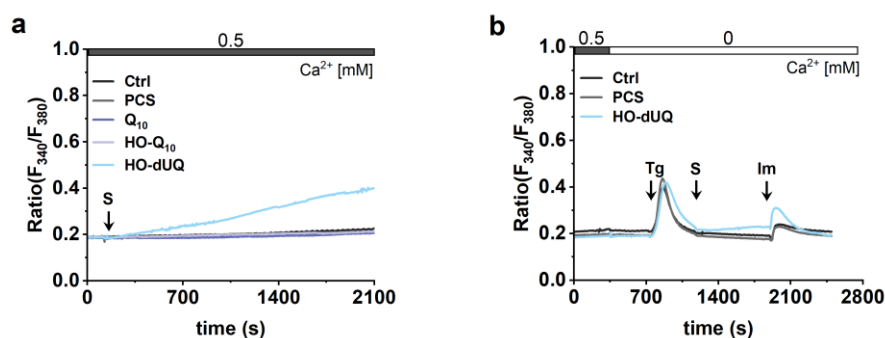
Figure 4-37 Ca^{2+} dynamics induced by HO-dUQ in HEK-293 cells. a) Representative traces of fura-2-loaded HEK-293 cells (ratio at 340/380 nm) corresponding to cytosolic $[Ca^{2+}]$ levels in the cells supplemented with 20 μM Q_{10} (dark violet), HO-Q_{10} (light violet), and HO-dUQ (light blue). b) Fura-2 ratio at 340/380 nm in HEK-293 cells challenged with 4 μM ionomycin (arrow, Im) in the presence or absence of 20 μM HO-dUQ (arrow, S), after ER store depletion with 1 μM thapsigargin (arrow, Tg) in Ca^{2+}-free buffer. S with arrow indicates addition of the HO-dUQ or control (PCS). External $[Ca^{2+}]$ (mM) is indicated above each graph. n = 120; 30 cells/per condition from 4 individual experiments.

The impact of mQ and HO-mQ on Ca^{2+} transients in HEK-293 cells is clearly demonstrated in Figure 4-38. Upon addition of both, mQ and HO-mQ to the cells, basal $[Ca^{2+}]_i$ started to rise (panel a). Notably, mQ (dark green trace) induced a rapid increase quickly reaching a plateau, while HO-mQ (light green trace) gradually elevated the Ca^{2+} levels in cytosol. Moreover, the impact of mQ was particularly pronounced, significantly affecting ΔTg Peak and ΔPeak parameters to such an extent that SOCE-mediated Ca^{2+} influx was not detectable (dark green bars, panel b). In contrast, in HO-mQ-treated cells both, ΔTg peak and SOCE-mediated Ca^{2+} influx, could be detected, albeit at significantly lower levels compared to the controls (light green bars, panel b). Furthermore, the data indicate that Ca^{2+} influx was considerably and significantly reduced in peak and plateau, accompanied by a substantially decreased influx rate.
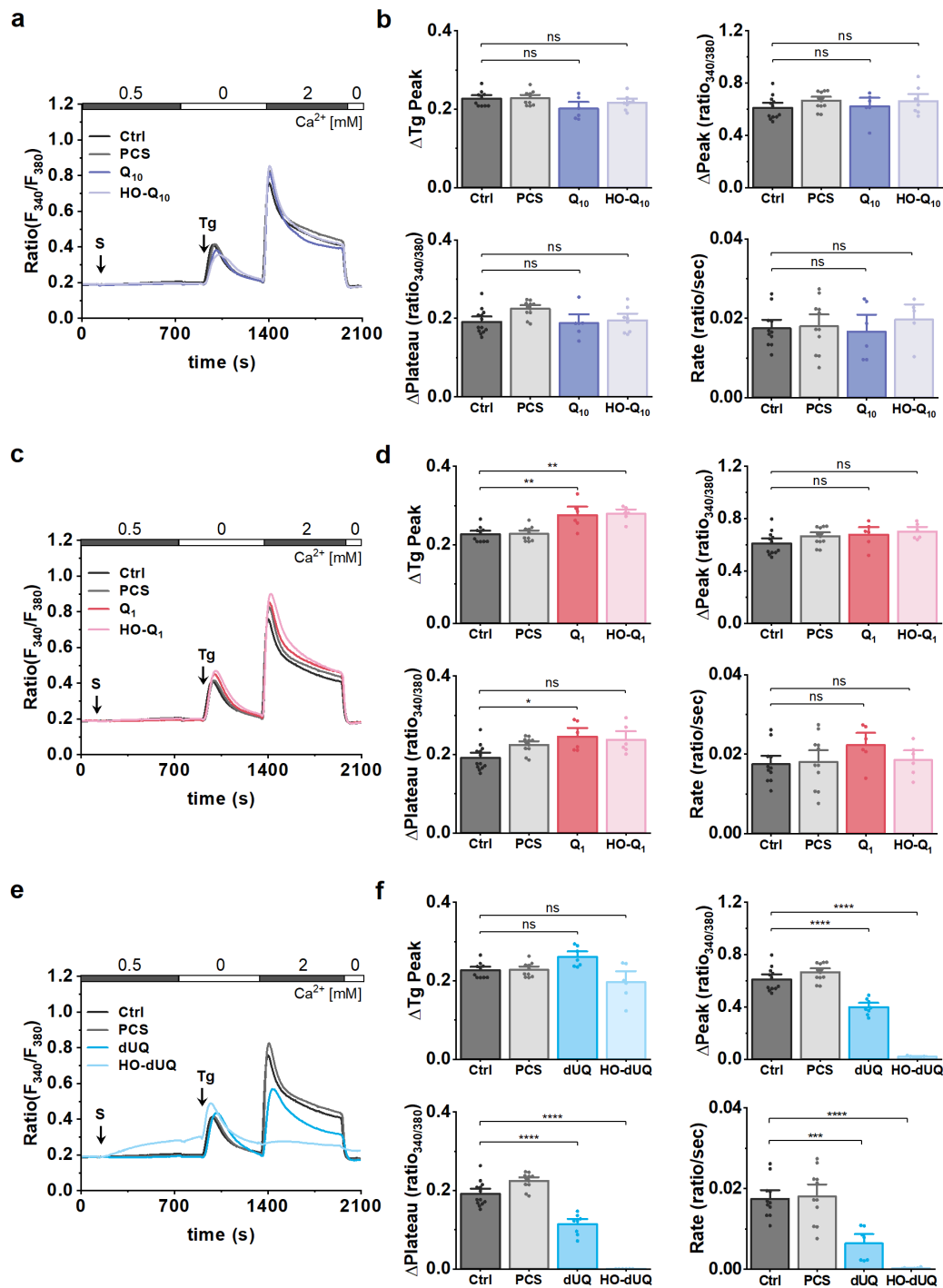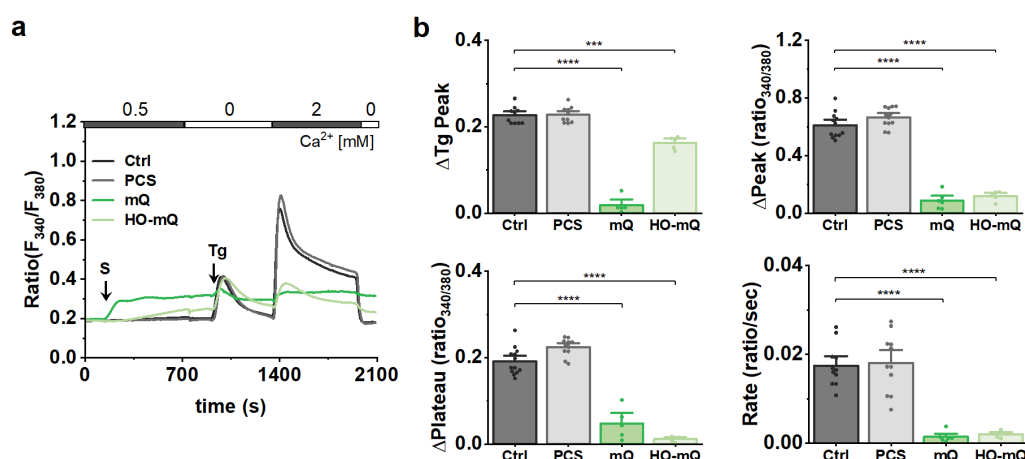

Figure 4-38 Effects of mQ and HO-mQ on the intracellular $[Ca^{2+}]$ in HEK-293 cells. a) Representative traces of fura-2 ratio at 340/380 nm corresponding to cytosolic $[Ca^{2+}]$ levels in HEK-293 cells supplemented with 20 μM mQ (dark green) and HO-mQ (light green). Cells were perfused with *Ringer* buffer with different $[Ca^{2+}]$ (mM) as indicated above each graph. ER Ca^{2+} release was triggered by 1 μM thapsigargin (arrow; Tg) and Ca^{2+} influx was prompted by 2 mM Ca^{2+} from the external solution. S with arrow indicates addition of 20 μM mQ, HO-mQ or control (PCS). Quantification of the changes in fura-2 ratio of b) ΔTg peak, ΔPeak, ΔPlateau and Ca^{2+} influx rate calculated from the experimental data in panel a). Statistical test: One-way ANOVA with *Dunnett* multiple comparisons test; ns, $p\geq0.05$; *, $p<0.05$; **, $p<0.01$; ***, $p<0.001$;****, $p<0.0001$. Controls: n = 360; 30 cells/per condition from 12 individual experiments; mQ, HO-mQ: n = 120; 30 cells/per condition from 4 individual experiments.

4.3.5 Mitochondrial membrane potential in quinone-treated HEK-293 cells

ER $[Ca^{2+}]$ and mitochondrial $[Ca^{2+}]$ depend on each other as well as on functioning Ca^{2+} influx across the plasma membrane. ER Ca^{2+} stores and their replenishment by SOCE can be affected by interferences in mitochondrial Ca^{2+} uptake, which is driven by the mitochondrial membrane potential ($\Delta\Psi_m$). $\Delta\Psi_m$ is not only used to generate ATP, but is also responsible for mitochondrial Ca^{2+} uptake, metabolite and protein transport, production of ROS and has also been related to the process of apoptosis[111,259]. Any factors impacting mitochondrial oxidative phosphorylation will change $\Delta\Psi_m$, consequently altering the mitochondrial Ca^{2+} uptake.

Considering the effects of HO-dUQ, mQ and HO-mQ on the $[Ca^{2+}]_i$ (Figure 4-36 panels e and f and Figure 4-38), the next plausible step was to investigate the influence of the Qs and HO-Qs on $\Delta\Psi_m$. $\Delta\Psi_m$ was determined using the fluorescent dye tetramethylrhodamine methyl ester (TMRM). For this purpose, HEK-293 cells were exposed to the Qs or HO-Qs (supplemented as water-soluble formulations, Q-PCS/HO-Q-PCS). In parallel, a positive control with CCCP was run for each condition. TMRM can pass the plasma membrane and is subsequently taken up by the mitochondria as the most negatively charged part of the cell. Consequently, changes in plasma

membrane potential ($\Delta\Psi_p$, −30 to −80 mV[204]) could affect the TMRM fluorescence. Applying a positive control with CCCP helps to distinguish between the $\Delta\Psi_p$ and $\Delta\Psi_m$, i.e., the difference of the fluorescent intensity of TMRM before and after applying CCCP corresponds specifically to the $\Delta\Psi_m$. As shown in Figure 4-39, untreated HEK-293 cells exhibited a high level of orange fluorescence, whereas untreated but metabolically stressed HEK-293 cells in the CCCP-stimulated sample exhibited a reduced level of orange fluorescence due to the depolarization of the mitochondria, consequently prevented accumulation of the positively charged TMRM.
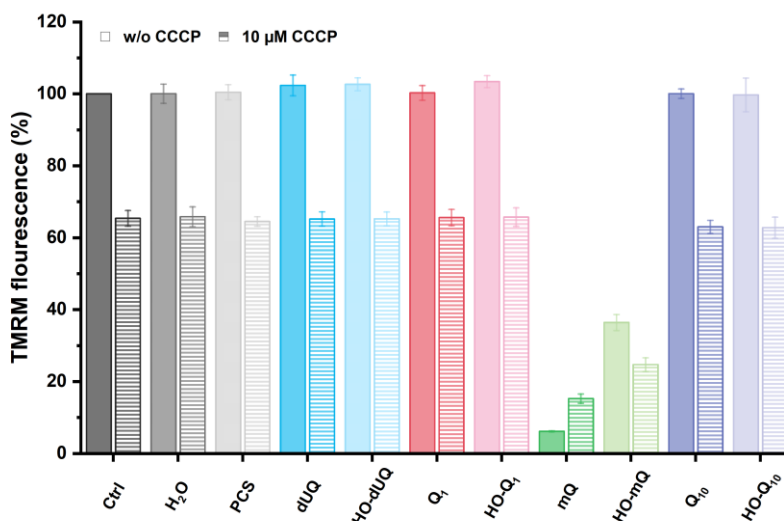
Figure 4-39 Effects of Qs and HO-Qs on the mitochondrial membrane potential in HEK-293 cells. HEK-293 cells were treated with 20 µM test compound (controls: water (grey) and PCS (light grey); test substances Q-PCS (WS formulations of the Qs and HO-Qs): dUQ/HO-dUQ (blue), Q_1/HO-Q_1 (red), mQ/HO-mQ (green) and Q_{10}/HO-Q_{10} (violet). After incubation for 30 minutes under standard culture conditions with the test compounds, TMRM was added to each well to a final concentration of 150 nM. In parallel, positive controls with 20 µM CCCP were run for each condition. The effects of the test compounds on the $\Delta\Psi_m$ were measured by the fluorescence intensity of TMRM. The average TMRM fluorescence intensity for each condition was normalized to the intensity measured for untreated HEK-293 cells (black). Data are expressed as mean±SEM of three independent experiments performed in triplicates.

HEK-293 cells treated with 20 µM mQ (green) and HO-mQ (light green) presented remarkably reduced $\Delta\Psi_m$ as monitored by the decreased uptake of the fluorescent dye TMRM when compared to the controls or to the cells treated with the other Qs and HO-Qs (Figure 4-39). For these compounds, no changes in $\Delta\Psi_m$ were detected with respect to the controls. Because mQ is the only positively charged molecule of our compounds, it is preferentially taken up by negatively charged mitochondria. As a result, it caused collapse of $\Delta\Psi_m$ and subsequent equilibration of TMRM between mitochondria and cytosol, which is responsible for the decrease in fluorescence. Interestingly, HO-mQ also showed a decrease in $\Delta\Psi_m$, but not as pronounced as for mQ. Besides its positive charge (on the TPP[+]-group, Figure 1-9 c), HO-mQ contains the added hydroxyl group which at neutral pH most likely is deprotonated as shown by the voltammetric measurements for HO-Q_1 in different pH (Figure 4-18), and thus partly counterbalances the positive charge.

4.3.6 Assessment of mitochondrial respiration in quinone-treated murine heart mitochondria

Considering the effects of HO-dUQ, mQ and HO-mQ on the on the intracellular [Ca^{2+}] in HEK-293 cells and as an addition to the $\Delta\Psi_m$ measurements, next the function of Qs- or HO-Qs-treated mitochondria, in particular mitochondrial respiration was assessed. Hence, O_2 consumption rate

(OCR) in freshly isolated mitochondria from murine heart (MHM) was evaluated using a high-resolution respirometry.

Before applying the Qs and HO-Qs on mitochondria, the integrity of the outer mitochondrial membrane (OMM) was tested as a quality control of the isolation procedure. OMM is of great importance when assessing the functions of isolated mitochondria. The OMM is easily damaged during tissue homogenization, washing and centrifugation procedures. In case of damaged OMM, cytochrome *c* (cyt *c*) leaks into the buffer and its reduced concentration in IMM becomes rate limiting for OCR and ATP synthesis. The quality and integrity of the prepared MHM were investigated by the cyt *c* test. Since cyt *c* cannot penetrate an intact OMM, exogenous addition of cyt *c* would not have any effect on OCR. Diverging, if the OMM was damaged, addition of cyt *c* would compensate for its loss which will be detected as increased OCR in the respiration experiments.

To this end, mitochondrial respiration was measured after sequential addition of pyruvate/malate (PM), ADP (A) to stimulate the respiration and finally cyt *c* (C). As shown in Figure 4-40, addition of exogenous cyt *c* enhanced the mitochondrial respiration for about 18%, indicating loss of cyt *c* from the mitochondria induced by OMM damage. It has been reported that mitochondria can lose cyt *c* independently of the intactness of the OMM[260], and that the effect of cyt *c* may depend on the used substrates[261,262]. The reasons for the latter are not completely clear. Nevertheless, our results were in the range of acceptably preserved integrity of the OMM (common practice is to accept up to 20% increase in respiration upon addition of cyt *c*)[263].
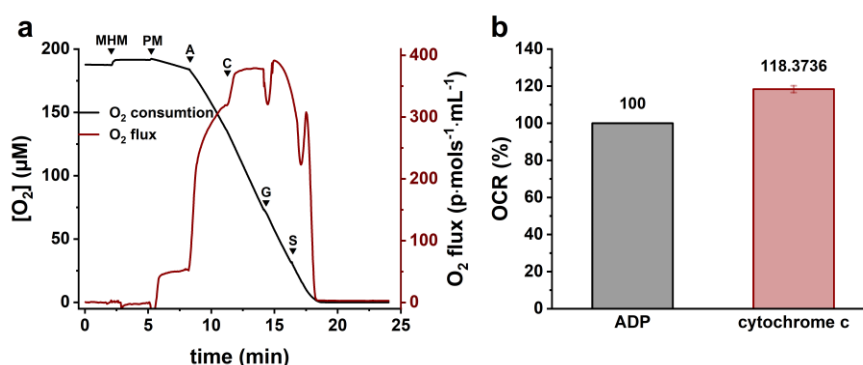
Figure 4-40 Integrity of the outer mitochondrial membrane of isolated mitochondria. a) Oxygen concentration (black line) and oxygen flux (red line) measured in 50 µg/mL mitochondrial protein (MHM) after substrate-stimulated respiration with 5 mM pyruvate and malate (PM) and 1 mM ADP (A). 10 µM cyt *c* (C) was added to assess OMM. b) Oxygen consumption rate (OCR) before (black) and after (red) addition of 10 µM cyt c. Respiration in the presence of cyt *c* was increased by about 18 %, a value in the range indicative for preserved OMM. Graph shows mean±SEM, n=8 from 4 individual mitochondrial preparations. MHM, murine heart mitochondria; G, glutamate; S, succinate.

After quality control of the mitochondria preparation procedure and before applying Qs and HO-Qs to mitochondria, the influence of Ca^{2+} on the mitochondrial respiration was examined. Respiration buffers with defined free Ca^{2+} concentrations (RB_0 – without free Ca^{2+} or RB_1 – 1 µM free Ca^{2+}, Table 2-7) were equilibrated to 37 °C in the sample chamber and then 50 µg/mL mitochondrial protein were added. Activation of the respiration either via Complex I (CI) or Complex II (CII) was achieved by applying complex-specific substrates and inhibitors, followed by addition of a saturating concentration of ADP (1 mM) to fully activate oxidative phosphorylation. Shortly afterwards, the sample or control was added, and the respiration was followed by changes

in [O_2]. Figure 4-41 panel a shows a typical set of O_2 consumption for CI-linked respiration for 50 µg/mL mitochondrial protein in absence (black line) and presence (red line) of 1 µM free Ca^{2+}. Looking at the individual O_2 consumption traces of CI-linked respiration (panel a), the presence of 1 µM free Ca^{2+} significantly slowed down mitochondrial respiration. In the presence of Ca^{2+}, the O_2 consumption trace was less steep (lower O_2 consumption) compared to the trace in the absence of Ca^{2+}. In addition, the presence of Ca^{2+} noticeably increased the time for complete depletion of O_2 in the chamber. In the absence of Ca^{2+}, O_2 was completely used up within 22 minutes (black line), while in presence of Ca^{2+} it was fully consumed within 34 minutes (red line).

CI-linked respiration rate is reported as O_2 consumption rate (OCR) for each addition (MHM, substrate – pyruvate/malate (PM), ADP (A)) normalized to ADP respiration rate in absence of Ca^{2+} (Figure 4-41 b). The average OCRs for each addition were calculated as the mean within 10 s before the addition of the substances. As seen from Figure 4-41 panel a, when [O_2] in the chamber reached 50 µM (grey dashed line), the respiration curve showed a bending which was a result of O_2 depletion. In that case, mitochondrial function is limited by the low O_2 concentration. To avoid a faulty data interpretation, the end point OCR was calculated as the mean within 10 s before an [O_2] of 50 µM was reached. Quantitative evaluation correlating OCRs after each addition for both conditions (0 and 1 µM free Ca^{2+}) illustrates the drastic influence of 1 µM Ca^{2+} on the CI-linked respiration (panel b). 1 µM free Ca^{2+} reduced ADP-dependent respiration rate by 50% compared to the ADP-dependent respiration in the absence of Ca^{2+}. On the other hand, Ca^{2+} did not alter PM-linked respiration rate (Figure 4-41 panels a and b).
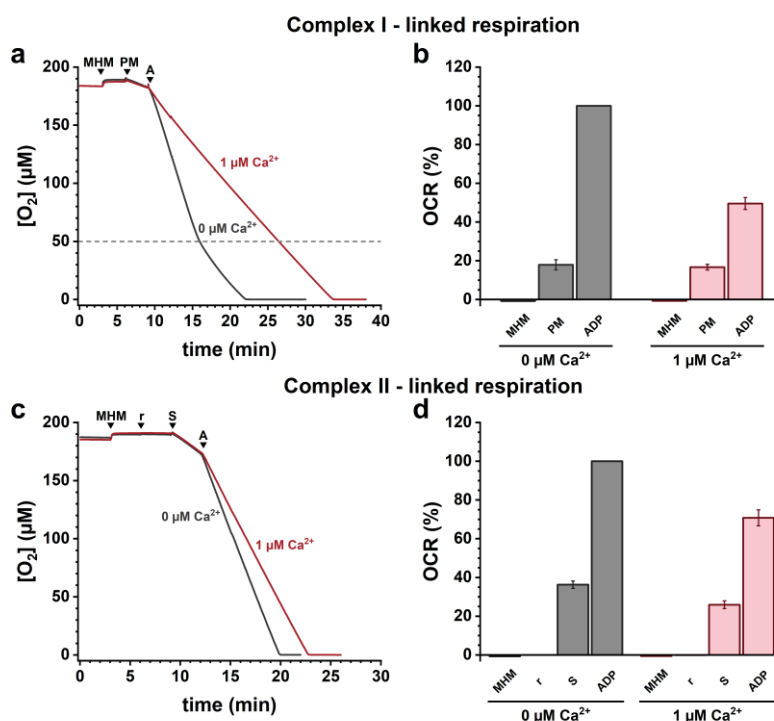
Figure 4-41 Ca^{2+} effects on the CI- and CII-linked respiration in isolated mitochondria. Oxygen (O_2) consumption of 50 µg/mL mouse heart mitochondria (MHM) in the absence (grey) and in the presence of 1 µM Ca^{2+} (red). O_2 consumption traces of a) CI-linked respiration activated by titration of 5 mM pyruvate/malate (PM) and 1 mM ADP (A) and c) CII-linked respiration activated by addition of 0.5 µM rotenone (r), 10 mM succinate (S) and 1 mM A. Quantitative evaluation of O_2 consumption rate (OCR) for b) CI-linked respiration and d) CII-linked respiration. OCR for each individual substance addition was normalized to ADP-stimulated respiration in the absence of Ca^{2+}. Grey dashed line in a) marks the start of the trace bending; the end point OCR was taken as a mean within 10 s before 50 µM [O_2] was reached. Graphs show mean±SEM, n = 8 from 4 individual mitochondria preparations.

To evaluate the effect of Ca^{2+} on the CII-linked respiration, rotenone (r) as a specific CI inhibitor was added prior to CII-substrate succinate (S) and ADP (A). Figure 4-41 panel c shows a typical set of O_2 consumption curves for CII-linked respiration in absence (black line) and presence (red line) of 1 µM free Ca^{2+}. Here, 1 µM Ca^{2+} reduced mitochondrial respiration as seen from the less steep O_2 consumption curve compared to the curve in the absence of Ca^{2+}. O_2 from the chamber was faster depleted in the absence than in the presence of Ca^{2+}. The time differences for complete O_2 depletion, 3 minutes for CII-linked respiration (panel c) and more than 10 minutes for CI-linked respiration (panel a), indicated that CI-linked respiration was more significantly affected by Ca^{2+} than CII-linked respiration. The analysis of the OCRs for CII-linked respiration (panel d) showed that ADP-dependent mitochondrial respiration was reduced by 30% in the presence of 1 µM Ca^{2+}. Moreover, 1 µM Ca^{2+} downgraded succinate-dependent respiration rate by 10% (panel d), which was opposite to CI-linked respiration where Ca^{2+} did not alter substrate-dependent respiration rate (panel b).

Furthermore, the effects of the Qs and HO-Qs on mitochondrial respiration parameters were investigated. The measurements of mitochondrial respiration profiles via CI (Table 3-8) and CII (Table 3-9) were achieved by applying complex-specific substrates and inhibitors as described in section 3.7.2. After subsequent addition of Q-PCS or HO-Q-PCS (or water and PCS as controls) changes in the respiration were measured. In Figure 4-42 typical O_2 consumption curves are shown for CI-linked respiration for 50 µg/mL MHM in the absence (left column) and presence (middle column) of 1 µM free Ca^{2+}.

Exogenous supplementation of dUQ (Figure 4-42 panel a) and HO-Q_{10} (panel j) did not show alteration in OCRs in the absence of Ca^{2+}. Addition of HO-dUQ (panel a), HO-Q_1 (panel d), mQ (panel g) and HO-mQ (panel g) induced less steep curves (lower OCRs). Exogenous supplementation of Q_1 (panel d) in a respiration medium without Ca^{2+} induced a steeper curve (higher OCRs) compared to the controls (water, black line and PCS, grey line).

The effects of exogenously applied Qs and HO-Qs in presence of 1 µM free Ca^{2+} on mitochondrial CI-linked respiration are shown in Figure 4-42 (middle column). Data showed that CI-linked respiration was generally slower (lower OCRs) in presence of 1 µM free Ca^{2+} (black and grey lines, middle column) compared to the respiration in absence of Ca^{2+} (black and grey lines, left column).

Quantitative evaluation of the OCR (Figure 4-42 right column) for both conditions (0 and 1 µM free Ca^{2+}) visualizes the drastic influence of exogenously supplied Qs and HO-Qs on CI-linked respiration. Q_1 (panel e) as well as dUQ (panel b) induced a higher OCRs in Ca^{2+} presence than the controls. An increase in the OCR of about 25% was detected after applying Q_1 in absence of Ca^{2+} which was amplified by 50% in the presence of 1 µM Ca^{2+}, compared to the respective controls (panel f). Significantly lower O_2 consumption was caused by applying HO-dUQ (panel b), HO-Q_1 (panel e), mQ/HO-mQ (panel h) and Q_{10}/HO-Q_{10} (panel k). CI-linked respiration dropped to about 25% for HO-dUQ (panel c) and HO-mQ (panel i) and to about 50% for HO-Q_1 (panel f) and mQ (panel i), independently of Ca^{2+}. Reduced respiration of about 10% for Q_{10} and

75% for HO-Q$_{10}$ (panel l) compared to the controls was observed only in presence of 1 µM Ca^{2+}. Q$_{10}$-treated MHM (panel l) showed an increase of about 25% in absence of Ca^{2+}, whereas in presence of 1 µM Ca^{2+} OCR was decreased for about 10%, compared to the corresponding controls.
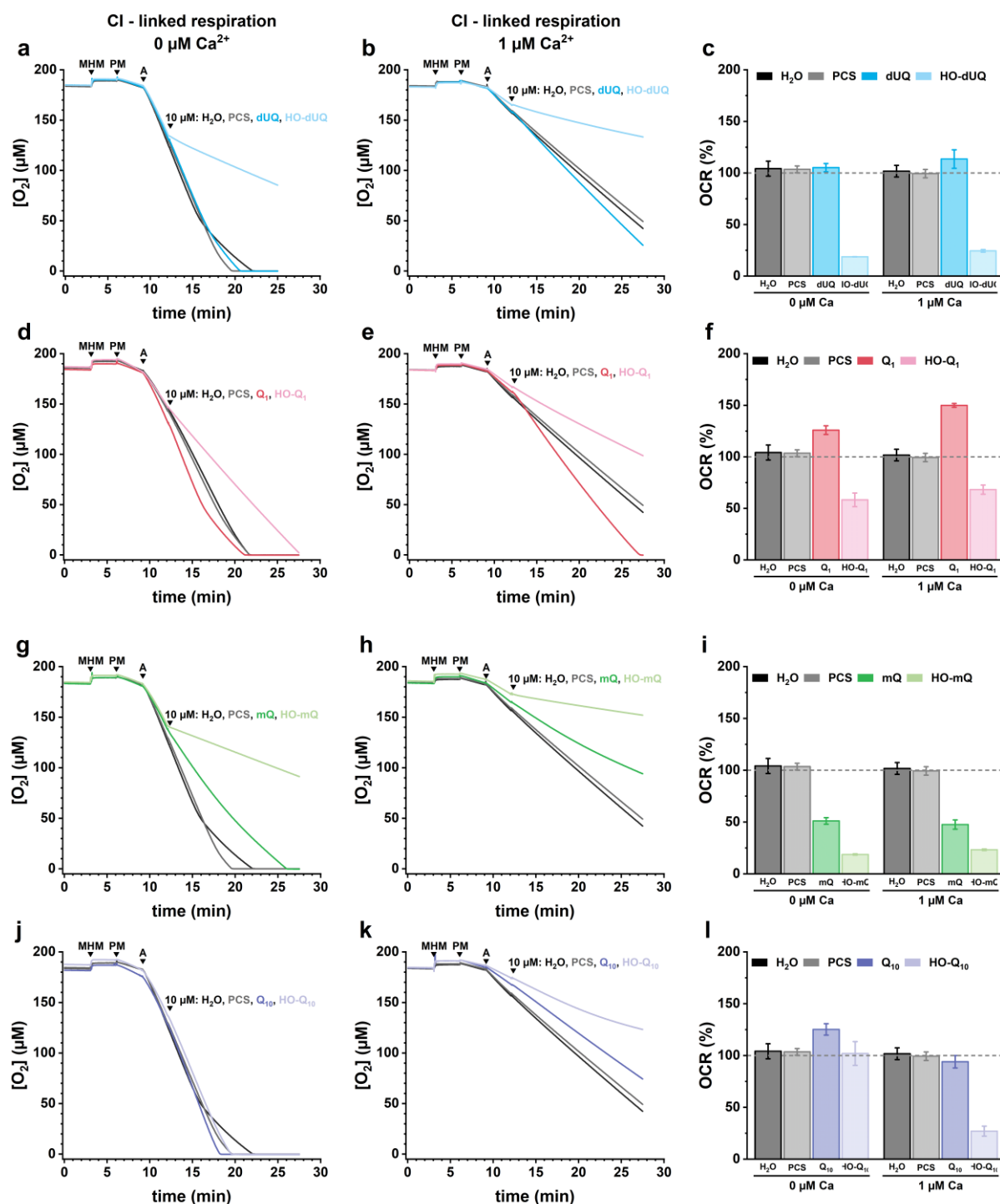
Figure 4-42 Effects of Qs and HO-Qs on the Complex I-linked respiration in isolated mitochondria. 50 µg/mL MHM were incubated at 37 °C in respiration buffer (panels a, d, g, j) in the absence of Ca^{2+} and (b, e, h, k) in the presence of 1 µM free Ca^{2+}. Complex I-specific substrates 5 mM pyruvate/malate (PM), 1 mM ADP (A) and the samples (10 µM Qs, HO-Qs or solvent controls) were added subsequently as indicated to stimulate CI-linked respiration. (a, b, d, e, g, h, j, k) Change of the [O$_2$] over time. (c, f, i, l) Oxygen consumption rate (OCR) after samples (or solvent controls) addition, normalized to OCR in presence of ADP, OCR = (OCR$_{after\ sample}$/OCR$_{after\ ADP}$)·100%. Graphs show mean±SEM, n = 3 from 3 individual mitochondria preparations.

Similar results were observed for CII-linked respiration in the absence and presence of Ca^{2+} after having applied Qs and HO-Qs (Figure 4-43). The OCR was significantly reduced in mitochondria treated with HO-dUQ (panels a, b), mQ and HO-mQ (panels g, h), for both, Ca^{2+}-free and Ca^{2+}-

containing conditions. Exogenous supplementation of HO-Q_{10} also induced decrease in OCR of about 10% compared to the respective controls, which was much more pronounced (~ 50%) in the presence of Ca^{2+} (panels j, k, l). For both conditions, Q_{10} did not show alteration of CII-linked respiration (panels j, k, l). Q_1 (panel e) stimulated higher O_2 consumption when compared to the controls (black and grey lines, panel e), but lower when compared to the consumption for CI-linked respiration (Figure 4-42 e).
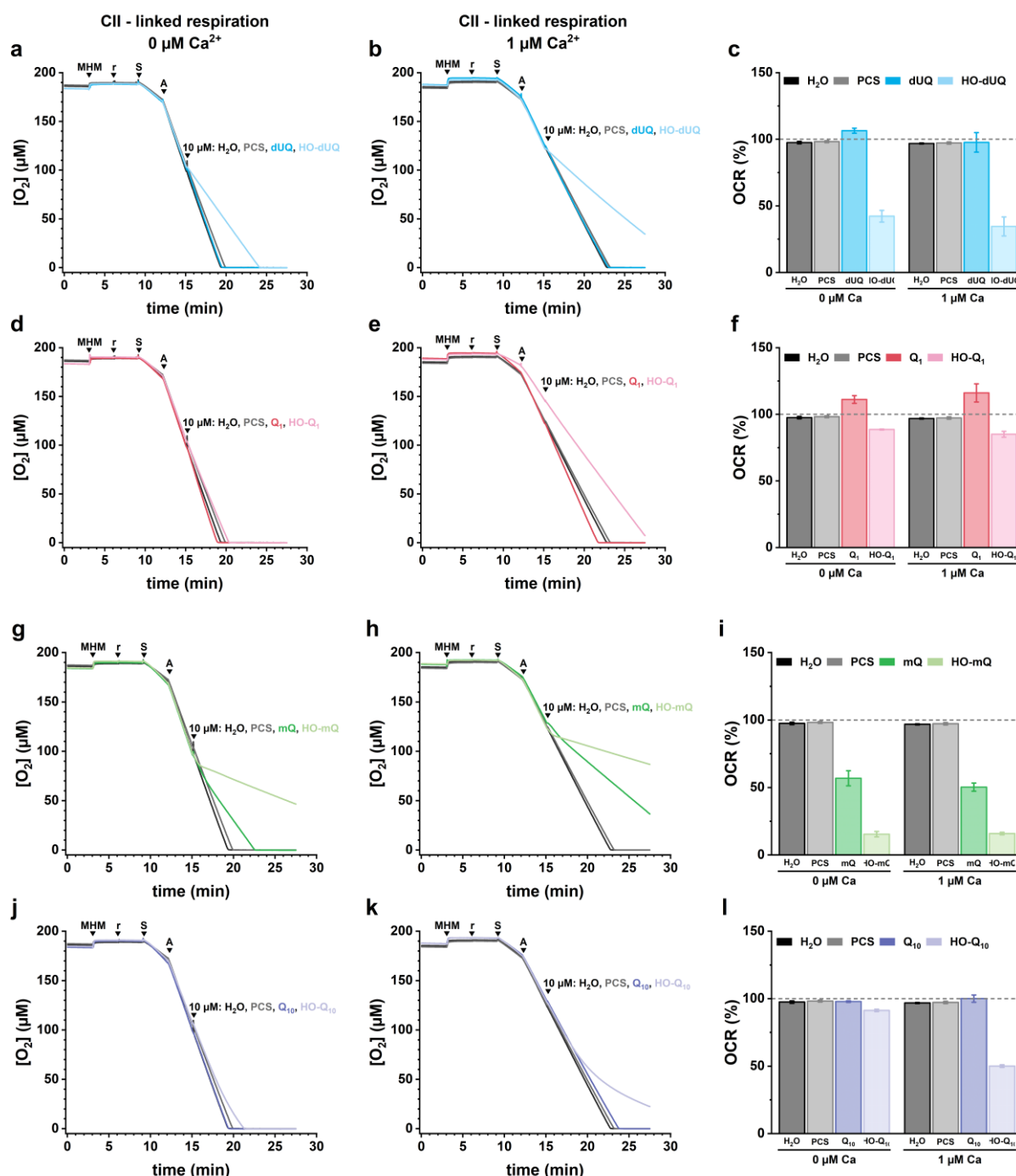
Figure 4-43 Effects of Qs and HO-Qs on the Complex II-linked respiration in isolated mitochondria. 50 µg/mL MHM were incubated at 37 ºC in respiration buffer (panels a, d, g, j) in the absence of Ca^{2+} and (b, e, h, k) in presence of 1 µM free Ca^{2+}. Complex-specific substrates 0.5 µM rotenone (r) and 10 mM succinate (S), 1 mM ADP (A) and the samples (10 µM Qs, HO-Qs or solvent controls) were added subsequently as indicated to stimulate CII-linked respiration. (a, b, d, e, g, h, j, k) Change of the [O_2] over time. (c, f, i, l) OCR after samples (or solvent controls) addition normalized to OCR in presence of ADP, OCR = ($OCR_{after\ sample}$/$OCR_{after\ ADP}$)·100%. Graphs show mean±SEM, n = 3 from 3 individual mitochondria preparations.

Quantitative evaluation of the OCR (Figure 4-43, right column) showed that CII-linked respiration drops to about 25% for HO-mQ (panel i), to about 40% for HO-dUQ (panel c) and to about 50%

for mQ (panel i), independent on Ca^{2+} presence. Slightly reduced CII-linked respiration of 15%, when compared to the controls, was caused by HO-Q_1 in both, Ca^{2+}-free and Ca^{2+} containing conditions (panel f). The effect of HO-Q_{10} was obviously amplified in the presence of Ca^{2+} where CII-linked respiration was reduced by 50% when compared to the controls as well as to the respiration in the absence of Ca^{2+} (panel l).

5. Discussion

5.1 Production and structural characterization of HO-Q_1 and HO-dUQ

Owing to their wide-spread distribution in nature and their biological relevance for many cellular processes, redox and physiological properties of a variety of coenzyme Q derivatives (Qs) have been extensively studied over the years[45,264–269]. However, the direct precursor for the biosynthesis of coenzyme Q_{10} (Q_{10}) which contains one hydroxyl group instead of a methoxy group at position 3 of the quinone ring[15,270] had never been in the focus of functional studies. Prompted by the observation that 2-palmitoylhydroquinone with two adjacent carbonyl-groups can bind Ca^{2+} in a redox-dependent manner and translocate them across artificial membranes[21,22], numerous *p*-benzoquinone (*p*-BQ) derivatives and their hydroxylated forms became a main focus in our group[13]. Bogeski *et al.*[10] and Gulaboski *et al.*[11–14] presented clear evidence for a chemical transformation of different *p*-BQs in alkaline media, i.e., they showed that substituted dimethoxy-*p*-BQs and Qs-like compounds react with hydroxide anions (HO⁻) giving mono- or di-hydroxylated *p*-BQs as products. This reaction known as alkaline hydrolysis was described in 1964 by Pettersson[20] for 2,3-dimethoxy-5,6-dimethyl-1,4-benzoquinone. Moreover, Bogeski *et al.*[10] demonstrated that the hydroxylated species can also be formed in the presence of cytochrome P450 (CYP450). As shown by liquid chromatography coupled to mass spectrometry (LC-MS) data[10] both of their approaches, chemical and biosynthetic, yielded mono-hydroxylated Q_1 as a major product and substantial amounts of di-hydroxylated Q_1. The biosynthetic approach of the synthesis is very important as CYP450 enzymes are present in mitochondria and in the endoplasmic reticulum (ER) and might transform Q_{10} into its hydroxylated form. Slowik[16], by analysing the content of Q_{10} and OH-Q_{10} in samples of beef heart mitochondria with tandem MS (MS/MS), found that ~0.3% of the total Q_{10} content is in the mono-hydroxylated form (HO-Q_{10}). Considering the high local concentrations of Q_{10} in mitochondria, this amount is not negligible. In several studies of our group, physico-chemical and physiological properties of several Qs or related *p*-BQs such as Q_1[10], Q_{10}[10,16], 2,6-dimethoxy-1,4-benzoquinone[11,14], Q_0[12], mitoquinone (mQ)[149] and their hydroxylated derivatives (HO-Qs) have been investigated.

Experiments with Q_{10} and HO-Q_{10} dissolved in aqueous solutions are extremely difficult due to their high hydrophobicity. Therefore, Q_1, decylubiquinone (dUQ), and their hydroxylated forms as more hydrophilic compounds were used in my project to explore the redox chemistry and physiological properties of the lipophilic compounds, Q_{10} and HO-Q_{10}. The hydroxylated species, HO-Q_1 and HO-dUQ are commercially not available, therefore they had to be synthesized and purified in sufficient amounts for further functional studies. The nucleophilic substitution of one methoxy group by a hydroxyl group was undoubtedly proven by MS and nuclear magnetic resonance (NMR). The new products, HO-Q_1 (Figure 4-10) and HO-dUQ (Figure 4-11), contained an intact sidechain and were chemically modified only at the positions of the methoxy groups. The final, isolated products were identified as a mixture of two molecules (isomers) that were hydroxylated either at position 2 or 3 of the quinone moiety (2- or 3- mono-hydroxylated Q_1 and dUQ, HO-Q_1 and HO-dUQ, respectively). These observations were consistent and revealed

nearly identical behaviour and comparable parameters with the NMR data of the HO-Q_{10}[16] and the mono-hydroxylated product of mQ (HO-mQ)[149]. By transferring the assignment of 2-OH-Q_{10} and 3-OH-Q_{10} signals, based on ^{1}H and ^{13}C heteronuclear 2-D NMR, the relative portions of isomers in HO-Q_1 and HO-dUQ were calculated as 58% for the 2-HO- and 42% for the 3-HO-isomer in both cases. These results were similar to the observed ratios for HO-Q_{10} isomers (64% and 36%)[16]. Unlike Bogeski *et al.*[10] who detected a di-hydroxylated form of Q_1 (with both methoxy groups being replaced by hydroxyl groups), neither of the synthesis methods applied within this thesis yielded di-substituted Q_1 or dUQ in detectable amounts. Production of di-hydroxylated derivatives could be limited by condensation reactions resulting in dimers as reported by Gulaboski *et al.*[11,12] who detected dimeric structures of di-hydroxylated Q_0. Additionally, long exposure of Qs to alkaline media is resulting in byproducts of the reaction with opened ring structures carrying two carboxylic acid groups as detected for the byproducts in HO-Q_{10} synthesis[16].

HO-Q_1 and HO-dUQ were produced with high purity of 89% for HO-Q_1 and 81% for HO-dUQ. The purity of the substances could be further increased by multiple runs of preparative HPLC, by reducing the sample amount and/or optimization of the used method. Additionally, separation and purification by HPLC of 2-HO- and 3-HO- isomers, that were found in the product, theoretically should be possible[163]. This is very crucial since it has been shown that the position and the type of substituents on the quinone ring can play a key role for the activity of the mitochondrial electron transport chain (ETC) complexes and the specific Q-binding sites in the ETC[264–266]. Nonetheless, separation of the isomers was not a priority task in this project, and the development of elution methods was focused on the isolation of the HO-Q_1 and HO-dUQ with high purity in the necessary amounts for functional studies.

5.2 Redox characterization of Qs and HO-Qs in different media

Extensive research has been carried out to investigate the redox properties of Q_{10} and elucidate its mechanism of action in biological systems. However, conducting classical electrochemical experiments with Q_{10} (i.e., experiments in aqueous solutions at solid working electrodes) is highly challenging due to its high hydrophobicity. To circumvent the challenges posed by its hydrophobic nature, electrochemical studies have primarily been conducted in organic solvents like DMF[271], ethanol[272], and mixtures of organic solvents[273–276]. Additionally, more complex approaches have been employed to investigate Q_{10} in aqueous environments. These approaches include utilizing modified electrodes in contact with aqueous electrolyte solutions, where Q_{10} is either deposited as a thin film on a carbon electrode[147], immobilized on a glassy-carbon electrode[277], incorporated into a carbon paste electrode[278], or adsorbed on pyrolytic graphite[279] or mercury electrodes[19,280]. To better simulate biologically relevant conditions, some authors have embedded Q_{10} into artificial self-assembled lipid monolayers attached to gold[281] or mercury electrodes[282,283], or within phospholipid bilayers[284–286], n-alkanethiol assemblies[287–289], or native membrane extracts[290] immobilized on gold electrodes. More recent studies have explored systems like lipid

functionalized carbon nanoparticles[291], quantum dots[292], multi-walled carbon nanotubes[293], or cyclodextrins[294] as matrices for Q_{10} immobilization.

Existing literature[147] as well as our own findings indicate that the length of the sidechain in various Q-compounds has minimal impact on their redox properties with only slight differences observed in their redox potentials (section 4.2.1). Despite their sidechain compositional differences, Q_1 and dUQ share the same substituents on the quinone ring as Q_{10}, thus serving as analogues that offer improved water solubility compared to Q_{10}, and models to investigate the redox chemistry of Qs family members in aqueous environment, in particular of the newly synthesized HO-Q_{10}.

The redox chemistry of the Qs, including Q_{10}, has been extensively studied for more than eight decades, and yet many aspects of their electrochemical behaviour still emerge and are not well understood even nowadays[230,235,295]. Their redox reactions could progress through several pathways which significantly depend on the solvent medium, the proton availability in the studied system, pH of the solution as well as formation of inter- and intramolecular hydrogen bonds and ion pairs with metal cations[230]. In reviewing the literature, to date, no comprehensive study on the redox chemistry of Q_1 and dUQ can be found. Only a few studies consider the properties of these Qs as antioxidants or as models for the quinone site in the ETC[269,296–298]. Therefore, voltammetric studies of Q_1 and dUQ, presented in this thesis, fill a gap in the literature and provide the first extensive investigation of their redox reactions. Moreover, this study is the first one to examine in detail the electrochemical behaviour of HO-Q_1 and HO-dUQ since they are for the first time isolated and purified in our laboratory. Additionally, these studies contribute to a better understanding of their interactions with Ca^{2+} which was one of the aims of this thesis. For an in-depth study, voltammetric experiments were conducted in aqueous (non-buffered and buffered) media, in organic protic and aprotic solvents, by applying several solvents and solutions of varying composition. These variable conditions are important for understanding the redox behaviour of Q_1, dUQ and their respective HO-Qs. Consequently, through these models, the redox behaviour of Q_{10} and HO-Q_{10} can be studied in membrane systems, for instance in mitochondria, where Qs encounter a strongly aprotic (non-aqueous) environment within the membrane which changes gradually to more protic conditions towards the membrane surface and to fully aqueous buffered properties in the mitochondrial matrix (pH_{MM} ~8)[299] or in the intermembrane space (pH_{IMS} ~7.1)[300]. As we have found analogous results for the investigated quinones, they will be described and discussed collectively. Unless specified otherwise, the findings refer to two categories: native quinones, represented as Qs, encompassing Q_1 and dUQ and their mono-hydroxylated forms, namely HO-Q_1 and HO-dUQ, denoted as HO-Qs.

The results of this study showed that Qs as well as HO-Qs followed the typical redox behaviour of other quinones previously discussed in the literature[12,13,230,235,295]. Their reduction involved two electrons that are transferred together in one step or one at a time in two individual steps depending on the nature of the solvent, the presence of protons, hydrogen bond donors or metal ions.

Since the overall reduction of Q_1 and HO-Q_1 in aqueous media consumes protons, peak potentials (E_p) in the voltammograms were affected by pH changes (Figure 4-15 and Figure 4-18) as described by *Nernst* equation (Eq. 4-1). The analysis of the dependence of E_p on the pH revealed two different slopes for Q_1 (~60 and ~30 mV/pH, Figure 4-15 b) and three different slopes for HO-Q_1 (~90, ~60 and ~30 mV/pH, Figure 4-18 b). Knowing that $2e^-$ are required for the reduction of the *p*-benzoquinones (*p*-BQ), the reduction of both, Q_1 and HO-Q_1, in the pH region where the slope was 60 mV/pH is described as $2e^-/2H^+$ process that follows the ECEC* mechanism to generate the hydroquinone QH_2. At pH ≥ 8, for both, Q_1 and HO-Q_1, the observed slope of 30 mV/pH indicated a change in the reduction mechanism from $2e^-/2H^+$ to $2e^-/1H^+$ (ECE) process. For both quinones, Q_1 and HO-Q_1, dependence of the E_p on the pH in the studied pH region (1-11) was not lost, i.e., a slope of 0 mV/pH which should indicate $2e^-/0H^+$ (EE) process was not observed, indicating participation of protons in the overall reduction of the Qs in buffered solutions (Figure 4-15 b and Figure 4-18 b). The observed slope of 90 mV/pH for HO-Q_1 in the lower pH range suggests that the reduction of HO-Q_1 follows a mechanism involving $2e^-/3H^+$ (Figure 4-18 b). The third proton is being consumed by the hydroxyl group located at the α-position. The theoretically calculated pK_{a3} value for the α-hydroxyl group present in HO-Qs was approximately 5.4[†]. Although the precise value of pK_{a3} could not be determined accurately from the experimental data, the experimental and theoretical values as well as reported values[18] for some α-hydroxylated *p*-BQ indicate that at physiological pH (7.4) most HO-Qs molecules (98%) exist in a deprotonated form. This finding holds significant importance for biological experiments involving the supplementation of HO-Qs to cells and mitochondria as these compounds need to traverse negatively charged plasma and mitochondrial membranes.

The electrode reaction of both, Q_1 and HO-Q_1, at buffered neutral pH was characterized as a diffusion-controlled process (Figure 4-14 c and Figure 4-17 c) where HO-Q_1 was estimated to exhibit higher diffusion rate compared to native Q_1. The reduction of Q_1 and HO-Q_1 in buffered aqueous solution (pH=7.4) showed pronounced kinetic barriers manifesting the quasi-reversible character of the redox reactions (Figure 4-14 and Figure 4-17). These kinetic limitations were illustrated by a substantial increase in peak-to-peak separation, increasing from 250 mV (at a scan rate of 10 mV/s) to over 450 mV (at a scan rate of 200 mV/s). A longstanding question has been whether these observed kinetic hindrances arise from sluggish electron transfer or a very slow proton transfer step. Numerous previous researchers have asserted that protonation is a fast process in quinone redox chemistry, attributing the kinetic limitations encountered in quinone voltammetric behaviour to the sluggish electron transfer step[19,301–306]. However, the studies conducted by Quan *et al.*[235], Gulaboski *et al.*[12], and our own findings strongly suggest that it is highly probable that the protonation steps proceed at a slow rate, ultimately contributing to the quasi-reversible features observed in the voltammograms of Qs.

---

* E, electron transfer step; C, chemical (proton) transfer step.
† pK_{a3} values calculated with MarvinSketch: 2-HO-Q_1 pK_{a3} = 5.46 (98.20%, pH=7.4); 3-HO-Q_1 pK_{a3} = 5.48 (98.11%, pH=7.4); 2-HO-dUQ pK_{a3} = 5.46 (98.22%, pH=7.4) and 3-HO-dUQ pK_{a3} = 5.42 (98.39%, pH=7.4).

In contrast to the buffered aqueous media, where reduction of Q_1 and HO-Q_1 showed pronounced kinetic barriers, reduction of Q_1 and HO-Q_1 in unbuffered aqueous solution at a pH of 7.4 exhibit almost no kinetic hindrances (Figure 4-19). Although a single voltammetric signal portrayed the redox reaction in both cases, the significant shift in the potential of Q_1 and HO-Q_1 as well as the difference in peak-to-peak separation indicated fundamentally distinct processes occurring under buffered and unbuffered conditions. In line with this, Quan *et al.*[235] have reported similar behaviour for the redox reaction of some *p*-BQs. Additionally, a study by Gulaboski *et al.*[12] revealed rather complex transformations of Q_0 under unbuffered conditions across a wide pH range. Both studies[12,235] suggested that the redox transformation of *p*-BQ in unbuffered media is influenced by the pH of the solutions, pK_a values of the reduced forms and the ratio of the concentrations of the quinones ([Q]) and protons ([H⁺]). Depending on these factors, at least three distinct scenarios are observed for the reduction of Qs in unbuffered aqueous solutions within a pH range spanning from 1.0 to 11.0. The voltammetric behaviour characterized by a $2e^-/2H^+$ process for reduction of Qs, observable in buffered aqueous systems (pH=1.0-8.0), is also evident in unbuffered highly acidic environments. Next to the $2e^-/2H^+$ reduction of Q to QH_2 at pH<2, two additional situations arise in unbuffered aqueous solutions (pH=2.0-11.0) where the reduction of Qs could occur via $2e^-/1H^+$ or $2e^-/0H^+$ process, resulting with monoanionic and dianionic reduced species of Qs as products. Given that the entire redox process in unbuffered aqueous media at pH~7 (at which [Q] approaches or exceeds the [H⁺]) occurs without involving protons[12,13,235], a reasonable assumption is that the kinetic constraints evident in the voltammograms of Q_1 and HO-Q_1 encountered in buffered environments are predominantly attributed to the slow proton transfer step. Hence, the redox transformation of Q_1 proceeds via a $2e^-$ mechanism, resulting in an equilibrium mixture of monoanionic Q_1H^- and dianionic Q_1^{2-} species as primary products, and hydroquinone Q_1H_2 as a minor product. Due to the presence of an α-hydroxyl group in HO-Q_1, the products of the reduction would exist in a mixture of at least four reduced species: hydroquinone (HO-Q_1H_2) and anions as monoanion (HO-Q_1H^-/⁻O-Q_1H_2), dianion (HO-Q_1^{2-}/⁻O-Q_1H^-) or trianion (⁻O-Q_1^{2-}). Quan *et al.*[235] suggested that stabilization of these anionic species is accomplished through the formation of hydrogen bonds with water (solvent) molecules. Undoubtedly, the interplay of hydrogen bonding, alongside protonation steps, stands as a fundamental determinant influencing the potentials and mechanisms governing the reduction of Qs, and will be discussed in the following chapter.

Organic protic solvents such as methanol, ethanol, 2-propanol are weaker acids than water, meaning that the [H⁺] will be lower than the [Q] resulting in stabilization of the quinone dianion via hydrogen bonding with the solvent molecules. By comparing the redox potentials of Q_1 and dUQ measured in different organic protic solvents (Table 4-4), it was found that the reduction of Qs occurred at more positive potentials (easier reduction) when methanol was used as a solvent, followed by ethanol and finally 2-propanol. It is well known that the strength of hydrogen bonding depends on the pK_a of the proton donors and proton acceptors as well as possible steric effects for molecular approach. Considering the literature data for pK_a, the acidity trend of the alcohols

in DMSO is methanol > ethanol > 2–propanol (Table 4-3). Methanol, being a stronger acid, has a higher [H$^+$] compared to ethanol and 2-propanol which results with an easier reduction of the Qs and HO-Qs in methanol. Moreover, by changing the electrolyte composition (LiClO$_4$ vs. TBAP)* in 2-propanol, redox reduction of Qs involved two electrons transferred one at a time in two separate steps, i.e., following an EE mechanism (Figure 4-31). The EE mechanism is generally observed in aprotic media where no protons or hydrogen bond sources are present. On the other hand, metal ions from the electrolyte might form ion pairs with Qs, thus stabilizing the semiquinone radical and causing the two electron transfer steps to occur at the same potential[230], which was demonstrated by replacing the cation of the electrolyte salt (Li$^+$ vs. TBA$^+$, Figure 4-31 and Figure 4-32). The absence of Li$^+$ as well as the fact that 2-propanol besides being a weak acid is a branched chain alcohol with steric hindrances for good molecular approach resulted in a switch from the EECC reduction mechanism to EE mechanism.

In organic protic solutions, two voltammetric signals were observed for the reduction of both, HO-Q$_1$ and HO-dUQ (Figure 4-20). Besides the intermolecular bonding with the alcohol molecules, HO-Q might form an intramolecular hydrogen bond between the hydrogen of the −OH (at position 2 or 3) and the oxygen atom of the neighbouring carbonyl group, leading to a five-membered ring structure. As previously reported in the literature for other α-hydroxy-*p*-BQ[241–245], the presence of an intramolecular bond in the HO-Q molecule would have an impact on its redox potential by stabilizing negative charges in the reduced forms. Therefore, under the same conditions, the reduction potential of HO-Q is expected to be more negative than that of the respective Q. In fact, HO-Qs showed more negative redox potentials than the corresponding native Qs, independently of the used solvent for the measurements (Figure 4-19, Figure 4-20, Figure 4-21, Figure 4-22, Table 4-4 and Table 4-5). Since the standard redox potential is the main thermodynamic parameter determining the antioxidative capacity of a particular compound, it was evident that the reduced forms of HO-Qs exhibit significantly higher antioxidant activity than the native Qs. The intramolecular hydrogen bonding is extremely weak and is more pronounced in aprotic solvents which are unable to form hydrogen bonds with the HO-Q molecules[307]. The later was confirmed with the voltammetric studies of HO-Qs in acetonitrile as an aprotic solvent (Figure 4-22).

Applying acetonitrile, where no possibility of hydrogen bonding or a proton source is present, redox transformation of Qs occurred in two steps with one electron being transferred in each step (EE mechanism), generating two well separated signals in the voltammograms (Figure 4-21), corresponding to the formation of semiquinone radical anion (Q/Q$^{•-}$) and final reduction product, quinone dianion (Q$^{•-}$/Q^{2-}). While electrochemical transformation of Qs was illustrated with only two well-resolved and well-separated consecutive voltammetric signals, the HO-Qs showed more complicated reduction mechanism (Figure 4-23). Due to the presence of the −OH group in α-position, the intermediates of the reduction could be protonated according to the self-protonation

---

* LiClO$_4$, lithium perchlorate; TBAP, tetrabutylammonium perchlorate.

mechanism (Eq. 4-3 to Eq. 4-9). Thus, the overall reaction of HO-Q involves both electron transfer processes coupled with chemical reaction.

5.3 Hydrogen bonding and protonation effects on the redox reaction of Qs

The presence or absence of protons (H^+) as well as the concentration ratio between H^+ and Qs significantly influence the redox reaction mechanism of Qs and HO-Qs. This highlights the fundamental role of hydrogen bonding and protonation in controlling the potentials and mechanisms involved in Q reduction. Moreover, these processes hold particular importance due to the crucial biological functions of Q_{10} as an electron and proton carrier in ETC. In the IMM, where Q_{10} molecules are localized, the existence of acidic compounds such as phosphatides and cardiolipin with varying levels of acidity could potentially alter the membrane properties near Q_{10} molecules, consequently influencing its redox reaction. Therefore, a series of experiments was performed in acetonitrile where variable amounts of hydrogen bond donors like water and alcohols were added to the solution of Qs.

The good separation of electron transfer steps of Qs in aprotic solvent allowed following the effect of various hydrogen bond donors (HBD) on the $Q^{\bullet-}$ and on the fully reduced Q^{2-} forms of the Qs. When HBD such as water or alcohols were added, the peak potentials of the first and second reduction step shifted towards more positive values (Figure 4-29). The potential of the second reduction step ($Q^{\bullet-}/Q^{2-}$) was shifted to a greater degree than the first voltammetric wave ($Q/Q^{\bullet-}$) until both peaks fully merged, meaning that both steps had approximately the same potential (Figure 4-29). Previous observations of similar potential shifts of different quinones by addition of HBD have been attributed to the fast stabilization of the Q^{2-} [249–251]. The notion that hydrogen bonds could stabilize the $Q^{\bullet-}$ can be dismissed based on the unfavourable pK_a values which are lower than the pK_a values of water and alcohols [18,238,252–254]. For instance, the pK_a values of $Q^{\bullet-}$ of BQ[*] and TMBQ[†] in aqueous solutions are 4.0 and 5.1, respectively [252]. These values are significantly lower than the pK_a of methanol (15.5)[238], ethanol (15.9)[240] and 2-propanol (17.1)[240] in aqueous media, suggesting a substantial difference in acetonitrile as well. It should be noted that water-based pK_a values are used here since, to the best of our knowledge, data for QH_2 in aprotic solvents are not available. Moreover, the charge distribution in unprotonated Q (Q^{2-}) would be more delocalized compared to that in simple alcohol anions. Consequently, when transitioning from water to acetonitrile or DMSO, the alcohols will exhibit even weaker acidity (pK_a values of methanol, ethanol, and 2-propanol in DMSO are 29, 29.8, and 30.2, respectively[238,239]) relative to the protonated quinone monoanions (QH^-), due to a greater loss of hydration energy for the alcohol anions. The analysis of the impact of the used HBD showed that the fastest stabilization of Q^{2-} occurred with methanol, followed by water, ethanol and finally 2-propanol, a tendency that aligns with the reported acidity trend (pK_a) of the used HBD (Figure 4-30). Further, this finding was consistent with the tendency observed for the reduction of Qs in different alcohols (Table 4-4) where easier reduction of Qs took place in methanol, followed by ethanol and least in

---

[*] BQ: 1,4-Benzoquinone
[†] TMBQ: 2,3,5,6-tetramethyl-1,4-benzoquinone

2-propanol. Due to its higher acidity compared to ethanol and 2-propanol (which in addition is a branched chain alcohol with steric hindrances for good molecular approach) methanol shows a faster and more efficient stabilization of Q^{2-}, consequently making the reduction of Q to Q^{2-} thermodynamically favourable.

5.4 Calcium affinity of Qs and HO-Qs

The further focus of this thesis revolved around the potential physiological significance of HO-Qs in terms of the potential influence of HO-Q_{10} on mitochondrial and cellular Ca^{2+} homeostasis, as suggested in various publications from our group[10–13,16]. A hypothesis was formulated proposing that the Ca^{2+} affinity of HO-Qs might play a crucial role in the buffering capacity of Ca^{2+} in mitochondria and/or ER.

Quinone-like compounds, particularly those based on *o*-benzoquinone (*o*-BQ) structures, have been identified as effective Ca^{2+} transporters across biomimetic membranes. It has been shown that *o*-BQ form both simple 1:1 complex and more intricate 1:2 complexes with metal ions[308–313]. These studies highlighted the role of two adjacent oxygen atoms in the structure of *o*-BQ, providing a binding site for cations. In contrast, naturally occurring coenzymes Q, which are based on the *p*-BQ structure, lack such neighbouring oxygens. Fukuzumi *et al.*[233,314] conducted a series of investigations on the interaction between *p*-BQ and metal ions in aprotic solvents. Their findings demonstrated that once the Qs were reduced, $Q^{\bullet-}$ interacted with the metal ions. However, limited information is available regarding the ability of these quinones to chelate cations in aqueous solutions. As it appears, only one article[315] has reported an interaction between a *p*-BQ and Ca^{2+} in aqueous conditions detected by voltammetric techniques.

An earlier publication[10] from our group investigated the Ca^{2+} affinity of HO-Qs in aqueous media. By voltammetric methods, it was demonstrated that HO-Q_{10} and HO-Q_1, but not their native forms (Q_{10} and Q_1), can bind and transport Ca^{2+} across a biomimetic membrane in a redox-dependent manner. Subsequent studies by Gulaboski *et al.*[11–13] on HO-Qs of various *p*-BQ revealed that all HO-Qs were sensitive to Ca^{2+}, whereas the native Qs were not. It has to be noted here that in these studies HO-Qs were not purified, and all experiments were conducted using neutralized and characterized reaction mixtures. These reaction mixtures contained significant amounts of byproducts with carboxyl (–COOH) groups resulting from opening of the quinone ring[16], which could form complexes with metal cations and should be considered when analysing data generated from unpurified reaction mixtures. Therefore, it was crucial to re-analyse the Ca^{2+} binding properties with purified HO-Qs to obtain accurate results.

Contrary to the anticipated significant positive shift in the peak potential as previously reported by Bogeski *et al.*[10], the addition of Ca^{2+} to an unbuffered aqueous solution containing purified HO-Q_1 resulted in pH changes so that the merged effect of pH alterations and Ca^{2+} interactions was observed (section 4.2.2.1). Moreover, not only for HO-Q_1 but also for the native Q_1 similar effects were found. As discussed earlier, the reduction of Qs consumes H^+. When the solution pH is not adequately buffered, the $[H^+]$ near the working electrode differs from that in the bulk solution resulting in a phenomenon known as "effective pH" near the electrode[316]. Consequently, any

changes in the mechanism become intertwined with pH fluctuations near the electrode, making accurate potential measurements very challenging. Furthermore, it is well established that the addition of salts to unbuffered aqueous solutions influences the acid-base equilibrium of the solution, thereby affecting the pH. When buffered solutions were employed, the addition of Ca^{2+} had negligible impact on the voltammetric signal of Q_1 and $HO-Q_1$. These findings suggest that the interaction between Ca^{2+} and Q_1 or $HO-Q_1$ in both, unbuffered and buffered aqueous solutions, is weak. It is likely that Ca^{2+} cannot effectively compete with H^+ when the latter are present in sufficient concentrations. To overcome this limitation, experiments were performed in organic solutions including protic solvents where the $[H^+]$ would be significantly lower compared to the concentration of Qs as well as aprotic solvents where protons are entirely absent.

Replacing the aqueous phase with organic protic solutions (alcohols) had a two-fold effect for the experiments. The more significant positive shift of the peak potential of HO-Qs compared to that of Qs (in the presence of same $[Ca^{2+}]$) is attributed to stronger interactions between Ca^{2+} and the reduced form of HO-Qs than with the reduced form of Qs. Additionally, the potential difference measured in absence of Ca^{2+} and presence of the same $[Ca^{2+}]$ was smaller in methanol compared to 2-propanol for both, HO-Qs and Qs (Table 4-6), which is caused by formation of stronger hydrogen bonds of methanol than 2-propanol. As 2-propanol is a weaker acid with additional steric hindrance, weaker hydrogen bonds with Qs are expected. Consequently, the Q^{2-} are less stabilized by 2-propanol but are more stabilized by Ca^{2+}. In addition, these findings align with the observation that the competition of H^+ and hydrogen bonding with Ca^{2+} took place in buffered and unbuffered aqueous solution, respectively. The varying stoichiometries for the Ca^{2+}-Qs and Ca^{2+}-HO-Qs associations (Table 4-6), inferred from the slopes of the peak potential dependence on the $[Ca^{2+}]$, indicated that Ca^{2+} is competing with hydrogen bonded alcohol molecules and solvated H^+ in binding to the Qs/HO-Qs. Considering once again the pK_a values of the alcohols, it can be noted that although all the alcohols are generally weak acids their dissociation levels differ. As a result, the $[H^+]$ will be higher in methanol, followed by ethanol, and lowest in 2-propanol. The data also revealed distinct interaction mechanisms between Qs and HO-Qs with Ca^{2+}. While the addition of Ca^{2+} resulted in the immediate appearance of a new peak for HO-Qs, the peak potentials of Qs gradually shifted in the presence of Ca^{2+}. This discrepancy suggests that HO-Qs interact with Ca^{2+} already in their oxidized form. At pH~7, the α-hydroxyl group in HO-Qs tends to deprotonate. Consequently, HO-Qs exist mainly in their monoanionic form (^-O-Q) which enables them to interact with Ca^{2+} without the necessity of a preceding reduction. In contrast, for Qs a reduction is a prerequisite to produce the Q^{2-} for interaction with Ca^{2+}.

The effective separation of the electron transfer steps for Qs in an aprotic solvent enabled us to study the impact of Ca^{2+} on both, $Q^{\bullet-}$ and Q^{2-}. It was found that under these conditions Ca^{2+} interacts with the semiquinone radical $Q^{\bullet-}$ (Figure 4-27). Conversely, the voltammetric behaviour of HO-Qs in aprotic solvents proved to be more complex. Nonetheless, the results revealed the presence of two distinct ion-pair formations (Figure 4-28). Each formation, owing to its unique energy state, underwent reduction at a different potential.

Combining the findings of this study with the knowledge on the coordination chemistry of Ca^{2+} [317,318], Figure 5-1 provides an overview of potential models for the observed Ca^{2+} associations with the major redox states of Qs and HO-Qs. The proposed structures in panels a-d are compatible with the stoichiometries derived in our voltammetric experiment. However, it is important to bear in mind that the interactions between Qs or HO-Qs and Ca^{2+} are primarily electrostatic in nature, hence generally weak and highly dependent on various factors such as the solvent, presence of hydrogen bonding donors, protons, and other ions, as demonstrated here. Furthermore, the solvation shell of Ca^{2+} exhibits considerable variation across different solvents which further affects the impact of Ca^{2+} on the behaviour of Qs and HO-Qs. Due to the intricate nature of redox chemistry of Qs and HO-Qs, determining the explicit ion-pair structures based solely on the identified stoichiometries is challenging and the proposed models are not definitively conclusive. Further investigations are required to fully understand the interactions between Qs, HO-Qs, and Ca^{2+}. For that goal additional techniques such as NMR and infrared spectroscopy (IR) along with DFT calculations can be employed to provide more details of these interactions.
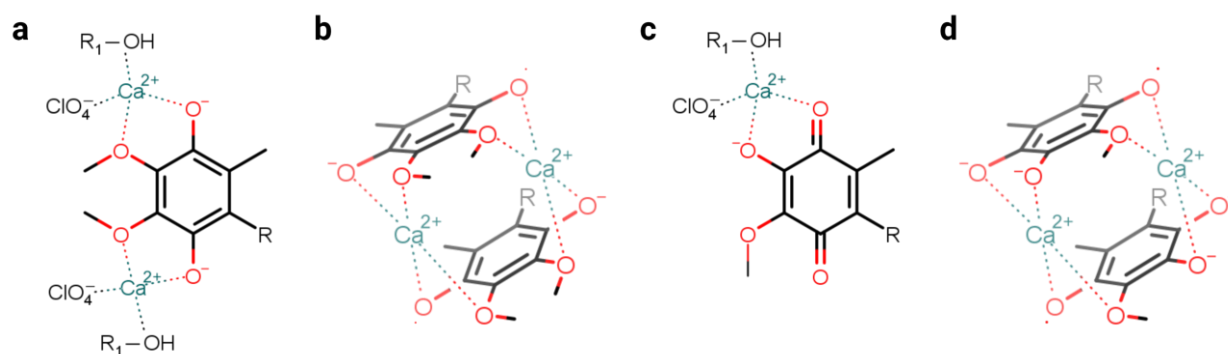
Figure 5-1 Proposed models of the Ca^{2+} ion-pair formation with Qs and HO-Qs. a) Q^{2-} ($Q^{2-}:Ca^{2+}$ = 1:2); b) $Q^{\bullet-}$ ($Q^{\bullet-}:Ca^{2+}$ = 2:2); c) oxidized form of HO-Q (HO-Q:Ca^{2+} = 1:1) and d) HO-$Q^{\bullet-}$ (HO-$Q^{\bullet-}:Ca^{2+}$ = 2:2). R, one isoprene unit or decyl hydrocarbon chain; R_1-OH, solvent molecules (methanol, ethanol, 2-propanol); ClO_4-, anion from the electrolyte.

5.5 Supplementation of Qs and HO-Qs to HEK-293 cells and isolated mitochondria

The primary functions of Q_{10} in mitochondrial bioenergetics and its antioxidant activity have led to its extensive use in the medical field as a therapeutic agent. In a recent review by Cirilli *et al.*[319] which focused on the research conducted in the last decade, the authors highlighted the diverse applications of Q_{10}, particularly in the fields of cardiovascular health, fertility, and skeletal muscle disorders. Despite the remarkable therapeutic outcomes associated with Q_{10}, its supplementation faces a significant challenge due to its low solubility and consequently bioavailability. This limitation is primarily attributed to the hydrophobic nature of its ten-unit long isoprenoid tail as well as its susceptibility to light and thermal instability which collectively affect its efficient absorption and utilization in the body.

The administration of Q_{10} and HO-Q_{10} to cells and isolated mitochondria is significantly limited due to their insolubility, not only in aqueous solutions but also in DMSO as commonly used solvents for substance supplementation. More importantly, this lack of solubility has a direct impact on their uptake by cells and their distribution within the cellular environment. To overcome

this challenge and enhance the bioavailability of Q_{10}, various formulations have been developed including liposomes, self-nanoemulsifying drug delivery systems (SNEDDs), Q_{10}-loaded oleogels, Q_{10} micellization and water-soluble formulations by encapsulating Q_{10} in β-cyclodextrin or cholesterol-PEG complexes[320,321]. On the other hand, considerable efforts have been directed towards discovering Q_{10} analogues with optimized properties and enhanced effectiveness, in particular greater solubility and stronger antioxidant effects. Various chemical strategies are employed to achieve this, such as shortening or modifying the isoprenoid chain (short-chain Qs) and/or adding specific functional groups to facilitate mitochondrial accumulation as in mitoquinone (mQ)[9].

Considering all these facts, the initial and critical step was to develop a reliable method to dissolve Q_{10} and HO-Q_{10} for successful implementation in biological experiments. Stable stock solutions of Q_{10} and HO-Q_{10} at room temperature could be prepared in ethanol, up to concentrations of 1 and 5 mM, respectively[16]. Even though a final concentration of 1% ethanol in buffer or medium for experiments with isolated mouse heart mitochondria did not affect mitochondrial respiration and ROS production[16], ethanol was not compatible for our measurements with HEK-293 cells. Several attempts to supplement HEK-293 cells with Q_{10} or HO-Q_{10} in alcoholic solution produced inconsistent results. Additionally, precipitation of Q_{10} and HO-Q_{10} was observed under the microscope, most probably due to evaporation of ethanol and promoting insolubility in aqueous solutions. In line with this, studies using ethanol in *in vitro* cell based assays have shown compromised cell viability at very low concentrations of ethanol (0.1%)[256]. Furthermore, ethanol was shown to induce mitochondrial impairment, mainly by damaging the mitochondrial morphology or by hindering mitochondrial respiration[257]. Syed *et al.*[255] observed ethanol-induced inhibition in a concentration-dependent manner by studying the effects of a variety of organic solvents on the mitochondrial respiration.

Following the procedure from Borowy-Borowski *et al.*[189], aqueous solutions of Q_{10} and HO-Q_{10} in the mM range were successfully prepared (Figure 4-33). After treating the cells for 30 minutes with Q_{10}-PCS, a 3-fold increase in the amount of Q_{10} compared to the untreated controls was observed (Figure 4-34 b and c). Although HO-Q_{10} could not be detected in the untreated cells, it clearly appeared in the cell homogenate after its application (Figure 4-35 b and c). In contrast to an earlier study[16] which has detected HO-Q_{10} in extracts from bovine heart mitochondria by LC-MS, HO-Q_{10} was not detected in the untreated HEK-293 cells or the HEK-293 cells treated with Q_{10}-PCS (Figure 4-34 b). One possible explanation for these differences is the limit of detection (LOD) of the used methods. The HPLC method applied in this study had a LOD of 10 nM (Figure 4-34 a), whereas MS has a LOD in the range of pM which is further increased by applying MS/MS. Another plausible explanation could be the difference in the solvents used for extraction of HO-Q_{10} from the biological tissues as well as the biological samples from which HO-Q_{10} was extracted (bovine heart mitochondria vs. HEK-293 cells). Nevertheless, the results demonstrated that Q_{10} and HO-Q_{10} in the water-soluble formulation efficiently passed through the plasma membrane and accumulated in the cells. The observation that HO-Q_{10} was able to cross the plasma

membrane and to accumulate within the cells was an important finding considering its formal negative charge in aqueous environment. As it was seen from the voltammetric data for HO-Q_1 at neutral pH (Figure 4-18), the −OH group in α-position acts as a weak acid and is deprotonated at physiological pH. Obviously, the embedding of HO-Q_{10} in PCS is shielding the formal charge or even may favour a protonated state.

Since Q_1, dUQ, mQ and their HO-Qs are less hydrophobic than Q_{10} and HO-Q_{10}, they can be easily dissolved in water or mixtures of water and organic solvents like ethanol or DMSO in sufficiently high concentrations. Nevertheless, the water-soluble (PCS) formulations were used for all studied quinones to assure comparable conditions.

5.6 Effects of Qs and HO-Qs on the cellular and mitochondrial functions

Given that the HO-Q_1 and HO-dUQ as well as HO-mQ[149] were synthesized and purified in our lab for the first time, nothing is known about their potential functions in cellular processes. One of the main goals was to investigate and gain initial insights into the impact of these substances on mitochondrial bioenergetics and cellular Ca^{2+} homeostasis. Previous studies[322,323] have reported cytotoxicity of Qs with shorter isoprenoid side chains than Q_4 in cultured cells. Additionally, these compounds have been found to induce apoptosis in the human leukaemia B-cell line BALL-1[324]. Furthermore, the impairment of tumour growth has been demonstrated with embelin, a hydroxylated 1,4-benzoquinone[258]. Hence, the first question was whether the newly synthesized derivatives exhibit any toxic effects in HEK-293 cells. A previous study[16], conducted by our group, demonstrated that despite enhancing ROS production and impairing mitochondrial respiration, HO-Q_{10} did not reduce proliferation or induce cell death in various cell lines. Our data confirmed these findings, as treatment of HEK-293 cells with Q_{10} and HO-Q_{10} in water-soluble formulation did also not affect cell viability (Figure 4-35). Similarly, the metabolic activity of the cells exposed to Q_1, dUQ, HO-Q_1, and HO-dUQ remained unaffected (Figure 4-35). In contrast, significant alterations in the cellular metabolic activity were observed following treatment with mQ, and to a lesser extent HO-mQ indicating cytotoxic effects (Figure 4-35). Additional data showed that mQ and HO-mQ substantially disturbed the mitochondrial membrane potential ($\Delta\Psi_m$), mitochondrial bioenergetics, and Ca^{2+} homeostasis. Thus, the effects of mQ and HO-mQ will be further discussed in a distinct chapter.

5.6.1 Mitochondrial bioenergetics

To evaluate the impact of Qs and HO-Qs on mitochondrial bioenergetics, freshly isolated murine heart mitochondria (MHM) were used. The results indicated an increase in complex I (CI)- and complex II (CII)-linked respiration following treatment of mitochondria with Q_1 and dUQ. This outcome was somewhat anticipated as Q_1 and dUQ have been employed as electron acceptors in previous investigations on the electron transport chain (ETC) complexes in isolated enzymes, subcellular fractions, and cultured intact cells. It has been demonstrated that they stimulate mitochondrial respiration, further supporting the observed results. In a study conducted by Chan *et al.*[325], it has been observed that Q_1 not only prevented rotenone-induced cytotoxicity in hepatocytes, but also restored ATP levels, $\Delta\Psi_m$, and respiration. The cytoprotective effects of Q_1

were ascribed to its capacity to function as an electron acceptor. dUQ is a synthetic Q_{10} analogue, whose structural modification (saturated decyl hydrocarbon chain) facilitates its passive localization to the mitochondrial membranes. Moreover, the interaction between dUQ and CI closely resembles that between endogenous Q_{10} and CI[326]. Similar to Q_{10}, dUQ can accept electrons from CI leading to its reduction into decylubiquinol ($dUQH_2$). Subsequently, $dUQH_2$ transfers the electrons to CIII. In a study by Telford *et al.*[298], the effects of dUQ on the mitochondrial complexes in rat brain synaptosomes were investigated. It was found that dUQ enhanced the activities of supercomplexes (SC), specifically SC CICIII and SC CIICIII.

CI-linked respiration after Q_{10} treatment of MHM increased only in the absence of Ca^{2+}, but was mildly hindered in presence of Ca^{2+} (Figure 4-42). No effect on the respiration by Q_{10} was observed for CII-linked respiration independently of the presence of Ca^{2+} (Figure 4-43). Slowik[16] has reported that Q_{10}, applied as ethanolic solution, intervened with CI- and CII-linked respiration, reducing oxygen consumption rates (OCRs) to approximately 50% or less. In line with the observation of reduced OCR by Q_{10}, Bergamini *et al.*[327] reported a reduced mitochondrial respiration in intact cells following a 24 hours pre-treatment with 10 µM Q_{10}. This outcome was observed only when Q_{10} was administered as an ethanol-based solution, but not when Q_{10} was used as water-soluble formulation. The authors suggested that the reason for the observed discrepancies is in the incorrect insertion of Q_{10} into the inner mitochondrial membrane (IMM). Contrary, when Q_{10} was applied as a water-soluble formulation it promoted mitochondrial respiration, in line with our data, where Qs and HO-Qs were also applied as water-soluble formulations.

All HO-Qs hindered CI and CII-mediated respiration but to a different extent. The most striking result is that only HO-Q_{10} showed Ca^{2+}-dependent inhibition of both CI- and CII-linked respiration, whereas the other hydroxylated forms (HO-Q_1, HO-dUQ and HO-mQ) inhibited OCR independently of Ca^{2+} (Figure 4-42 and Figure 4-43).

It was observed that Qs and HO-Qs influenced both, CI- and CII-linked respiration, in varying degrees either by stimulating or hindering it. Notably, HO-Qs consistently showed inhibitory effects on respiration compared to the controls and the native Qs, although the extent of inhibition differed. This suggests that the effects are likely attributed to two mechanisms of action. One mechanism appears to be complex-specific arising from either different interactions of Qs and HO-Qs with the Q-binding sites in the complexes, and/or the ability of these complexes to reduce Qs and HO-Qs. The other underlying mechanism could be membrane-associated caused by the effects of the Qs and HO-Qs on the physico-chemical properties of the IMM.

Complex-specific mechanisms

Studies have highlighted the significance of the position and type of substituents on the quinone ring in relation to the specific Q-binding sites and the activities of the ETC complexes[264–266,269]. Quinone ring and the sidechain moieties contribute together to the interaction with the ETC complexes. On one hand, a long isoprenoid sidechain enhances the incorporation of the Qs in IMM, while on the other hand the electron-acceptor activity of Qs relies on the substituents of the

quinone ring. For instance, short-chain Qs (except Q_1) with a sidechain ranging from 0 to 5 isoprene units failed to restore CI activity. Additionally, the inhibitory effects of short-chain quinones were unique to CI and were not observed for CII or CIII[269]. In a study by Fato *et al.*[192], it was discovered that dUQ, which only differs from Q_2 by having a decyl saturated sidechain instead of a diprenyl sidechain (which also has ten carbon atoms), did not inhibit CI activity, whereas Q_2 strongly inhibited it. This behaviour was attributed to the improper positioning of the sidechain of Q_2 at the Q-binding site in CI, hindering optimal electron transfer. Furthermore, another study[264] found that replacing the methoxy group at position 3 in the structure of dUQ with hydrogen resulted in the complete loss of the electron-acceptor activity for CII, while replacement at position 2 decreased the activity by 70%. The redox potentials of these compounds can be influenced by modifications on the quinone ring, as observed in voltammetric experiments where the reductions of HO-Qs occurred at more negative potentials than those of Qs, irrespective of the solvent used. Therefore, even under the assumption that Qs and HO-Qs can bind to the Q-binding sites, it does not guarantee their reduction.

The last Fe-S cluster in the CI of ETC responsible for transferring electrons to Q_{10} exhibits a redox potential of -200 mV[328], whereas in CII it is $+60$ mV[329]. Since these clusters transfer electrons one at a time, redox potentials of dUQ and HO-dUQ obtained in aprotic solutions are used for comparison. However, it is important to note that these potentials are highly dependent on the surrounding medium, especially the presence of hydrogen bond donors, H^+, or metal ions (for instance Ca^{2+}). When comparing the redox properties of dUQ and HO-dUQ (Table 4-5), it is observed that the first electron transfer in the reduction of HO-dUQ occurs at a more positive potential compared to the same electron transfer step for dUQ. This suggests that the first reduction of HO-dUQ is easier compared to dUQ. However, the second electron transfer for HO-dUQ leading to the formation of the radical dianion ($^-O\text{-}Q^{\bullet-}$) occurs at more negative potentials than that of dUQ (Q^{2-}). This indicates that the reduction of dUQ to its Q^{2-} is more facilitated than the reduction of HO-dUQ to $^-O\text{-}Q^{\bullet-}$. Consequently, the complete reduction of HO-Qs by electrons from the Fe-S clusters in CI and CII may be impeded due to thermodynamically unfavourable reduction potentials. This can result in an overproduction of radical anions, thereby inhibiting mitochondrial respiration.

However, the available data do not allow precise conclusions. Further experiments need to be conducted focusing on investigating the production of ROS and/or employing EPR studies of the semiquinone radicals. Additionally, it should be acknowledged that the impact on mitochondrial respiration may be influenced by the binding of Qs/HO-Qs to other sites within the complexes or the membranes. It is also crucial to not overlook the potential impact of Qs and HO-Qs on CIII-linked respiration, as experiments focusing on this complex have not been conducted. Thus, a complete understanding requires additional research.

Membrane-associated mechanisms

Another underlying mechanism for the distinct activities of CI- and CII-linked respiration after treatment with different Qs could be a membrane-associated mechanism. In a comprehensive

study in three distinct cell lines, Erb *et al.*[330] have screened 70 quinone compounds including idebenone, decylubiquinone, and various short-chain Qs to assess their potential in rescuing ATP levels. The findings revealed that modifications of the sidechains had a significant impact on the ability of Qs to rescue ATP levels. Besides the quinone ring moiety, the structure of the sidechains also determines the physico-chemical properties of the Qs. Consequently, the length and composition (saturated or unsaturated bonds) of the sidechain plays important roles for the interaction between Qs and membrane phospholipids. Q_{10} has been recognized to affect biophysical properties of membranes[29,30,39,41]. Fluorescence anisotropy measurements on various Qs, including Q_{10}, indicated significant and concentration-dependent effects on the membrane organization[331]. According to Skowronek *et al.*[331], Q_{10} appears to induce a greater increase in acyl chain organization within the lipid membrane compared to cholesterol. Moreover, research by Agmo Hernández *et al.*[29] highlights the ability of Q_{10} to modulate fundamental characteristics of lipid membranes, specifically heightened lipid packing order, increased membrane density, reduced permeability, and enhanced mechanical stability.

The activities of the proteins spanning the biological membranes are tightly regulated by the composition of the phospholipids in the membranes[332]. This regulation is particularly relevant in the IMMs, where it can influence the respiratory function of the complexes and their assembly in supercomplexes (SC). It has been observed that increased membrane density leads to a decrease in respiration rates, which can be restored by the addition of sterols that promote membrane fluidity[333]. In both, membranes of *E. coli* and yeast mitochondria, an increase in unsaturated lipid content enhanced membrane fluidity, consequently enhancing respiration rates[334]. Changes in the properties of the membrane impact the diffusivity of Qs within the ETC. For instance, an increase in the membrane viscosity would hinder the mobility of Qs. Consistent with this, it has been reported that diffusivity of Q was enhanced with an increase of membrane-fluidizing lipids[333,334]. The varying saturation of the sidechains of the applied Qs and HO-Qs could lead to distinct effects on the membrane viscosity when compared to Q_{10}. Moreover, due to the different length of the sidechains, these Qs are expected to occupy different locations within the membrane. These differences may contribute to the diverse effects observed in mitochondrial respiration. In addition to its impact on the diffusivity of Qs, as suggested by Budin *et al.*[334] membrane viscosity may influence the efficiency of the respiratory chain through other mechanisms such as impairing substrate uptake or altering the activity of individual ETC complexes. It has been suggested that Q_{10} could act as a physical barrier, effectively preventing H^+ leakage in mitochondria[39] and reducing the leakage of small hydrophilic molecules in Q_{10}-enriched IMMs[30]. Decreased membrane viscosity reduces the physical barrier to O_2 permeation[335], which means increased membrane viscosity would hinder passive diffusion of O_2. Considering the distinct effects of Qs/HO-Qs on CI-linked (Figure 4-42) and CII-linked (Figure 4-43) respiration, it can be assumed that reduced respiration in our experiments is not due to decreased O_2 supply in the mitochondria. However, further experiments examining mitochondrial O_2 levels would be necessary to confirm this statement.

Ca^{2+} ions tend to form ion pairs with the negatively charged moieties from acidic lipids, which are abundantly found in mitochondrial membranes. Moreover, it is widely accepted that the presence of Ca^{2+} induces rigidity of the lipid bilayers[336–339]. Additionally, studies have reported that Ca^{2+} leads to conformational changes in the lipid headgroup region[340], increased acyl chain order[336,337,340,341], lipid dehydration[336,342], and a decrease in membrane fluidity[343]. Therefore, the viscosity of the membrane would be increased, and consequently would cause reduction in the respiration rates, as it was observed in the presence of Ca^{2+} compared to Ca^{2+}-free conditions (Figure 4-41). Additionally, the fact that CI-linked respiration is more significantly affected by the presence of Ca^{2+} compared to CII-linked respiration along with considering the location of these complexes within the IMM (small part of CII is embedded in the IMM and the bigger part in the MM) further suggests a membrane-dependent mechanism for the observed respiration rates.

Voltammetric experiments showed that HO-Qs and Qs form ion pairs with Ca^{2+} (section 4.2.2), suggesting that they could potentially provide additional sites for Ca^{2+}-binding within membranes. Qs and HO-Qs interact with Ca^{2+} in various stoichiometries (Figure 5-1) where the possibility of forming agglomerates consisting of multiple Qs or HO-Qs molecules bound to Ca^{2+} could not be excluded. This in turn could lead to a more pronounced impact on membrane properties, and consequently on mitochondrial respiration. Moreover, it can be expected that HO-Q_{10} and Q_{10} exhibit a similar interaction with Ca^{2+} as found for HO-Q_1 and Q_1, and that HO-Q_{10} has a higher affinity for Ca^{2+} than Q_{10}. This could explain the observed Ca^{2+}-dependent inhibition of mitochondrial respiration by HO-Q_{10}.

The inhibitory effects observed with HO-Q_1 and HO-dUQ, which in our studies appear to be independent of Ca^{2+}, imply distinct mechanisms by which they hinder mitochondrial respiration compared to HO-Q_{10}. Hydrophilic Qs tend to localize closer to the polar surface in the lipid bilayer than does the hydrophobic Q_{10}. Consequently, their impact on the acyl chain order may be negligible. Moreover, dUQ with its saturated decyl hydrocarbon sidechain would interact differently with the acyl chains of the membrane compared to Q_{10}. The different localizations of Qs within the membrane, which are influenced by the sidechain, suggest that they may have access to different reductases, thereby most likely acting at different sites within the ETC.

The precise mechanisms of action for Qs and HO-Qs can only be hypothesized based on the available data. Additional research should be directed towards examining the impact of these compounds on mitochondrial membrane fluidity with varying $[Ca^{2+}]$ as well as assessing their diffusion coefficients within the membranes.

5.6.2 Cellular Ca^{2+} homeostasis

Mitochondria can store up to 500 µM Ca^{2+}[111,118,132], therefore playing diverse roles in intracellular Ca^{2+} signalling, acting as effectors in processes such as energy metabolism and cell death, and modulators of cytosolic Ca^{2+} signals. To fulfil these functions effectively, mitochondrial Ca^{2+} uptake and extrusion must be tightly coordinated. Mitochondrial Ca^{2+} uptake is an electrogenic process driven by the large negative potential ($\Delta\Psi_m = -180$ mV) within the mitochondria. The primary mediator of this uptake is the mitochondrial Ca^{2+} uniporter (MCU) complex[111,344,345]. Ca^{2+}

efflux from the MM mainly occurs through the activity of the $Na^+/Ca^{2+}/Li^+$ exchanger (NCLX)[111]. However, it is suggested that NCLX alone may not be the sole pathway for Ca^{2+} extrusion from the MM. It has been proposed that under certain conditions the mitochondrial permeability transition pore (mPTP) could serve as an additional pathway for Ca^{2+} efflux[128,129], although this hypothesis is subject of debate due to conflicting results[130].

Bogeski *et al.*[10], based on the discovery of OH-Qs and their redox properties that allow them to transfer Ca^{2+} through artificial bio-membranes, have suggested another component, e.g., Q_{10} and HO-Q_{10} in the IMM to mobilize Ca^{2+} and support Ca^{2+} buffering activity of mitochondria. Furthermore, the voltammetric measurements performed in this thesis unquestionably proved that there is interaction of HO-Qs (Figure 4-26 and Figure 4-28) as well as their native forms Qs (Figure 4-25 and Figure 4-27) with Ca^{2+}, where HO-Qs showed higher affinity for Ca^{2+} compared to Qs (Table 4-6). Considering the interplay between mitochondrial Ca^{2+} transport and respiratory chain function with Q_{10} playing a vital role in the mitochondrial ETC, and the significance of mitochondrial Ca^{2+} accumulation and ROS production in cellular fate regulation, our study aimed to explore the impact of externally supplemented Qs and HO-Qs on intracellular Ca^{2+} metabolism.

The observed impact of Qs and HO-Qs on the ETC (Figure 4-42 and Figure 4-43) can potentially disrupt the delicate regulation of the cellular Ca^{2+} homeostasis. Nonetheless, our results indicated no significant alterations in cytosolic Ca^{2+} levels following treatment of HEK-293 cells with Q_{10}, Q_1, and their HO-Qs (Figure 4-36). A study conducted by Xu *et al.*[346] revealed that a 24 hours treatment of HepG2 cells with Q_{10} led to a substantial increase in the expression of SERCA. On the other hand, Q_{10} treatment did not exert any direct effects on Ca^{2+} channels.

Our data revealed notable transient fluctuations in $[Ca^{2+}]_i$ in HEK-293 cells that were supplemented with dUQ, HO-dUQ (Figure 4-36 panels e and f), mQ, and HO-mQ (Figure 4-38). Surprisingly, these effects exhibited significant variations among the compounds despite their relatively similar structures (Figure 1-9). When comparing the structures of mQ and dUQ as well as HO-mQ and HO-dUQ, the main distinction is the presence of the mitochondrial targeting component triphenylphosphonium cation (TPP$^+$) which facilitates the accumulation of mQ/HO-mQ within mitochondria. Studies have demonstrated that mQ and mitoE* can elevate mitochondrial Ca^{2+} levels in HeLa cells, an effect which has been attributed to inhibition of the NCLX by the TPP$^+$ component[347]. Additionally, it has been reported that mQ disrupted $\Delta\Psi_m$ and caused ROS production, consequently inducing mitochondrial fragmentation and elevated cytosolic Ca^{2+} levels in cancer cells[348]. Our data showed that mQ, and to some extent HO-mQ, led to a collapse of the $\Delta\Psi_m$ (Figure 4-39) and strongly affected cell viability (Figure 4-35), which are indications for a change in mitochondrial metabolism and cytotoxic effects. On the other side, dUQ and HO-dUQ neither altered the $\Delta\Psi_m$ (Figure 4-39) nor cell viability (Figure 4-35).

HO-dUQ-treatment induced a gradual increase in the $[Ca^{2+}]_i$ immediately after its application to the cells in the absence of extracellular Ca^{2+} (Figure 4-37 b), which was shown to be caused by

---

* Vitamin E conjugated to TPP$^+$

Ca^{2+} release from the intracellular Ca^{2+} stores. Moreover, the activities of plasma membrane Ca^{2+} pump (PMCA) and NCX were not hindered by HO-dUQ since the extrusion of Ca^{2+} from the cell after treatment with ionomycin was detected (Figure 4-37 b). Although $[Ca^{2+}]$ in lysosomes is relatively high, their volume is about 1% of the cell volume[349], thus the lysosomal pool is a rather small Ca^{2+} reservoir and lysosomal Ca^{2+} might not be sufficient for the observed increase in the $[Ca^{2+}]_i$. Since thapsigargin (Tg) was applied before HO-dUQ to irreversibly empty the ER Ca^{2+} stores (Figure 4-37 b), only mitochondria remain as Ca^{2+} sources. Therefore, most probably the gradual increase in the $[Ca^{2+}]_i$ is due to Ca^{2+} leak or release from mitochondria.

It has been demonstrated that dUQ inhibits the opening of mPTP[45,296,350,351]. Walter *et al.*[45] conducted a screening of various ubiquinone analogues to assess their effects on the mPTP and have identified three groups of mPTP modulators, among them: inhibiting, inducing, and inactive ubiquinones. Interestingly, their results highlighted the profound impact of even minor changes in the chemical structure on the interaction between Qs and mPTP. For example, dUQ acted as an inhibitor of the mPTP, while structural analogues such as idebenone, which contains a HO-group at the end of the 10-carbon sidechain, and 2,5-dihydroxy decylubiquinone, acted as inducers of mPTP opening. This suggests that particular substituents at position 2-, 3-, 5-, and 6- of the quinone ring may be crucial for modulating the mPTP. Based on this, it appears highly probably that HO-dUQ serves as an inducer of the mPTP, due to the presence of hydroxyl group at position 2- or 3- of the quinone ring. Recent findings suggest that mPTP may have physiological functions beyond its well-known association with pathological conditions[259,352]. These functions of the mPTP have been attributed to its conductance state which can exist in two modes: low and high conductance. In the high conductance mode, primarily observed under pathological conditions, the pore becomes permeable to large molecules leading to irreversible opening, dissipation of the $\Delta\Psi_m$, and initiation of cell death. On the other hand, the low conductance mode occurs in a transient and flickering manner enabling selective permeability to small ions such as Ca^{2+}, H^+, and K^+. Therefore, the transient opening of the mPTP in the low conductance mode could play a role in maintaining cellular Ca^{2+} homeostasis by allowing controlled release of Ca^{2+} from mitochondria[259]. This controlled release helps prevent mitochondrial Ca^{2+} overload without impairing mitochondrial functions. Considering this and the findings that HO-dUQ stimulated release of Ca^{2+} from mitochondria into the cytosol without altering the potential and the cell viability, it could be assumed that HO-dUQ induces opening of the mPTP in the low conductance mode. Nevertheless, since HO-dUQ hindered both CI- and CII-linked respiration, it becomes challenging to draw definitive conclusions. Consequently, further experiments are necessary to investigate the specific influence of HO-dUQ on the mPTP. The mPTP could be assessed by mitochondrial swelling assay which measures the volume of the MM, and/or the Ca^{2+} retention capacity method which evaluates the ability of mitochondria to accumulate Ca^{2+} within the MM before initiating mPTP opening. These experimental approaches will enable a more comprehensive understanding of the effects of HO-dUQ on the mPTP.

Given the distinct outcomes observed between the Qs and HO-Qs, where certain compounds have no effect, while others influence specific Ca^{2+} transients, it is essential to consider membrane-associated effects. The properties and functions of Ca^{2+} transport proteins and channels are known to be influenced by the lipid environment[339]. Additionally, since a portion of the supplemented Qs and HO-Qs most likely incorporates into the plasma membrane (PM) alongside the IMM, they could potentially disrupt the physico-chemical properties of the PM. For example, the PMCA is more active in liquid ordered lipids, while the SERCA, physiologically located in a more fluid membrane, shows reduced Ca^{2+} pumping in environments with increased lipid order. Ca^{2+} channels are also affected by membrane fluidity as disruption or fluidization of the lipid membrane decreases voltage-gated channels (VGCs) activation, whereas TRP channels tend to segregate into phases with increased order of the lipids but still fluid[339]. dUQ contains a saturated ten carbon sidechain and its incorporation in the membranes by analogy to saturated fatty acids[353] would increase the lipid order and decrease membrane fluidity. This would make the membrane more rigid which could be the reason for the observed effects on Ca^{2+} release from ER as well as the reduced Ca^{2+} influx (Figure 4-36 panels e and f). Indeed, it is important to acknowledge that a direct interaction between the Qs, HO-Qs, and the Ca^{2+} transport proteins and channels cannot be ruled out. While the influence on the lipidic environment is one possible explanation, it is also plausible that the Qs and HO-Qs directly interact with these proteins and channels, thereby affecting their functionality. Further investigations are necessary to explore potential mechanisms and ascertain whether the physico-chemical properties of the PM are affected or if there is a direct interaction between the Qs, HO-Qs, and the Ca^{2+} transport proteins and channels.

5.6.3 The case of mQ and HO-mQ

Mitochondria are integral to diverse cellular functions and overall cellular health. Consequently, mitochondrial defects or dysfunctions significantly contribute to major diseases[354]. In many instances, mitochondria-associated diseases are primarily attributed to the damaging effects of ROS produced within mitochondria (mtROS)[102,355,356]. Significant efforts have been devoted to the development of therapeutic compounds specifically designed to target mitochondria and selectively inhibit mtROS-induced damage[357–360]. One notable example of a mitochondrial-targeted antioxidant is mitoquinone (mQ)[151]. Since its discovery[151], mQ has been extensively studied both *in vitro* and *in vivo* to evaluate its therapeutic potential in diseases associated with oxidative stress and mitochondrial dysfunction. Numerous *in vitro* studies have consistently demonstrated the ability of mQ to scavenge ROS and protect cells of different types from oxidative damage[150,361–365]. Further, *in vivo* studies have shown successful treatment by mQ in animal models of cardiac fibrosis[366], Parkinson's[362] and Alzheimer's[367] disease. The encouraging outcomes obtained from these studies have prompted the advancement of mQ into human clinical trials for various diseases[360]. The effectiveness of mQ varies with positive results seen in some conditions, while showing no efficiency in others, suggesting that the molecular

mechanisms underlying its action are not yet fully comprehended, highlighting the need for additional research.

Considering the documented beneficial effects of mQ, our research group has recently developed a novel mono-hydroxylated analogue of mQ, designated as HO-mQ[149]. Through physico-chemical techniques, in particular voltammetry and EPR, it has been demonstrated that HO-mQ possesses stronger antioxidant properties and exhibits a higher affinity for Ca^{2+} compared to mQ[149]. Hence, motivated by these findings, we conducted *in vitro* experiments to investigate the effects of the newly synthesized HO-mQ. We administered both mQ and HO-mQ to HEK-293 cells and to isolated mitochondria from murine heart. To our surprise, treatment with mQ led to strong adverse effects such as depolarization of the mitochondrial membrane in HEK-293 cells (Figure 4-39) accompanied by considerable alterations in Ca^{2+} signalling (Figure 4-38) and adverse effects on cell viability (Figure 4-35). Furthermore, the administration of mQ to isolated mitochondria rapidly impeded mitochondrial respiration, irrespective of the presence of Ca^{2+} (Figure 4-42 and Figure 4-43). Although limited in number, certain reports are lining up with our findings and have raised concerns about potential adverse effects of mQ. For instance, Gottwald *et al.*[368] recently have reported that mQ induced rapid and severe mitochondrial swelling and depolarization of the IMM in kidney proximal tubular cells. Despite of mQ altering the mitochondrial morphology, the oxidative phosphorylation function was not inhibited and no decrease in the OCR was observed[368]. Furthermore, earlier studies[369] have also demonstrated that mQ lowered the $\Delta\Psi_m$ in bovine aortic endothelial cells (BAECs). Interestingly, these studies revealed no toxicity when evaluating cell viability and mQ was found to enhance respiration in both BAECs and isolated mitochondria. In contrast to these findings, our own data show a significant impact on viability of HEK-293 cells after mQ treatment and align with another study[370] where mQ has been found to inhibit the proliferation of two breast cancer cell lines, MDA-MB-231 and MCF-7. Nevertheless, in the same study mQ did not affect the proliferation rate of the non-tumor MCF-12A cell line. A similar toxicity induced by mQ was observed in MDA-MB-231 and H23 lung cancer cell lines[371]. Recent research has demonstrated that mQ, when applied at concentrations over 1 µM, exhibit a prooxidant effects and can potentially be used as chemotherapeutic drugs to kill tumour cells[371,372]. Cancer cells have a more negative $\Delta\Psi_m$ than healthy cells, consequently accumulating higher amounts of mQ in mitochondria. It is important to note that not only mQ but also other TPP⁺-conjugated compounds such as mitoTEMPOL and mitoE have shown limited effectiveness in mtROS-induced injuries and have a negative impact on mitochondrial function[373]. The adverse effects of mQ treatment in previous studies were attributed either to its prooxidant activity or to the presence of the TPP⁺ cation. The TPP⁺ moiety, although typically considered inert and biologically inactive, has a strong affinity for phospholipid membranes[374]. This property increases the likelihood of disrupting membrane integrity, especially in mitochondria where these compounds accumulate. Such disruption can alter the function of mitochondrial membrane proteins including inhibiting ETC complexes[373,375–377], Krebs cycle enzymes[378], and NCLX[347]. The occurrence of side effects from TPP⁺-conjugated compounds,

mediated by either the cation moiety or prooxidant behaviour, depends critically on their concentration[375,377]. Therefore, selecting the appropriate concentration is crucial and it depends on the cell type under investigation. Here, we acknowledge the limitations of our study as we only utilized a single concentration of mQ, 20 µM for HEK-293 cells and 10 µM for mitochondria. While these concentrations fall within the range (0.1-20 µM) commonly employed in other *in vitro* studies reported in the literature, they are considerably higher than the concentrations observed in *in vivo* studies following oral administration[379]. However, these concentrations were selected to ensure consistent conditions for all Qs used in this study.

Interestingly, both mQ and HO-mQ possess a TPP$^+$ cation, but their effects differ. mQ induced significant alterations in Ca^{2+} signalling, $\Delta\Psi_m$, and cell viability, while HO-mQ exhibited milder effects. Treatment with HO-mQ led to a decrease in $\Delta\Psi_m$, albeit to a lesser extent compared to mQ (Figure 4-39). Although HO-mQ affected Ca^{2+} signalling, it does not completely impair it as observed with mQ (Figure 4-38). Notably, within the initial 2 hours of treatment, cell viability remained unaffected by HO-mQ, unlike mQ (Figure 4-35). In contrast, HO-mQ demonstrated a higher inhibition of mitochondrial respiration compared to mQ, and like mQ showed a Ca^{2+}-independent inhibition (Figure 4-42 and Figure 4-43). One possible explanation for these differences lies in the structure of HO-mQ itself. In addition to the positive charge on the TPP$^+$ group, HO-mQ possesses an additional −OH group. Thus, at physiological pH as indicated by its theoretically calculated pK_a (~5.6), HO-mQ would exists as a mixture of protonated and deprotonated forms, with the latter acting as a zwitterion. As a zwitterion it would behave as a neutral molecule due to the balance between positive and negative charges. Consequently, it is theoretically less likely to be taken up by mitochondria (driven by the $\Delta\Psi_m$). Lesser uptake of HO-mQ by the mitochondria could explain the milder effects observed with HO-mQ compared to mQ. Nevertheless, Finichiu *et al.*[380] by using two model compounds, TPP$^+$-linked aliphatic carboxylic acid (weak acid, pK_a~4.9) and TPP$^+$-linked aliphatic amine (weak base, pK_a~10.6), and a simple methyl-TPP$^+$ derivative as a control, had demonstrated that TPP$^+$-linked carboxylic acid was accumulated in the mitochondria to a greater extent than the TPP$^+$-linked amine and the control. Additionally, the TPP$^+$-linked aliphatic amine (dication) accumulated to lesser amounts than methyl-TPP$^+$ (monocation). Despite mostly existing as a zwitterion, TPP$^+$-linked carboxylic acid accumulated in mitochondria. In this case, the uptake into mitochondria depended not only on the $\Delta\Psi_m$ but also on the pH gradient between the cytosol (pH~7.2)[299] and the mitochondrial matrix (pH~8)[299]. The presence of protonated and deprotonated forms of the acid depends on its pK_a and the local pH. In line with this, it has been reported that TPP$^+$ linked to stronger acids (pK_a~2) were not taken up by mitochondria as they exist primarily in the deprotonated form[380–383]. It would be intriguing to investigate if a similar trend could be observed for mQ and HO-mQ considering the pK_a of the α-hydroxyl group (~5.6) which fulfils the conditions for a weak acid. If this trend holds true and considering the observed biological effects of HO-mQ compared to mQ, HO-mQ could be a potentially better therapeutic candidate.

6. Conclusion

In conclusion, Q_{10}-like compounds, albeit having similar redox properties, showed different biological activities compared to Q_{10}. Besides the quinone ring moiety which confers the redox properties of Qs, the structure of the sidechains is crucial for their location within cellular membrane phospholipids, consequently for their function. Thus, most likely membrane-associated effects by Qs and HO-Qs are causing distinct impacts on mitochondrial respiration, on cellular Ca^{2+} homeostasis, and other essential parameters of cellular metabolism.

Our studies showed that the studied Qs and HO-Qs cannot substitute for each other and calling them analogues of Q_{10} should be taken with caution. The presented data, while contributing to our current knowledge, also shows limitations in our understanding of the role of Q_{10}-like compounds in cellular processes. Moreover, these results raise concerns regarding the use of some of these quinones as analogues of Q_{10} or as antioxidants, in particular their utilization as therapeutic agents in clinical trials.

7. Appendices

Appendix A

Appendix to section 4.2.1.

Table A - 1 Electrochemical parameters from the cyclic voltammograms of the Q_1 and HO-Q_1 measured in 0.1 M HEPES at pH 7.4. $E_{p,a}$, anodic peak potential; $E_{p,c}$, cathodic peak potential; $I_{p,a}$, anodic peak current; $I_{p,c}$, cathodic peak current; $\Delta E_p = E_{p,a} - E_{p,c}$, peak-to-peak separation; $E_{p,mid} = (E_{p,a} - E_{p,c})/2$, midpoint peak potential.

	$E_{p,a}$	$E_{p,c}$	ΔE_p	$E_{p,mid}$	$I_{p,a}/I_{p,c}$
	V	V	mV	V	
Q_1	+0.050	−0.238	288	−0.094	0.53
HO-Q_1	−0.095	−0.365	270	−0.230	0.94

Table A - 2 Electrochemical parameters from the cyclic voltammograms of the Q_1 and HO-Q_1 measured in 0.1 M KCl at pH 7.4. $E_{p,a}$, anodic peak potential; $E_{p,c}$, cathodic peak potential; $I_{p,a}$, anodic peak current; $I_{p,c}$, cathodic peak current; $\Delta E_p = E_{p,a} - E_{p,c}$, peak-to-peak separation; $E_{p,mid} = (E_{p,a} - E_{p,c})/2$, midpoint peak potential.

	$E_{p,a}$	$E_{p,c}$	ΔE_p	$E_{p,mid}$	$I_{p,a}/I_{p,c}$
	V	V	mV	V	
Q_1	−0.202	−0.286	84	−0.244	0.66
HO-Q_1	−0.332	−0.500	168	−0.416	0.85
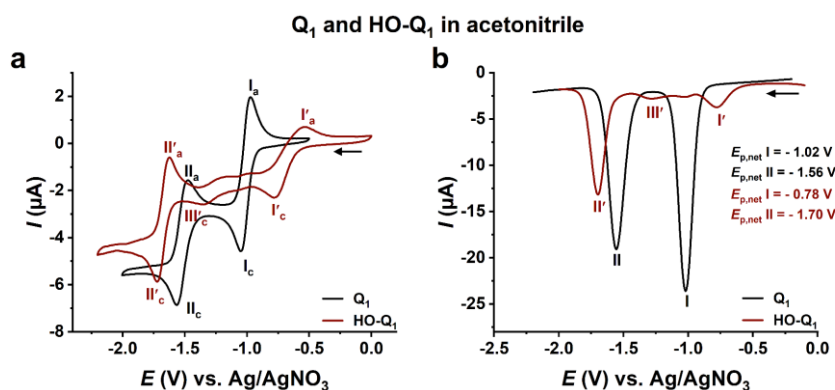
Figure A - 1 Redox reaction of Q_1 and HO-Q_1 in aprotic organic solvent. a) Cyclic voltammograms and b) square-wave voltammograms of 0.5 mM of Q_1 (black) and HO-Q_1 (red) in acetonitrile with 0.1 M TBAP as electrolyte at glassy carbon electrode. The subscripts c and a in the peak descriptions (e.g., Ic, Ia) indicate cathodic (reduction) and anodic (oxidation) reaction. Arrows indicate the direction of the applied potential. CV parameters: v = 20 mV/s, ΔE = 1 mV; SWV parameters: f = 10 Hz, E_{sw} = 50 mV, ΔE = 1 mV.

Appendix B

Appendix to section 4.2.2.
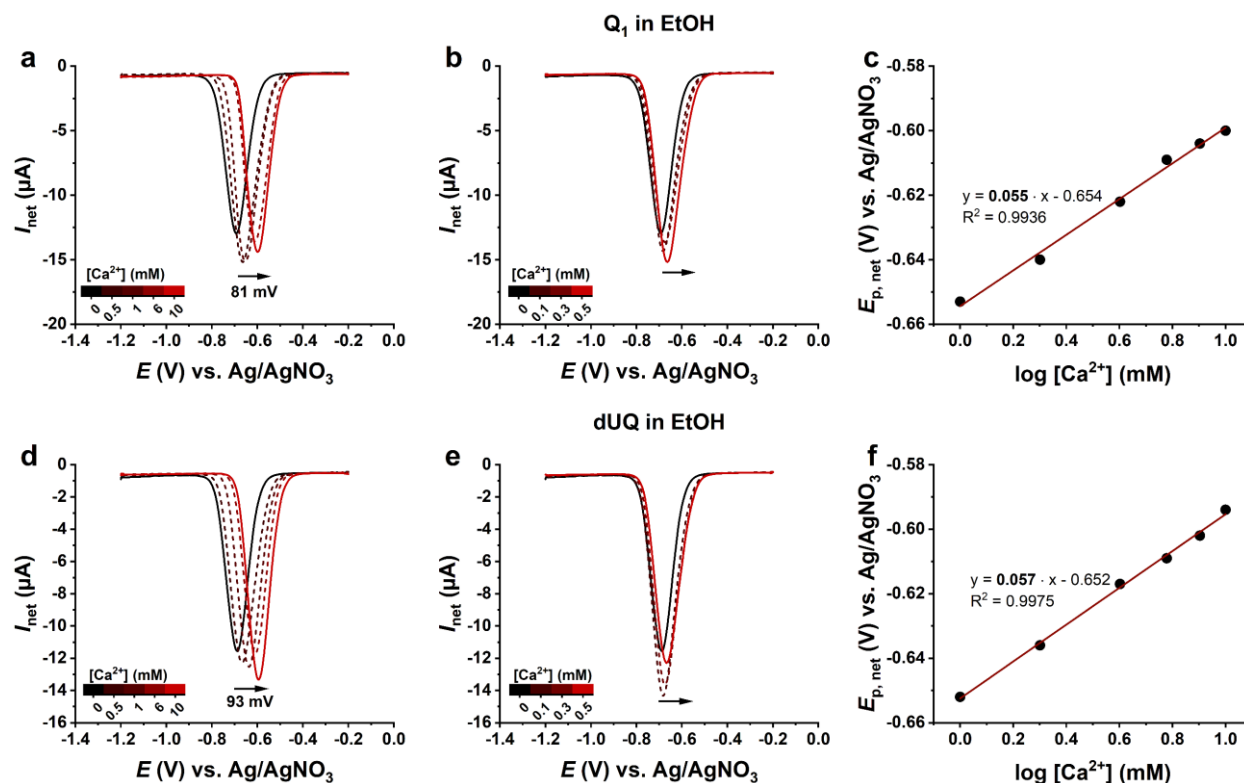
Figure B - 1 Effects of Ca^{2+} on the voltammetric responses of Q_1 and dUQ recorded in ethanol. Square-wave voltammograms of 0.5 mM Q_1 (panels a, b) and dUQ (panels d, e) in the absence (black line) and in the presence of different concentrations of Ca^{2+} (0.1-10 mM, red dashed and solid lines), in de-aerated ethanol with 0.1 M $LiClO_4$ as electrolyte at GC electrode. Dependence of the net peak potential ($E_{p,net}$) of c) Q_1 and f) dUQ on the logarithm of $[Ca^{2+}]$ from panels a and d, respectively. SWV parameters: f = 8 Hz, E_{sw} = 50 mV, ΔE = 1 mV.
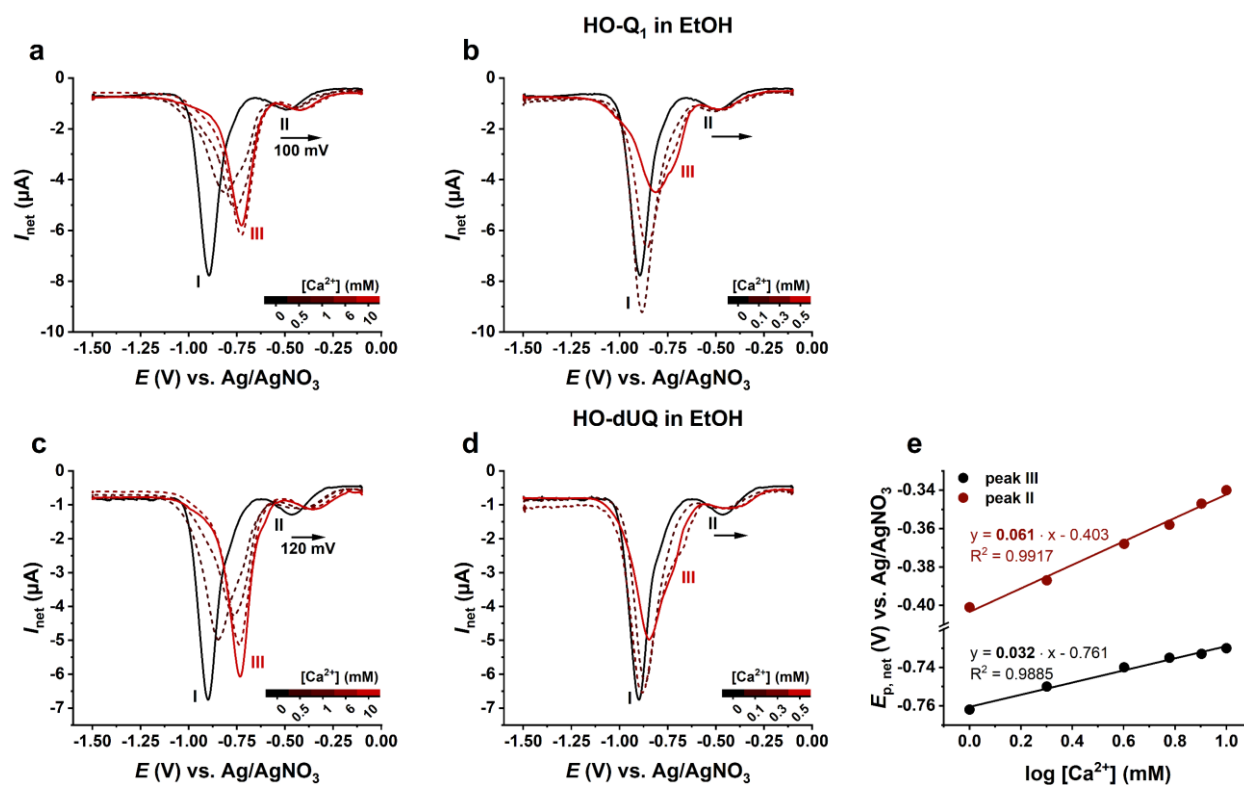
Figure B - 2 Effects of Ca^{2+} on the voltammetric responses of HO-Q_1 and HO-dUQ recorded in ethanol. Square-wave voltammograms of 0.5 mM HO-Q_1 (panels a, b) and HO-dUQ (panels c, d) in the absence (black line) and in the presence of different concentrations of Ca^{2+} (0.1-10 mM, red dashed and solid lines), in de-aerated ethanol with 0.1 M $LiClO_4$ as electrolyte at GC electrode. e) Dependence of the net peak potential ($E_{p,net}$) of peak III (black) and peak II (red) of dUQ on the logarithm of $[Ca^{2+}]$ from panel c. SWV parameters: f = 8 Hz, E_{sw} = 50 mV, ΔE = 1 mV.

Figure B - 3 Effects of Ca^{2+} on the voltammetric response of Q$_1$ and dUQ recorded in methanol. Square-wave voltammograms of 0.5 mM Q$_1$ (panels a, b) and dUQ (panels d, e) in the absence (black line) and in the presence of different concentrations of Ca^{2+} (0.1-10 mM, red dashed and solid lines), in de-aerated methanol with 0.1 M LiClO$_4$ as electrolyte at GC electrode. Dependence of the net peak potential ($E_{p,net}$) of c) Q$_1$ and f) dUQ on the logarithm of [Ca^{2+}] from panels a and d, respectively. SWV parameters: f = 8 Hz, E_{sw} = 50 mV, ΔE = 1 mV.

Figure B - 4 Effects of Ca^{2+} on the voltammetric responses of HO-Q$_1$ and HO-dUQ recorded in methanol. Square-wave voltammograms of 0.5 mM HO-Q$_1$ (panels a, b) and HO-dUQ (panels c, d) in the absence (black line) and in the presence of different concentrations of Ca^{2+} up to 10 mM concentration (red dashed and solid lines), in de-aerated methanol with 0.1 M LiClO$_4$ as electrolyte at GC electrode. SWV parameters: f = 8 Hz, E_{sw} = 50 mV, ΔE = 1 mV.

8. Bibliography

1. Silva, T. L. *et al.* Quinone-based molecular electrochemistry and their contributions to medicinal chemistry: A look at the present and future. *Curr Opin Electrochem* **24**, 79–87 (2020).

2. Thomson, R. H. *Naturally Occurring Quinones*. (Academic Press Inc., 1971).

3. Nohl, H., Jordan, W. & Youngman, R. J. Quinones in Biology: Functions in electron transfer and oxygen activation. *Advances in Free Radical Biology and Medicine* **2**, 211–279 (1986).

4. El-Najjar, N. *et al.* The chemical and biological activities of quinones: Overview and implications in analytical detection. *Phytochemistry Reviews* **10**, 353–370 (2011).

5. Crane, F. L., Hatefi, Y., Lester, R. L. & Widmer, C. Isolation of a quinone from beef heart mitochondria. *BBA - Biochimica et Biophysica Acta* **25**, 220–221 (1957).

6. Morton, R. A. Ubiquinone. *Nature* **182**, 1764–1767 (1958).

7. Wolf, D. E. *et al.* Coenzyme Q. I. Structure studies on the coenzyme Q group. *J Am Chem Soc* **80**, 4752 (1958).

8. Mitchell, P. Coupling of phosphorylation to electron and hydrogen transfer by a chemi-osmotic type of mechanism. *Nature* **191**, 144–148 (1961).

9. Suárez-Rivero, J. M. *et al.* Coenzyme q10 analogues: Benefits and challenges for therapeutics. *Antioxidants* **10**, 1–20 (2021).

10. Bogeski, I. *et al.* Calcium binding and transport by coenzyme Q. *J Am Chem Soc* **133**, 9293–9303 (2011).

11. Gulaboski, R. *et al.* Hydroxylated derivatives of dimethoxy-1,4-benzoquinone as redox switchable earth-alkaline metal ligands and radical scavengers. *Scientific Reports 2013 3:1* **3**, 1–8 (2013).

12. Gulaboski, R. *et al.* New insights into the chemistry of Coenzyme Q-0: A voltammetric and spectroscopic study. *Bioelectrochemistry* **111**, 100–108 (2016).

13. Gulaboski, R., Markovski, V. & Jihe, Z. Redox chemistry of coenzyme Q—a short overview of the voltammetric features. *Journal of Solid State Electrochemistry* **20**, 3229–3238 (2016).

14. Haeri, H. H. *et al.* An EPR and DFT study on the primary radical formed in hydroxylation reactions of 2,6-dimethoxy-1,4-benzoquinone. **114**, 1856–1866 (2016).

15. Stefely, J. A. & Pagliarini, D. J. Biochemistry of Mitochondrial Coenzyme Q Biosynthesis. *Trends Biochem Sci* **42**, 824–843 (2017).

16. Slowik, E. J. Synthesis, endogenous detection, and mitochondrial function of the hydroxyl-substituted Coenzyme Q10 derivative HO-CoQ10. (Saarland University, 2019).

17. Brunmark, A. & Cadenas, E. Redox and addition chemistry of quinoid compounds and its biological implications. *Free Radic Biol Med* **7**, 435–477 (1989).

18. Bailey, S. I. & Ritchie, I. M. A cyclic voltammetric study of the aqueous electrochemistry of some quinones. *Electrochim Acta* **30**, 3–12 (1985).

19. Gordillo, G. J. & Schiffrin, D. J. Redox properties of ubiquinon (UQ10) adsorbed on a mercury electrode. *Journal of the Chemical Society, Faraday Transactions* **90**, 1913–1922 (1994).

20. Pettersson, G., Forshell, G. P., Jackman, L. M. & Sparrow, D. R. Synthesis of 2,3-Dihydroxy-5,6-dimethyl-1,4-benzoquinone and its Monomethyl Ether. *Acta Chem Scand* **18**, 2309–2312 (1964).

21. Bennett, I. M. *et al.* Active transport of Ca2+ by an artificial photosynthetic membrane. *Nature* **420**, 398–401 (2002).

22. Mirčeski, V., Gulaboski, R., Bogeski, I. & Hoth, M. Redox chemistry of Ca-transporter 2-palmitoylhydroquinone in an artificial thin organic film membrane. *Journal of Physical Chemistry C* **111**, 6068–6076 (2007).

23. Bhagavan, H. N. & Chopra, R. K. Coenzyme Q10: Absorption, tissue uptake, metabolism and pharmacokinetics. *Free Radic Res* **40**, 445–453 (2006).

24. Braasch-Turi, M. M., Koehn, J. T. & Crans, D. C. Chemistry of Lipoquinones: Properties, Synthesis, and Membrane Location of Ubiquinones, Plastoquinones, and Menaquinones. *Int J Mol Sci* **23**, (2022).

25. Braasch-Turi, M. M. *et al.* Electron Transport Lipids Fold Within Membrane-Like Interfaces. *Front Chem* **10**, (2022).

26. Trumpower, B. L. New concepts on the role of ubiquinone in the mitochondrial respiratory chain. *J Bioenerg Biomembr* **13**, 1–24 (1981).

27. Afri, M. *et al.* Active oxygen chemistry within the liposomal bilayer: Part III: Locating Vitamin E, ubiquinol and ubiquinone and their derivatives in the lipid bilayer. *Chem Phys Lipids* **131**, 107–121 (2004).

28. Hauß, T., Dante, S., Haines, T. H. & Dencher, N. A. Localization of coenzyme Q10 in the center of a deuterated lipid membrane by neutron diffraction. *Biochim Biophys Acta Bioenerg* **1710**, 57–62 (2005).

29. Agmo Hernández, V., Eriksson, E. K. & Edwards, K. Ubiquinone-10 alters mechanical properties and increases stability of phospholipid membranes. *Biochim Biophys Acta Biomembr* **1848**, 2233–2243 (2015).

30. Eriksson, E. K., Agmo Hernández, V. & Edwards, K. Effect of ubiquinone-10 on the stability of biomimetic membranes of relevance for the inner mitochondrial membrane. *Biochim Biophys Acta Biomembr* **1860**, 1205–1215 (2018).

31. Kingsley, P. B. & Feigenson, G. W. 1H-NMR study of the location and motion of ubiquinones in perdeuterated phosphatidylcholine bilayers. *BBA - Bioenergetics* **635**, 602–618 (1981).

32. Stidham, M. A., McIntosh, T. J. & Siedow, J. N. On the localization of ubiquinone in phosphatidylcholine bilayers. *BBA - Bioenergetics* **767**, 423–431 (1984).

33. Ulrich, E. L., Girvin, M. E., Cramer, W. A. & Markley, J. L. Location and Mobility of Ubiquinones of Different Chain Lengths in Artificial Membrane Vesicles. *Biochemistry* **24**, 2501–2508 (1985).

34. Lenaz, G. *et al.* Localization and preferred orientations of ubiquinone homologs in model bilayers. *Biochem Cell Biol* **70**, 504–514 (1992).

35. Turunen, M., Olsson, J. & Dallner, G. Metabolism and function of coenzyme Q. *Biochim Biophys Acta Biomembr* **1660**, 171–199 (2004).

36. Lucy, J. A. & Dingle, J. T. Fat-soluble vitamins and biological membranes. *Nature* **204**, 156–160 (1964).

37. Lucy, J. A. Functional and structural aspects of biological membranes: a suggested structural role for vitamin E in the control of membrane permeability and stability. *Ann N Y Acad Sci* **203**, 4–11 (1972).

38. De Maria, P. *et al.* Cardanol as a replacement for cholesterol into the lipid bilayer of POPC liposomes. *Colloids Surf B Biointerfaces* **40**, 11–18 (2005).

39. Haines, T. H. Do sterols reduce proton and sodium leaks through lipid bilayers? *Prog Lipid Res* **40**, 299–324 (2001).

40. Sévin, D. C. & Sauer, U. Ubiquinone accumulation improves osmotic-stress tolerance in Escherichia coli. *Nat Chem Biol* **10**, 266–272 (2014).

41. Katsikas, H. & Quinn, P. J. The polyisoprenoid chain length influences the interaction of ubiquinones with phospholipid bilayers. *BBA - Biomembranes* **689**, 363–369 (1982).

42. Crane, F. L. Biochemical Functions of Coenzyme Q10. *J Am Coll Nutr* **20**, 591–598 (2001).

43. Echtay, K. S., Winkler, E. & Klingenberg, M. Coenzyme Q is an obligatory cofactor for uncoupling protein function. *Nature* **408**, 609–613 (2000).

44. Echtay, K. S., Winkler, E., Frischmuth, K. & Klingenberg, M. Uncoupling proteins 2 and 3 are highly active H+ transporters and highly nucleotide sensitive when activated by coenzyme Q (ubiquinone). *Proc Natl Acad Sci U S A* **98**, 1416–1421 (2001).

45. Walter, L. *et al.* Three classes of ubiquinone analogs regulate the mitochondrial permeability transition pore through a common site. *Journal of Biological Chemistry* **275**, 29521–29527 (2000).

46. Papucci, L. *et al.* Coenzyme Q10 prevents apoptosis by inhibiting mitochondrial depolarization independently of its free radical scavenging property. *Journal of Biological Chemistry* **278**, 28220–28228 (2003).

47. Morré, D. J. & Morré, D. M. Non-mitochondrial coenzyme Q. *BioFactors* **37**, 355–360 (2011).

48. Gutierrez-Mariscal, F. M., Yubero-Serrano, E. M., Villalba, J. M. & Lopez-Miranda, J. Coenzyme Q10: From bench to clinic in aging diseases, a translational review. *Crit Rev Food Sci Nutr* **59**, 2240–2257 (2019).

49. Nelson, D. L. & Cox, M. M. *Lehninger Principles of Biochemistry*. (W.H. Freeman, 2017).

50. Nolfi-Donegan, D., Braganza, A. & Shiva, S. Mitochondrial electron transport chain: Oxidative phosphorylation, oxidant production, and methods of measurement. *Redox Biol* **37**, (2020).

51. Rugolo, M., Zanna, C. & Ghelli, A. M. Organization of the respiratory supercomplexes in cells with defective complex III: Structural features and metabolic consequences. *Life* **11**, (2021).

52. Mitchell, P. Protonmotive redox mechanism of the cytochrome b-c1 complex in the respiratory chain: Protonmotive ubiquinone cycle. *FEBS Lett* **56**, 1–6 (1975).

53. Milenkovic, D., Blaza, J. N., Larsson, N. G. & Hirst, J. The Enigma of the Respiratory Chain Supercomplex. *Cell Metab* **25**, 765–776 (2017).

54. Lobo-Jarne, T. & Ugalde, C. Respiratory chain supercomplexes: Structures, function and biogenesis. *Semin Cell Dev Biol* **76**, 179–190 (2018).

55. Enríquez, J. A. Supramolecular Organization of Respiratory Complexes. *Annu Rev Physiol* **78**, 533–561 (2016).

56. Chance, B. & Williams, G. R. A method for the localization of sites for oxidative phosphorylation. *Nature* **176**, 250–254 (1955).

57. Hackenbrock, C. R., Chazotte, B. & Gupte, S. S. The random collision model and a critical assessment of diffusion and collision in mitochondrial electron transport. *J Bioenerg Biomembr* **18**, 331–368 (1986).

58. Hochman, J., Ferguson-Miller, S. & Schindler, M. Mobility in the Mitochondrial Electron Transport Chain. *Biochemistry* **24**, 2509–2516 (1985).

59. Schägger, H. & Pfeiffer, K. Supercomplexes in the respiratory chains of yeast and mammalian mitochondria. *EMBO Journal* **19**, 1777–1783 (2000).

60. Acín-Pérez, R., Fernández-Silva, P., Peleato, M. L., Pérez-Martos, A. & Enriquez, J. A. Respiratory Active Mitochondrial Supercomplexes. *Mol Cell* **32**, 529–539 (2008).

61. Acin-Perez, R. & Enriquez, J. A. The function of the respiratory supercomplexes: The plasticity model. *Biochim Biophys Acta Bioenerg* **1837**, 444–450 (2014).

62. Enriquez, J. A. & Lenaz, G. Coenzyme Q and the respiratory Chain: Coenzyme Q pool and mitochondrial supercomplexes. *Mol Syndromol* **5**, 119–140 (2014).

63. Guan, S., Zhao, L. & Peng, R. Mitochondrial Respiratory Chain Supercomplexes: From Structure to Function. *Int J Mol Sci* **23**, (2022).

64. Althoff, T., Mills, D. J., Popot, J. L. & Kühlbrandt, W. Arrangement of electron transport chain components in bovine mitochondrial supercomplex I 1 III 2 IV 1. *EMBO Journal* **30**, 4652–4664 (2011).

65. Sousa, J. S., Mills, D. J., Vonck, J. & Kühlbrandt, W. Functional asymmetry and electron flow in the bovine respirasome. *Elife* **5**, (2016).

66. Gu, J. *et al.* The architecture of the mammalian respirasome. *Nature* **537**, 639–643 (2016).

67. Letts, J. A., Fiedorczuk, K. & Sazanov, L. A. The architecture of respiratory supercomplexes. *Nature* **537**, 644–648 (2016).

68. Davies, K. M., Blum, T. B. & Kühlbrandt, W. Conserved in situ arrangement of complex I and III2 in mitochondrial respiratory chain supercomplexes of mammals, yeast, and plants. *Proc Natl Acad Sci U S A* **115**, 3024–3029 (2018).

69. Letts, J. A., Fiedorczuk, K., Degliesposti, G., Skehel, M. & Sazanov, L. A. Structures of Respiratory Supercomplex I+III2 Reveal Functional and Conformational Crosstalk. *Mol Cell* **75**, 1131-1146.e6 (2019).

70. Vercellino, I. & Sazanov, L. A. Structure and assembly of the mammalian mitochondrial supercomplex CIII2CIV. *Nature* **598**, 364–367 (2021).

71. Hernansanz-Agustín, P. & Enríquez, J. A. Functional segmentation of CoQ and cyt c pools by respiratory complex superassembly. *Free Radic Biol Med* **167**, 232–242 (2021).

72. Javadov, S., Jang, S., Chapa-Dubocq, X. R., Khuchua, Z. & Camara, A. K. Mitochondrial respiratory supercomplexes in mammalian cells: structural versus functional role. *J Mol Med* **99**, 57–73 (2021).

73. Sousa, P. M. F. *et al.* Supramolecular organizations in the aerobic respiratory chain of Escherichia coli. *Biochimie* **93**, 418–425 (2011).

74. Kulawiak, B. *et al.* The mitochondrial protein import machinery has multiple connections to the respiratory chain. *Biochim Biophys Acta Bioenerg* **1827**, 612–626 (2013).

75. Guo, R., Zong, S., Wu, M., Gu, J. & Yang, M. Architecture of Human Mitochondrial Respiratory Megacomplex I2III2IV2. *Cell* **170**, 1247-1257.e12 (2017).

76. Guo, R., Gu, J., Zong, S., Wu, M. & Yang, M. Structure and mechanism of mitochondrial electron transport chain. *Biomed J* **41**, 9–20 (2018).

77. Acín-Pérez, R. *et al.* Respiratory complex III is required to maintain complex I in mammalian mitochondria. *Mol Cell* **13**, 805–815 (2004).

78. Diaz, F., Fukui, H., Garcia, S. & Moraes, C. T. Cytochrome c Oxidase Is Required for the Assembly/Stability of Respiratory Complex I in Mouse Fibroblasts. *Mol Cell Biol* **26**, 4872–4881 (2006).

79. Blanchi, C., Genova, M. L., Castelli, G. P. & Lenaz, G. The mitochondrial respiratory chain is partially organized in a supercomplex assembly: Kinetic evidence using flux control analysis. *Journal of Biological Chemistry* **279**, 36562–36569 (2004).

80. Maranzana, E., Barbero, G., Falasca, A. I., Lenaz, G. & Genova, M. L. Mitochondrial respiratory supercomplex association limits production of reactive oxygen species from complex i. *Antioxid Redox Signal* **19**, 1469–1480 (2013).

81. Lopez-Fabuel, I. *et al.* Complex I assembly into supercomplexes determines differential mitochondrial ROS production in neurons and astrocytes. *Proc Natl Acad Sci U S A* **113**, 13063–13068 (2016).

82. Hernansanz-Agustín, P. *et al.* Na+ controls hypoxic signalling by the mitochondrial respiratory chain. *Nature* **586**, 287–291 (2020).

83. Luongo, T. S. *et al.* The mitochondrial Na+/Ca2+ exchanger is essential for Ca2+ homeostasis and viability. *Nature* **545**, 93–97 (2017).

84. Chouchani, E. T. *et al.* Ischaemic accumulation of succinate controls reperfusion injury through mitochondrial ROS. *Nature* **515**, 431–435 (2014).

85. Lapuente-Brun, E. *et al.* Supercomplex assembly determines electron flux in the mitochondrial electron transport chain. *Science (1979)* **340**, 1567–1570 (2013).

86. Berndtsson, J. *et al.* Respiratory supercomplexes enhance electron transport by decreasing cytochrome c diffusion distance. *EMBO Rep* **21**, (2020).

87. Stuchebrukhov, A., Schäfer, J., Berg, J. & Brzezinski, P. Kinetic advantage of forming respiratory supercomplexes. *Biochim Biophys Acta Bioenerg* **1861**, (2020).

88. Blaza, J. N., Serreli, R., Jones, A. J. Y., Mohammed, K. & Hirst, J. Kinetic evidence against partitioning of the ubiquinone pool and the catalytic relevance of respiratory-chain supercomplexes. *Proc Natl Acad Sci U S A* **111**, 15735–15740 (2014).

89. Hirst, J. Open questions: Respiratory chain supercomplexes-why are they there and what do they do? *BMC Biol* **16**, (2018).

90. Fedor, J. G. & Hirst, J. Mitochondrial Supercomplexes Do Not Enhance Catalysis by Quinone Channeling. *Cell Metab* **28**, 525-531.e4 (2018).

91. Bentinger, M., Brismar, K. & Dallner, G. The antioxidant role of coenzyme Q. *Mitochondrion* **7**, (2007).

92. Pallotti, F., Bergamini, C., Lamperti, C. & Fato, R. The roles of coenzyme Q in disease: Direct and indirect involvement in cellular functions. *Int J Mol Sci* **23**, (2022).

93. Villalba, J. M. *et al.* Role of cytochrome b5, reductase on the antioxidant function of coenzyme Q in the plasma membrane. *Mol Aspects Med* **18**, 7–13 (1997).

94. Ross, D. & Siegel, D. The diverse functionality of NQO1 and its roles in redox control. *Redox Biol* **41**, (2021).

95. James, A. M., Smith, R. A. J. & Murphy, M. P. Antioxidant and prooxidant properties of mitochondrial Coenzyme Q. *Arch Biochem Biophys* **423**, 47–56 (2004).

96. Stocker, R., Bowry, V. W. & Frei, B. Ubiquinol-10 protects human low density lipoprotein more efficiently against lipid peroxidation than does α-tocopherol. *Proc Natl Acad Sci U S A* **88**, 1646–1650 (1991).

97. Tribble, D. L. *et al.* Oxidative susceptibility of low density lipoprotein subfractions is related to their ubiquinol-10 and α-tocopherol content. *Proc Natl Acad Sci U S A* **91**, 1183–1187 (1994).

98. Bersuker, K. *et al.* The CoQ oxidoreductase FSP1 acts parallel to GPX4 to inhibit ferroptosis. *Nature* **575**, 688–692 (2019).

99. Doll, S. *et al.* FSP1 is a glutathione-independent ferroptosis suppressor. *Nature* **575**, 693–698 (2019).

100. Rizzardi, N. *et al.* Coenzyme q10 phytosome formulation improves coq10 bioavailability and mitochondrial functionality in cultured cells. *Antioxidants* **10**, (2021).

101. Dennis, M. K. *et al.* Ferroptosis: An Iron-Dependent Form of Non-Apoptotic Cell Death. **127**, 358–366 (2012).

102. Murphy, M. P. How mitochondria produce reactive oxygen species. *Biochemical Journal* **417**, 1–13 (2009).

103. Wang, Y. & Hekimi, S. Understanding Ubiquinone. *Trends Cell Biol* **26**, 367–378 (2016).

104. Giorgi, C., Marchi, S. & Pinton, P. The machineries, regulation and cellular functions of mitochondrial calcium. *Nat Rev Mol Cell Biol* **19**, 713–730 (2018).

105. Bagur, R. & Hajnóczky, G. Intracellular Ca2+ Sensing: Its Role in Calcium Homeostasis and Signaling. *Mol Cell* **66**, 780–788 (2017).

106. Wu, Y., Huang, P. & Dong, X. P. Lysosomal calcium channels in autophagy and cancer. *Cancers (Basel)* **13**, 1–18 (2021).

107. Parys, J. B. & Guse, A. H. Full focus on calcium. *Sci Signal* **12**, (2019).

108. Machaca, K. Ca2+ signaling, genes and the cell cycle. *Cell Calcium* **48**, 243–250 (2010).

109. Clapham, D. E. Calcium Signaling. *Cell* **131**, 1047–1058 (2007).

110. Lloyd-Evans, E. & Waller-Evans, H. Lysosomal Ca2+ homeostasis and signaling in health and disease. *Cold Spring Harb Perspect Biol* **12**, 1–20 (2020).

111. Raffaello, A., Mammucari, C., Gherardi, G. & Rizzuto, R. Calcium at the Center of Cell Signaling: Interplay between Endoplasmic Reticulum, Mitochondria, and Lysosomes. *Trends Biochem Sci* **41**, 1035–1049 (2016).

112. Saul, S., Stanisz, H., Backes, C. S., Schwarz, E. C. & Hoth, M. How ORAI and TRP channels interfere with each other: Interaction models and examples from the immune system and the skin. *Eur J Pharmacol* **739**, 49–59 (2014).

113. Samanta, A., Hughes, T. E. T. & Moiseenkova-Bell, V. Y. Transient receptor potential (TRP) channels. *Subcell Biochem* **87**, 141–165 (2018).

114. Quintana, A. *et al.* T cell activation requires mitochondrial translocation to the immunological synapse. *Proc Natl Acad Sci U S A* **104**, 14418–14423 (2007).

115. Schwindling, C., Quintana, A., Krause, E. & Hoth, M. Mitochondria Positioning Controls Local Calcium Influx in T Cells. *The Journal of Immunology* **184**, 184–190 (2010).

116. Quintana, A. *et al.* Calcium microdomains at the immunological synapse: How ORAI channels, mitochondria and calcium pumps generate local calcium signals for efficient T-cell activation. *EMBO Journal* **30**, 3895–3912 (2011).

117. Quintana, A. & Hoth, M. Mitochondrial dynamics and their impact on T cell function. *Cell Calcium* **52**, 57–63 (2012).

118. Rizzuto, R. *et al.* Close contacts with the endoplasmic reticulum as determinants of mitochondrial Ca2+ responses. *Science (1979)* **280**, 1763–1766 (1998).

119. Marchi, S. *et al.* Mitochondrial and endoplasmic reticulum calcium homeostasis and cell death. *Cell Calcium* **69**, 62–72 (2018).

120. Hilgemann, D. W., Yaradanakul, A., Wang, Y. & Fuster, D. Molecular control of cardiac sodium homeostasis in health and disease. *J Cardiovasc Electrophysiol* **17**, (2006).

121. Reeves, J. P. The Sarcolemmal Sodium-Calcium Exchange System. *Curr Top Membr Transp* **25**, 77–127 (1985).

122. Boyman, L., Mikhasenko, H., Hiller, R. & Khananshvili, D. Kinetic and equilibrium properties of regulatory calcium sensors of NCX1 protein. *Journal of Biological Chemistry* **284**, 6185–6191 (2009).

123. Perocchi, F. *et al.* MICU1 encodes a mitochondrial EF hand protein required for Ca2+ uptake. *Nature* **467**, 291–296 (2010).

124. Ryu, S. Y., Beutner, G., Dirksen, R. T., Kinnally, K. W. & Sheu, S. S. Mitochondrial ryanodine receptors and other mitochondrial Ca2+ permeable channels. *FEBS Lett* **584**, 1948–1955 (2010).

125. Feng, S. *et al.* Canonical transient receptor potential 3 channels regulate mitochondrial calcium uptake. *Proc Natl Acad Sci U S A* **110**, 11011–11016 (2013).

126. Trenker, M., Malli, R., Fertschai, I., Levak-Frank, S. & Graier, W. F. Uncoupling proteins 2 and 3 are fundamental for mitochondrial Ca2+ uniport. *Nat Cell Biol* **9**, 445–452 (2007).

127. Jiang, D., Zhao, L. & Clapham, D. E. Genome-wide RNAi screen identifies Letm1 as a mitochondrial Ca 2+/H+ antiporter. *Science (1979)* **326**, 144–147 (2009).

128. Elrod, J. W. *et al.* Cyclophilin D controls mitochondrial pore - Dependent Ca2+ exchange, metabolic flexibility, and propensity for heart failure in mice. *Journal of Clinical Investigation* **120**, 3680–3687 (2010).

129. Lu, X., Kwong, J. Q., Molkentin, J. D. & Bers, D. M. Individual cardiac mitochondria undergo rare transient permeability transition pore openings. *Circ Res* **118**, 834–841 (2016).

130. De Marchi, E., Bonora, M., Giorgi, C. & Pinton, P. The mitochondrial permeability transition pore is a dispensable element for mitochondrial calcium efflux. *Cell Calcium* **56**, 1–13 (2014).

131. Kowaltowski, A. J. *et al.* Mitochondrial morphology regulates organellar Ca2+ uptake and changes cellular Ca2+ homeostasis. *FASEB Journal* **33**, 13176–13188 (2019).

132. Rizzuto, R., De Stefani, D., Raffaello, A. & Mammucari, C. Mitochondria as sensors and regulators of calcium signalling. *Nat Rev Mol Cell Biol* **13**, 566–578 (2012).

133. McCormack, J. G. & Denton, R. M. The effects of calcium ions and adenine nucleotides on the activity of pig heart 2-oxoglutarate dehydrogenase complex. *Biochemical Journal* **180**, 533–544 (1979).

134. Jouaville, L. S., Pinton, P., Bastianutto, C., Rutter, G. A. & Rizzuto, R. Regulation of mitochondrial ATP synthesis by calcium: Evidence for a long-term metabolic priming. *Proc Natl Acad Sci U S A* **96**, 13807–13812 (1999).

135. Boehning, D. *et al.* Cytochrome c binds to inositol (1,4,5) trisphosphate receptors, amplifying calcium-dependent apoptosis. *Nat Cell Biol* **5**, 1051–1061 (2003).

136. Rasola, A. & Bernardi, P. Mitochondrial permeability transition in Ca2+-dependent apoptosis and necrosis. *Cell Calcium* **50**, 222–233 (2011).

137. Giorgio, V., Guo, L., Bassot, C., Petronilli, V. & Bernardi, P. Calcium and regulation of the mitochondrial permeability transition. *Cell Calcium* **70**, 56–63 (2018).

138. Denton, R. M., McCormack, J. G. & Edgell, N. J. Role of calcium ions in the regulation of intramitochondrial metabolism. Effects of Na+, Mg2+ and ruthenium red on the Ca2+-stimulated oxidation of oxoglutarate and on pyruvate dehydrogenase activity in intact rat heart mitochondria. *Biochemical Journal* **190**, 107–117 (1980).

139. McCormack, J. G., Halestrap, A. P. & Denton, R. M. Role of calcium ions in regulation of mammalian intramitochondrial metabolism. *Physiol Rev* **70**, 391–425 (1990).

140. Denton, R. M. Regulation of mitochondrial dehydrogenases by calcium ions. *Biochim Biophys Acta Bioenerg* **1787**, 1309–1316 (2009).

141. Palmieri, L. *et al.* Citrin and aralar1 are Ca2+-stimulated aspartate/glutamate transporters in mitochondria. *EMBO Journal* **20**, 5060–5069 (2001).

142. Satrústegui, J., Pardo, B. & Del Arco, A. Mitochondrial transporters as novel targets for intracellular calcium signaling. *Physiol Rev* **87**, 29–67 (2007).

143. Nosek, M. T., Dransfield, D. T. & Aprille, J. R. Calcium stimulates ATP-Mg/P(i) carrier activity in rat liver mitochondria. *Journal of Biological Chemistry* **265**, 8444–8450 (1990).

144. Anunciado-Koza, R. P. *et al.* Inactivation of the mitochondrial carrier SLC25A25 (ATP-Mg2+/Pi transporter) reduces physical endurance and metabolic efficiency in mice. *Journal of Biological Chemistry* **286**, 11659–11671 (2011).

145. Territo, P. R., Mootha, V. K., French, S. A. & Balaban, R. S. Ca2+ activation of heart mitochondrial oxidative phosphorylation: Role of the F0/F1-ATPase. *Am J Physiol Cell Physiol* **278**, (2000).

146. Glancy, B., Willis, W. T., Chess, D. J. & Balaban, R. S. Effect of calcium on the oxidative phosphorylation cascade in skeletal muscle mitochondria. *Biochemistry* **52**, 2793–2809 (2013).

147. Ksenzhek, O. S., Petrova, S. A. & Kolodyazhny, M. V. 452 - Redox properties of ubiquinones in aqueous solutions. *Bioelectrochemistry and Bioenergetics* **9**, 167–174 (1982).

148. Lenaz, G. *et al.* Coenzyme Q deficiency in mitochondria: Kinetic saturation versus physical saturation. *Mol Aspects Med* **18**, 25–31 (1997).

149. Stankoska, K. Personal communication. (Saarland University, 2022).

150. Kelso, G. F. *et al.* Selective targeting of a redox-active ubiquinone to mitochondria within cells: Antioxidant and antiapoptotic properties. *Journal of Biological Chemistry* **276**, 4588–4596 (2001).

151. Smith, R. A. J., Kelso, G. F., James, A. M. & Murphy, M. P. Targeting Coenzyme Q Derivatives to Mitochondria. *Methods Enzymol* **382**, 45–67 (2004).

152. Graham, F. L., Smiley, J., Russell, W. C. & Nairn, R. Characteristics of a Human Cell Line Transformed by DNA from Human Adenovirus Type 5. *Journal of General Virology* **36**, 59–72 (1977).

153. Graham, F. Cell Line Transformation. *Current Contents* **8**, 8 (1992).

154. Shaw, G., Morse, S., Ararat, M. & Graham, F. L. Preferential transformation of human neuronal cells by human adenoviruses and the origin of HEK 293 cells. *The FASEB journal : official publication of the Federation of American Societies for Experimental Biology* **16**, 869–871 (2002).

155. Louis, N., Evelegh, C. & Graham, F. L. Cloning and sequencing of the cellular-viral junctions from the human adenovirus type 5 transformed 293 cell line. *Virology* **233**, 423–429 (1997).

156. Malm, M. *et al.* Evolution from adherent to suspension: systems biology of HEK293 cell line development. *Sci Rep* **10**, 18996 (2020).

157. Kang, M., Ryu, H. H. & Lee, Y. S. Comparisons of behavior and synaptic plasticity among three C57BL/6 substrains. *Anim Cells Syst (Seoul)* **19**, (2015).

158. Mekada, K. *et al.* Genetic differences among C57BL/6 substrains. *Exp Anim* **58**, (2009).

159. Freeman, H. C., Hugill, A., Dear, N. T., Ashcroft, F. M. & Cox, R. D. Deletion of nicotinamide nucleotide transhydrogenase: A new quantitive trait locus accounting for glucose intolerance in C57BL/6J mice. *Diabetes* **55**, (2006).

160. Toye, A. A. *et al.* A genetic and physiological study of impaired glucose homeostasis control in C57BL/6J mice. *Diabetologia* **48**, (2005).

161. Christian, G. D., Dasgupta, P. K. & Schug, K. A. Spectrochemical Methods. in *Analytical Chemistry* (eds. Christian, G. D., Dasgupta, P. K. & Schug, K. A.) (John Wiley & Sons, Inc., 2013).

162. Pretsch, E., Bühlmann, P. & Badertscher, M. UV/Vis Spectroscopy. in *Structure Determination of Organic Compounds* (2020).

163. Meyer, V. R. *Practical High-Performance Liquid Chromatography*. *Practical High-Performance Liquid Chromatography: Fifth Edition* (John Wiley and Sons, 2010).

164. Schulenberg-Schell, H. & Tei, A. Principles and practical aspects of preparative liquid chromatography. *Agilent Technologies* (2015).

165. Pitt, J. J. Principles and applications of liquid chromatography-mass spectrometry in clinical biochemistry. *Clin Biochem Rev* **30**, (2009).

166. Rankin, N. J. *et al.* The emergence of proton nuclear magnetic resonance metabolomics in the cardiovascular arena as viewed from a clinical perspective. *Atherosclerosis* **237**, 287–300 (2014).

167. Aitken, A. Mass spectrometric techniques. in *Principles and Techniques of Biochemistry and Molecular Biology* (eds. Wilson, K. & Walker, J.) 352–398 (Cambridge: Cambridge University Press, 2010).

168. Bruins, A. P. Mechanistic aspects of electrospray ionization. *J Chromatogr A* **794**, 345–357 (1998).

169. Perry, R. H., Cooks, R. G. & Noll, R. J. Orbitrap mass spectrometry: Instrumentation, ion motion and applications. *Mass Spectrom Rev* **27**, 661–699 (2008).

170. Richter, L. H. J., Kaminski, Y. R., Noor, F., Meyer, M. R. & Maurer, H. H. Metabolic fate of desomorphine elucidated using rat urine, pooled human liver preparations, and human

hepatocyte cultures as well as its detectability using standard urine screening approaches. *Anal Bioanal Chem* **408**, 6283–6294 (2016).

171. Richter, L. H. J., Flockerzi, V., Maurer, H. H. & Meyer, M. R. Pooled human liver preparations, HepaRG, or HepG2 cell lines for metabolism studies of new psychoactive substances? A study using MDMA, MDBD, butylone, MDPPP, MDPV, MDPB, 5-MAPB, and 5-API as examples. *J Pharm Biomed Anal* **143**, 32–42 (2017).

172. Helfer, A. G., Michely, J. A., Weber, A. A., Meyer, M. R. & Maurer, H. H. Orbitrap technology for comprehensive metabolite-based liquid chromatographic-high resolution-tandem mass spectrometric urine drug screening - Exemplified for cardiovascular drugs. *Anal Chim Acta* **891**, 221–233 (2015).

173. Hofmann, A. Spectroscopic techniques: II Structure and interactions. in *Principles and Techniques of Biochemistry and Molecular Biology* (eds. Wilson, K. & Walker, J.) 522–552 (Cambridge: Cambridge University Press, 2010).

174. Friebolin, H. *Basic one- and two-dimensional NMR spectroscopy. Basic one- and two-dimensional NMR spectroscopy* (VCH Verlagsgesellschaft, 1991).

175. Keeler, J. *Understanding NMR Spectroscopy. Wiley* (John Wiley & Sons, Ltd., 2010).

176. Marion, D. An introduction to biological NMR spectroscopy. *Molecular and Cellular Proteomics* **12**, 3006–3025 (2013).

177. Malz, F. & Jancke, H. Validation of quantitative NMR. *J Pharm Biomed Anal* **38**, (2005).

178. Diehl, B., Holzgrabe, U., Monakhova, Y. & Schönberger, T. Quo Vadis qNMR? *J Pharm Biomed Anal* **177**, (2020).

179. Jaki, B. U., Bzhelyansky, A. & Pauli, G. F. Quantitative NMR (qNMR) for pharmaceutical analysis: The pioneering work of George Hanna at the US FDA. *Magnetic Resonance in Chemistry* **59**, (2021).

180. Choi, K., Myoung, S., Seo, Y. & Ahn, S. Quantitative nmr as a versatile tool for the reference material preparation. *Magnetochemistry* **7**, 1–12 (2021).

181. Akoka, S., Barantin, L. & Trierweiler, M. Concentration Measurement by Proton NMR Using the ERETIC Method. *Anal Chem* **71**, 2554–2557 (1999).

182. Bard, A. J. & Faulkner, L. R. *Electrochemical Methods. Fundamentals and Applications*. (John Wiley & Sons Inc., 2001).

183. Wang, J. *Analytical Electrochemistry*. (John Wiley & Sons Inc., 2000).

184. Mirceski, V., Skrzypek, S. & Stojanov, L. Square-wave voltammetry. *ChemTexts* **4**, 1–14 (2018).

185. Scholz, F. Voltammetric techniques of analysis: the essentials. *ChemTexts* **1**, 1–24 (2015).

186. Zoski, C. G. *Handbook of Electrochemistry*. (Elsevier , 2007).

187. Elgrishi, N. *et al.* A Practical Beginner's Guide to Cyclic Voltammetry. *J Chem Educ* **95**, 197–206 (2018).

188. Mirceski, V., Komorsky-Lovric, S. & Lovric, M. *Square-Wave Voltammetry*. (Springer, 2007).

189. Borowy-Borowski, H., Sodja, C., Docherty, J., Roy Walker, P. & Sikorska, M. Unique Technology for Solubilization and Delivery of Highly Lipophilic Bioactive Molecules. *J Drug Target* **12**, 415–424 (2004).

190. Proksch, G. J. & Bonderman, D. P. A water-soluble cholesterol derivative for use in augmenting serum control materials. *Clin Chem* **24**, (1978).

191. Tang, P. H. *et al.* Measurement of reduced and oxidized coenzyme Q9 and coenzyme Q10 levels in mouse tissues by HPLC with coulometric detection. *Clinica Chimica Acta* **341**, 173–184 (2004).

192. Fato, R. *et al.* Steady-state kinetics of the reduction of coenzyme Q analogs by complex I (NADH:ubiquinone oxidoreductase) in bovine heart mitochondria and submitochondrial particles. *Biochemistry* **35**, (1996).

193. Thermo Scientific. User Guide: Pierce™ BCA Protein Assay Kit (MAN0011430, Rev. B.0).

194. Takada, M., Ikenoya, S., Yuzuriha, T. & Katayama, K. Simultaneous Determination of Reduced and Oxidized Ubiquinones. *Methods Enzymol* **105**, 147–155 (1984).

195. Riss, T. L. *et al.* Cell Viability Assays. *Assay Guidance Manual* (2016).

196. O'Brien, J., Wilson, I., Orton, T. & Pognan, F. Investigation of the Alamar Blue (resazurin) fluorescent dye for the assessment of mammalian cell cytotoxicity. *Eur J Biochem* **267**, 5421–5426 (2000).

197. Chen, J. L., Steele, T. W. J. & Stuckey, D. C. Metabolic reduction of resazurin; location within the cell for cytotoxicity assays. *Biotechnol Bioeng* **115**, 351–358 (2018).

198. Promega Corporation. CellTiter-Blue ® Cell Viability Assay Technical Bulletin #TB317. (2016).

199. Simpson, A. W. M. Fluorescent Measurement of [Ca2+]c: Basic Practical Considerations. in *Calcium Signaling Protocols. Methods in Molecular Biology* (eds. Lambert, D. & Rainbow, R.) vol. 937 3–36 (Humana Press, 2013).

200. Patel, A., Hirst, R. A., Harrison, C., Hirota, K. & Lambert, D. G. Measurement of [Ca2+]i in Whole Cell Suspensions Using Fura-2. in *Calcium Signaling Protocols. Methods in Molecular Biology* (eds. Lambert, D. & Rainbow, R.) vol. 937 37–47 (Humana Press, 2013).

201. Grynkiewicz, G., Poenie, M. & Tsien, R. Y. A new generation of Ca2+ indicators with greatly improved fluorescence properties. *Journal of Biological Chemistry* **260**, 3440–3450 (1985).

202. Kircher, S., Merino-Wong, M., Niemeyer, B. A. & Alansary, D. Profiling calcium signals of in vitro polarized human effector CD4+ T cells. *Biochimica et Biophysica Acta (BBA) - Molecular Cell Research* **1865**, 932–943 (2018).

203. Perry, S. W., Norman, J. P., Barbieri, J., Brown, E. B. & Gelbard, H. A. Mitochondrial membrane potential probes and the proton gradient: A practical usage guide. *Biotechniques* **50**, (2011).

204. Gerencser, A. A. & Brand, M. D. Exploiting Mitochondria In Vivo as Chemical Reaction Chambers Dependent on Membrane Potential. *Mol Cell* **61**, 642–643 (2016).

205. Duchen, M. R. Mitochondria in health and disease: perspectives on a new mitochondrial biology. *Mol Aspects Med* **25**, 365–451 (2004).

206. Heytler, P. G. Uncoupling of Oxidative Phosphorylation by Carbonyl Cyanide Phenylhydrazones. I. Some Characteristics of m-Cl-CCP Action on Mitochondria and Chloroplasts. *Biochemistry* **2**, 357–361 (1963).

207. Heytler, P. G. [58] Uncouplers of oxidative phosphorylation. *Methods Enzymol* **55**, 462–472 (1979).

208. Wei, A. C., Aon, M. A., O'Rourke, B., Winslow, R. L. & Cortassa, S. Mitochondrial energetics, pH regulation, and ion dynamics: A computational-experimental approach. *Biophys J* **100**, 2894–2903 (2011).

209. Nickel, A. G. *et al.* Reversal of mitochondrial transhydrogenase causes oxidative stress in heart failure. *Cell Metab* **22**, 472–484 (2015).

210. Bio-Rad Laboratories Inc. DC™ Protein Assay Instruction Manual. *Bulletin 6837 Ver A*.

211. Lowry, O. H., Rosebrough, N. J., Farr, A. L. & Randall, R. J. Protein measurement with the Folin phenol reagent. *J Biol Chem* **193**, (1951).

212. Severinghaus, J. W. & Astrup, P. B. History of blood gas analysis. IV. Leland Clark's oxygen electrode. *J Clin Monit* **2**, (1986).

213. Gnaiger, E. Polarographic Oxygen Sensors, the Oxygraph, and High-Resolution Respirometry to Assess Mitochondrial Function. in *Drug-Induced Mitochondrial Dysfunction* (eds. Dykens, J. A. & Will, Y.) 325–352 (John Wiley & Sons, Inc., 2008).

214. Gnaiger, E. The Oxygraph for High-Resolution Respirometry (HRR). *Mitoch. Physiol. Network* **MiPNet 12.06**, 1–18 (2011).

215. Gnaiger, E. MitoPathways: Respiratory States and Coupling Control Ratios. *Mitoch. Physiol. Network* **MiPNet 12.15**, 1–11 (2011).

216. Chance, B. & Williams, G. R. Respiratory Enzymes in Oxidative Phosphorylation: I. Kinetics of Oxygen Utilization. *Journal of Biological Chemistry* **217**, 383–393 (1955).

217. Chance, B. & Williams, G. R. Respiratory Enzymes in Oxidative Phosphorylation: II. Difference Spectra. *Journal of Biological Chemistry* **217**, 395–407 (1955).

218. Chance, B. & Williams, G. R. Respiratory Enzymes in Oxidative Phosphorylation: III. The Steady State. *Journal of Biological Chemistry* **217**, 409–427 (1955).

219. Chance, B. & Williams, G. R. Respiratory Enzymes in Oxidative Phosphorylation: IV. The Respiratory Chain. *Journal of Biological Chemistry* **217**, 429–438 (1955).

220. Chance, B., Williams, G. R., Holmes, W. F. & Higgins, J. Respiratory Enzymes in Oxidative Phosphorylation: V. A Mechanism for Oxidative Phosphorylation. *Journal of Biological Chemistry* **217**, 439–451 (1955).

221. Gnaiger, E. & MitoEAGLE Task Group. Mitochondrial physiology. *Bioenergetics Communications* **2020**, (2020).

222. Gnaiger, E. O2k Quality Control 1: Polarographic oxygen sensors and accuracy of calibration. *Mitoch. Physiol. Network* **MiPNet 06.03(19)**, 1–19 (2021).

223. Gnaiger, E. O2k-calibration by DatLab. *Mitoch. Physiol. Network* **MiPNet 19.18(D04)**, 1–12 (2016).

224. Gnaiger, E. Service of the polarographic oxygen sensor OroboPOS. *Mitoch. Physiol. Network* **MiPNet 19.01(B01)**, 19–24 (2014).

225. Fasching, M. & Gnaiger, E. O2k Quality Control 2: Instrumental oxygen background correction and accuracy of oxygen flux. *Mitoch. Physiol. Network* **MiPNet 14.06(08)**, 1–16 (2020).

226. Gnaiger, E., Plangger, I. & Hunger, M. Mitochondrial respiration medium: MiR05-Kit. *Mitoch. Physiol. Network* **MiPNet 22.10(03)**, 1–2 (2019).

227. Ahmed, M. & Khan, Z. H. Electronic absorption spectra of benzoquinone and its hydroxy substituents and effect of solvents on their spectra. *Spectrochim Acta A Mol Biomol Spectrosc* **56**, 965–981 (2000).

228. Flaig, W., Salfeld, J. -C & Baume, E. UV-Spektren und Konstitution von p-Benzochinonen. *Justus Liebigs Ann Chem* **618**, 117–139 (1958).

229. Schellinger, A. P. & Carr, P. W. Isocratic and gradient elution chromatography: A comparison in terms of speed, retention reproducibility and quantitation. *J Chromatogr A* **1109**, 253–266 (2006).

230. Guin, P. S., Das, S. & Mandal, P. C. Electrochemical Reduction of Quinones in Different Media: A Review. *International Journal of Electrochemistry* **2011**, 1–22 (2011).

231. Jacq, J. Schema carre. Etablissement et Discussion de L'equation Generale de la Courbe Intensite-Potentiel en Regime Stationnaire et Diffusion Convective. *Journal of Electroanalytical Chemistry* **29**, (1971).

232. Costentin, C. Electrochemical approach to the mechanistic study of proton-coupled electron transfer. *Chem Rev* **108**, 2145–2179 (2008).

233. Fukuzumi, S., Ohkubo, K. & Morimoto, Y. Mechanisms of metal ion-coupled electron transfer. *Physical Chemistry Chemical Physics* **14**, 8472–8484 (2012).

234. Laviron, E. Electrochemical reactions with protonations at equilibrium. Part X. The kinetics of the p-benzoquinone/hydroquinone couple on a platinum electrode. *Journal of Electroanalytical Chemistry* **164**, 213–227 (1984).

235. Quan, M., Sanchez, D., Wasylkiw, M. F. & Smith, D. K. Voltammetry of quinones in unbuffered aqueous solution: Reassessing the roles of proton transfer and hydrogen bonding in the aqueous electrochemistry of quinones. *J Am Chem Soc* **129**, 12847–12856 (2007).

236. Walczak, M. M., Dryer, D. A., Jacobson, D. D., Foss, M. G. & Flynn, N. T. pH Dependent Redox Couple: An Illustration of the Nernst Equation. *J Chem Educ* **74**, undefined-undefined (1997).

237. Silverstein, T. P. & Heller, S. T. pKa Values in the Undergraduate Curriculum: What Is the Real pKa of Water? *J Chem Educ* **94**, 690–695 (2017).

238. Gao, D. Acidities of water and methanol in aqueous solution and dmso. *J Chem Educ* **86**, 864–868 (2009).

239. Olmstead, W. N., Margolin, Z. & Bordwell, F. G. Acidities of Water and Simple Alcohols in Dimethyl Sulfoxide Solution. *Journal of Organic Chemistry* **45**, 3295–3299 (1980).

240. Gupta, N. & Linschitz, H. Hydrogen-bonding and protonation effects in electrochemistry of quinones in aprotic solvents. *J Am Chem Soc* **119**, 6384–6391 (1997).

241. Ferraz, P. A. L. *et al.* Electrochemical aspects of the reduction of biologically active 2-hydroxy-3-alkyl-1, 4-naphthoquinones. *Journal of Electroanalytical Chemistry* **507**, 275–286 (2001).

242. Bautista-Martínez, J. A., González, I. & Aguilar-Martínez, M. Correlation of voltammetric behavior of α-hydroxy and α-methoxy quinones with the change of acidity level in acetonitrile. *Journal of Electroanalytical Chemistry* **573**, 289–298 (2004).

243. Frontana, C., Frontana-Uribe, B. A. & González, I. Electrochemical and ESR study on the transformation processes of α-hydroxy-quinones. *Journal of Electroanalytical Chemistry* **573**, 307–314 (2004).

244. Frontana, C. & González, I. The role of intramolecular hydrogen bonding in the electrochemical behavior of hydroxy-quinones and in semiquinone stability. *J Braz Chem Soc* **16**, 299–307 (2005).

245. Frontana, C. & González, I. Effects of the molecular structure on the electrochemical properties of naturally occurring α-hydroxyquinones. An electrochemical and ESR study. *Journal of Electroanalytical Chemistry* **603**, 155–165 (2007).

246. Piljac, I. & Murray, R. W. Nonaqueous Electrochemistry of 1-Hydroxy-9,10-Anthraquinone and Its Conjugate Base. *J Electrochem Soc* **118**, undefined-undefined (1971).

247. Traven, V. F. *et al.* One-electron reactions in biochemical systems as studied by pulse radiolysis. 3. Ubiquinone. *Photochem Photobiol* **245**, 1890–1894 (1970).

248. Kotake, Y. & Kuwata, K. An ENDOR Study of the Relaxation Behavior of the Nuclei in Several Semiquinone Anion Radicals. *Bull Chem Soc Jpn* **47**, 45–49 (1974).

249. Kolthoff, I. M. & Reddy, T. B. Polarography and Voltammetry in Dimethylsulfoxide. *J Electrochem Soc* **108**, 980 (1961).

250. Hayano, S. & Fujihira, M. The Effect of Water on the Reduction Potentials of Some Aromatic Compounds in the DMF-Water System. *Bull Chem Soc Jpn* **44**, 2051–2055 (1971).

251. Fujihira, M. & Hayano, S. The Solvent Effect on the Visible Absorption Spectra of the Radical Anion and the Dianion of Anthraquinone. *Bull Chem Soc Jpn* **45**, 644–645 (1972).

252. Patel, K. B. & Willson, R. L. Semiquinone free radicals and oxygen. Pulse radiolysis study of one electron transfer equilibria. *Journal of the Chemical Society, Faraday Transactions 1: Physical Chemistry in Condensed Phases* **69**, 814–825 (1973).

253. Bailey, S. I., Ritchie, I. M. & Hewgill, F. R. The construction and use of potential-pH diagrams in organic oxidation-reduction reactions. *Journal of the Chemical Society, Perkin Transactions 2* 645–652 (1983).

254. Bauscher, M. & Mäntele, W. Electrochemical and infrared-spectroscopic characterization of redox reactions of p-quinones. *Journal of Physical Chemistry* **96**, 11101–11108 (1992).

255. Syed, M., Skonberg, C. & Hansen, S. H. Effect of some organic solvents on oxidative phosphorylation in rat liver mitochondria: Choice of organic solvents. *Toxicology in Vitro* **27**, 2135–2141 (2013).

256. Timm, M., Saaby, L., Moesby, L. & Hansen, E. W. Considerations regarding use of solvents in in vitro cell based assays. *Cytotechnology* **65**, 887–894 (2013).

257. Ma, L. *et al.* Spectroscopic, Polarographic, and Microcalorimetric Studies on Mitochondrial Dysfunction Induced by Ethanol. *Journal of Membrane Biology* **250**, 195–204 (2017).

258. Coutelle, O. *et al.* Embelin inhibits endothelial mitochondrial respiration and impairs neoangiogenesis during tumor growth and wound healing. *EMBO Mol Med* **6**, 624–639 (2014).

259. Wacquier, B., Combettes, L. & Dupont, G. Cytoplasmic and mitochondrial calcium signaling: A two-way relationship. *Cold Spring Harb Perspect Biol* **11**, (2019).

260. Doran, E. & Halestrap, A. P. Cytochrome c release from isolated rat liver mitochondria can occur independently of outer-membrane rupture: Possible role of contact sites. *Biochemical Journal* **348**, 343–350 (2000).

261. Gnaiger, E. & Kuznetsov, A. V. Mitochondrial respiration at low levels of oxygen and cytochrome c. *Biochem Soc Trans* **30**, 252–258 (2002).

262. Toleikis, A., Trumbeckaite, S. & Majiene, D. Cytochrome c effect on respiration of heart mitochondria: Influence of various factors. *Biosci Rep* **25**, 387–397 (2005).

263. Krajčová, A. *et al.* High resolution respirometry to assess function of mitochondria in native homogenates of human heart muscle. *PLoS One* **15**, (2020).

264. Gu, L. Q., Yu, L. & Yu, C. A. Effect of substituents of the benzoquinone ring on electron-transfer activities of ubiquinone derivatives. *BBA - Bioenergetics* **1015**, 482–492 (1990).

265. He, D. Y., Yu, L. & Yu, C. A. Protein ubiquinone interaction. Synthesis and biological properties of 5- alkyl ubiquinone derivatives. *Journal of Biological Chemistry* **269**, 27885–27888 (1994).

266. Ohshima, M. *et al.* Characterization of the ubiquinone reduction site of mitochondrial complex I using bulky synthetic ubiquinones. *Biochemistry* **37**, 6436–6445 (1998).

267. Matsumoto, Y. *et al.* Kinetic mechanism of quinol oxidation by cytochrome bd studied with ubiquinone-2 analogs. *J Biochem* **139**, 779–788 (2006).

268. Duveau, D. Y. *et al.* Synthesis and characterization of mitoQ and idebenone analogues as mediators of oxygen consumption in mitochondria. *Bioorg Med Chem* **18**, 6429–6441 (2010).

269. Lenaz, G. Quinone specificity of Complex I. *Biochim Biophys Acta Bioenerg* **1364**, 207–221 (1998).

270. Acosta, M. J. *et al.* Coenzyme Q biosynthesis in health and disease. *Biochim Biophys Acta Bioenerg* **1857**, 1079–1085 (2016).

271. Ferri, E., Gattavecchia, E., Feroci, G. & Battino, M. Interaction between reactive oxygen species and Coenzyme Q10 in an aprotic medium: A cyclic voltammetry study. *Mol Aspects Med* **15**, (1994).

272. Li, D. *et al.* Electrochemical Investigation of Coenzyme Q10 on Silver Electrode in Ethanol Aqueous Solution and Its Determination Using Differential Pulse Voltammetry. *J Lab Autom* **21**, 579–589 (2016).

273. Litescu, S. C., David, I. G., Radu, G. L. & Aboul-Enein, H. Y. Voltammetric determination of coenzyme Q10 at a solid glassy carbon electrode. *Instrum Sci Technol* **29**, 109–116 (2006).

274. Kondo, T., Sakai, K., Watanabe, T., Einaga, Y. & Yuasa, M. Electrochemical detection of lipophilic antioxidants with high sensitivity at boron-doped diamond electrode. *Electrochim Acta* **95**, 205–211 (2013).

275. Michalkiewicz, S. Cathodic reduction of coenzyme Q10 on glassy carbon electrode in acetic acid-acetonitrile solutions. *Bioelectrochemistry* **70**, 495–500 (2007).

276. Michalkiewicz, S. Anodic oxidation of oxidized forms of coenzymes Q 10 and Q 0 on carbon electrodes in acetic acid solutions. *Bioelectrochemistry* **82**, 103–111 (2011).

277. Takehara, K. & Ide, Y. Electrochemical behaviour of the ubiquinone-Q10 film coated onto a glassy carbon electrode by the spinner method. *Bioelectrochemistry and Bioenergetics* **26**, 297–305 (1991).

278. Kawakami, M., Tanaka, K., Uriuda, N. & Gondo, S. Effects of nonionic surfactants on electrochemical behavior of ubiquinone and menaquinone incorporated in a carbon paste electrode. *Bioelectrochemistry and Bioenergetics* **52**, 51–56 (2000).

279. Schrebler, R. S., Arratia, A., Sánchez, S., Haun, M. & Durán, N. Electron transport in biological processes. Electrochemical behaviour of ubiquinone Q,10 adsorbed on a pyrolytic graphite electrode. *Bioelectrochemistry and Bioenergetics* **23**, 81–91 (1990).

280. Sęk, S. & Bilewicz, R. Voltammetric probing of molecular assemblies of ubiquinone-10 at the air-water interfaces. *Journal of Inclusion Phenomena* **35**, 55–62 (1999).

281. Laval, J. M. & Majda, M. Electrochemical investigations of the structure and electron transfer properties of phospholipid bilayers incorporating ubiquinone. *Thin Solid Films* **244**, 836–840 (1994).

282. Moncelli, M. R., Becucci, L., Nelson, A. & Guidelli, R. Electrochemical modeling of electron and proton transfer to ubiquinone-10 in a self-assembled phospholipid monolayer. *Biophys J* **70**, 2716–2726 (1996).

283. Moncelli, M. R., Herrero, R., Becucci, L. & Guidelli, R. Kinetics of electron and proton transfer to ubiquinone-10 and from ubiquinol-10 in a self-assembled phosphatidylcholine monolayer. *Biochim Biophys Acta Bioenerg* **1364**, 373–384 (1998).

284. Marchal, D., Boireau, W., Laval, J. M., Moiroux, J. & Bourdillon, C. An electrochemical approach of the redox behavior of water insoluble ubiquinones or plastoquinones incorporated in supported phospholipid layers. *Biophys J* **72**, 2679–2687 (1997).

285. Mårtensson, C. & Agmo Hernández, V. Ubiquinone-10 in gold-immobilized lipid membrane structures acts as a sensor for acetylcholine and other tetraalkylammonium cations. *Bioelectrochemistry* **88**, 171–180 (2012).

286. Hoyo, J., Guaus, E., Oncins, G., Torrent-Burgués, J. & Sanz, F. Incorporation of Ubiquinone in supported lipid bilayers on ITO. *Journal of Physical Chemistry B* **117**, 7498–7506 (2013).

287. Takehara, K., Takemura, H., Ide, Y. & Okayama, S. Electrochemical behavior of ubiquinone and vitamin K incorporated into n-alkanethiol molecular assemblies on a gold electrode. *Journal of Electroanalytical Chemistry* **308**, 345–350 (1991).

288. Shiota, K., Ueki, M. & Osakai, T. A role of the membrane|solution interface in electron transfer at self-assembled monolayer modified electrodes. *Journal of Electroanalytical Chemistry* **745**, 22–27 (2015).

289. Osakai, T., Yamamoto, T. & Ueki, M. Directional Electron Transfer from Ubiquinone-10 to Cytochrome c at a Biomimetic Self-Assembled Monolayer Modified Electrode. *Electrochemistry* **87**, 59–64 (2019).

290. Jeuken, L. J. C. *et al.* Direct electrochemical interaction between a modified gold electrode and a bacterial membrane extract. *Langmuir* **21**, 1481–1488 (2005).

291. Lawrence, K. *et al.* Dioctylamine-Sulfonamide-Modified Carbon Nanoparticles as High Surface Area Substrates for Coenzyme Q10-Lipid Electrochemistry. *Electroanalysis* **24**, 1003–1010 (2012).

292. Ma, W. *et al.* Ubiquinone-quantum dot bioconjugates for in vitro and intracellular complex i sensing. *Sci Rep* **3**, (2013).

293. Arthisree, D. *et al.* A hydrophobic coenzyme Q10 stabilized functionalized-MWCNT modified electrode as an efficient functional biomimetic system for the electron-transfer study. *Colloids Surf A Physicochem Eng Asp* **504**, 53–61 (2016).

294. Barsan, M. M. & Diculescu, V. C. New electrochemical sensor based on CoQ 10 and cyclodextrin complexes for the detection of oxidative stress initiators. *Electrochim Acta* **302**, 441–448 (2019).

295. Kim, R. S. & Chung, T. D. The electrochemical reaction mechanism and applications of quinones. *Bull Korean Chem Soc* **35**, 3143–3155 (2014).

296. Armstrong, J. S., Whiteman, M., Rose, P. & Jones, D. P. The Coenzyme Q10 analog decylubiquinone inhibits the redox-activated mitochondrial permeability transition: role of mitcohondrial [correction mitochondrial] complex III. *J Biol Chem* **278**, 49079–49084 (2003).

297. Bénit, P., Slama, A. & Rustin, P. Decylubiquinol impedes mitochondrial respiratory chain complex I activity. *Mol Cell Biochem* **314**, 45–50 (2008).

298. Telford, J. E., Kilbride, S. M. & Davey, G. P. Decylubiquinone increases mitochondrial function in synaptosomes. *Journal of Biological Chemistry* **285**, 8639–8645 (2010).

299. Casey, J. R., Grinstein, S. & Orlowski, J. Sensors and regulators of intracellular pH. *Nat Rev Mol Cell Biol* **11**, 50–61 (2010).

300. Jaworska, A., Malek, K. & Kudelski, A. Intracellular pH – Advantages and pitfalls of surface-enhanced Raman scattering and fluorescence microscopy – A review. *Spectrochim Acta A Mol Biomol Spectrosc* **251**, (2021).

301. Chambers, J. Q. Electrochemistry of quinones. in *The Quinonoid Compounds, Part 2* (ed. Patai, S.) 737–791 (John Wiley & Sons Ltd., 1974).

302. Chambers, J. Q. Electrochemistry of quinones. in *The Quinonoid Compounds, Part 1* (eds. Patai, S. & Rappoport, Z.) vol. II 719–757 (John Wiley & Sons Ltd., 1988).

303. Dryhurst, G., Kadish, K. M., Scheller, F. & Renneberg, R. Quinones. in *Biological Electrochemistry* (eds. Dryhurst, G., Kadish, K. M., Scheller, F. & Renneberg, R.) vol. I 1–115 (Academic Press Inc., 1982).

304. Laviron, E. Electrochemical reactions with protonations at equilibrium. Part XIII. Experimental study of the homogeneous electron exchange in quinone/dihydroquinone systems. *Journal of Electroanalytical Chemistry* **208**, 357–372 (1986).

305. Sasaki, K., Kashimura, T., Ohura, M., Ohsaki, Y. & Ohta, N. Solvent Effect in the Electrochemical Reduction of p-Quinones in Several Aprotic Solvents. *J Electrochem Soc* **137**, 2437–2443 (1990).

306. Emons, H., Wittstock, G., Voigt, B. & Seidel, H. Voltammetric trace determination of ubiquinones at mercury electrodes. *Fresenius J Anal Chem* **342**, 737–739 (1992).

307. Nagy, P. I. Competing intramolecular vs. Intermolecular hydrogen bonds in solution. *Int J Mol Sci* **15**, 19562–19633 (2014).

308. Itoh, S. *et al.* An active site model for calcium(II)-containing quinoproteins. *J Chem Soc Chem Commun* 2077–2078 (1995).

309. Itoh, S., Kawakami, H. & Fukuzumi, S. Modeling of the chemistry of quinoprotein methanol dehydrogenase. Oxidation of methanol by calcium complex of coenzyme PQQ via addition-elimination mechanism. *J Am Chem Soc* **119**, 439–440 (1997).

310. Itoh, S., Kawakami, H. & Fukuzumi, S. Catalysis by calcium ion of the reoxidation of reduced PQQ by molecular oxygen. *Chemical Communications* 29–30 (1997).

311. Itoh, S., Kawakami, H. & Fukuzumi, S. Model studies on calcium-containing quinoprotein alcohol dehydrogenases. Catalytic role of Ca2+ for the oxidation of alcohols by coenzyme PQQ (4,5-dihydro-4,5-dioxo-1H-pyrrolo[2,3-f]quinoline-2,7,9-tricarboxylic acid). *Biochemistry* **37**, 6562–6571 (1998).

312. Wanner, M., Sixt, T., Klinkhammer, K.-W. & Kaim, W. First experimental structure of a 1:1 metal complex with a PQQ cofactor derivative outside dehydrogenase enzymes. *Inorg Chem* **38**, 2753–2755 (1999).

313. Ernst, S. *et al.* Stable Binuclear o- and p-Semiquinone Complexes of [Ru(bpy)2]2+. Radical Ion versus Mixed Valence Dimer Formulation. *J Am Chem Soc* **111**, 1733–1738 (1989).

314. Fukuzumi, S. & Ohkubo, K. Metal ion-coupled and decoupled electron transfer. *Coord Chem Rev* **254**, 372–385 (2010).

315. Kim, Y. R. *et al.* Modulation of quinone PCET reaction by Ca2+ ion captured by calix[4]quinone in water. *J Am Chem Soc* **135**, 18957–18967 (2013).

316. Wang, J. *et al.* The Impact of "Effective pH" on the Voltammetric Behavior of p - Benzoquinone and Hydroquinone in Acetonitrile. *J Electrochem Soc* **163**, H201–H204 (2016).

317. Martin, R. B. Bioinorganic chemistry of calcium. in *Metal Ions in Biological Systems Volume 17: Calcium and its Role in Biology* (ed. Sigel, H.) vol. 17 1–51 (CRC Press, 1984).

318. Einspahr, H. & Bugg, C. E. Crystal structure studies of calcium complexes and implications for biological systems. in *Metal Ions in Biological Systems Volume 17: Calcium and its Role in Biology* (ed. Sigel, H.) vol. 17 51–99 (CRC Press, 1984).

319. Cirilli, I. *et al.* Role of coenzyme q10 in health and disease: An update on the last 10 years (2010–2020). *Antioxidants* **10**, (2021).

320. Paroha, S., Chandel, A. K. S. & Dubey, R. D. Nanosystems for drug delivery of coenzyme Q10. *Environ Chem Lett* **16**, 71–77 (2018).

321. Pastor-Maldonado, C. J. *et al.* Coenzyme q10: Novel formulations and medical trends. *Int J Mol Sci* **21**, 1–23 (2020).

322. Kishi, T., Okamoto, T., Takahashi, T., Goshima, K. & Yamagami, T. Cardiostimulatory action of coenzyme Q homologues on cultured myocardial cells and their biochemical mechanisms. *Clin Investig* **71**, (1993).

323. Takahashi, T., Mine, Y. & Okamoto, T. Intracellular reduction of coenzyme Q homologues with a short isoprenoid side chain induces apoptosis of HeLa cells. *J Biochem* **163**, 329–339 (2018).

324. Esaka, Y., Nagahara, Y., Hasome, Y., Nishio, R. & Ikekita, M. Coenzyme Q2 induced p53-dependent apoptosis. *Biochim Biophys Acta Gen Subj* **1724**, 49–58 (2005).

325. Chan, T. S. *et al.* Coenzyme Q cytoprotective mechanisms for mitochondrial complex I cytopathies involves NAD(P)H: Quinone oxidoreductase 1(NQO1). *Free Radic Res* **36**, 421–427 (2002).

326. Degli Esposti, M. *et al.* The specificity of mitochondrial complex I for ubiquinones. *Biochemical Journal* **313**, 327–334 (1996).

327. Bergamini, C., Moruzzi, N., Sblendido, A., Lenaz, G. & Fato, R. A water soluble CoQ 10 formulation improves intracellular distribution and promotes mitochondrial respiration in cultured cells. *PLoS One* **7**, (2012).

328. Sazanov, L. A. A giant molecular proton pump: Structure and mechanism of respiratory complex I. *Nat Rev Mol Cell Biol* **16**, 375–388 (2015).

329. Van Vranken, J. G., Na, U., Winge, D. R. & Rutter, J. Protein-mediated assembly of succinate dehydrogenase and its cofactors. *Crit Rev Biochem Mol Biol* **50**, 168–180 (2015).

330. Erb, M. *et al.* Features of idebenone and related short-chain quinones that rescue ATP levels under conditions of impaired mitochondrial complex I. *PLoS One* **7**, (2012).

331. Skowronek, M., Jemioła-Rzemińska, M., Kruk, J. & Strzałka, K. Influence of the redox state of ubiquinones and plastoquinones on the order of lipid bilayers studied by fluorescence anisotropy of diphenylhexatriene and trimethylammonium diphenylhexatriene. *Biochim Biophys Acta Biomembr* **1280**, 115–119 (1996).

332. Andersen, O. S. & Koeppe, R. E. Bilayer thickness and membrane protein function: An energetic perspective. *Annu Rev Biophys Biomol Struct* **36**, 107–130 (2007).

333. Torres, M. J. *et al.* 17β-Estradiol Directly Lowers Mitochondrial Membrane Microviscosity and Improves Bioenergetic Function in Skeletal Muscle. *Cell Metab* **27**, 167-179.e7 (2018).

334. Budin, I. *et al.* Viscous control of cellular respiration by membrane lipid composition. *Science (1979)* **362**, 1186–1189 (2018).

335. Dumas, D. *et al.* Membrane fluidity and oxygen diffusion in cholesterol-enriched erythrocyte membrane. *Arch Biochem Biophys* **341**, 34–39 (1997).

336. Binder, H. & Zschörnig, O. The effect of metal cations on the phase behavior and hydration characteristics of phospholipid membranes. *Chem Phys Lipids* **115**, 39–61 (2002).

337. Pedersen, U. R., Leidy, C., Westh, P. & Peters, G. H. The effect of calcium on the properties of charged phospholipid bilayers. *Biochim Biophys Acta Biomembr* **1758**, 573–582 (2006).

338. Melcrová, A. *et al.* The complex nature of calcium cation interactions with phospholipid bilayers. *Sci Rep* **6**, (2016).

339. Conrard, L. & Tyteca, D. Regulation of membrane calcium transport proteins by the surrounding lipid environment. *Biomolecules* **9**, (2019).

340. Boettcher, J. M. *et al.* Atomic view of calcium-induced clustering of phosphatidylserine in mixed lipid bilayers. *Biochemistry* **50**, 2264–2273 (2011).

341. Akutsu, H. & Seelig, J. Interaction of Metal Ions with Phosphatidylcholine Bilayer Membranes. *Biochemistry* **20**, 7366–7373 (1981).

342. Mirza, M., Guo, Y., Arnold, K., Van Oss, C. J. & Ohki, S. Hydrophobizing effect of cations on acidic phospholipid membranes. *J Dispers Sci Technol* **19**, 951–962 (1998).

343. Sauerheber, R. D., Lewis, U. J., Esgate, J. A. & Gordon, L. M. Effect of calcium, insulin and growth hormone on membrane fluidity. A spin label study of rat adipocyte and human erythrocyte ghosts. *BBA - Biomembranes* **597**, 292–304 (1980).

344. Marchi, S. & Pinton, P. The mitochondrial calcium uniporter complex: Molecular components, structure and physiopathological implications. *Journal of Physiology* **592**, 829–839 (2014).

345. De La Fuente, S. *et al.* Spatial Separation of Mitochondrial Calcium Uptake and Extrusion for Energy-Efficient Mitochondrial Calcium Signaling in the Heart. *Cell Rep* **24**, 3099-3107.e4 (2018).

346. Xu, Z. *et al.* Coenzyme Q10 improves lipid metabolism and ameliorates obesity by regulating CaMKIIMediated PDE4 inhibition. *Sci Rep* **7**, (2017).

347. Leo, S., Szabadkai, G. & Rizzuto, R. The mitochondrial antioxidants MitoE2 and MitoQ10 increase mitochondrial Ca2+ load upon cell stimulation by inhibiting Ca2+ efflux from the organelle. *Ann N Y Acad Sci* **1147**, 264–274 (2008).

348. Yoon, N. G. *et al.* Mitoquinone Inactivates Mitochondrial Chaperone TRAP1 by Blocking the Client Binding Site. *J Am Chem Soc* **143**, 19684–19696 (2021).

349. Penny, C. J., Kilpatrick, B. S., Han, J. M., Sneyd, J. & Patel, S. A computational model of lysosome-ER Ca2+ microdomains. *J Cell Sci* **127**, 2934–2943 (2014).

350. Fontaine, E., Ichas, F. & Bernardi, P. A ubiquinone-binding site regulates the mitochondrial permeability transition pore. *Journal of Biological Chemistry* **273**, 25734–25740 (1998).

351. Devun, F. *et al.* Ubiquinone analogs: A mitochondrial permeability transition pore-dependent pathway to selective cell death. *PLoS One* **5**, 1–8 (2010).

352. Bernardi, P., Carraro, M. & Lippe, G. The mitochondrial permeability transition: Recent progress and open questions. *FEBS Journal* **289**, 7051–7074 (2022).

353. Hac-Wydro, K. & Wydro, P. The influence of fatty acids on model cholesterol/phospholipid membranes. *Chem Phys Lipids* **150**, 66–81 (2007).

354. Nicolson, G. L. Mitochondrial dysfunction and chronic disease: treatment with natural supplements. *Altern Ther Health Med* **20 Suppl 1**, 18–25 (2014).

355. Raffaello, A. & Rizzuto, R. Mitochondrial longevity pathways. *Biochim Biophys Acta Mol Cell Res* **1813**, 260–268 (2011).

356. Bratic, A. & Larsson, N. G. The role of mitochondria in aging. *Journal of Clinical Investigation* **123**, 951–957 (2013).

357. Zielonka, J. *et al.* Mitochondria-Targeted Triphenylphosphonium-Based Compounds: Syntheses, Mechanisms of Action, and Therapeutic and Diagnostic Applications. *Chem Rev* **117**, 10043–10120 (2017).

358. Zinovkin, R. A. & Zamyatnin, A. A. Mitochondria-Targeted Drugs. *Curr Mol Pharmacol* **12**, 202–214 (2018).

359. Wang, J. Y., Li, J. Q., Xiao, Y. M., Fu, B. & Qin, Z. H. Triphenylphosphonium (TPP)-Based Antioxidants: A New Perspective on Antioxidant Design. *ChemMedChem* **15**, 404–410 (2020).

360. Weissig, V. Drug Development for the Therapy of Mitochondrial Diseases. *Trends Mol Med* **26**, 40–57 (2020).

361. Neuzil, J. *et al.* Mitochondria transmit apoptosis signalling in cardiomyocyte-like cells and isolated hearts exposed to experimental ischemia-reperfusion injury. *Redox Report* **12**, 148–162 (2007).

362. Ghosh, A. *et al.* Neuroprotection by a mitochondria-targeted drug in a Parkinson's disease model. *Free Radic Biol Med* **49**, 1674–1684 (2010).

363. Yancey, D. M. *et al.* Cardiomyocyte mitochondrial oxidative stress and cytoskeletal breakdown in the heart with a primary volume overload. *Am J Physiol Heart Circ Physiol* **308**, H651–H663 (2015).

364. Oliver, D. M. A. & Reddy, P. H. Small molecules as therapeutic drugs for Alzheimer's disease. *Molecular and Cellular Neuroscience* **96**, 47–62 (2019).

365. Ribeiro Junior, R. F. *et al.* MitoQ improves mitochondrial dysfunction in heart failure induced by pressure overload. *Free Radic Biol Med* **117**, 18–29 (2018).

366. Goh, K. Y. *et al.* Mitoquinone ameliorates pressure overload-induced cardiac fibrosis and left ventricular dysfunction in mice. *Redox Biol* **21**, (2019).

367. Young, M. L. & Franklin, J. L. The mitochondria-targeted antioxidant MitoQ inhibits memory loss, neuropathology, and extends lifespan in aged 3xTg-AD mice. *Molecular and Cellular Neuroscience* **101**, (2019).

368. Gottwald, E. M. *et al.* The targeted anti-oxidant MitoQ causes mitochondrial swelling and depolarization in kidney tissue. *Physiol Rep* **6**, (2018).

369. Fink, B. D. *et al.* Mitochondrial targeted coenzyme Q, superoxide, and fuel selectivity in endothelial cells. *PLoS One* **4**, (2009).

370. Rao, V. A. *et al.* The antioxidant transcription factor Nrf2 negatively regulates autophagy and growth arrest induced by the anticancer redox agent mitoquinone. *Journal of Biological Chemistry* **285**, 34447–34459 (2010).

371. Pokrzywinski, K. L., Biel, T. G., Kryndushkin, D. & Rao, V. A. Therapeutic Targeting of the Mitochondria Initiates Excessive Superoxide Production and Mitochondrial Depolarization Causing Decreased mtDNA Integrity. *PLoS One* **11**, (2016).

372. Plotnikov, E. Y. & Zorov, D. B. Pros and cons of use of mitochondria-targeted antioxidants. *Antioxidants* **8**, (2019).

373. Reily, C. *et al.* Mitochondrially targeted compounds and their impact on cellular bioenergetics. *Redox Biol* **1**, 86–93 (2013).

374. James, A. M., Cochemé, H. M., Smith, R. A. J. & Murphy, M. P. Interactions of mitochondria-targeted and untargeted ubiquinones with the mitochondrial respiratory chain and reactive oxygen species: Implications for the use of exogenous ubiquinones as therapies and experimental tools. *Journal of Biological Chemistry* **280**, 21295–21312 (2005).

375. Doughan, A. K. & Dikalov, S. I. Mitochondrial redox cycling of mitoquinone leads to superoxide production and cellular apoptosis. *Antioxid Redox Signal* **9**, 1825–1836 (2007).

376. O'Malley, Y., Fink, B. D., Ross, N. C., Prisinzano, T. E. & Sivitz, W. I. Reactive oxygen and targeted antioxidant administration in endothelial cell mitochondria. *Journal of Biological Chemistry* **281**, 39766–39775 (2006).

377. Kafkova, A. *et al.* Selective and reversible disruption of mitochondrial inner membrane protein complexes by lipophilic cations. *Mitochondrion* **68**, 60–71 (2023).

378. Elkalaf, M., Tuma, P., Weiszenstein, M., Polák, J. & Trnka, J. Mitochondrial Probe Methyltriphenylphosphonium (TPMP) Inhibits the Krebs Cycle Enzyme 2- Oxoglutarate Dehydrogenase. *PLoS One* **11**, (2016).

379. Rodriguez-Cuenca, S. *et al.* Consequences of long-term oral administration of the mitochondria-targeted antioxidant MitoQ to wild-type mice. *Free Radic Biol Med* **48**, 161–172 (2010).

380. Finichiu, P. G., James, A. M., Larsen, L., Smith, R. A. J. & Murphy, M. P. Mitochondrial accumulation of a lipophilic cation conjugated to an ionisable group depends on membrane potential, pH gradient and pK a: Implications for the design of mitochondrial probes and therapies. *J Bioenerg Biomembr* **45**, 165–173 (2013).

381. Finichiu, P. G. *et al.* A mitochondria-targeted derivative of ascorbate: MitoC. *Free Radic Biol Med* **89**, 668–678 (2015).

382. Pala, L. *et al.* Enhancing the Mitochondrial Uptake of Phosphonium Cations by Carboxylic Acid Incorporation. *Front Chem* **8**, (2020).

383. Prag, H. A. *et al.* Selective Delivery of Dicarboxylates to Mitochondria by Conjugation to a Lipophilic Cation via a Cleavable Linker. *Mol Pharm* **17**, 3526–3540 (2020).

Publications

Barayeu U., Schilling D., Eid M., Xavier da Silva T. N., Schlicker L., **Mitreska N.**, Zapp C., Gräter F., Miller A.K., Kappl R., Schulze A., Friedmann Angeli J.P., Dick T.P. (2023) Hydropersulfides inhibit lipid peroxidation and ferroptosis by scavenging radicals. *Nat Chem Biol*, *19*, 28-37.

Mirceski, V., Mitrova, B., Ivanovski, V., **Mitreska N.**, Aleksovska A., Gulaboski R. (2015) Studying the ion transfer across liquid interface of thin organic-film-modified electrodes in the presence of glucose oxidase. *J Solid State Electrochem*, *19*, 2331-2342.

Mirceski V., Aleksovska A., Pejova B., Ivanovski V., Mitrova B., **Mitreska N.**, Gulaboski R. (2014) Thiol anchoring and catalysis of gold nanoparticles at the liquid interface of thin-organic film-modified electrodes. *Electrochemistry Communications*, *39*, 5-8.

Aleksovska A., Bukleski M., Mavromihailov I., **Mitreska N.**, Petruševski V.M.*, Radevska M., Stojanovska M., Tanatarec J. (2012) An Evening with Magic: Eight Colorless Liquids. *Chem. Educator*, *17*, 203-205.

Mitreska N., Stankoska K., Gulaboski R., Mirčeski V., Bogeski I., Hoth M., Kappl R. Redox properties and calcium affinity of coenzyme Q_1, decylubiquinone and their mono-hydroxylated derivatives. (*in preparation*)

Mitreska N., Stankoska K., Slowik E. J., Gulaboski R., Mirčeski V., Bogeski I., Bozem M., Hoth M., Kappl R. The impact of mono-hydroxylated forms of Q_1, decylubiqinone and related quinones on cellular metabolism. (*in preparation*)

Conferences

XXV International Symposium on Bioelectrochemistry and Bioenergetics.
26-30 May 2019, Limerick, Ireland
Mitreska N., Stankoska K., Slowik E. J., Gulaboski R., Mirčeski V., Bogeski I., Hoth M., Kappl R.: Hydrogen bonding and Ca^{2+} affinity of coenzyme Q_1 and decylubiquinone.

XXIV International Symposium on Bioelectrochemistry and Bioenergetics.
3-7 July 2017, Lyon, France.
Stankoska K., **Mitreska N.**, Slowik E. J., Gulaboski R., Mirčeski V., Bogeski I., Hoth M., Kappl R.: Electrochemical study of CoQs and their hydroxylated derivatives.

116th General Assembly of the German Bunsen Society for Physical Chemistry.
25-27 May 2017, Kaiserslautern, Germany
Slowik E. J., Stankoska K., **Mitreska N.**, Reindl K., Gulaboski R., Mirceski V., Hoth M., Bogeski I., Kappl R.: Exploring the properties of hydroxylated coenzyme Q and its analogues.

13th Leipzig Research Festival for Life Sciences.
18 December 2014, Leipzig, Germany
Mitreska N., Oehme R., Birkemeyer C.: Electrospray ionization mass spectrometric studies of iron and zinc complexes with *p*-benzoquinones/hydroquinones.

Acknowledgements

Completing my doctorate has been one of the most rewarding activities in my life thus far, and I still find it hard to believe that I have reached this milestone.

I would like to express my deepest gratitude to my supervisor Dr. Reinhard Kappl for his constant guidance, support, and encouragement throughout the entire period. I am grateful for the freedom he gave me in my work and for every advice and help he provided me, professionally and personally. Reinhard thank you for going far and beyond your duties as supervisor to make my life in Germany as smooth as possible.

I owe a tremendous debt of gratitude to Dr. Monika Bozem who has helped me to overcome challenges, generously provided her expertise, and support on all levels. This thesis would not be anywhere near the quality it is without her assistance. Monika thank you for your unwavering belief in me and for never giving up on me.

I would like to thank Prof. Dr. Markus Hoth who welcomed me in his working group and gave me an opportunity to be a part of an outstanding research team. Markus thank you for your constant interest, not only in the work but also in the well-being of all your group members, and for the warm and friendly working atmosphere, rarely found in academia.

I am grateful to DAAD for providing me with the opportunity to do my doctoral studies in Germany as well as for all the resources and financial support they provided, not just during these studies but also in my overall education.

My gratitude is also extended to my office colleagues for the great time and the many discussions: Katerina Stankoska, Dr. Ewa Slowik, Dr. Phillip Knapp, Hannah Heintz and Sofia Schnell. My special thanks go to Phillip for teaching me cell culture and fluorescence microscopy.

Special thanks to the people who have collaborated on my project, moving it forward: Dr. Jozef Zapp for the NMR measurements and Prof. Dr. Markus R. Meyer for the MS experiments.

Thanks to Regine Kaleja for her assistance with official paperwork from the initial enrolment at the University to the final step-submission of this thesis.

Thanks to PD Dr. rer. nat. Dalia Alansary for her help with Ca-imaging experiments and data analysis, and most importantly for showing me the green side of Homburg and keeping me fit. Dalia thank you for all the enjoyable bike tours and long forest walks, I will certainly miss these moments.

Thanks to Prof. Dr. Leticia Prates Roma and her team for being such a wonderful group of people. Leticia thank you for including me in all your team activities both in and out of the lab. Meeting you and all the people that you brought in the lab was the silver lining in my monotonic life in Homburg. Special thanks to Christopher Carlein and Markus Hoffmann for being the best lab mates and friends, for the encouraging and motivating words, for all the laughs and joys, for all their support and help in improving my skills in German.

To my former professor from Macedonia Prof. Dr. Valentin Mirceski not only for arousing my interest in scientific research but also for providing help and support all these years.

My heartfelt gratitude goes to my friends and family who have been my pillars of strength all these years.

To Igor, Bisera, Goran, Joana, Tome and Elena for their uplifting words and for always being there for me, although km apart.

To my aunt Mitana for being my biggest cheerleader throughout these years.

To my sisters, Natasha and Violeta, for always believing in me and encouraging me to follow my dreams.

To my parents whose love and support are with me in whatever I pursue.

Curriculum Vitae

The curriculum vitae was removed from the electronic version of the doctoral thesis for reasons of data protection.